Structural evolution during the preparation and heating of nanophase zirconia gels

A thesis submitted in fulfilment of the requirements for the degree of Doctor of Philosophy

by

Peter Southon

University of Technology, Sydney

November 2000

Certificate of authorship and originality

I certify that the work in this thesis has not previously been submitted for a degree, nor has it been submitted as part of requirements for a degree, except as fully acknowledged within the text.

I also certify that the thesis has been written by me. Any help that I have received in my research work and the preparation of the thesis itself has been acknowledged. In addition, I certify that all information sources and literature used are indicated in the thesis.

Acknowledgments

In the researching and writing of this thesis I have been helped by a great many people in many ways, only a few of whom I can acknowledge on this page.

I would first like to thank my supervisor, Associate Professor Besim Ben-Nissan, for his encouragement, guidance, and confidence in me. Secondly, this work could not have been completed without the invaluable advice and assistance from a number of people in the ANSTO Materials Division: Dr. Jim Woolfrey (co-supervisor), Dr. John Bartlett, Dr. Victor Luca, Dr. Kim Finnie and David Cassidy. They have generously given me a grounding in their respective fields of expertise, from which this thesis has grown.

There are many other colleagues who I would like to thank for practical assistance, discussion, advice and friendship (all are affiliated with ANSTO except where indicated):

Anton Stampfl (ASRP), Bill Bertram, Christophe Barbé, David Mitchell, Dick Ashby (formerly UTS), Elizabeth Drabarek, Erden Sizgek, Frank Van Luyt, Gary Foran (ASRP), Gerry Triani, James Hester (ASRP), Jin Wang (SRICAT), Professor John White (ANU), Jonathan Watson, Kamali Kannangara (UTS), Kath Smith, Laurie Aldridge, Mark Blackford, Mike Colella, Naomi Haworth (USyd), Peter Lee (SRICAT), Puyam Singh (formerly ANU), Terry Sabine, Therese Donlevy, Trevor Dowling (ANU) and the ANSTO library staff . To thank all these people properly would take a book in itself.

I am indebted to my family and friends for their love, encouragement, understanding and patience during this long journey. Most especially I would like to thank my wife, Rochelle, and my parents, Gray and Ngaire, for their unstinting support throughout, which kept me going to the end. Thanks also to my friends Vanessa, Renée and Harriet, who made life in the Sol-Gel group so much more lively. Above all, I thank our saving God for giving me all these people to help and encourage me, and for the skills and opportunity to complete this thesis.

I would like to acknowledge the support of the Commonwealth Government in providing an Australian Postgraduate Award, and that of the Australian Institute for Nuclear Science and Engineering for giving me a Postgraduate Research Award, which provided me access to ANSTO facilities. I would also like to acknowledge the support of ANSTO Materials Division.

Access to synchrotron beam-lines at the Photon Factory and the Advanced Photon Source was provided by the Australian Synchrotron Research Program, which is funded by the Commonwealth of Australia under the Major National Research Facilities Program. Use of the Advanced Photon Source was supported by the U.S. Department of Energy, Basic Energy Sciences, Office of Energy Research, under Contract No. W-31-109-Eng-38.

ANSTO: Australian Nuclear Science and Technology Organisation
ANU: Australian National University
ASRP: Australian Synchrotron Research Program
SRICAT: Synchrotron Research Instrumentation Collaborative Access Team (Advanced Photon Source)
USyd: University of Sydney
UTS: University of Technology, Sydney

Abstract

The chemical preparation of ceramic materials has been widely studied over the past few decades, and provides the potential for excellent control over the microstructure and properties of the final product. This control is dependent on a comprehensive understanding of the microstructure and physical/chemical processes that occur at each stage. Aqueous routes have much potential for adoption by industry, but in many cases a comprehensive understanding of the microstructure and chemistry is lacking, partly due to the complicated aqueous chemistry of many transition-metals.

This investigation has focussed on a specific inorganic, aqueous, sol-gel route for the preparation of pure zirconia (ZrO_2). Zirconia is a ceramic with a wide range of current and potential applications, such as catalysis, fuel-cells, coatings and biomaterials. The emphasis has been placed on the characterisation of the structure at each stage of the route, leading to an understanding of the various mechanisms that are at work. This project has also provided an opportunity to investigate broader issues concerning the solution-based processing of zirconia, particularly those involving the 'metastable' tetragonal phase. This phase is frequently observed to be formed by non-equilibrium methods, but the mechanisms of formation and de-stabilisation are not properly understood.

The studied route consists of a number of stages: the preparation of an aqueous *sol* of 'zirconium hydroxide' particles by forced hydrolysis of a zirconyl nitrate solution; the conversion of the sol to a *gel* by removal of the aqueous phase; the conversion of the gel to a crystalline tetragonal zirconia powder by heating; and transformation of the tetragonal phase to the stable monoclinic phase with further treatment. At each stage of processing a number of aspects of the material structure have been investigated, including the short-range order, crystalline lattice parameters, particle packing, porosity, and speciation of the nitrate anion. This has required a wide range of complementary characterisation techniques, including Raman spectroscopy, XRD, TEM, DTA/TGA, SAXS, dynamic light scattering, EXAFS, NMR, and nitrogen sorption. The importance of techniques that allow changes in structure to be characterised *in-situ* during heating has been emphasised.

The particles in the sol and gel are plate-shaped, approximately 0.5 nm thick and 3 - 4 nm across. They are composed of up to several stacked 'sheets' of zirconium hydroxide, each of which is composed of zirconium atoms arranged in a regular square lattice, joined by double hydroxy-bridges. Detailed evidence for this structure has not been previously reported.

The stages of decomposition of the precursor have been elucidated, including the stages at which oxolation and loss of nitrate occur. The complex crystallisation process at 450°C has been investigated, and a structural mechanism for crystallisation of the 'metastable' tetragonal phase proposed, based on similarities between the tetragonal crystal structure and the disordered sheet structure in the amorphous material just prior to crystallisation. The crystalline material consists of nano-sized crystals, containing unusual intracrystalline mesopores.

The lattice parameters of the tetragonal phase change with increasing heat-treatment, with the unit-cell tetragonality (c/a) increasing from 1.017 to 1.020. This is a previously-unreported phenomenon which may be associated with the stability of the phase. The tetragonal phase transforms to the monoclinic phase after heating to a 'critical temperature' between 900 and 950°C; this temperature is associated with the loss of residual surface nitrate species and/or a substantial increase in the mass diffusion rate. The crystal size and surface area has little influence on the tetragonal-to-monoclinic transformation, a result which is contrary to much previously-published work and that has significant implications for certain theories explaining the stability of the tetragonal phase. The transformation itself occurs during cooling, over a range between 400 and 100°C, and has been studied *in-situ* by time-resolved Raman spectroscopy.

The conclusions of this investigation contribute not only to the understanding of this particular route for processing zirconia, but also to a broader understanding of aqueous zirconium systems, the chemical processing of zirconia, and the tetragonal-to-monoclinic zirconia transformation mechanisms.

Table of contents

1. Introduction

Zirconia

Zirconium oxide (ZrO_2) is a colourless, inorganic compound, which is used as a major component in certain engineering ceramics. When used as a ceramic, the oxide is generally known as *zirconia*.

Zirconia-based ceramics have many desirable properties and potential applications. Zirconia is chemically inert under many conditions, but may be treated by sulfur to become catalytically active. The mechanical properties of pure zirconia are not highly attractive, but when alloyed with certain other oxides, it gains high strength and exceptionally high fracture toughness for a ceramic. The mechanical properties are strongly affected by composition and microstructure,[1] and can thus be tailored. Like most transition-metal oxides, zirconia possesses very high melting and softening points, and is also a good thermal insulator. It is also an electrical insulator at ambient temperature, but when alloyed with trivalent oxides to form oxygen vacancies, it becomes an ionic conductor at high temperature. Even the optical properties of zirconia are useful, being colourless, transparent, and possessing a high refractive index.

It is the combination of these properties, and the ability to tailor the structure, that make zirconia-based ceramics suitable for a very wide range of applications. Some examples are: wear-resistant or load-bearing structural components, wear or corrosion-resistant coatings, refractories, medical implants, optical films, toughening components in nanocomposites, catalysts, catalyst supports, and ionic conductors in solid-oxide fuel cells.

Chemical synthesis of ceramics from solution

The chemical synthesis of ceramics from solution has been an area of considerable interest for two decades.[2-8] Solution-based routes have a number of distinguishing characteristics:

1. All such routes begin with **chemically reactive precursors**, containing the components that are to be incorporated into the final product. The ease by which many precursor chemicals can be purified, in comparison to oxide powders, makes chemical routes highly attractive for preparing ceramics where composition must be closely controlled.

2. The importance of **reaction chemistry** and the **structure of intermediate materials** on the structure and properties of the product cannot be under-emphasised. It is vital to understand these aspects at each stage of the process, in order to control the properties of the product.

3. The reactions that occur are frequently **non-equilibrium**, and occur at much **lower temperature** than conventional ceramic powder processing. The control over reaction kinetics that this provides means that various *metastable* phases may be prepared that cannot produced by other routes. Furthermore, this approach also permits the synthesis of materials that are only stable at relatively low temperatures.

4. Any crystalline oxide produced generally possesses a very **small crystal size**,* which has a number of important implications. Rapid and uniform sintering may be achieved, leading to a reduced defect density. This also means that further processing may take place at lower temperatures, reducing costs and allowing better control over the mesostructure, and even leading to entirely different material properties.

5. Excellent **control over composition** can be achieved, most notably in the preparation of multicomponent oxides that are homogenous at a near-atomic scale. Monoliths with a gradient composition are also possible to prepare.

6. A range of mechanisms allow excellent **control over porosity** and other mesostructures, and a very wide range of densities can be achieved. Different processes can produce ceramic bodies that are very close to theoretical density after sintering, or extremely low-density aerogels. The formation of an oxide around organic 'templates' allows the preparation of materials with very precisely controlled mesostructure, and open frameworks such as zeolites.

7. Finally, in many routes the oxide can be formed into a wide **range of shapes** without firing, either as an intermediate stage, or to form a final product. Examples include uniform sub-micron powders, microspheres, thin films, multilayer films, nanocomposites, fibres, and monoliths (*via* gel-casting).

These characteristics give solution-based ceramic synthesis a very great potential, which is well recognised.

The solution-based preparation of zirconia

A great many different routes for the solution-based preparation of zirconia have been reported in the literature, using a range of precursor chemicals (inorganic and metal-organic),

* Although hydrothermal conditions may allow *very large* crystals to be grown.

media (aqueous or non-aqueous) and methods (*e.g.* chemical precipitation, hydrothermal), leading to products with a wide range of structures (*e.g.* thin films, uniform powders).

Although many of these routes have been extensively studied, there are still many unresolved questions. Some of these questions are related to the short- and medium-range structure of any intermediate 'amorphous'[*] phase that is formed during the process; how this structure is formed, its relationship to the structure of the precursor chemicals, and how it changes with further thermal treatment.

Other questions relate to the crystallisation and stability of the 'metastable' tetragonal zirconia phase. The formation of this phase from solution-based routes is very common but, although it has been widely studied, there is little consensus on a mechanism for its formation or an explanation for its transformation to a stable phase.

These issues are all discussed in detail in the literature review in Chapter 2.

Inorganic, aqueous, sol-gel routes for zirconia

This thesis concentrates on a processing route that is distinguished by three major characteristics: Firstly, it is entirely inorganic, with no organic or metal-organic reactants. Secondly, it is aqueous based. Thirdly, it is a true *sol-gel*[†] process, which produces a stable, aqueous, colloidal *sol*,[‡] which reversibly aggregates to form an amorphous *gel*.[§]

All three of these characteristics have certain advantages, particularly for large-scale commercial processing of zirconia-containing ceramics. Inorganic precursors are readily available and relatively inexpensive, and the use of water as a solvent is attractive on the grounds of convenience, cost, and the effect on the natural environment.

---

[*] The term *amorphous* in this thesis will be used in the broad sense to describe a material with no long-range order, such as that which leads to diffraction. Amorphous materials may still have considerable short-range order.

[†] Strictly speaking, the term *sol-gel process* should only be applied to those procedures which yield gel materials after formation of a true sol. However, in practice the term *sol-gel* is often loosely used for a much wider range of processes, broadly all solution-based preparations of ceramic materials involving hydrolysis reactions to form colloidal particles and/or a gel.

[‡] A *sol* may be loosely defined as a stable dispersion of colloidal particles in a fluid. Colloidal particles are characterised by primary dimensions roughly between 1 nm and 1 μm.[7]

[§] A *gel* is a 'solid' three-dimensional network, of colloidal dimensions, that extends throughout a second, continuous liquid phase.[7] A gel may be formed when a sol is destabilised, with the colloidal particles aggregating to form the network. The physical properties of a gel may vary widely, according to the relative volume of the two phases, and the nature of the bonding in the network (primary bonds, van der Waal's forces, entanglements, *etc*).

Sol-gel routes have advantages over other solution-based processes that, for instance, form a precipitated gel or fine oxide powders. Stable sols may be readily mixed to form homogenous mixed oxides, and the gelation process may be controlled to form a gel product in the shape of microspheres, films, or fibres. If the gelation process is physical, then it may also be reversed; mis-shaped products may be redispersed, and sols may even be gelled in bulk for storage, then redispersed for processing.[2]

Aqueous 'sol-gel' routes for the processing of zirconia have been studied and used for many decades.[2] However, very little has been published in the literature over the last 10 years, and aqueous routes in general have been largely eclipsed by the strong interest in routes using metal-organic precursors.

Aims and approach of the thesis

There are two broad aims of this thesis. The first is to investigate some of the above-mentioned fundamental questions concerning the solution-based processing of zirconia. The second aim is to investigate a specific inorganic, aqueous, sol-gel route for the preparation of zirconia, which may be commercially viable, so the knowledge gained could be put to immediate practical use.

The approach used is to study the chosen preparation route, in detail, over all stages from the precursor chemicals to the crystalline zirconia, focusing on the *structure* of the material at each stage of the route. In this way an overall picture is gained of the reactions and changes in structure for this route, while also investigating some of the more fundamental questions concerning the chemical processing of zirconia.

A thorough investigation of structure requires the application of a range of complementary characterisation techniques. The use wherever possible of *in-situ* characterisation techniques is important, in order to gain a complete picture of the interaction of various stages. Important techniques include Raman spectroscopy, X-ray diffraction (XRD), transmission electron microscopy (TEM), differential thermal and thermogravimetric analysis (DTA/TGA), small-angle X-ray scattering (SAXS), dynamic light scattering (DLS), extended X-ray absorption fine-structure (EXAFS) spectroscopy, and nuclear magnetic resonance (NMR).

The particular route studied is fully discussed in Chapter 3, along with its various advantages and disadvantages with respect to other routes. A flow chart, showing each stage that is studied in the thesis, is given in Figure 1-1. Chapters 3 through to 7 follow the evolution of the structure through each stage of the process. Each chapter examines a particular stage, and in this way an overall picture of the route is built up.

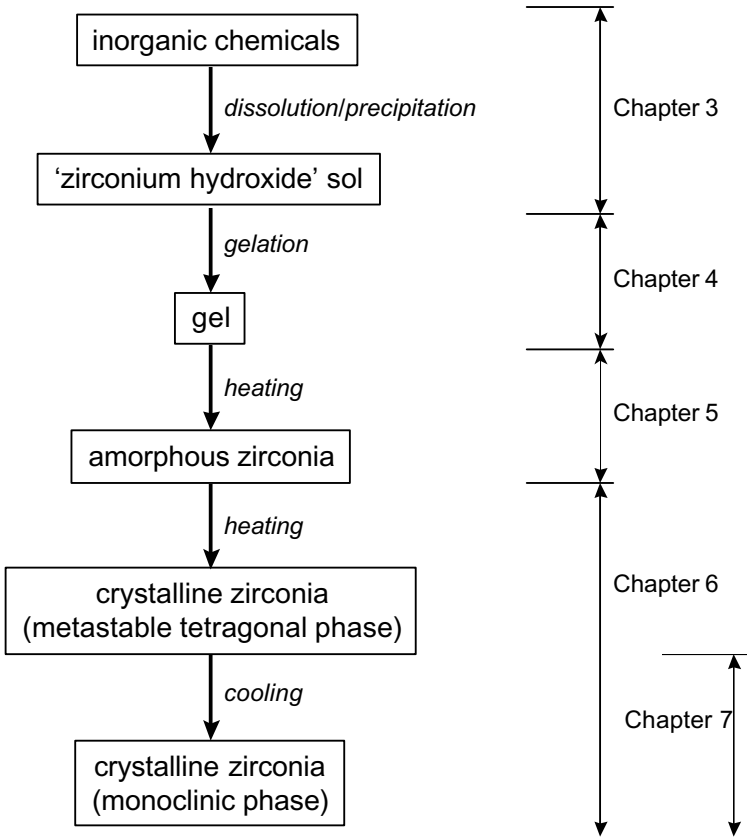

Figure 1-1: Flow chart for the aqueous sol-gel route studied in this thesis, along with an indication of which Chapters discuss each stage.

The remaining three chapters contain more specialist discussion for specific characterisation techniques, including a more detailed discussion of the theory behind each technique. Chapter 8 is focussed on Raman spectroscopy, particularly the assignment of the spectra of zirconyl salts and solutions, and includes results of an *ab-initio* vibrational modelling study. Chapter 9 contains a full discussion of the SAXS study of the sol, while Chapter 10 does the same for the EXAFS study. Characterisation techniques that are widely used in materials science, such as diffraction, microscopy and thermal analysis, are not discussed in any detail.

Note that the units of measurement used throughout this thesis adhere to the SI standard, except for the use of the Ångstrom (1 Å = 0.1 nm), which has been used where it is the commonly-accepted unit for a particular technique (XRD, EXAFS, SAXS).

References

1. E.H. Kisi and C.J. Howard, "Crystal structure of zirconia phases and their inter-relation" *Key Engineering Materials 153-154* 1-36 (1998)
2. J.L. Woodhead, "Sol-gel process to ceramic particles using inorganic precursors" *J. Mater. Ed. 6* 887-925 (1984)
3. L.L. Hench and J.K. West, "The sol-gel process" *Chem. Rev. 90* 33-72 (1990)
4. C.N.R. Rao, "Chemical synthesis of solid inorganic materials" *Mater. Sci. Eng. B18* 1-21 (1993)
5. H. Schmidt, "Relevance of sol-gel methods for synthesis of fine particles" *Kona 14* 92-103 (1996)
6. D.R. Uhlmann, "The future of sol-gel science and technology" *J. Sol-gel Sci. Tech. 8* [1-3] 1083-1091 (1997)
7. C.J. Brinker and G.W. Scherer, *Sol-gel Science*, Academic Press, San Diego (1990)
8. *Sol-Gel Technology for Thin Films, Fibers, Preforms, Electronics, and Specialty Shapes*, Ed. L.C. Klein, Noyer Publications, New Jersey USA (1988)

2. Literature review

This review is divided into four major Sections. Section 2.1 provides background information on the structure and transformations of the phases of zirconia. Section 2.2 discusses the preparation of zirconia precursors from aqueous solutions, including a review of aqueous zirconium chemistry. The structural evolution of zirconia precursors as they are heated is discussed in Section 2.3, while Section 2.4 discusses the 'metastable' tetragonal phase and the various theories proposed to account for its formation and transformation.

This review incorporates background information to assist in understanding the aims and results of this investigation, and also reviews recent studies reported by other investigators with which these results can be compared. The review finds far too many 'holes' and unresolved questions in the literature than can be filled by a single research project.

2.1 Zirconia

2.1.1 The phases of zirconia

At atmospheric pressure, pure zirconia may exist as one of three phases: cubic, tetragonal and monoclinic. The monoclinic and tetragonal phases can be thought of as distortions of the 'parent' cubic fluorite structure. At pressures above 3.5 GPa, several orthorhombic phases may be formed, but these phases will not be discussed in this review. This section will discuss the structure and properties of the phases of zirconia, and the effect of additional oxides on their relative stability. For more detail see the review article by Kisi and Howard.[1]

Cubic phase

The cubic phase, *c*-ZrO_2, is the simplest structure formed by pure zirconia, and is stable from the melting point at 2710°C to 2380°C.[2] The structure is based on the fluorite (CaF_2) structure, in which each zirconium atom is coordinated by 8 equidistant oxygen atoms. This can be visualised by cations occupying FCC positions in a cubic lattice, with eight interstitial oxygen atoms and a large vacancy in the centre, as shown in Figure 2-1. The space group of this structure is $Fm\bar{3}m$ (No. 225), with Zr and O located at 0 0 0 and ¼ ¼ ¼ positions respectively. The lattice parameter, *a*, is approximately 5.15 Å, which when extrapolated to room temperature becomes approximately 5.12 Å.[1]

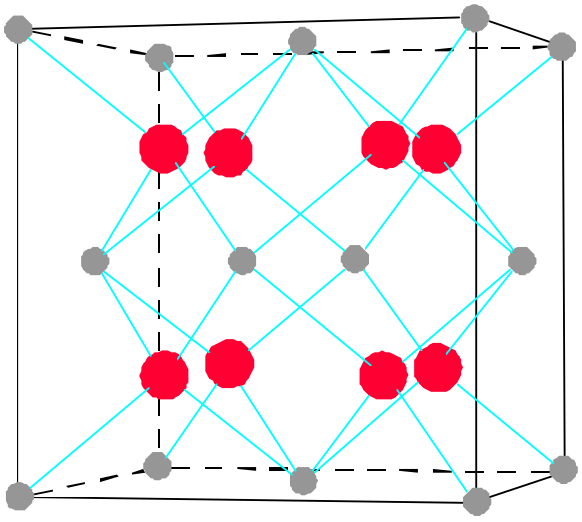

Figure 2-1: Unit cell of the cubic zirconia phase.
Zirconium atoms are grey, oxygen atoms are red.

Tetragonal phase

The tetragonal phase, *t*-ZrO_2, is thermodynamically stable in bulk zirconia from 2380°C to approximately 1100°C*. It is closely related to the cubic structure, as shown in Figure 2-2, but differs in two respects. Firstly, there is a distortion in the lattice, corresponding to a slight elongation along the *c* axis. Secondly, there is a displacement of columns of oxygen atoms alternately up or down the *c* axis. The effect is to move four oxygen neighbours closer to the zirconium atom, and the other four oxygen neighbours away from it. These interdependent distortions are required to prevent O–O contact.[1] Each zirconium atom maintains its eight-fold co-ordination of oxygen: four oxygen atoms at a distance of ~ 2.1 Å, and four at a distance of ~ 2.3 Å. Note that the 'outer' oxygen neighbours for one zirconium atom, are also the 'inner' neighbours for neighbouring zirconium atoms.

The space group of the body-centred, primitive unit cell is $P4_2/nmc$ (No. 137), with approximate dimensions a = 3.6 Å and c = 5.2 Å, and the assignment of diffraction peaks, *etc*, is generally made using this unit cell. The tetragonal phase can also be indexed to a higher-symmetry, face-centred 'supercell', $P\bar{4}m2$ (No. 115). This 'supercell' has a parallel *c* axis and the same *c* value as the primitive unit cell, and *a* and *b* axes at 45° to those of the primitive unit cell. In this thesis the *a* values of the primitive cell and 'supercell' will be referred to as a_p and a_s, respectively, where $a_s = \sqrt{2} \cdot a_p$. The near-cubic 'supercell' is useful when examining phase transformations and comparing the structure to the other phases, as its axes are parallel to those of the cubic FCC fluorite cell, and near-parallel to those of the monoclinic cell. The *c*/*a* value, a measure of 'tetragonality', is usually calculated using the $P\bar{4}m2$ unit cell (*ie* so that it is close to unity). It is unfortunate that in the literature the distinction between the primitive cell and 'supercell' is rarely made clear.

The positions of the zirconium and oxygen atoms in the primitive unit cell are given in Table 2-1. The zirconium atoms are fixed with respect to their unit cell positions, while the position of the oxygen atoms in the *c*-axis, *z*, can vary. The oxygen atoms in the undistorted cubic structure have an equivalent position of z = ¼, so the above-mentioned 'displacement' of the oxygen atoms along the *c* axis can be defined as $\delta = ¼ - z$.[1]

---

* The lower limit of the stability range is dependent on a range of factors, and will be discussed in Section 2.1.3.

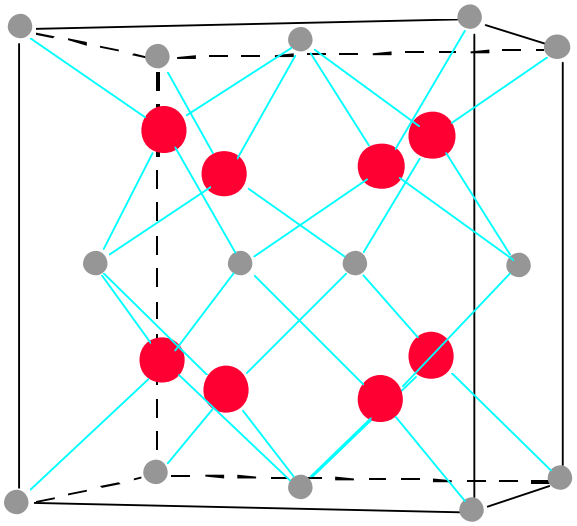

Figure 2-2: Unit cell of the tetragonal zirconia phase, using the $P\bar{4}m2$ 'supercell'. Zirconium atoms are grey, oxygen atoms are red.

Table 2-1

Atom	Wyckoff letter	Positions in unit cell
Zr	a	0,0,0; ½,½,½
O	d	0, ½, z; ½, 0, $-z$; 0, ½+z; ½, 0, ½–z

The values of z and the lattice parameters a and c vary with temperature and composition. Some typical values are shown in Table 2-2, along with the volume of the superlattice cell, V_s.

Table 2-2: Typical lattice parameters for the tetragonal zirconia phase.

Structure	a_p (Å)	a_s (Å)	c (Å)	c/a_s	V_s (Å^3)	z
t-ZrO_2 at 1250°C [3]	3.64	5.15	5.27	1.024	140	0.185
t-ZrO_2, extrapolated to 20°C*	3.588	5.074	5.188	1.022	134	0.204
t-Zr(Y)O_2 (4 mol % Y_2O_3) [4]	3.610	5.105	5.168	1.012	135	0.199
'metastable' t-ZrO_2 [5]	3.591	5.078	5.169	1.018	133	0.204

* These values have been extrapolated by Kisi & Howard to 20°C from high temperature data.[1]

The diffraction pattern of the tetragonal phase is almost identical to that of the cubic phase, except for the 'splitting' of a number of peaks to form doublets, caused by the slight elongation of the c axis. When the peaks are broad, for instance due to small crystal size, it can be difficult to distinguish the diffraction patterns of the two phases unless the high-angle peaks are examined[6,7] or vibrational spectroscopy is used.[8]

Monoclinic phase

The monoclinic phase (m) is thermodynamically stable in bulk zirconia at temperatures below approximately 1100°C. The unit cell can be described as a distorted cubic cell, although the structure is significantly more complex than that of the cubic and tetragonal phases. Unlike the simpler phases, each zirconium atom in the monoclinic structure is coordinated by 7 oxygen atoms, with bond lengths varying from 2.04 - 2.26 Å, and with a range of O-Zr-O bond angles.[9] The oxygen atoms are arranged in two parallel (100) planes, separated by layers of zirconium atoms. The structure is indexed with the space group $P2_1/c$ (14). The unit cell parameters at room temperature vary somewhat between studies.[9-13] The values treated as 'authoritative' for a recent round-robin on powder diffraction[10] are listed in Table 2-3, and will be used in this thesis.

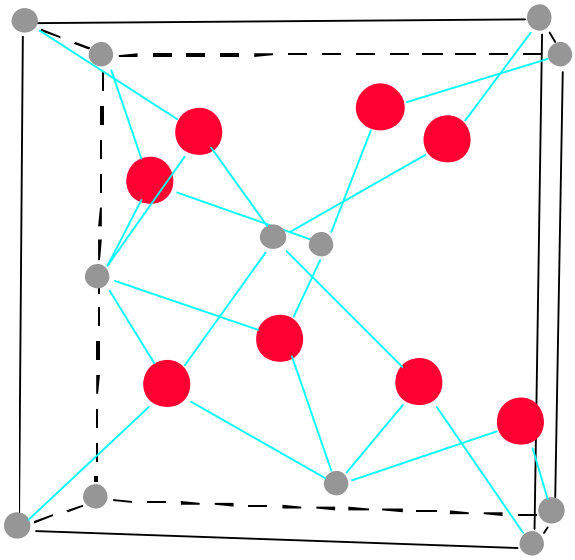

Figure 2-3: Unit cell of the monoclinic zirconia phase. Zirconium atoms are grey, oxygen atoms are red.

Table 2-3

a	5.1454(5) Å
b	5.2075(5) Å
c	5.3107(5) Å
β	99.23 (8)°

2.1.2 Phase stabilisation

It is well known that the addition of relatively small amounts of certain other oxides into zirconia will drastically alter the relative stability of the phases.[1,14,15,15b] The transformation temperatures are lowered, and the tetragonal or cubic phases may become stable or

metastable at ambient temperature. The 'dopant' oxides that achieve this effect are usually oxides of divalent or trivalent metals, such as MgO, CaO, Y_2O_3, or lanthanide oxides. Zirconia that is 'partially stabilised' ('PSZ'), containing a mixture of phases, is an important engineering ceramic with a high toughness. This toughness is derived from the transformation of 'metastable' tetragonal crystals into the monoclinic phase.[1,16]

The mechanism for stabilisation is generally associated with the presence of oxygen vacancies in the lattice, These are created to balance the charge of the di- or trivalent cations, which are substituted on the Zr^{4+} sites. The anion vacancy sites are, in effect, positively charged, so that neighbouring oxygen anions move closer to the vacancy and cations are displaced outward, permitting relaxation of the lattice structure. Although it is generally thought that this mechanism is largely responsible for the stabilisation of the cubic phase,[1,17] it remains uncertain what role oxygen vacancies play in the stabilisation of the tetragonal phase.[1,18] Other critical factors include the size of the stabilising cation and the crystal structure of the stabilising oxide.[1,14,19,20] All these mechanisms have been investigated and reviewed extensively in the references cited. The variation of the lattice parameters of the stabilised tetragonal phase with dopant concentration will be discussed a little in Section 6.3.2.

2.1.3 The tetragonal-to-monoclinic phase transformation

The transformation from the tetragonal phase to the monoclinic (t → m) has been widely studied over many years.[21-24] This rapid transformation involves a significant volume increase (~3.5 %), which has practical importance to zirconia ceramics in two respects. Firstly, the expansion causes considerable cracking in dense zirconia when it is cooled through the transition temperature, which is why pure zirconia monoliths are not prepared. Secondly, the transformation plays a central role in the "transformation toughening" of partially-stabilised zirconia.[1,16] For these reasons the t → m transformation is far more closely studied than the reverse m → t transformation. The tetragonal-to-monoclinic transformation is also of interest in the investigation of the metastability of the pure tetragonal zirconia phase at ambient temperature.

The nature of the t → m transformation is dominated by two main characteristics: the sharp change in volume, and the martensitic character. The change in volume is illustrated in Figure 2-4, which plots the volume of the unit cell for the various phases against temperature. An approximately 3 % increase in volume occurs with the t → m transformation, equivalent with an decrease in density from 5.83 g/cm^3 to 6.1 g/cm^3. The transformation also has a martensitic

character; martensitic reactions are rapid, diffusionless and displacive, and highly dependent on nucleation kinetics.[23,25]

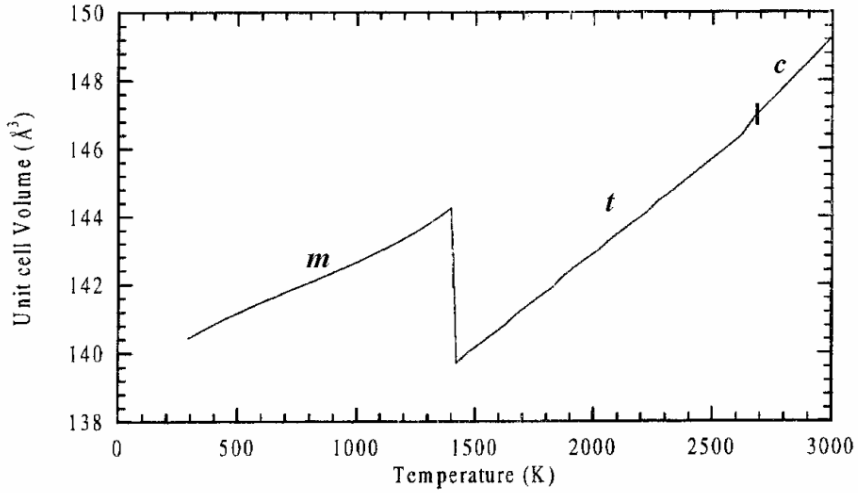

Figure 2-4: Change in unit cell volume with temperature for zirconia, from Kisi and Howard.[1] Note that the $P\bar{4}m2$ 'supercell' would have been used for the tetragonal phase so that it could be compared with the other phases.

Both the volume change and the martensitic character contribute towards the sensitivity of the transformation to stress. Firstly, the density difference between the phases allows stress to affect their relative thermodynamic stability; compressive stress will decrease the thermodynamic t⇋ m transformation temperature.[1] Secondly, the rapid and displacive nature of the martensitic transformation means that the kinetics are dominated by nucleation, which is also strongly affected by stress.[15,22] This also causes a considerable temperature hysteresis in the transformation, generally in the range of 100-200°C. The effect of stress can be clearly seen by the stabilisation of tetragonal particles in a constraining matrix.[26-28] Garvie and Goss have presented evidence that the crystal size will also affect the temperature at which the transformation takes place.[29]

These factors have made it difficult to define a temperature for the transformation, and a wide variety of temperatures have been reported for both the t→ m and m → t transformations, depending on the sample and experimental conditions. A number of these are given in Table 2-4. On cooling the t → m transformation occurs between approximately 1100 and 950°C, while the reverse m→ t occurs during heating between approximately 1050 and 1175°C. There have also been differences observed between the t→ m and m → t transformations, with evidence presented that the latter is composed of two distinct stages.[21,24]

Table 2-4: Previously-reported transformation temperatures between the monoclinic and tetragonal phases.

Reference	Transformation temperature (°C)	
	m → t (heating)	t → m (cooling)
Frey and Boysen [24]	800 - 1150 (stage 1) 1150 - 1400 (stage 2)	1020 - 870
Garvie and Chan [30]	1160 - 1190	1100 - 1020
Perry and Liu [31]	1070 - 1150	1000 - 950
Osiko *et al*. [32]	1030 - 1130	1000 - 890
Patil and Subbarao [21]	930 - 1100 (stage 1) 1100 - 1220 (stage 2)	1020 - 700

Twinning is commonly observed by TEM in monoclinic crystals that have been transformed from the tetragonal phase.[33-35] Kelly predicts that the twin relationship will not be precise, but normally less than 0.5° from an exact twin relationship, and so should properly be called twin-related.[33] Twinning will decrease the diffraction crystal size of the monoclinic phase, and it has been observed that the 'crystal size' measured by XRD line broadening decreases after the transformation.[35-37]

The details of the crystallographic changes and lattice correspondences during the transformation have been thoroughly reviewed elsewhere,[23,33,34] and will not be discussed here.

There have been many attempts to formulate theoretical models with which to interpret these observations. The simplest approach is to define a temperature M_s, at which the martensitic transformation starts during cooling.[33] The observation that this temperature is highly dependent on a range of conditions, as discussed above, has driven the development of more complex models. A number of these models propose the existence of monoclinic or transitional-structure 'nuclei' or 'embryos' in the tetragonal matrix,[38-41] but this idea is not universally accepted.[42] The tetragonal and monoclinic structures are a normal mode of vibration of each other, so that in the tetragonal structure certain vibrational modes may form small 'clusters' of the monoclinic structure, and vice versa. If these clusters reach a critical size, which may be temperature dependent, they will nucleate the martensitic transformation. This theory may explain the apparent dependence of transformation temperature on parent phase crystal size, in that smaller crystals are statistically less likely to contain nuclei of a critical size.[39,40] However, as yet there has been no direct evidence of the existence of such nuclei.[42]

2.2 Zirconium salt solutions and the preparation of zirconia precursors

The aqueous solution chemistry of zirconium is complex and, despite much study over the past 40 years, only partially understood. During the 1950's through to the early 1970's, much research was carried out on aqueous zirconium systems, using techniques such as small-angle X-ray scattering (SAXS), ultracentrifugation, and light scattering. This work resulted in a basic understanding of the behaviour of these systems, and was reviewed extensively by Clearfield in 1964,[43] Mukherji in 1970,[44] and Baes and Mesmer in 1976.[45] Much of the general discussion in this section is based on these reviews, as well as that by Livage.[46] There was little further investigation until the late 1980's, when there was an increased interest in the use of aqueous solutions as precursors in the preparation of zirconia and in the processing of nuclear fuel. During the last decade the hydrolysis of zirconium solutions has been studied by techniques such as Raman spectroscopy,[47,48] nuclear magnetic resonance,[47,49] small-angle X-ray scattering,[50,51] and X-ray adsorption spectroscopy.[52]

This review will concentrate on those aspects of zirconium solution chemistry that are relevant to aqueous, inorganic sol-gel methods, *ie* high concentration solutions of chloride and nitrate salts. Sulfate solutions, although used in industry, will not be covered, as the chemistry of these solutions is even more complex and less well understood, and sulfates will not be used in the experimental part of this thesis.

There are three characteristics of zirconium salt solutions that make their chemistry quite complicated. The first is that the Zr^{4+} cations are very easily *hydrolysed*. The zirconium atom favours seven or eight-fold oxygen coordination, and in solution is coordinated by water or hydroxy groups, usually eight. In the hydrolysis process a coordinated water molecule is spontaneously converted to a terminal hydroxy group, due to electron transfers within M-OH_2 bonds, losing a proton into solution:

$$Zr\cdots OH_2 \leftrightharpoons Zr\text{–}OH^- + H^+$$

Hydrolysis occurs readily, making zirconium-containing cationic species moderately strong acids.

The second complicating factor is that a number of cation species, containing more than one zirconium atom, may be formed in solution.[46] There has been considerable work in

investigating the structure of these species using various techniques, which will be reviewed in Section 2.2.1. A third factor is that these cation species may polymerise, via condensation reactions, to form oligomeric cations and colloidal particles, and this is discussed in Section 2.2.2.

The condensation reaction between cations to form colloidal particles is the main mechanism for the formation of zirconia-precursors from aqueous solution. Depending on the particle growth rate and the chemical conditions in solution, the product can be a *sol*, consisting of a suspension of colloidal particles, a *gel*, made up of aggregated colloidal particles, or a denser *precipitate*. The vast majority of so-called 'sol-gel' processes for preparing zirconia that are reported produce a gel or precipitate directly from the solution, with no stage where a stable sol is formed.

The final three Sections will discuss three broad classes of route for the preparation of zirconia-precursors. Section 2.2.3 deals with the common method of direct precipitation of zirconium hydroxide from solution by addition of a base. This method is by far the most widely used and studied of aqueous 'sol-gel' routes and, although not the main focus in the experimental section, it is important to review this method to understand previous work on aqueous zirconia precursors. Section 2.2.4 will examine a range of methods by which stable, aqueous *sols* can be prepared from solution by chemically altering the equilibrium. One of these is the main method used in the experimental section of this thesis. Finally, the formation of crystalline zirconia by hydrothermal treatment will be briefly reviewed in Section 2.2.5.

Note that there are also many routes for the preparation of zirconia-precursors using metal-organic precursors, but these will not be reviewed here.

2.2.1 The structure of polynuclear species in solution

The Zr^{4+} ion does not occur in isolation in concentrated solution, being stable only at concentrations below approximately 10^{-4} M.[44,45] Instead, a range of '*polynuclear*' cation species may be formed, each containing a number of zirconium atoms, generally linked by hydroxy (Zr–OH–Zr) bridges. The basic repeating structural unit that occurs in the polynuclear cations is generally $[Zr(OH)_2^{2+}]$, with each zirconium atom linked to others by two hydroxy bridges. Any given solution may have a range of species present, each with different size and degree of hydrolysis.

There are two types of zirconium salt commonly studied, with forms ZrX_4, and $Zr(OH)_2X_2$, where X is a monovalent anion. In the chloride system, the only system for which systematic studies have been done, the $[Zr(OH)_2^{2+}]_n$ cation is formed for both types of the salt. To early researchers it appeared that zirconium existed in solution as the *zirconyl* species 'ZrO^{2+}', and there was some debate over the presence of a Zr=O bond.[53,54] Although a consensus later formed that this species does not exist, at least under most conditions,[44,45] the term zirconyl is still frequently used for zirconium compounds of the type $Zr(OH)_2X_2$.

There are three main factors that control the size and structure of the cation species. *Solution concentration* and *pH* determine the degree of hydrolysis and the equilibrium size of the species, while the *anion* present may form complexes, influencing the bonding and geometry depending on their electronegativity.[43,46] Some anions, such as chloride and perchlorate, interact very weakly, while some, such as sulfate, can complex strongly and form bridges.

Solutions of zirconyl chloride, $Zr(OH)_2Cl_2$, or zirconium chloride, $ZrCl_4$, have been extensively studied for many years. Chloride solutions are also the most widely used inorganic precursor for producing zirconia precursors. Unfortunately, far less is known about nitrate and sulfate solutions.

The remainder of this section reviews a range of published work on the structures in zirconyl solutions. We start with a description of the 'cyclic-tetramer', which is the only well-characterised structure known to exist in chloride solution. Published characterisation work is then reviewed, classified by characterisation technique. Much of this work has been published in the last decade, and there has been no comprehensive review of these later developments published. It should be noted that in many of these studies some additional acid has been added to the zirconyl solution, to prevent polycondensation of the cations.

The cyclic-tetramer species

The cyclic-tetramer species, with core framework $Zr_4(OH)_8^{8+}$, is the one polynuclear complex that has been firmly identified in zirconyl solutions by a range of characterisation techniques. Early ultracentrifgation investigations of relatively dilute zirconyl chloride solutions were able to identify various discrete species that contained up to four or five zirconium atoms, but was difficult to determine their actual structure.[45] Diffraction studies of zirconyl halide crystals identified a structure involving four zirconium atoms linked in a ring, bridged by hydroxy

groups.[43,55,56] This structure has subsequently been identified in zirconyl chloride solutions by WAXS,[57] SAXS,[50] and EXAFS.[52]

The structure of the tetramer species is that of four zirconium atoms at the corners of a square, each joined by two bridging hydroxy groups along each edge (OH^b). Four water molecules, or hydroxy ligands (OH^t), around each zirconium atom complete the eight-fold coordination, to give a formula of $[Zr_4(OH^b)_8(OH^t)_h(H_2O)_{16-h}]^{(8-h)+}$. This structure is illustrated in Figure 2-5.

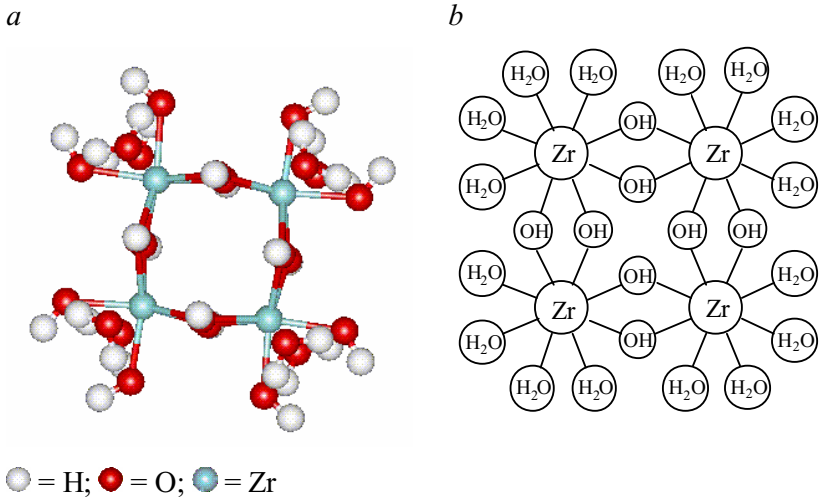

Figure 2-5: Illustrations of the cyclic-tetramer cation, using a) a ball and stick model (with $h = 8$), and b) a schematic model (with $h = 0$).

The tetramer is the dominant species in concentrated chloride solutions at pH below 1.5, co-existing with minority species such as the trimers $[Zr_3(OH)_4]^{8+}$ and $[Zr_3(OH)_5]^{7+}$.[45] However, there is little evidence for its existence in other zirconyl salt solutions, such as nitrates. The cyclic-tetramer has been sometimes assumed to be the predominant zirconyl species in nitrate solutions,[49,50,58,59] with little direct evidence.

Nuclear magnetic resonance

Nuclear magnetic resonance (NMR) can provide much information on bonding, structure and chemical activity of species that is otherwise very difficult to obtain. The major restriction is the range of isotopes that are amenable to examination by NMR. For example, ^{91}Zr is a difficult nucleus to work with due to its large quadrupole moment,[60] and has not been successfully used in solution NMR. It should also be noted that NMR does not detect atoms in all environments. For instance, if the atom or molecule is exchanging at a rapid rate with respect to the NMR frequency, it is not detected.

^{1}H can give some useful information on the behaviour of the hydrogen atoms associated with the zirconyl species. Most ^{1}H NMR studies of concentrated zirconyl perchlorate and chloride solutions at ambient temperatures have reported a single strong peak at approximately 8 ppm, down-field from the main bulk water peak at 5 ppm.[47,49,61,62] This peak corresponds to approximately two slowly-exchanging protons per zirconium in concentrated solution, and it has been observed that the intensity decreases with dilution and increasing pH. Hannane *et al.* assigned this peak to the protons of the bridging hydroxy group between zirconium atoms,[47] and attributed the intensity decrease to the *oxolation* of the bridging hydroxy bonds:

$$Zr–(OH)_2–Zr \rightarrow Zr–O–Zr$$

This assignment has been disputed on the grounds that there is no other evidence for oxolation occurring under these conditions.[49]

The location of the detected proton was clarified when Åberg and Glasser observed that the addition of nitrate anions to the zirconyl chloride solution, in the form of HNO_3, reduced the number of slowly exchanging protons from two per zirconium to one.[49] Since the bridging hydroxy groups are highly stable, and the displacement of their protons by nitrate unlikely, the peak was instead assigned to protons on the water groups coordinated around each zirconium cation. The fall in intensity with both dilution and increase in pH can then be attributed to the hydrolysis of the cation, with the associated loss of a hydrogen into solution.

$$Zr–OH_2 \rightarrow Zr–OH^- + H^+$$

Åberg and Glasser also studied zirconyl complexes using ^{17}O NMR.[49] A peak at 180 ppm was assigned to two slowly-exchanging water groups per zirconium. These groups exchanged relatively easily with bulk water, and were displaced when nitrate was added. This behaviour is strikingly similar to that of the proton detected by ^{1}H NMR. An earlier ^{17}O NMR study of zirconyl chloride in 2 M nitric acid reported signals only for nitrate and bulk water,[62b] and Åberg and Glasser suggested that in this case the nitrate replaced all of the coordinated water. To date there has been no reported attempt to enrich zirconyl species with ^{17}O, to detect any weak signal from the hydroxy bridges.

NMR can also be used to directly study the role of the anion in forming complexes with the zirconium-containing cation. There have been two such studies published. A ^{14}N NMR investigation of $Zr(OH)_2(NO_3)_2$ solutions,[63] with pH adjusted by NaOH or $HClO_4$, showed

that the chemical shift of ^{14}N remained constant, but the relaxation rate varied with pH and NO_3^- concentration. The variation in relaxation rate was used to distinguish between a 'free' aquated state, and a state where the nitrate ions formed a complex with the zirconyl species, in which the immediate environment of the ^{14}N nucleus differs from that of the free anion. The fraction of 'bound' nitrate ions increased from ~ 10 % at pH 0 to 100 % at pH 1.8, at which point precipitation of zirconyl hydroxide polymers began. A slight difference between the rates of spin-spin and spin-lattice relaxation at pH > 1 was interpreted as indicating colloidal particles in solution.

A quantitative ^{14}N NMR study of $ZrO(NO_3)_2$ solution indicated that only about 50% of the nitrates groups in solution were detected.[46] Based on the crystal structure of $ZrO(NO_3)_2$ (discussed below), it was concluded that half of the nitrate groups in solution were directly bonded to zirconium ions, and could not be detected by NMR due to quadrupolar broadening. The same study also used ^{35}Cl NMR to confirm that the Cl^- ion complexes only weakly with the zirconyl species.

Vibrational spectroscopy

Vibrational spectroscopy has been used to study the bonding present in zirconyl complexes. Studies have concentrated entirely on $ZrOCl_2$ salts and solutions, which are known to contain the well-characterised cyclic-tetramer structure.

A number of IR studies of $ZrOCl_2$ crystal and solutions have given a range of results. Bands at frequencies above 1000 cm^{-1} were assigned to bending and stretching of terminal hydroxy groups.[54,64] Bands at frequencies below 700 cm^{-1} that shifted with deuteration were assigned as librational modes of coordinated water groups, and those that did not shift were attributed to Zr-O bonds.[54,64,65]

Although infrared (IR) spectroscopy can provide valuable information, it is extremely sensitive to water, and is not well suited to studying aqueous systems. Raman spectroscopy is relatively insensitive to water, and can be used to characterise almost any solution or salt, although the results can be difficult to interpret. For these reasons, recent investigations has tended to use Raman spectroscopy. The Raman spectrum of zirconyl chloride solutions contains two strong bands: a polarised band at 580 cm^{-1}, and a depolarised band at 450 cm^{-1}, usually with a shoulder at 420 cm^{-1}.[47,64,66,67] The main bands show only a minor isotopic shift when the solvent was replaced with deuterium. A range of assignments have been given to the bands in the Raman spectrum, and assignment of these bands is discussed in detail in Section 8.3.

X-ray absorption spectroscopy

X-ray absorption spectroscopy is a method by which the short-range structure around the atoms of a particular element can be investigated. The extended X-ray absorption fine structure (EXAFS) technique gives information on the distance and number of atoms in the coordination shells surrounding the probe atom, in this case zirconium. There has been one EXAFS study on the crystal and aqueous solution of $ZrOCl_2$, and the solution of $Zr(NO_3)_4$.[52] The spectrum for both the crystal and solution of $ZrOCl_2$ were very similar, and gave interatomic distances and coordination numbers for the Zr-O and Zr-Zr pairs that closely corresponded to those expected for the cyclic-tetramer. Most importantly, a signal was observed that corresponded to the Zr-Zr distance diagonal across the square, which is characteristic of the cyclic structure. The spectrum for the $Zr(NO_3)_4$ solution was very similar. In this case the diagonal Zr-Zr peak was weaker, although the conclusion was made that the tetramer was also predominant in this solution.

The importance of this EXAFS study is it shows that the short-range structure in the aquated zirconyl chloride species is very similar to that in the crystalline tetramer.

Small angle X-ray scattering

The size and geometry of polynuclear complexes in $Zr(OH)_2Cl_2$ [50,68] and $Zr(NO_3)_4$ [51] solutions have been examined by small-angle X-ray scattering (SAXS). In all studies the primary complex was found to have a low aspect ratio, and reported values of the radius of gyration, R_g, varied from 3.8 to 4.6 Å. Values for the radius of gyration of the cyclic-tetramer species were calculated by Singhal *et al.*, and found to be consistent with the data.[50] Singhal *et al.* also found a larger species in solutions in which a base had been added, which had a R_g value of 5.2 Å and was identified as an 'octomer' structure. These studies are discussed in more detail in Section 9.1.

Crystalline structure of zirconyl salts

An indirect method of investigating the complex structures found in a solution is to examine the crystal structure formed by drying the solution. The species in solution are often structurally similar to the repeating units in the crystal.[69] This approach was successful in the identification of the cyclic-tetramer structure in crystalline $Zr(OH)_2Cl_2 \cdot 7H_2O$ in 1956,[43,55,56] well before it was firmly identified in solution. The tetramer structure in the crystal has also been found in the crystal structure of other zirconyl halide salts.[43]

Recently the crystalline structure of zirconyl nitrate was solved from powder XRD data,[70] and the formula stated as $Zr(OH)_2(NO_3)_2{\cdot}(4+x)H_2O$ ($x \leq 1$). The structure is made up of parallel cationic chains, with the repeating unit $[Zr(OH)_2(NO_3)(H_2O)_2]^+$. The zirconium atoms within each chain are linked by double hydroxy bridges, and each zirconium is coordinated by four bridging hydroxy groups, two water molecules, and a bidentate nitrate group. This structure can be visualised as 'cyclic-tetramers' that have been opened up and joined into a chain, with a nitrate group coordinated to each zirconium atom. For each zirconium atom, there are also 2 to 3 water molecules and an additional nitrate group located in between the chains. Thus, half of the nitrate groups present are directly (covalently) coordinated to the Zr atoms, and the other half are ionically bound in the crystal lattice between the chains.

Summary

The chemistry of the zirconium and zirconyl chloride solutions has by now been extensively studied, and the structure of the cyclic-tetramer species is well understood. The discovery of the octomer as a stable species now provides an opportunity to understand the steps that occur as tetramers combine to form larger species.

The structure of the species in nitrate solutions is less certain. SAXS and EXAFS studies provide consistent evidence that the tetramer, or a polynuclear species of approximately the same size and shape, also predominates in $Zr(NO_3)_4$ solutions.[51,52] However, there is yet no evidence for the $Zr(OH)_2(NO_3)_2$ solution. The crystal structure of $Zr(OH)_2(NO_3)_2$, described above, provides the first suggestion that the structure of the complex may not be that of the cyclic tetramer, and it has been suggested that the solution species is based on the linear $[Zr(OH)_2]_n$ chains.[46] The chains and the tetramers would be almost indistinguishable to NMR and vibrational spectroscopy, depending on the selection rules, and scattering techniques such as SAXS have the best potential to definitively make a distinction. Clearly, further work is required to clarify this issue.

2.2.2 Polycondensation reactions

Although the polynuclear zirconyl species described in the previous section are reasonably stable at low pH, they are easily hydrolysed, and are thus susceptible to *condensation* reactions to form larger oligomers.[45,46]

$$Zr–OH^- + {}^-HO–Zr \rightarrow Zr–OH^-Zr + OH^-$$

Condensation releases OH^- ions, which neutralise half as many protons as were released by the initial hydrolysis process, thus promoting further hydrolysis.

It is also possible that subsequent *oxolation* of the bridges may occur under some conditions with the elimination of water, although this reaction has never been positively identified during the hydrolysis of zirconyl solutions.*

$$Zr–(OH)_2–Zr \rightarrow Zr–O–Zr + H_2O$$

The formation of oligomers has been observed when zirconyl chloride solutions are aged over periods of weeks to months under ambient conditions.[45,71,72] The average number of metal atoms in each 'particle' has been variously reported between 10 and 40.

Under some conditions the condensation process may continue as a *polymerisation* reaction (polycondensation) to form colloidal particles and/or precipitates. In particular, the rate of polymerisation is strongly accelerated when the pH or temperature is increased. There have been a large number of studies of this process, but only of zirconyl chloride solutions. The remainder of this section reviews some of these studies and the proposed mechanisms of polymerisation, focussing on the effect of pH.

Effect of pH on polymerisation

The rate of condensation between species is particularly sensitive to the pH of solution. Although gradual polymerisation will occur under most conditions, the rate of reaction is greatly enhanced by the addition of a base, and can be inhibited by addition of an acid.[45] When enough base is added, the polymerisation of zirconyl species will proceed to

---

* Åberg and Glasser pointed out that oxolation may significantly *increase* the Zr–Zr distance from approximately 3.6 Å to 3.9 Å, and on this basis concluded that oxolation did not occur in the oxolation reaction that they studied by wide-angle X-ray scattering .[49] However, the Zr–O–Zr bonds may be significantly bent, such has been observed for basic zirconium sulfates,[70b] and in this case the Zr–Zr distance is not a good indicator of oxolation.

completion, consuming all or most of the original species. The resulting solid can be a precipitate or gel, which is frequently used as a zirconia precursor, and this type of reaction is further discussed in Section 2.2.3. This section will cover the early stages of condensation.

Larsen and Gammill carried out a detailed titration study on the solutions of zirconyl salts with formula $Zr(OH)_2X_2$, where X was Cl, NO_3 or ClO_4.[73] The appearance of turbidity, indicating the precipitation of a solid, was observed in the range of pH 1.9 – 2.3, and OH:Zr ratio 0.3 – 0.9. Coagulation of the precipitate, so that the supernatant solution was clear, occurred at pH approximately 3.5 and OH:Zr ratio approximately 1.8. These values were found to vary with the cation and anion concentrations. After each addition of base, the solution required some time to reach equilibrium. Subsequent studies have reported similar observations.[47,67]

Hannane, Bertin and Bouix measured the Raman spectrum of the supernatant solution after a base was added to zirconyl chloride solutions at OH:Zr ratios of 0.35 and 1.[47] There was a substantial difference between the spectra of the starting solution and the hydrolysed solutions, with the peaks at approximately 450 and 580 cm^{-1} replaced by peaks at 425 and 530 cm^{-1}. This observation clearly indicated that a substantial change had occurred in the short-range structure of the species by OH:Zr ratio 0.35, and was interpreted by the authors as oxolation of the bridging hydroxy groups. Similar changes to the Raman spectrum have been reported elsewhere.[67,74]

^1H NMR studies of the hydrolysis of zirconyl chloride solution by NaOH have shown that the number of protons detected per zirconium atom Zr decreases from approximately 1.5 in the untreated solution, to 0.5 [61] or zero [47]. Although the interpretation varies with the assignment of the peak, if we use the assignments discussed above in Section 2.2.1, this would indicate that as the pH increases either the hydrogen atoms on the coordinated water molecules are being lost though hydrolysis, or the water molecules are being replaced. Hannane *et al.* interpreted this to mean that oxolation was occurring.[47]

Mechanisms

The reactions and changes in structure that take place as a zirconyl solution is hydrolysed by a base are still uncertain. A decade ago Srinivasan *et al.* observed that "the detailed mechanisms proposed to date are based more in chemical intuition than on reliable experimental data",[75] and this remains the case despite some subsequent work.[47,49,67,76] For the most part, any discussion of mechanisms is based on the hydrolysis and condensation reactions outlined

above.[43,77-80] With the exception of Hannane *et al.*,[47] it is also generally assumed that oxolation does not take place.

The zirconyl species, such as the cyclic-tetramer in the chloride solution, are stable at low pH. As a base is added, water groups coordinated around each Zr atom will hydrolyse, which may affect condensation in two ways. Firstly, hydrolysis forms reactive terminal-hydroxy groups, which are the required for the condensation reaction. Secondly, hydrolysis will reduce the positive charge on the zirconyl species, so diminishing the electrostatic repulsion and increasing the chance of them interacting and reacting. Condensation polymerisation of zirconyl species is thus promoted, forming a network. If an acid is added to the solution, further condensation is inhibited, and possibly reversed. If sufficient base is added, the polymerisation will proceed to completion, consuming all or most of the zirconium in solution, and the resultant 'hydrous zirconia' precipitates from solution.

In 1964 Clearfield proposed a relatively simple mechanism for polymerisation. It first assumes the presence of only the cyclic-tetramer species.[43] These species hydrolyse and react to be bridged by hydroxy groups, in the same manner that zirconium atoms are connected within the tetramer. Clearfield suggested two cases. In the first 'optimum' case, each tetramer reacts with four others, to form an ordered sheet structure with the repeating unit and stoichiometric formula $Zr(OH)_4$. In this structure, each zirconium atom is in a square matrix connected to four others by a double hydroxy bridge $-(OH)_2-$. The second case considered the same reaction at a greater rate, for example induced by rapid addition of a base, where the tetramers would polymerise together into a disordered network. In either case the type of bonding present is essentially the same as found in the tetramer.

The simplicity and elegance of this model has made it by far the most widely discussed and supported in the field, but there remains little experimental evidence for it. The theory does not explicitly account for the significant changes in the Raman spectra of the solution during polymerisation, which indicates strong shifts in bond energies. One possible problem with this mechanism was pointed out by Mukherji.[44] The hydroxy bridges in the tetramer lie in planes that are nearly at right-angles to each-other; any condensation between tetramer units would occur in a way as to place the new hydroxy bridges at right angles to those already present, thus inhibiting the formation of a sheet and promoting the formation of a three dimensional structure.

It is feasible that oxolation to form a double oxy bridge Zr=O_2=Zr or a single Zr-O-Zr bridge may take place in solution. Åberg and Glasser pointed out that oxolation will result in a significant increase in the Zr–Zr distances, from 3.57 to 3.89 Å.[49] Such a characteristic change in bond length has not yet been observed in the hydrolysis of zirconyl salt solutions.

It is clear from the published Raman and ^{1}H NMR spectra that some significant changes in the short-range structure are taking place in the solution as the pH is increased, but it is not yet clear as to what they are. The mechanism suggested by Clearfield is intuitive, plausible, and widely quoted, but conclusive evidence to support it has yet to be published. (However, the evidence provided in this thesis clearly supports Clearfield's mechanism.) Suggestions that oxolation of the bridging hydroxy groups occurs also require more evidence.

Polymerisation at increased temperature (thermal ageing)

It is also worthwhile to note that polymerisation and condensation in the solution is greatly accelerated at elevated temperatures, particularly above 80°C.[45,68,81,82] When polymerisation is allowed to continue at temperatures above 90°C, precipitation will occur, along with crystallisation of the monoclinic zirconia phase. This method has frequently been used to prepare colloidal particles of zirconia, and is briefly discussed in Section 2.2.5. Two SAXS studies have found that the primary particle formed by condensation at elevated temperature is rod-shaped.[68,81] One study has suggested that complicated polymeric species, containing both hydroxy (Zr–OH–Zr) and oxo (Zr–O–Zr) bridges, are formed at temperatures above 80°C.[82]

2.2.3 Formation of a precipitate

It has long been observed that increasing the pH of a zirconium salt solution will cause the precipitation of a gelatinous, amorphous 'hydroxide'. The composition of this precipitate is not fixed, and may be described as an amorphous mixed oxide/hydroxide/hydrate, which may contain bridging oxo and hydroxo bonds, terminal hydroxy groups, coordinated aquo groups, and adsorbed water.[83] The composition may be expressed by the general formula $Zr(OH)_xO_{(4-x)/2}\cdot nH_2O$. A variety of names have been given to its various forms, often the not-very-accurate term *hydrous zirconia*.[43,75,83-85] In this review the term *zirconium hydroxide* will be used, although it must be recognised that the composition is not necessarily the stoichiometric $Zr(OH)_4$.

For some time this material has been used widely as a precursor for microcrystalline zirconia powders. The advantages of this route include its relative simplicity and low cost in comparison to other routes, and also the ability to co-precipitate small quantities of 'stabilising' oxides along with the zirconia.[86-93] However, as this review will demonstrate, there are still many aspects of this system that are not well understood.

This method is discussed at length in this review, as the structure of the precipitate can be treated as an analogue for the hydrous sol particles formed in solution, which are harder to study.

Precipitation conditions

In most reports of this route, the precursor solution is a concentrated solution of $Zr(OH)_2Cl_2$ or $ZrCl_4$.[93-96] Occasionally nitrate solutions are used,[75,87,90,97-100] and nitrate may be easier to remove than chloride in the calcination stage.[99] Sulfate solutions have also been used,[78,85,101] but many researchers may have avoided the use of sulfate precursors, as the sulfate anion is difficult to remove and has been shown to have a strong effect on the phase behaviour of microcrystalline zirconia.[94,96,100,102-105] The base added to the zirconyl solution to cause precipitation is usually ammonia, as ammonium salts will fully decompose during heating.

In practice the conditions used to precipitate the hydroxide can vary quite considerably, both between and within studies. The main reason for this variation is the striking dependence of the structure of the crystalline oxide on the precipitation conditions, which has been the subject of many studies and is discussed in Section 2.3.3. In most reports, gelation is usually induced by the rapid addition of an excess of the base into a zirconyl solution. A method providing more control over the rate of precipitation, and the final pH, is the slow addition of a limited amount of base.[75] Most commonly, the pH of the supernatant solution at the end of precipitation is reported. As a result of this range of methods, the quoted 'pH of precipitation/gelation' is not necessarily comparable between studies.

The gelatinous precipitate is generally washed with copious quantities of water to remove most of the residual anions,[75,90,95,97,106-109] often until no anions are detected in the wash water, and then dried. It is also reported that washing the precipitate with an organic solvent will prevent hard agglomerates forming during calcination,[88,98,108] resulting in a powder that will sinter more readily.

Effect of precipitation conditions on the phase of calcined zirconia

It has been known for some time that certain properties of zirconia calcined from precipitated zirconium hydroxide, particularly the crystalline phase composition, are strongly affected by the chemical conditions of precipitation. It has been widely observed that when two batches of zirconium hydroxide are precipitated from identical precursors under different conditions, the oxides that remains after calcination of one batch may be predominantly monoclinic phase, while the other may be predominantly 'metastable' tetragonal.

Control over the phases of zirconia has been of great interest to ceramic engineers for some decades, and investigation of this phenomenon may assist the understanding of the whole zirconia system. It is clear that there is some connection between the precipitation conditions and the phase of the calcined oxide, but there is little consensus on the mechanism. For this reason the mechanisms of precipitation, and the nanostructure of the resulting material, have been of great interest. Unfortunately, the complexity of zirconium aqueous chemistry, and the amorphous nature of the precipitate, has combined to make such investigations very difficult. In the absence of detailed data on the nanostructure of the precipitate, the general approach of researchers has been to alter the gelation conditions, and study the effect this has on the crystalline phases after calcination.

The condition that has been found to have the greatest effect on the final phase composition is the pH at which precipitation takes place.[35,75,101,105,106,110-112] However, many reports have given conflicting results for the nature of this dependence, and the phenomenon is not well understood. The general trend is that hydroxide precipitated at an extreme pH (< 4 or > 10) will crystallise into a 'metastable' tetragonal phase that is quite resistant to transformation to the stable monoclinic phase. Srinivasan *et al.* have identified other important solution conditions, such as the rate of precipitation,[75,96,113] and the source of the precursor salt.[114]

A range of mechanisms have been proposed, but as yet there seems to be little evidence to distinguish them. Examples are the precipitated particle size, surface area, lattice strain, pore distribution, anion content and nature of the short-range order. These theories will be further discussed in Section 2.3.2.

Structural studies of the precipitates

It is frequently suggested that the nanostructure may be responsible for the relationship between the precipitation conditions and the phase structure of the calcined oxide, and indeed this seems to be a reasonable hypothesis. In the study of the precipitation method, the principle

difficulty in understanding the processes that occur is in the lack of definite data on the structure of the precipitate. There have been many studies of the structure of precipitated materials, using a wide range of characterisation techniques. This section summaries the current state of knowledge of the structure of the precipitated material. It is also useful for understanding the structure of colloidal particles that are formed from zirconyl solutions by polycondensation processes.

The chemical bonding of precipitated 'zirconium hydroxides' has been investigated,[43,83,115] and it has been demonstrated that a range of compositions may exist within the general formula $Zr(OH)_yO_{(4-y)/2}\cdot nH_2O$. The material freshly precipitated from solution contains four hydroxy groups per zirconium atom, and is thus a 'true' *zirconium hydroxide* $Zr(OH)_4\cdot nH_2O$.[83,115,116] All bonds between zirconium atoms must be via hydroxy bridges, but up to half of the hydroxy groups may be present as terminal groups. The hydroxide is not highly stable, and if heated, washed in methanol, aged or boiled in water will transform into a material containing two hydroxy groups per zirconium atoms, $ZrO(OH)_2\cdot mH_2O$.[83,115,116] This second structure was found to be reasonably stable, and has been called *zirconium oxy-hydroxide*, or the rather misleading name *zirconyl hydroxide*.

Infrared spectroscopy of precipitated hydroxides has not been successful in identifying the presence or nature of hydroxy groups, as the broad absorption band of water masks the O-H stretching frequency expected in the 3200 – 3600 cm^{-1} region.[43] Tosan *et al.* has reported the Raman spectra of a range of gelatinous hydroxides precipitated from solution.[76] A broad peak at approximately 450 cm^{-1} was observed in the spectrum of all samples, while some also had a strong peak at 550 cm^{-1}. Like the Raman bands for the species in solution, these peaks were shifted only very weakly with isotopic substitution, and thus it is not likely that the Raman-active modes involve coordinated water molecules. These spectra were not assigned with any degree of certainty, and there is plenty of room for more work in this area.

The short-range structure of precipitated hydroxides was first studied by Livage, who inferred the characteristic interatomic distances of a precipitated hydroxide from the wide angle X-ray and neutron scattering profiles.[117] However, more detailed information became available with the much later development of X-ray absorption spectroscopy (XAS), in particular the EXAFS technique. By examining the X-ray absorption edge of the zirconium atoms present, information can be extracted on the average short-range structure around those atoms, such as interatomic distances and coordination numbers (See Chapter 10). There have been several

studies of precipitated hydroxides,[85,118] the most detailed by Turrillas *et al.* who reported the room-temperature EXAFS spectrum of a material precipitated from a basic zirconium sulfate solution.[85] Only data for the first (oxygen) and second (zirconium) neighbours of the zirconium atoms were modelled, but from these values a structural model was proposed based on a planar, square lattice of zirconium atoms bridged by oxo and hydroxy bridges. The validity of this model can only be tested by obtaining data for shells beyond the second neighbour, and preferably minimising the structural disorder by collecting data at low-temperature.

All diffraction studies of precipitated hydroxides indicate that they are amorphous to X-rays.[95,101,105,119] Some published diffraction patterns show two or three very broad peaks,[101,119] with positions that roughly correspond to the main peaks in the tetragonal or cubic diffraction patterns. Corresponding rings have been found in electron diffraction patterns.[119] It has been suggested that the structure of the 'amorphous' material may be crystalline, composed of crystallites too small to diffract X-rays,[105] but there is no evidence for this from the vibrational spectroscopy or EXAFS studies discussed above.

Fryer *et al.* reported an early TEM study of very fine precipitates, obtained by spray-drying a zirconyl chloride solution that had been refluxed for two hours.[119b] The transmission images of these precipitates gave evidence for a very thin, coherent, amorphous film, consisting of structural units 5-10 Å in diameter. These observations were interpreted as indicating that the tetramer units had polymerised in a random, two-dimensional sheet, similar to Clearfield's mechanism discussed above in Section 2.2.2.[43] This kind of study holds much promise for the identification of the polymerisation mechanisms, at least for the early stages, but it is interesting to note that in the past 30 years these observations have not been reported again.

The surface area and pore-distribution of vacuum-dried precipitates have been characterised by nitrogen adsorption-desorption.[108,110,112,120,121] It has been shown that the degree of mesoporosity (diameter 2 - 50 nm), specific surface area, and total pore volume increase with increasing pH of precipitation. Crucean and Rand showed that pH of precipitation increased from 4 to 10, the pore size distribution changed from being almost entirely microporous (< 2 nm) to predominantly mesoporous, with the mesopores probably being formed in addition to the micropores.[110] Thus the mesostructure of the precipitate formed at high pH is much more open than the low pH precipitate.

In addition to the microstructure, it is important to consider the presence of ions adsorbed or otherwise trapped within the precipitate. The quantity of anions retained decreases with

increasing precipitation pH,[43] and it is widely observed that it is very difficult to completely eliminate anions from materials that have been precipitated at a pH below 7.[75,95,110,112] Relating this to the pore distribution measured in the vacuum-dried precipitates, it can be seen that residual ions can be more easily removed from a mesoporous structure than from micropores. Clearfield reported that residual anions may be removed from a precipitate by washing with a dilute base,[43] which implies that residual anions may be chemically bound to the hydroxide.

2.2.4 Formation of aqueous sols

Preparation of aqueous sols from salt solutions involves forcing hydrolysis, and subsequent polycondensation, to occur in a controlled way so that the colloidal hydroxide particles that are formed remain dispersed, rather than precipitating from solution. Condensation may be promoted either chemically or thermally; this section will review the chemical routes, and thermal routes will be discussed briefly in Section 2.2.5.

The chemical promotion of hydrolysis generally involves the removal of the counter anion from solution. The nitrate ions in zirconyl nitrate solution can be removed by solvent extraction to produce concentrated sols.[122,123] Centi *et al.* used an alkyl tertiary amine diluted in an organic solvent for this method.[122] Woodhead described a method by which the nitrate ions in solution are removed by the addition of formaldehyde.[123] Zirconyl chloride solutions have been electrochemically treated to remove the chloride ions.[74,124] In all these cases, the removal of the anion has promoted polycondensation and formed colloidal systems. These routes have problems in scale-up to industrial applications: solvent extraction is complex, and negates many of the advantages of using aqueous precursors; denitration with formaldehyde is a violent reaction; and electrolysis is relatively slow.

Woodhead's route

A considerably simpler route for effecting the same reaction was proposed by Woodhead.[125,126] Instead of removing anions from the salt solution, additional cations are added in the form of a hydroxide or carbonate, to give a $Zr:NO_3$ ratio of 1:1. The decomposition of the added material consumes acid, promoting hydrolysis, and colloidal particles are formed. The resultant sol will gel reversibly when the pH is raised, and irreversibly if the nitrate anions are removed. Woodhead described the method as "deaggregating zirconium hydroxide with nitric acid",[125] the "nitric acid" being present in the acidic salt

solution, but there has been no evidence published for either the mechanisms that occur or the size or structure of the sol particles. This route has since been reported occasionally in the literature.[127-129] A diffraction pattern of the gel (mixed with amorphous aluminium chloride) has been published,[128,129] showing somewhat more distinct peaks than are observed in the diffraction patterns of the precipitated materials. This diffraction pattern is very similar to that reported in Section 4.3.6 of this thesis, and so will not be discussed further here.

Aside from the broader advantages of using an aqueous sol for processing, Woodhead's route has two major advantages. Firstly, it is simple and quick to carry out, and highly suited to industrial scale-up. Secondly, it is capable of producing sols of much higher oxide concentrations than the hydrothermal route. Woodhead describes the preparation of sols of 2 M, whereas in the hydrothermal route yield is highly limited at concentrations above 0.5 M.[80,130] *For these reasons, this route for the preparation of aqueous 'zirconia' sols has been chosen as the main route to be studied in this thesis.*

One further study of an aqueous sol is worth mentioning. Ramsay *et al*. studied a sol described as an 'anion deficient solution', with a $Zr:NO_3$ ratio of 1:1.[52] Although no preparation details are given, it is quite likely that one of the routes described in this section was used. The average 'molecular weight' of the colloids was reported as ~ 60,000, which is equivalent to 375 $Zr(OH)_4$ units. The Zr K-edge EXAFS spectrum was reported, and was significantly different from that of either the zirconyl nitrate or chloride solutions, with a much stronger signal due to the first Zr neighbour at radius ~3.6 Å. This difference is consistent with the polymerisation of small species together into larger particles, in which each zirconium atom would be adjacent to a larger number of other zirconium atoms. The peak due to the second Zr neighbour at 5.1 Å, characteristic of the diagonal distance across the Zr_4 square, was also stronger in the sol. No coordination numbers were reported.

2.2.5 Hydrothermal treatment

Hydrolysis and condensation of zirconyl cations can also be promoted under hydrothermal conditions. Although this approach is not used in the experimental section of this thesis, it is worthwhile to briefly mention for the sake of completeness.

The products of hydrothermal treatment of zirconyl solutions is quite different to those from the route described above. A zirconyl salt solution heated at, or above, 100°C will hydrolyse to produce fine crystals of monoclinic zirconia. Crystallisation of large amounts of zirconia takes

place within hours at 100°C under reflux,[80,131] and within minutes if the temperature and pressure are raised sufficiently.[132,133] The forced hydrolysis causes the pH of solution to decrease substantially, and the hydrolytic acid may peptise the crystalline particles *in-situ* to form a sol.[80,131] Alternatively, the particles can be separated, washed, and then peptised.[123] Although most workers have prepared from 10-100 nm particles, others have aimed to produce larger particles for conventional powder ceramic preparation.[134]

2.2.6 Summary

Section 2.2 has covered a range of issues concerning the aqueous chemistry of zirconium, and the formation of zirconia precursors from solution. The structure of the cations in zirconyl solutions have been characterised by a range of techniques, and in the case of zirconyl chloride solutions the structure of the 'cyclic-tetramer' species is well known. The structure of cations in other zirconyl solutions is subject to more uncertainty.

The hydrolysis and polycondensation of these cations to form zirconia precursors has been discussed. The most widely studied method, the formation of a precipitate with a base, has been reviewed, along with formation of a sol and hydrothermal processing. A range of unresolved issues concerning the effect of processing parameters on the structure and properties of the precipitate have also been considered.

2.3 Evolution of structure during heating

The preparation of zirconia precursors by solution chemistry usually produces an amorphous, porous material containing much water. The most common way to convert this zirconia precursor into the desired ceramic material is to heat it in a furnace, usually in an air atmosphere (calcination). The transition between amorphous precursor and fully-densified ceramic involves many important changes of structure, which will be reviewed in this chapter.

This section is divided into subsections, based on the stages of heating: drying and decomposition are discussed in Section 2.3.1, crystallisation in Section 2.3.2, and further phase transformations in Section 2.3.3. In the first two Sections this review will concentrate on studies where inorganic precursors have been used, and in most of these cases the precursor has been precipitated from an inorganic salt solution. In the final section the scope of the review will broaden to include a materials from broader range of 'sol-gel' routes.

2.3.1 Drying and decomposition

Drying and decomposition of the chemically-produced zirconia precursor involves the loss of liquid from the pores, adsorbed or bound water, any organic groups and volatile inorganic groups, and also the oxolation of hydroxy bridges.

Oxy-hydroxide materials that are precipitated from solution are difficult to shape, so they are generally used only to prepare powders. Drying processes in these materials are not considered critical, and have not been much studied except by DTA/TGA methods.[75,108,135] It is usually found that there are two separate endothermic mass losses that occur during heating: the first is the loss of free water at approximately 100°C, and the second is the loss of bound water at approximately 150 - 200°C.

The thermal decomposition of precipitated oxy-hydroxides has not been widely studied, and is generally assumed to involve gradual loss of terminal water and hydroxyl groups, and oxolation of hydroxy bridges. Turrillas *et al.* used *in-situ* neutron diffraction, XRD and EXAFS in a detailed study,[109,136] and identified several distinct decomposition stages in materials precipitated from sulfate solutions, although the details of the reactions are still not clear. In the first stage, between approximately 120 and 250°C, terminal water and hydroxy groups are lost, along with limited oxolation of hydroxy bonds. The second stage was thought to involve loss of 'inner water' and non-bridging hydroxy groups between 300 and 400°C. The third stage is final oxolation of all remaining hydroxy bridges immediately before crystallisation. It

was found that the pH of precipitation affected the kinetics of these stages, and the temperatures at which they occurred. Much more further work needs to be done before this scheme can be generally applied to the decomposition of hydroxides.

2.3.2 Crystallisation and crystal growth

Crystallisation occurs when nuclei of a crystalline phase form in the amorphous material, and grow to convert it to a polycrystalline material. The melting point of zirconia is greater than 2700°C, and thus at ambient temperatures the driving force for the crystallisation of amorphous zirconia is very large. The low mobility of the constituent atoms is the barrier to immediate crystallisation. As the temperature of the amorphous material is raised, so does the vibrational energy and mobility of the atoms, until a point is reached in some regions where they may rearrange into energetically-favourable crystalline structures.

Crystallisation of zirconia precursors is frequently studied by heating the precursor at a constant rate, usually 5-20°C/min, through the crystallisation reaction. The most direct method for identifying crystallisation is by *in-situ* diffraction, but this method has only begun to be used recently.[78,105,109] Far more common has been the use of DTA or DSC methods to measure the sharp 'glow' exotherm which is associated with crystallisation, and which will be discussed further below. [90,95,96,108,117,137-139] The temperature at which crystallisation is observed varies a little with heating rate and preparation method, but usually falls in the range 410 - 470°C.

Alternatively, the material can be heated to a lower temperature, and maintained at that temperature while crystallisation occurs slowly.[87,97,117] For instance, Garcia *et al.* crystallised a zirconium hydroxide precipitate after 12 hours of heating at 375°C.[97] The minimum temperature required for isothermal crystallisation has not been firmly established.

The 'glow' phenomenon

When amorphous zirconia is heated at a constant rate, a rapid exothermic reaction occurs between 400 and 500°C, causing the oxide to emit light briefly. This is often referred to as the 'glow' effect,[139] and it is usually associated with crystallisation.

Some XRD, SEM and DSC studies have strongly indicated that the exotherm is due to the energy released during rapid crystallisation,[87,95] and this explanation is widely accepted.[106,107,112,139-141] However, a number of other studies have indicated that the exotherm is due to the rapid coalescence of primary particles, with corresponding loss of surface energy.[86,90,113,142] While in pure zirconia the exotherm occurs concurrently with crystallisation,

the addition of MgO [90] or HfO_2 [86] will separate them so that they occur at different temperatures. While this latter mechanism does not seem to have gained widespread recognition, the available evidence seems to favour it.

Recent DSC measurements of the enthalpy of the exothermic event indicate a value between 15 and 30 $kJ \cdot mol^{-1}$.[75,90,106,107] It has been pointed out that quite high temperatures may be reached in the material during crystallisation, due to a highly exothermic reaction in a refractory material.[138] The activation energy for 'crystallisation' has also been calculated by measuring the shift in the position of the exothermic peak as the heating rate changes. Although values vary widely, the most recent values for inorganic precipitates are around 250 $kJ \cdot mol^{-1}$.[139,140]

The initial crystal structure

Studies of the crystalline material formed from amorphous zirconia precursors generally show that the structure formed is the tetragonal phase. As discussed in Section 2.1.1, the tetragonal phase is known to be *thermodynamically stable* above approximately 1100°C, and the monoclinic phase at lower temperatures. The tetragonal phase formed from crystallisation is thus termed *metastable*. Section 2.4 discusses in some detail its structure, conditions of formation and destabilisation, and the theories proposed to explain various behaviours.

The vast majority of reports find that the tetragonal phase is formed on crystallisation of amorphous precursor materials that have been formed from both inorganic [79,97,101,108,113, 144,145] and metal-organic [5,38,137,146-150] chemicals. The initial diffracting crystal size is often reported to be below 10 nm, and it seldom exceeds 30 nm before transformation to monoclinic occurs.[79,105,112,137,144,149,151] Earlier reports of mixed tetragonal and monoclinic phase [75,110,111] are now thought to be due to a partial transformation to the monoclinic phase that occurs *after* crystallisation, which is discussed in Section 2.3.3. *In-situ* studies always report that only the tetragonal phase is formed during the crystallisation of zirconia precursors.[38,78,101,105,109,113,136]

The cubic phase is also occasionally reported to crystallise when amorphous zirconia is heated. A number of these early reports [97,152-155] can be explained as an insufficient resolution of peaks in the XRD pattern of very fine tetragonal crystals. Where the particle size is very small the characteristic peak-splitting of the tetragonal phase can be unclear,[8,119,156,157] leading to a confusion between the diffraction patterns of the two phases. There are a number of reports of crystalline zirconia that have a cubic-like diffraction pattern, but are shown to have the tetragonal structure when non-diffraction techniques are used, such as Raman

spectroscopy,[38,119] infra-red spectroscopy,[89] EXAFS,[158] and Perturbed Angular Correlations method,[159,160] or where a high-resolution diffraction technique is applied.[157]

However, this does not account for all reports of the cubic phase, including one in which the cubic structure has been identified by IR spectroscopy.[161] These reports are of materials crystallised from metal-organic [161-166] or organic-containing [95,167] precursors. The formation of the cubic phase has been strongly associated with the presence of residual carbon,[166] and one recent report demonstrates that diffusing carbon into monoclinic zirconia will cause a cubic/tetragonal phase to form.[168] The mechanism for this effect is unclear, but may be associated with the formation of oxygen vacancies in a strongly reducing environment (see Section 2.1.2), or the substitution of oxygen anions by carbon in the lattice.

Effects of precursor and humidity on crystallisation

There have been a range of studies examining the effect of precursor-preparation or calcination conditions on the crystallisation reaction. It have been reported that both the pH of precipitation [78,109,136,169] and the concentration of the original solution [94] have a very strong influence in the temperature at which crystallisation occurs. One suggested mechanism is that the precipitation conditions affect the size of the primary particles, which need to agglomerate to a 'critical size' before crystallisation.[94] It has also been shown that humidity in the calcining atmosphere strongly promotes nucleation.[170,171]

Crystal growth

There have been many studies on the crystal-growth and sintering process in 'sol-gel' derived zirconia.[88,110,135,144,170,172-174] A detailed discussion of these studies lies out of the scope of this review. Of particular interest, with regard to the phase transformation discussed in Section 2.3.3, is the observation that grain-growth and densification are enhanced by the presence of water, either from atmospheric moisture, or evolved from the precursor material itself.[37,96,97,135,170] The mechanisms for this are thought to be related to an increase in surface mass transport, and apply to both monoclinic and metastable tetragonal phases.[37]

2.3.3 The tetragonal-to-monoclinic phase transformation

The transformation of the 'metastable' tetragonal structure into the stable monoclinic structure is the last major phase transformation in the processing of pure zirconia. This section reviews previously published results for 'sol-gel' derived zirconia. The phenomena of the crystallisation

and transformation of the tetragonal phase will be discussed further in Section 2.4, including the various conflicting theories for the mechanism of transformation.

The metastable tetragonal phase will partly, or fully, transform to the equilibrium monoclinic phase after heat treatment at 500 - 600°C or greater. Until relatively recently, all studies of the tetragonal-to-monoclinic (t → m) transformation were carried out after the material had been cooled from heat treatment.[37,75,97,144,170,175] These studies showed that samples contained a small fraction of monoclinic zirconia after heating in air to approximately 500°C, and that the fraction transformed increased with increasing temperature or heating time, up to approximately 900°C, by which point the transformation to monoclinic was complete. Naturally, this data was interpreted assuming that the transformation occurred during heating. Recent *in-situ* studies have shown that the tetragonal phase is largely stable at high temperature, and that the t → m transformation mainly occurs *during cooling* from high temperature.[38,78,101,105] The temperature at which transformation occurs may be as low as 300°C or less. Much of the previously-gathered data now needs to be reinterpreted in the light of these recent discoveries.

The extent of the tetragonal-to-monoclinic transformation, and the temperature at which it takes place on cooling, have been shown to be dependant on a wide variety of factors, the most important of which of which are reviewed below. Although many of the issues discussed in this section are not directly dealt with in the experimental sections of this thesis, they are raised here to provide a background to the discussion in Section 2.4, and to indicate the breadth of the unresolved questions which remain for this system, for which this thesis provides a starting point.

Effect of water vapour and atmosphere

There have been a number of studies in which the tetragonal phase is heated both in dried and humidified atmosphere, either air [37,97,170] or nitrogen,[37,97,112] all of which show that water vapour strongly promotes the t → m transformation. As mentioned in Section 2.3.2, water vapour has been shown to accelerate crystal growth, and it has been suggested that these two effects are related.[37] One possible mechanism is related to the theory that the stability of the tetragonal phase is determined by crystal size or surface area, as discussed in Section 2.4. If this is the case, then crystal growth will promote the t→ m transformation. Alternatively, enhanced mass transport with water vapour may somehow promote the transformation by annealing.

There have also been studies which fail to sufficiently distinguish between the effects of water and oxidation/reduction conditions, and which have been interpreted in a number of ways. The application of a vacuum [97,117,176] or inert atmosphere [147,148,167,176] retards the t → m transformation, but this could be due to the absence of either oxygen or atmospheric water. These observations have been used to support the theory that the metastable tetragonal phase is related to oxygen vacancies,[96,113,176] but other comparisons of materials treated in dry O_2 and N_2 have shown no difference in phase composition.[37,170] In summary, the effect of water in promoting the transformation is probably far greater than any effect due to the presence of oxygen.

Effect of precursor structure and composition

A much-studied aspect of the tetragonal-to-monoclinic transformation is the relationship between the structure of the original precursor material, as controlled by the preparation conditions, and the characteristics of the transformation. Many aspects of precursor preparation appear to influence the stability of the tetragonal phase in some way, presumably through short-range or meso-structure. Unfortunately, the evidence is not always consistent, and there is very little understanding of the mechanisms.

As with previous studies, zirconia precursors prepared by the 'precipitation' route have been the most studied. In particular, the relationship between the pH during precipitation and the stability of the tetragonal phase has been a much-studied subject. Although a large number of studies have demonstrated that there is a significant relationship, many have given conflicting results for the actual nature of the dependence.[35,75,95,101,105,110-113] The general trend is that hydroxide precipitated at an extreme pH (< 4 or > 10) will crystallise into a tetragonal phase that is quite resistant to the t → m transformation, and the stability increases with more extreme pH. Recent studies have found indications of a more complex relationship between pH and transformation characteristics.[101,136] The rate of precipitation [96,113] and the concentration of the solution [94] have also been shown to affect the stability of the tetragonal phase, with the stability increasing with slower precipitation and more dilute solution. One study found that the presence of NH_4Cl inhibited the t → m transformation,[89] while others found that the presence of Cl^- anions had no effect.[75,112] However, it is clear that sulfate ions strongly inhibit the t → m transformation,[94,96,100,102-105] and a similar effect has been reported for phosphate ions.[177]

It is worthwhile to note that the preparation conditions of precursors from metal-organic routes have also been reported to affect the t → m transformation.[38,84,164]

Various mechanisms for the effects of structure on the t → m transformation have been suggested, but few satisfactorily explain all the evidence. The search for a reasonable mechanism is hampered because the principles governing the crystallisation and 'destabilisation' of the tetragonal phase are not properly understood. The structure of the precursor material may well influence the size, strain defect density and surface energy of the calcined crystals, all of which have been suggested to determine the stability of the tetragonal phase (see Section 2.4). It has been suggested that surface ions, remaining from the original solution, could retard the nucleation and growth of monoclinic domains[89] or prevent oxygen being adsorbed onto the surface.[105,113] Further systematic studies on the relationship between microstructure and the t → m transformation will be required before these effects can be fully explained.

Crystal size and strain

One implication of the 'surface energy' theory proposed by Garvie,[29,156,179] and discussed in Section 2.4.2.6, is that *crystal surface area* determines the relative stability of the tetragonal and monoclinic phases. This is generally expressed as a 'critical crystal/particle size', and there has been considerable interest in the measurement of 'crystal size' in order to evaluate the theory. However, most studies have used diffraction to measure the *average diffracting crystal size*, which is not necessarily a reliable measure of crystal surface area, and the evidence remains inconclusive.

Some recent studies on the t → m transformation with heating have found a weak correlation between crystal size and the point at which the transformation takes place, but have generally found that other factors, such as chemical preparation conditions, were more important.[89,100,112,146] Other studies have found no significant correlation.[36,38,105,149] A recent *in-situ* diffraction study has found a strong, *linear* correlation between the diffracting crystal 'size' of the tetragonal phase at 900°C, and the subsequent transformation temperature.[136] Although this last study does not consider the possible effect of crystal strain on the broadening of the diffraction peaks, it provides the strongest evidence so far for a 'crystal size effect'.

It is worth noting that some XRD studies have observed that the diffracting crystal size of the monoclinic phase immediately after transformation is significantly smaller than that of the parent tetragonal phase.[37,38,75,100,113,146] This may be attributed to the formation of 'twinned' monoclinic crystals,[35] which are often observed after transformation.[33-35] The observation of a greater *average* diffracting crystal size for tetragonal phase than for monoclinic has led many researchers to conclude that there can be no 'crystal size effect'.[35,36,38,89,100,113,146-149] However, it is often neglected that a twinned monoclinic crystal may well have a smaller diffracting size, but a greater surface area, than an un-twinned tetragonal crystal.

Other researchers have investigated strain in the crystals. One study has shown that stress is relieved during the transformation, and may be a driving force.[175] Another study shows that the t → m transformation appears to take place when strain generated by realignment of crystals during heating exceeds ~ 2 %.[170] These studies are important, as it is well known that stress can influence martensitic transformations (see Section 2.1.3). Although it is difficult, at best, to accurately measure strain in small crystals by XRD, more work in this area is required.

***In-situ* studies**

A great deal has been learnt about the t → m transformation through recent *in-situ* studies, using conventional XRD,[38,105,113,180] synchrotron XRD,[78,101,109,136] and neutron diffraction.[109,151] The precursor materials used have ranged from a precipitate from a sulfate solution,[101] to an aerogel prepared from an alkoxide.[38] The main observations of these studies are summarised here.

The metastable tetragonal phase can be held for some hours at any temperature while remaining largely stable. Some studies have found that transformation occurs slowly during holding at temperatures below 800°C,[38,113] while others reported no transformation over several hours at temperatures above 900°C.[101,136] These different observations are most probably due to differences in preparation and structure of the precursor.

When the material is cooled from a holding temperature of 800°C or higher, a t → m transformation begins at a point well below the holding temperature. Two important characteristics of the transformation have been reported; the onset temperature, and the reaction profile of fraction transformation plotted against temperature. The onset temperature has been likened to the 'transformation start' temperature, M_s, in classical martensitic-transformation theory.[38] The onset temperature under various conditions ranged from over

1000°C to below 300°C. The profiles could be narrow, spaning less than 50°C, or quite broad, spanning several hundred degrees.

Both onset temperature and transformation profile were found to be sensitive to precipitation pH, rate of polymerisation (both inorganic and alkoxide) and furnace atmosphere, as discussed in the previous sections. It was also found that the differences in transformation behaviour between materials prepared by different methods decreased with extensive heating, particularly above 1000°C. This indicated that whatever structural features that affect the transformation were annealed or removed.

The extent and conditions of heat treatment also strongly affected the t → m transformation. A greater maximum heating temperature, and a longer holding time, increased the onset temperature and the fraction of material transformed. Increasing the rate of cooling decreased (ie delayed) the onset temperature.[78,101,136] By reducing the heat treatment, the onset temperature could be delayed so that the transformation did not go to completion, resulting in mixed phases after cooling. These results are completely consistent with the earlier, non-*in-situ* studies.

These observations have strong implications for the various theories proposed to explain the formation of the tetragonal phase, and characteristics of the t → m transformation. These will be discussed in Section 2.4.2.

2.3.4 Summary

As discussed in this section, the changes in the structure of a zirconia precursor as it is heated are not always well understood. The following points can be made in summary:

1. Removal of water and hydroxide groups from a precipitate occurs in two, distinct, endothermic events, at approximately 100 and 150 - 200°C.
2. Crystallisation generally takes place between 410 and 470°C, accompanied by a strong exotherm which may be associated with a reduction in surface area.
3. The crystalline phase formed is always the 'metastable' tetragonal phase, unless some carbon is present, in which case the 'metastable' cubic phase may be formed. Observations of monoclinic phase are attributed to partial t → m transformation after crystallisation.
4. The presence of atmospheric water promotes both the nucleation and crystal-growth processes.
5. The 'metastable' tetragonal phase is largely stable when heated, but may partially or fully transform to the stable monoclinic phase during cooling. Higher temperatures and longer heating times increase the transformation temperature on cooling and the fraction transformed.
6. The presence of atmospheric water promotes the t → m transformation, possibly with a mechanism associated with crystal growth. The role of oxygen in the transformation appears to be minor, but remains uncertain.
7. The chemical conditions under which the precursor material is prepared affects the transformation characteristics substantially. A range of mechanisms have been suggested, but none have been confirmed.
8. The role of crystal size and strain on the transformation appears to be relatively minor under most conditions, but any relationship is still not certain.
9. The presence of sulfate strongly inhibits the transformation.

2.4 Low-temperature formation and stability of the tetragonal phase in pure zirconia

Ruff and Elbert first reported in 1929 that nominally-pure zirconia could exist in the tetragonal phase at room temperature,[181] and in the following decades a few other papers were published on the phenomenon.[182,183] These papers attributed the appearance of this phase to trapped anions in the crystal lattice. The low-temperature tetragonal phase is generally referred to as '*metastable*' (*ie* stabilised by kinetic factors), and this usage is continued in this thesis although it was later suggested that some thermodynamic factors may be important. In 1965, Garvie suggested that differences in the surface energy between the tetragonal and monoclinic phases could cause the tetragonal phase to be *thermodynamically stable* in very small crystals,[156] and since then many other theories have been suggested, based on various thermodynamic and kinetic arguments.

Over the past 30 years the preparation of zirconia by 'sol-gel' and other non-equilibrium methods has become increasingly common, and the practical importance of controlling the structural phases has been recognised. Despite this extended period of investigation, a consensus on the mechanisms for the stability of the 'metastable' phase has not been reached. Even the most recent *in-situ* investigations into the crystallisation and destabilisation ($t \rightarrow m$) of the 'metastable' tetragonal phase are not able to fully support any particular theory.[101,113,136] Indeed, recent *in-situ* results have shown that the behaviour is more complicated than originally thought. Consequently, the various theories have been a point of both substantial interest and considerable disagreement for many researchers.

Unfortunately, despite many observations reported and theories proposed, there is very little in the way of comprehensive reviews published in the literature. The aim of this part of the literature review is to collate and summarise these reports, so that the various theories can be assessed. Section 2.4.1 is a summary of the conditions under which the metastable tetragonal phase is formed in pure zirconia and transformed to the monoclinic phase, and structural studies of the phase. Section 2.4.2 discusses the major theories suggested to explain these observations.

Metastable phases

Metastable phases are generally produced by non-equilibrium processing routes, such as sol-gel, and are associated with small particles size, high surface areas, and low processing temperatures. Levi has reviewed metastable phases in oxide ceramics, and states that "the key

to metastability is the generation of a highly energized system which, when de-energized, is kinetically constrained from achieving the configuration most favored thermodynamically". Such non-equilibrium systems are created by processes such as the pyrolysis of precursor materials, rapid solidification, vapour deposition, etc.[184]

The crystallisation of metastable phases from amorphous materials is not unusual in transition metal oxides, although the mechanisms vary. Well known examples include the crystallisation of amorphous titania into the anatase phase, alumina into the γ-Al_2O_3 phase, and yttria into a monoclinic phase.[185] An early study of a range of rare-earth oxides, prepared from hydrates, concluded that phases that are stable at high temperature will crystallise at low temperatures in oxides with the ionic radius of the metal greater than approximately 0.94 Å.[152] Metastable phases also occur in non-oxide ceramics, such as SiC.[186]

2.4.1 Observations

Conditions for low-temperature crystallisation of the tetragonal phase

As discussed in Section 2.3.2, whenever carbon-free, amorphous zirconia-precursors are crystallised in air by heating, the tetragonal phase always forms, regardless of preparation route. However, the chemical conditions under which the precursor material is prepared may affect the crystallisation temperature considerably, and this is attributed to primary particle size in the precursor.

The decomposition of a range of zirconium-containing inorganic and metal-organic compounds has been studied. The compounds $Zr(OH)_2Cl_2$,[103] $Zr(OH)_2(NO_3)_2$,[103,187,221] and $ZrSe_2$ [188] all decompose to form an amorphous oxide, which then crystallises into the tetragonal phase. However, an intermediate amorphous phase is not always formed. A detailed study of the decomposition of zirconium sulfate hydrate has shown that a crystalline structure is present immediately before a rapid decomposition reaction and crystallisation of t-ZrO_2.[189] This result is interesting, as it has been claimed that the structure of α-$Zr(SO_4)_2$ is 'not compatible' with that of t-ZrO_2.[100] A range of zirconium-organic compounds also decompose to form the tetragonal phase.[147,148,190,191] In some cases the cubic phase is reported,[162,163,192] and this is attributed to the presence of residual carbon, as discussed in Section 2.3.2. Zirconium carbide also oxidises to form a cubic [190,194] or tetragonal [195] crystal phase. *No study has been found in the literature which demonstrates that a pure monoclinic phase is formed from the thermal decomposition of any zirconium-containing compound in air.*

Hydrothermal routes are also used for the preparation of nano- and microcrystalline zirconia, and these also can form the tetragonal phase. Two approaches are generally used; either a hydroxide 'gel' is precipitated by treating a zirconyl solution with a base and then treated in an autoclave, or a zirconyl solution is directly hydrolysed under hydrothermal conditions. When the former approach is used, the tetragonal phase usually crystallises first, followed by an transformation to the monoclinic phase with further heating.[6,196-199b] It is not clear whether the monoclinic phase ever directly crystallises from the amorphous material. It has been found that the phase composition, or the transformation rate, is dependant on the pH of the surrounding solution,[6,196] the temperature,[6,199,196] and the presence of various other ions (particularly metal-alkali halides).[197,198] Results from different studies are not always consistent, and possibly the structure of the initial material is more important than originally thought.

In other studies where zirconyl chloride or nitrate solution is directly hydrolysed, the monoclinic phase usually crystallises instead. Monoclinic crystals as small as 6 nm[172] and 3 nm[80,200] have been reported by this route. It should be noted that in these experiments the solution would have been much more acidic than when the starting material was a hydroxide precipitate.

The tetragonal phase has also been formed in pure zirconia by a number of other non-equilibrium techniques, such as ball milling of monoclinic zirconia,[201] and rapid cooling of evaporated zirconia.[202,203]

This very wide range of preparation methods that lead to the tetragonal phase points to a universal, rather than precursor-dependent, mechanism for the crystallisation of the metastable phase.

The tetragonal-to-monoclinic transformation

A full understanding of the t → m transformation, and factors that influence it, will assist in a better understanding of the mechanisms of metastability. The thermal transformation of the 'metastable' tetragonal phase to the stable monoclinic phase has been most thoroughly studied in the heating and cooling of zirconia precursors. The results of these studies are discussed in detail in Section 2.3.3, and can be summarised by the following points:

1. The 'metastable' tetragonal phase is largely stable when heated, but may partially or fully transform to the stable monoclinic phase during cooling. Higher temperatures and longer

heating times increase the transformation temperature on cooling and the fraction transformed

2. The presence of atmospheric water promotes the t → m transformation, possibly associated with crystal growth. The role of oxygen in the transformation appears to be minor, but remains uncertain.
3. The chemical conditions under which the precursor material is prepared affects the transformation characteristics substantially. A range of mechanisms have been suggested, but none have been confirmed.
4. The role of crystal size and strain on the transformation appears to be relatively minor under most conditions, but the reported data is contradictory and the relationship is not certain.
5. The presence of sulfate strongly inhibits the transformation.

Partial or complete transformation of metastable tetragonal to the monoclinic phase has also been reported to be caused by mechanical treatment, such as grinding,[174,199] ball milling,[176,201] and pressing.[104,203]

The relationship between crystal size and phase stability has also been studied for other routes that lead to the metastable tetragonal phase. One recent study of the hydrothermal crystallisation of zirconia found a correlation between particle size and crystal phase,[196] while earlier ones did not.[172,197] A 'critical particle size' of 6 nm was reported from a recent TEM study of condensation-formed, nano-sized zirconia particles.[204]

It is also important to note that the transformation of metastable phases is often accompanied by rapid grain growth driven, by the release of excess free energy,[184] so that any crystal growth associated with the t → m transformation may be either a *cause* or an *effect* of the transformation. This point has received virtually no attention in the literature.

Structural studies of the metastable tetragonal phase

The first point to note is that the metastable tetragonal phase is only ever observed to occur as very fine crystals. In most cases, the 'average diffraction size' reported does not exceed 30 nm.

All diffraction studies have indexed this phase to the $P4_2/nmc$ or $P\bar{4}m2$ space groups, which is the same indexing made for the stable high-temperature and rare-earth-stabilised structures.

(This indexing, and the different lattice parameters used, is discussed in Section 2.1.1.) There have been two studies using the Rietveld method for structure determination, using neutron[5] and X-ray[205] radiation, the results for which are summarised in Table 2-5. Lattice parameters given by other XRD studies of the metastable phase vary somewhat, falling in the range a_p = 3.59 - 3.60 Å and c = 5.15 - 5.19 Å.[6,7,137,157,180]

Table 2-5: Reported lattice parameters of the tetragonal phase.

	a_p (Å)	a_s (Å)	c (Å)	c/a_s	z
Igawa *et al.*[5]	3.591(1)	5.078	5.169(1)	1.018	0.204(4)
Málek *et al.*[205]	3.5984(5)	5.089	5.152(1)	1.012	0.210(1)

Values in parentheses are the uncertainty in the final decimal place

There has been no previous attempt to relate the lattice parameters with the causes or mechanisms of metastability, possibly because it is generally believed that the mechanisms are short-range. However, it may be of value to determine whether a relationship exists between the spread of reported lattice parameters, and the variation in phase stability. Such a study would require a substantial amount of work.

There have been other, non-diffraction studies on the metastable phase as well. Raman spectra have been reported and, despite their relatively poor quality, appear to be close to the spectra of the stabilised and high-temperature phases.[38,119] One EPR study suggests that anion vacancies, associated with trapped electrons, may be formed during the crystallisation of the tetragonal phase,[191] but no further work with this technique has been reported. An IR and NMR study has found OH anions are present mostly at surface of crystals, but also within the structure of the t-ZrO_2 crystals.[199] A perturbed-angular-correlation study has shown that metastable t-ZrO_2 contains some 'very defective' zirconium environments.[160]

2.4.2 Theories

Over the past 30 years there have been many theories proposed to explain the crystallisation and metastability of the tetragonal phase, and its eventual transformation to the monoclinic phase. However, none have achieved universal acceptance. This section reviews a number of the most important theories.

There has been a wide range of suggested mechanisms for the nucleation and stabilisation of the tetragonal phase at low temperature, such as lattice defects, non-stoichiometry, structural similarity with the amorphous precursor, retention of various anions or water, strain, surface energy, etc. Although the low-temperature tetragonal zirconia phase is generally referred to as

'metastable', these mechanisms may rely on both thermodynamic and kinetic factors, and a clear distinction between them is not usually made. There may well be a number of mechanisms, each of which may dominate under different conditions.

Very few of the theories attempt to account for all of the observations; rather they suggest mechanisms for either the formation of the tetragonal phase at low temperature, its stabilisation, or various aspects of the tetragonal-to-monoclinic transformation. The 'surface area' theory, discussed in Section 2.4.2.6, comes close to a full explanation, but this is because it takes into account many difficult-to-measure properties, such as surface area, microstrain, etc, and is difficult to assess quantitatively.

Until recent *in-situ* studies were carried out, researchers have been able to observe only the phase structure after cooling, and have been unable to separate crystallisation behaviour from transformation. To complicate matters, characteristics of the t → m transformation have been found to be heavily dependent on processing conditions.

2.4.2.1 Structural similarity

When crystallisation takes place under non-equilibrium conditions, the *kinetics* of the transformation often has more importance in the selection of the crystallisation phase than the thermodynamic driving force.[184] In other words, the formation of a metastable phase may be favoured over the stable phase if a simpler atomic rearrangement is required during crystallisation. If this occurs, the resulting phase remains 'metastable' until sufficient energy is provided to overcome the kinetic barrier to forming the stable phase. On this basis, it has been suggested that the short-range structure of amorphous zirconia is more similar to the tetragonal phase than to the monoclinic phase, so the crystallisation of the tetragonal phase will require less energy and produce less internal strain.[67,76,77,79,108,117,119,148] Once crystallised, some kind of kinetic barrier (impurities, vacancies, strain, lack of nucleation sites *etc.*) keeps the phase stable until further heating. This is referred to here as the 'structural similarity' theory.*

* This theory has been used to explain the relationship between the precipitation conditions in a salt solution, and the phases present after calcination. It was suggested by Clearfield that slowly polymerised materials would be closer to the ideal crystalline 'hydroxide' structure, and thus would topotacticly crystallise in the tetragonal phase.[43,77] Materials that had been rapidly precipitated would be highly disordered, and would crystallise in the monoclinic phase. Although at the time this theory fitted much of the known data, it has been found to be insufficient in the light of subsequent *in-situ* investigations that have shown that only the tetragonal phase crystallises from all types of precursors.[38,113,136]

A variation on this theory is the possibility that 'X-ray amorphous' material contains very short-range, non-diffracting crystals,[94,105,119] which then grow rapidly upon 'crystallisation'. Leaving aside the debate on the actual definition of a 'crystal', this suggestion can be treated on a similar basis to the structural similarity theory.

The validation of this theory would require a detailed study of the short-range structure of various 'amorphous' precursors. Probably the most promising technique is measuring and modelling the *extended X-ray absorption fine structure* (EXAFS) around the zirconium X-ray absorption edge. There have been several EXAFS spectra reported for amorphous zirconia precursors, prepared using inorganic [85,206] and metal-organic [158] routes, all of which are for 'as-prepared' materials without any heat treatment. Comparison of the reported Zr-O and Zr-Zr coordination environments does not indicate that the short-range structure of any of these materials is significantly closer to the tetragonal phase than to the monoclinic phase. Furthermore, a recent *wide-angle x-ray scattering* (WAXS) study of an 'amorphous' zirconia xerogel and aerogel indicated that the structure is significantly closer to that of the monoclinic phase, well beyond the first coordination shell.[207]

In summary, despite much discussion of this theory in the literature, there is presently insufficient evidence to support it. The major obstacle to acceptance of this theory is the wide range of zirconium-containing materials, prepared from many different routes, with different levels and types of impurities, that will form the tetragonal phase. For this theory to be accepted, a mechanism would have to be shown for the topotatic transformation of amorphous zirconia to tetragonal phase *for each of these materials*. Much further work is required, including a comprehensive *in-situ* study of the crystallisation of zirconia from a range of sources, using time-resolved EXAFS and XRD techniques.

2.4.2.2 Oxygen vacancies

It has been suggested that the metastable tetragonal phase in pure zirconia is slightly sub-stoichiometric, causing stabilisation by oxygen vacancies.[117,138,147,148,191,208] Further heating in air will fully oxidise the sample, allowing the transformation to monoclinic to occur.

This theory has been prompted by a number of observations. Firstly, vacancies play a role in the stabilisation of rare-earth doped cubic zirconia, and may also play a role in the stabilisation of doped tetragonal zirconia,[1] as discussed in Section 2.1.2. Secondly, a number of researchers have found that the calcination atmosphere has a considerable effect on the tetragonal-to-monoclinic phase transformation. The transformation is inhibited when the

material is in a oxygen-free atmosphere, or under a vacuum.[96,112,113,117,147,170,176] However, these studies do not rule out the possibility that it is the absence of moisture that inhibits the transformation, not of oxygen. Thirdly, there is some evidence from EPR spectra that oxygen vacancies, associated with trapped electrons, are formed during the crystallisation of the tetragonal phase.[191] The origin of the vacancies is usually attributed in some way to the decomposition of the precursor material.[117,147,148,191,208] It has also been suggested that the high temperatures reached momentarily during the rapid crystallisation reaction could be responsible for oxygen vacancies.[138]

Although the role of oxygen vacancies in the stabilisation of rare-earth doped tetragonal zirconia is still uncertain,[1] Kountouros and Petzow have calculated that the vacancy concentration required to stabilise the tetragonal phase gives an equivalent stoichiometry of $ZrO_{1.98}$.[208] Pure, sub-stoichiometric zirconia, with composition approximately $ZrO_{1.97}$, has been reported to be prepared by heating in a reducing atmosphere.[117,138,209] However, this material is always described as being black or grey due to the Zr^{3+} cation, and the only report of the crystalline phase found it to remain in the equilibrium monoclinic phase during reduction and re-oxidation.[209] The metastable tetragonal phase is generally prepared by heating in oxidising conditions, and is always reported to be white. Furthermore, from the published Zr–O phase diagrams,[2,210,211] there does not appear to be any evidence that sub-stoichiometry expands the stability range of the tetragonal phase to lower temperatures than usual.[1]

The case is different for zirconia prepared from metal-organic compounds, which frequently contains some residual carbon. It is possible that the carbon may cause oxygen vacancies in zirconia,[147] or alternatively that substitution of oxygen by carbon stabilises the tetragonal phase.[166] These theories are not applicable to inorganic-derived zirconia.

In summary, there is insufficient evidence to support this theory, except for the case of zirconia prepared from metal-organic precursors. However, the possibility remains that a very small fraction of oxygen vacancies may act as point defects, inhibiting the martensitic $t \rightarrow m$ transformation.

2.4.2.3 Trapped ions or impurities

The earliest suggestions for the stabilisation of the tetragonal phase was that it was caused by small amounts of anion impurities from the salt precursor,[181] or hydroxy groups from the hydroxide precursor.[183] This idea has been considered subsequently,[1,6,8,75,95,103,152,199b] and impurities including Cl^-, SO_4^{2-}, NO_3^-, OH^- and Na^+ have been suggested,[208] but no clear

mechanism has been shown. The impurities may act as point defects which inhibit the martensitic t → m transformation. Presumably the impurities are removed after heating at sufficient temperature, and the transformation is free to occur.

There is little unambiguous evidence for the effect of anions available, except for the case of sulfate impurities, where it is quite well established.[96,100,102-105] One difficulty with the theory is that the tetragonal phase seems to always crystallise first, regardless of the precursor preparation method. In many studies of the crystallisation of zirconia, great care is taken to wash out all anions from the precursor before crystallisation of the tetragonal phase. Other zirconia precursors have been prepared from very high purity alkoxides,[162,163,148] in which the only significant impurity could be carbon, which is absent from the oxide in most other studies. The conclusion must be that either the structure of zirconia is extremely sensitive to very low concentrations of a wide range of impurities, or that impurities do not play a decisive role in the stabilisation of the tetragonal phase (other than trivalent cations).

2.4.2.4 Stress/strain energy

The rapid crystallisation of amorphous oxides, with accompanying densification and reduction of surface area, is likely to cause considerable strain in the structure. Two mechanisms have been suggested in which stress/strain in the material may stabilise the tetragonal phase. Firstly, the effect of strain on martensitic transformations is well known, and is discussed in Section 2.1.3. Stress in the crystals may inhibit the martensitic t → m transformation until the driving forces overcome the opposing stress, or the stress is annealed.[94,146,151,175,199] Secondly, the stress energy could combine with surface energy effects to thermodynamically stabilise the t-ZrO_2 phase,[29,179,212] as discussed in Section 2.4.2.6.

The effect of strain on the stability of the tetragonal phase is difficult to assess, as it is hard to directly measure strain in small crystals, particularly when the crystal size is not well defined. As a result, there is no firm evidence for any decisive role that stress-strain may play in the stabilisation of the tetragonal phase.*

* It is observed that the effect of strain tends to be invoked by authors only when their observations do not completely correlate with their favoured theory.[146,151,179]

2.4.2.5 Lack of nucleation sites

As discussed in Section 2.1.3, it has been suggested that the t → m transformation is dependent on a nucleation site of some kind. Suggestions vary widely as to the actual nature of this site, such as static defects, dislocations or 'dynamic embryos', but if such structures are required to trigger the t→ m transformation, then their absence in a particular crystal will prevent the transformation from taking place.[26,27,30,38,41,199] This theory has usually been invoked to explain the apparent crystal-size dependence of the transformation. The smaller the crystal, then the less likely that each crystal will contain a nucleation site. This, of course, assumes that nucleation is predominantly a bulk effect, and does not occur at the surface of the crystal (including grain boundaries).

The suggested properties of 'dynamic embryo' sites (structure, size, growth rate, etc) can be tailored to account for many of the characteristics of the t → m transformation, including the transformation during cooling.[38,30,39,41] This has led to some of the most sophisticated theories so far. The concept has been applied to the transformation of both 'metastable' zirconia, and the reversible t ⇋ m transformation at ~1100°C. The nature of chemical preparation may even affect the density of nucleation sites in the crystals.[38]

However, there remain three major difficulties with this theory. Firstly, it does not explain why the tetragonal phase crystallises in the first place. Secondly, it does not explain the dependence of the t → m transformation on cooling rate and atmosphere (see Section 2.3.3). Third, there is no direct evidence for the existence of nucleation sites, particularly of the 'dynamic embryo' kind, or their absence/shortage in tetragonal zirconia.

2.4.2.6 Relative surface energy

The 'surface energy' theory for the stabilisation of the tetragonal phase has become both one of the most widely quoted, and most controversial, theories. Unlike most other theories, it proposes that under certain conditions the tetragonal phase is thermodynamically stable at low temperature, and attempts to explain both the crystallisation and transformation of the tetragonal phase.

The theory, based on classical thermodynamics, proposes that the ratio of surface area to bulk volume will influence the relative thermodynamic stabilities of the monoclinic and tetragonal phases. Although this ratio can be roughly determined by crystal size, this is not a 'particle size' effect as it is frequently understood, but a *surface energy* effect. The concept behind the

theory was proposed independently in 1965 by Krauth and Meyer[213] and by Garvie.[156] Garvie subsequently developed the theory over following decades, introducing a detailed mathematical treatment.[29,179]

Thermodynamic principles

The thermodynamic stability of a phase is determined by its total *free energy*; whichever of the possible phases that has the lowest free energy is the most stable. The free energy of a phase is usually dominated by the *bulk* free energy, but the total also includes contributions from the surface energy, as well as any strain energy. Where the surface-to-volume ratio is very high, the *surface free energy* may become more important than the bulk term in determining phase stability. Note that the actual values of the surface and bulk energy of each phase are not important, only the *difference* between the values for the possible phases.

The basic assertion of this theory is that the tetragonal phase has an intrinsically lower *surface* free energy than the monoclinic phase. Thus, although at temperatures below approximately 1100°C the tetragonal phase has a higher *bulk* free energy than the monoclinic phase, when the surface area is very large the difference in surface free energy may become greater than the difference between the bulk free energy. The essential result of this situation is that, at a given temperature, there is a certain surface-to-volume ratio above which the tetragonal phase is thermodynamically stable. Another way of expressing this is that for a given surface-to-volume ratio, there exists a 'critical temperature' below which the tetragonal phase is stable.

A convenient way of expressing the surface-to-volume ratio is by the 'particle size', although this requires some considerable simplifications. If we neglect the effect of strain, and assume spherical crystals which have a uniform surface free energy, a 'critical crystal radius' r_c for transformation at a given temperature T can be defined by the Equation 2-1, as given by Garvie.[179] The values S and S' represent the surface free energy of the monoclinic (low temperature) and tetragonal (high temperature) phases, respectively, q is the heat of transformation per unit volume of infinite crystal, and T_b is the transformation temperature of an infinite crystal. The critical crystal radius increases to infinity as T approaches T_b.

$$r_c = \frac{-3 \cdot (S' - S)}{q \cdot (1 - T/T_b)} \qquad \textbf{Equation 2-1}$$

Garvie suggested values for zirconia of r_c = 5 nm (at 273 K), ΔS = 0.36 Jm^{-2}, $q = 2.82 \times 10^8$ Jm^{-3}, T_b = 1175°C = 1448 K, from various sources.[179] From these values it is apparent that

the equilibrium transformation temperature is only significantly altered for crystals with diameter ($2r$) below 100 nm, and particularly below 50 nm.

There are several implications of this theory that are not explicitly stated by Garvie. Firstly, any transformation from tetragonal phase to monoclinic caused by thermal treatment will only occur during cooling, or during isothermal hold as the crystal size increases. It is remarkable to note that this prediction was borne out by *in-situ* experiments (Section 2.3.3) decades after the theory was first proposed. Secondly, during cooling the large tetragonal particles will transform first, followed by the small ones, and *vice versa* for the heating of monoclinic crystals. This prediction would be difficult to test in practice. Thirdly, the t → m transformation will be reversible, provided that grain growth does not occur, and subject to the hysteresis in transformation temperature that is normal for martensitic transformations. Although the observed transformations of comparatively large crystals (> 150 nm) at temperatures above 1000°C are consistent with this prediction,[29] there is no report of this occurring at low temperatures for very small crystals.

Variations in surface energy

This theory becomes more complicated when variations in surface energy are taken into account. According to the surface-energy theory, it is the difference between the surface free energy of the two phases (ΔS) that controls their relative stability in small particles. However, there has been very little discussion in the literature about the possible effects of the difference kind of surfaces that may be present, the degree of coherence in crystal/crystal interfaces, adsorbed water and other species, or the presence of a reducing atmosphere or vacuum. All of these factors could alter the value of ΔS considerably, and may explain many of the observed variations in the behaviour of the 'metastable' tetragonal phase.

There are a number of observations that may be explained, at least partially, by the effect of surface energy on the phase stability. The role of water vapour in promoting the t→ m transformation may be due to adsorbed water molecules decreasing the ΔS term, as suggested by Murase.[37,176]

An opposite role may be played by various adsorbed anions, which may increase ΔS and thus 'stabilise' the tetragonal phase. This is most probably the case for surface sulfate groups, which have been strongly associated with increased stability of the tetragonal phase. This argument is more speculative for other species, but may be connected with the observation

that the 'pH of precipitation', which may influence the amount of anions retained in the precipitate, may affect the stability of the tetragonal phase. However, it seems also clear that surface impurities are not necessary for the formation of the 'metastable' phase, and it is unclear how large a role such surface species actually play.

A layer of hydroxide is thought to form on the surface of zirconia crystals when immersed in water,[174] which has a great potential for altering the surface energies of the two crystalline phases. The structure of such a phase could well alter greatly with pH; this can be associated with the hydrothermal formation of very small (< 6 nm) monoclinic zirconia crystals in acidic zirconyl solutions,[80,172,200] and the predominance of the tetragonal phase (at least at first) in more basic reaction mixtures.

The surface-energy theory has yet to be properly evaluated with respect to most of these possibilities. Many questions exist in this area, and will remain until it becomes possible to reliably measure, or calculate, the surface energy of very small crystals with adsorbed species.

There have been some advances in the study of zirconia surfaces in the last decade. Surface hydroxyl groups are known to exist on monoclinic crystals that have been calcined, and these have been studied extensively.[214,215]

Other complicating issues

The effects of stress on the thermodynamic stability have been discussed at length in several papers by Garvie.[29,179,216] A uniform compressive stress, such as that experienced by a particle in a confining matrix, will lower the transformation temperature. Non-uniform stress will broaden the range of temperatures over which the transformation may take place. The influence of stress on stability has been used to explain observations of tetragonal crystals larger than monoclinic crystals.[179]

As discussed in Section 2.1.3, thermodynamic factors are not always dominant in martensitic transformations. This has been recognised by Garvie who has suggested that once the thermodynamic conditions are favourable for transformation, it must then be nucleated.[30,179] The observation of large tetragonal crystals may be explained by lack of a nucleation site,[179] in an argument similar to that discussed in Section 2.4.2.5. This argument may also be applied to the reverse m → t transformation.

The tetragonal-to-monoclinic transformation is frequently accompanied by twinning, or the formation of twin-related structures (Section 2.1.3). It is unlikely that twinning in a crystal will

have much effect on its surface energy, since the surface energy of a twin interface is highly coherent.[217] Thus a twinned monoclinic crystal may be more stable than a untwinned tetragonal crystal with a larger 'diffraction size'. This effect has not been previously discussed in relation to the surface-energy theory.

Evaluation

The 'surface-energy' theory has been widely discussed since it was first proposed. One major difficulty in evaluation of this theory is that it involves several properties that are very difficult to measure, such as the strain and surface energy of very small crystals. This makes it not only hard to 'disprove', but also difficult to apply in practical situations, and at present is limited to a semi-quantitative explanation only.

The merits of the surface-energy theory have been debated mainly with regard to the existence and value of a 'critical crystal size', $2 \cdot r_c$, below which a tetragonal zirconia particle would be stable. Garvie initially proposed a 'size' of 30 nm based on experimental observations,[156] while Krauth & Meyer suggested a critical size of about 17 nm.[213] Based on subsequent observations and theoretical calculations, Garvie later reduced his estimate to 10 nm,[179] which has been supported by some later observations.[29,196,218] Various other values have been calculated, such as 6 nm[219] and 4 nm[204], and other researchers have measured a critical particle size experimentally.[112,151,204,218,220]

The main grounds for criticism of the surface-energy theory has been the observation of tetragonal crystals that are larger than monoclinic crystals, either within the same or in different samples.[35,36,38,89,100,113,148,149,170] On this basis the theory has often been claimed to have been 'disproved'. However, many of these criticisms do not do justice to the complexities of the theory, treating it purely as a 'critical size' effect, and neglecting surface energy, stress and twinning effects.

A stronger criticism is the observation of very small monoclinic crystals, such as those produced by hydrothermal processing, which cannot be easily explained by the surface-energy theory. Monoclinic crystals with sizes of 6 nm[35,172] and even 3 nm[80,200] have been observed by TEM. It has been suggested that differences in surface energy of hydrothermally prepared crystals may be responsible for a much smaller 'critical size',[172] but no detailed work has been done.

The true evaluation of this complex theory still requires more detailed study, including the accurate measurements of true crystal size (not 'diffraction size'), surface-to-volume ratio, surface energy, crystal strain, and nucleation mechanisms.

2.5 References

1. E.H. Kisi and C.J. Howard, "Crystal structure of zirconia phases and their inter-relation" *Key Engineering Materials 153-154* 1-36 (1998)
2. *Alloy Phase Diagrams*, Edited by H. Baker, ASM International, Ohio, USA (1992)
3. G. Teufer, "The crystal structure of tetragonal ZrO_2" *Acta Cryst. 15*, 1187 (1962)
4. D. Michel, L. Mazerolles and M.P.Y. Jorber, "Fracture of metastable tetragonal crystals" *J. Mater. Sci. 18* 2618-2628 (1983)
5. N. Igawa, Y. Ishii, T. Nagasaki, Y. Morii, S. Funahashi and H. Ohno, "Crystal structure of metastable tetragonal zirconia by neutron powder diffraction study" *J. Am. Ceram. Soc. 76* [10] 2673-2676 (1993)
6. H. Nishizawa, N. Yamasaki, K. Matsuoka and H. Mitsushio, "Crystallisation and transformation of zirconia under hydrothermal conditions" *J. Am. Ceram. Soc. 65* [7] 343-346 (1982)
7. M. Yashima, M. Kakihana, K. Ishii, Y. Ikuma and M. Yoshimura, "Synthesis of metastable tetragonal (t′) zirconia-calcia solid solution by pyrolysis of organic precursors and coprecipitation route" *J. Mater. Res. 11* [6] 1410-1420 (1996)
8. R. Srinivasan, S.F. Simpson, J.M. Harris and B.H. Davis, "Discrepancies in the crystal structures assigned to precipitated zirconia" *J. Mater. Sci. Lett. 10* [6] 352-354 (1991)
9. D.K. Smith and H.W. Newkirk, "The crystal structure of baddeleyite (monoclinic ZrO_2) and its relation to the polymorphism of ZrO_2" *Act Cryst. 18*, 989-991 (1965)
10. R.J. Hill and L.M.D. Cranswick, "International Union of Crystallography Commission on Powder Diffraction Rietveld round robin. II. Analysis of monoclinic ZrO_2" *J. Appl. Cryst. 27*, 802-844 (1994)
11. C.J. Howard, R.J. Hill and B.E. Reichart, *Acta Crystallographa B44*, 116 (1988)
12. R.E. Hann, P.R. Suitch and J.L. Pentecost, "Monoclinic crystal structures of ZrO_2 and HfO_2 refined from X-ray powder diffraction data" *Commun. Am. Ceram. Soc. 1985* C285-C286 (1985)
13. J. Adam and M.D. Rogers, "The crystal structure of ZrO_2 and HfO_2" *Acta Crys. 12* 951 (1959)
14. M. Yoshimura, "Phase stability of zirconia" *Bull. Am. Ceram. Soc. 67* [12] 1950-1955 (1988)
15. A.H. Heuer, R. Chaim and V. Lanteri, "Review: Phase transformations and microstructural characterisation of alloys in the system Y_2O_3-ZrO_2" *Advances in Ceramics 24* 3-20 (1988)

15b. R.C. Garvie, "A personal history of the development of transformation toughened PSZ ceramics" *Materials Science Forum 34-36*, 65-77 (1988)

16. E. P. Butler, "Transformation-toughened zirconia ceramics" *Mater. Sci. Tech. 1* 417-431 (1985)
17. R.L. Withers, J.G. Thompson, N. Gabbitas, L.R. Wallenberg and T.R. Welberry, "Microdomains, solid solutions and the "defect fluorite" to c-type sesquioxide transition in CeO_2-$RO_{1.5}$ and ZrO_2-$RO_{1.5}$ systems" *J. Solid State Chem. 120* 290-298 (1995)
18. X. Lu, K. Liang, S. Gu, Y. Zheng and H. Fang, "Effect of oxygen vacancies on transformation of zirconia at low temperatures" *J. Mater. Sci. 32* [24] 6653-6656 (1997)
19. C.J. Howard, B.A. Hunter and D.-J. Kim, "Oxygen position and bond lengths from lattice parameters in tetragonal zirconias" *J. Am. Ceram. Soc. 81* [1] 241-243 (1998)
20. D.-J. Kim, "Effect of tetravalent dopants on Raman spectra of tetragonal zirconia" *J. Am. Ceram. Soc. 80* [6] 1453-1461 (1997)
21. R.N. Patil and E.C. Subbarao, "Monoclinic-tetragonal phase transition in zirconia: mechanism, pretransformation and coexistence" *Acta. Cryst. A26* 535-542 (1970)
22. A.H. Heuer and M. Rühle, "On the nucleation of the martensitic transformation in zirconia (ZrO_2)" *Acta Metall. 33* [12] 2101-2112 (1985)
23. B.C. Muddle and G.R. Hugo, "Martensitic transformations in ceramics" *Proceedings of the International Conference on Martensitic Transformations, Monterey 1992*, 647-658 (1993)
24. F. Frey and H. Boysen, "Neutron diffraction study of the martensitic monoclinic-to-tetragonal phase transformation in zirconia ZrO_2" *Proceedings of the International Conference on Martensitic Transformations, Monterey 1992*, 659-664 (1993)
25. J. Ortín, "Thermodynamics and kinetics of martensitic transformations" *Proceedings of the International Conference on Martensitic Transformations, Monterey 1992*, 305-316 (1992)
26. T. Kanno, "Stability of metastable tetragonal zirconia in compound powders and nucleation arguments" *J. Mater. Sci. 25* 1987-1990 (1990)
27. A.H. Heuer, N. Claussen, W.M. Kriven and M. Rühle, "Stability of tetragonal ZrO_2 particles in ceramic matricies" *J. Am. Ceram. Soc. 65* [12] 642-650 (1982)

28. Y.-C. Lin, D. Gan and P. Shen, "Phase transformation of ZrO_2 in MnZn-ferrite under magnetic field" *J. Am. Ceram. Soc. 79* [2] 559-61 (1996)
29. R.C. Garvie and M.F. Goss, "Intrinsic size dependence of the phase transformation temperature in zirconia microcrystals" *J. Mater. Sci. 21* 1253-1257 (1986)
30. R.C. Garvie and S.K. Chan, "Mechanism and thermodynamics of the monoclinic-tetragonal transformations of zirconia" *Material Science Forum 34-36* 95-101 (1988)
31. C.H. Perry and D.-W. Liu "Phase characterization of partially stabilized zirconia by Raman spectroscopy", *J. Am. Ceram. Soc.* 68 [8] C184-C187 (1985)
32. V.V. Osiko, Y.K. Voron'ko and A.A. Sobol, in *Growth and Defect Structures - Crystal 10*, Edited by H.C. Freyhard, Springer-Verlag, Berlin (1984)
33. P.M. Kelly, "Martensitic transformations in ceramics" *Mater. Sci. Forum 56-58* 335-346 (1990)
34. N.K. Simha, "Crystallography of the tetragonal → monoclinic transformation in zirconia" *Journal de Physique IV 5* [C8] 1121-1126 (1995)
35. R. Srinivasan, B.H. Davis, L.A. Rice and R.J. De Angelis, "Electron microdiffraction studies of zirconia particles" *J. Mater. Sci. 27* 661-670 (1992)
36. R. Srinivasan, L. Rice and B.H. Davis, "Critical particle size and phase transformation in zirconia: transmission electron microscopy and X-ray studies" *J. Am. Ceram. Soc. 73* [11] 3528-3530 (1990)
37. Y. Murase and E. Kato, "Role of water vapor in crystallite growth and tetragonal-monoclinic phase transformation of ZrO_2" *J. Am. Ceram. Soc. 66* [3] 196-200 (1983)
38. D.A. Ward and E.I. Ko, "Synthesis and structural transformation of zirconia aerogels" *Chem. Mater. 5* 956-969 (1993)
39. S.-K. Chan, "Theory of the energetics and non-classical nucleation for the tetragonal-monoclinic transformation of zirconia" *Advances in Ceramics 24* 983-995 (1988)
40. T. Suzuki and K. Takahashi, "Computer simulation of the nucleation process of martensite in a small particle" *Proceedings of the International Conference on Martensitic Transformations, Monterey 1992*, 173-178 (1993)
41. C.A. Andersson and T.K. Gupta, "Phase stability and transformation toughening in zirconia" *Advances in Ceramics 3* 184-201 (1981)
42. A/Prof. Pat Kelly, University of Queensland, personal communication (1996)
43. A. Clearfield, "Structural aspects of zirconium chemistry" *Rev. Pure and Appl. Chem. 14* 91-108 (1964)
44. A.K. Mukherji, *Analytical Chemistry of Zirconium and Hafnium*, Pergamon, Oxford (1970)
45. C.F. Baes and R.E. Mesmer, *The hydrolysis of cations*, Wiley-Interscience 152-159 (1976)
46. J. Livage, M. Chatry, M. Henry and F. Taulelle, "Complexation of Zr(IV) precursors in aqueous solutions" *Mat. Res. Soc. Symp. Proc 271* 201-212 (1992)
47. S. Hannane, F. Bertin and J. Bouix, "Etude de l'hydrolyse de Zr(IV) par spectrométrie Raman et RMN du proton. I. Mise en évidence et formation des espèces en solution" *Bull. Soc. Chim. Fr. 127* 43-49 (1990)
48. S. Hannane, F. Bertin and J. Bouix, "Etude de l'hydrolyse de Zr(IV) par spectrométrie Raman et RMN du proton. II. Influence de l'acidité et du vieillissement des solutions sur les proportions des espèces formées" *Bull. Soc. Chim. Fr. 127* 50-56 (1990)
49. M. Åberg and J. Glaser, "^{17}O and ^{1}H NMR study of the tetranuclear hydroxo zirconium complex in aqueous solution" *Inorg. Chim. Acta 206* 53-61 (1993)
50. A. Singhal, L.M. Toth, J.S. Lin and K. Affholter, "Zirconium(IV) tetramer/octomer hydrolysis equilibrium in aqueous hydrochloric acid solution" *J. Am. Chem. Soc. 118* [46] 11529-11534 (1996)
51. L.M. Toth, J.S. Lin and L.K. Felker, "Small-angle X-ray scattering from zirconium(IV) hydrous tetramers" *J. Phys. Chem. 95* 3106-3108 (1991)
52. J.D.F. Ramsay, "EXAFS study of polynuclear ions in solution" *Synchrotron radiation, Appendix to the Daresbury annual report 1988/89*, Compiled by C. Nave *et al*., Science and Engineering Research Council 38-39 (1989)
53. K. Dehnicke and J. Weidlein, "Existence of the VO_2^+, TiO^{2+} and ZrO^{2+} cations" *Angew. Chem. Internat. Edit. 5* [12] 1041 (1966)
54. C.J. Hardy, B.O. Field, D.Scargil, "Bonding of ligands in hydrated nitrates and chlorides of zirconium (IV)" *J. Inorg. Nucl. Chem. 28* 2408-2409 (1966)

55. A. Clearfield and P.A. Vaugan, "The crystal structure of zirconyl chloride ocathydrate and zirconyl bromide octahydrate" *Acta Cryst. 9* 555-558 (1956)
56. T. C. W. Mak, "Refinement of the crystal structure of zirconyl chloride octahydrate" *Can. J. Chem. 46* 3493-3497 (1968)
57. G. M. Muha, "Structure of the complex ion in aqueous solutions of zirconyl and hafnyl oxyhalides" *J. Chem. Phys 33* [1] 194-199 (1960)
58. G.A. Yagodin, "Stable polymeric zirconium compounds in nitric acid solutions" *Russ. J. Inorg. Chem. 15* [5] 659-662 (1970)
59. J.H. Adair, H.G. Krarup, S. Venigalla and T. Tsukada, "A review of the aqueous chemistry of the zirconium - water system to 200°C" *Mat. Res. Soc. Symp. Proc. 432* 101-111 (1997)
60. T.J. Bastow, M.E. Smith and S.N. Stuart, "Observation of ^{91}Zr NMR in zirconium-based metals and oxides" *Chem. Phys. Lett. 191* [1-2] 125-129 (1992)
61. R. Claude and D. Vivien, "Solvation de sels de zirconium en solution aqueuse. Étude RMN" *Bulletin de la Société Chimique de France* (1974) [1-2] 65-66 (in French)
62. K.I. Arsenin, L.A. Malinko, I.A. Sheka, I. Ya Pishchai and A.N. Antishko, "The ^{1}H NMR spectra of aqueous solutions of zirconium and hafnium hydroxide chlorides" *Russ. J. Inorg. Chem. 36* [10] 1496-1500 (1991)
62b. J.M. Coddington, R.F. Howe and M.J. Taylor, "Natural abundance ^{17}O NMR spectra of molybdenyl, uranyl and zirconyl complexes" *Inorg. Chim. Acta 166*, 13-15 (1989)
63. I.S. Pronin and A.A. Vashman, "^{14}N nuclear magnetic relaxation in aqueous and nitric acid solutions of zirconium nitrate" *Russ. J. Inorg. Chem. 32* [3] 338-341 (1987)
64. K.A. Burkov, G.V. Kozhevnikova, L.S. Lilich and L.A. Myund, "The vibrational spectra of the tetrameric hydroxo -complex of zirconium (IV)" *Russ. J. Inorg. Chem. 27* [6] 804-802 (1982)
65. J.L. Woodhead, "The preparation and properties of a polynuclear uranyl nitrate" *J. Inorg. Nucl. Chem. 28* 2175-2185 (1966)
66. G.V. Kozhevnikova, L.A. Myund and K.A. Burkov, "Raman spectra of zirconium oxyxhloride crystalline hydrate and solutions" *Izvestiya Akademii Nauk SSSR, Neorganicheskie Materialy 24* [3] 470-473 (1988)
67. J.-L. Tosan, B. Durand, M. Roubin, F. Chassagneux, L. Mosoni, F. Bertin and B. Moraweck, "pH-metric and Raman investigations of zirconium aqueous solutions and gels submitted to a reflux" *J. Non-Cryst. Sol. 160* 167-176 (1993)
68. J.A. Jutson, R.M. Richardson, S.L. Jones and C. Norman, "Small angle X-ray scattering studies of polymeric zirconium species in aqueous solution" *Mat. Res. Soc. Symp. Proc. 180* 123-128 (1990)
69. L.G. Sillén, "Aqueous hydrolytic species" *Proceedings of The Robert A. Welch Foundation Conference on Chemical Research, IV. Topics in Modern Inorganic Chemistry* (Held in Houston, Texas, 1962) 187-234
70. P. Benard, M. Louër and D. Louër, "Crystal structur determination of $Zr(OH)_2(NO_3)_2{\cdot}4.7H_2O$ from X-ray powder diffraction data" *J. Solid State Chem. 94*, 27-35 (1991)
70b. P.J. Squattrito, P.R. Rudolf and A. Clearfield, "Crystal structure of a complex basic zirconium sulfate" *Inorg. Chem. 26*, 4240-4244 (1987)
71. J.A. Johnson and K.A. Kraus, *J. Am. Chem. Soc. 78*, 3937 (1956)
72. D.B. Copley and S.Y. Tyree, "Time and temperature variations in the hydrolytic behaviour of hafnium(IV) in aqueous chloride media" *Inorganic Chemistry 7* [7] 1472-1474 (1968)
73. E.M. Larsen and A.M. Gammill, "Electrometric titrations of zirconium and hafnium solutions" *J. Am. Chem. Soc. 72*, 3615-3619 (1950)
74. L.M. Sharygin, V.M. Galkin, S.M. Vovk and A.V. Korenkova, *Colloid Journal of the USSR 47* 95-99 (1985)
75. R. Srinivasan, M.B. Harris, S.F. Simpson, R.J. De Angelis and B.H. Davis, "Zirconium oxide crystal phase: the role of the *p*H and time to attain the final *p*H for precipitation of the hydrous oxide" *J. Mater. Res. 3* [4] 787-797 (1988)
76. J.-L. Tosan, B. Durand, M. Roubin, F. Bertin and H. Loiseleur, "Potentiometric and Raman spectroscopic characterization of gelatinous precipitates formed by hydrolysis of zirconium oxychloride solutions" *Eur. J. Solid State Inorg. Chem. 30* 179-193 (1993)
77. A. Clearfield, "The mechanisms of hydrolytic polymerisation of zirconyl solutions" *J. Mater. Res. 5* [1] 161-162 (1990)

78. G.T. Mamott, P. Barnes, S.E. Tarling, S.J. Jones and C.J. Norman, "Dynamic studies of zirconia crystallisation" *J. Mater. Sci. 26* 4054-4061 (1991)
79. M.A. Blesa, A.J.G. Maroto, S.I. Passaggio, N.E. Figliolia and G. Rigotti, "Hydrous zirconium dioxide: interfacial properties, the formation of monodisperse spherical particles, and its crystallization at high temperatures" *J. Mater. Sci. 20* [12] 4601-4609 (1985)
80. A. Bleier and R.M. Cannon, "Nucleation and growth of uniform m-ZrO_2" *Mat. Res. Soc. Symp. Proc. 72* (Better Ceramics Through Chemistry II) 71-78 (1986)
81. A. Singhal, L.M. Toth, G. Beaucage, J. Lin and J. Peterson, "Growth and structure of zirconium hydrous polymers in aqueous solutions" *Journal of Colloid and Interface Science 194* 470-481 (1997)
82. M.D. Atherton and H. Sutcliffe, *J. Less-Common Met. 138* 63 (1998)
83. S.L. Jones and C.J. Norman, "Dehydration of hydrous zirconia with methanol" *J. Am. Ceram. Soc. 71* [4] C190-C191 (1988)
84. B.E. Yoldas, "Zirconium oxides formed by hydrolytic condensation of alkoxides and parameters that affect their morphology" *J. Mater. Sci. 21* 1080-1086 (1986)
85. X. Turrillas, P. Barnes, A.J. Dent, S.L. Jones and C.J. Norman, "'Hydroxide' precursor to zirconia: Extended X-ray absorption fine structure study" *J. Mater. Chem. 3* [6] 583-586 (1993)
86. R. Srinivasan and B.H. Davis, "Glow phenomenon and crystallisation: evidence that they are different events for hafnium-zirconium mixed oxides" *Journal of Colloid and Interface Science 156* 400-405 (1993)
87. R. Srinivasan and B.H. Davis, "Crystallisation exotherms of zirconia-hafnia mixtures" *J. Am. Ceram. Soc. 73* [6] 1780-1782 (1990)
88. T. Sato, K. Dosaka, T. Yoshioka and A. Okuwaki, "Sintering of ceria-doped tetragonal zirconia crystallised in organic solvents, water, and air" *J. Am. Ceram. Soc. 75* [3] 552-556 (1992)
89. S. Gutzov, J. Ponahlo, C.L. Lengauer and A. Beran, "Phase characterisation of precipitated zirconia" *J. Am. Ceram. Soc. 77* [6] 1649-1652 (1994)
90. A. Keshavaraja, N.E. Jacob and A.V. Ramaswamy, "Thermal decomposition of co-precipitated oxide hydrates of zirconium and manganese" *Thermochimica Acta 254*, 267-275 (1995)
91. D.-J. Kim, "Effect of Ta_2O_5, Nb_2O_5, and HfO_2 alloying on the transformability of Y_2O_3-stabilised tetragonal ZrO_2" *J. Am. Ceram. Soc. 73* [1] 115-120 (1990)
92. D.-J. Kim and T.-Y. Tien, "Phase stability and physical properties of cubic and tetragonal ZrO_2 in the system ZrO_2-Y_2O_3-Ta_2O_5" *J. Am. Ceram. Soc 74* [12] 3061-3065 (1991)
93. D.-J. Kim and H.-J. Jung "Raman spectroscopy of tetragonal zirconia solid solutions" *J. Am. Ceram. Soc. 76* [8] 2106-2108 (1993)
94. W. Stichert and F. Schüth, "Influence of crystallite size on the properties of zirconia" *Chem. Mater. 10* [7] 2020-2026 (1998)
95. G. Gimblett, A.A. Rahman and K.S.W. Sing, "Thermal and related studies of some zirconia gels" *J. Chem. Tech. Biotechnol. 30*, 51-64 (1980)
96. R. Srinivasan, T.R. Watkins, C.R. Hubbard and B.H. Davis, "Sulfated zirconia catalysts. The crystal phases and their transformations" *Chem. Mater. 7* [4] 725-730 (1995)
97. M.A. Villa Garcia, M.C. Trobajo Fernandez and C. Otero Arean, "Effect of water vapour on the thermal evolution of the metastable phases of zirconium dioxide" *Thermochimica Acta 126* 33-41 (1988)
98. H.P. Li, J. Wang and R. Stevens, "The effects of hydroxide gel drying on the characteristics of co-precipitated zirconia-hafnia powders" *J. Mater. Sci. 28*, 553-566 (1993)
99. S.D. Ramamurthi, Z. Xu, D.A. Payne, "Nanometer-sized ZrO_2 particles prepared by a sol-emulsion-gel method" *J. Am. Ceram. Soc. 73* [9] 2760-2763 (1990)
100. F.-C. Wu and S.-C. Yu, "Effects of H_2SO_4 on the crystallization and phase transformation of zirconia powder in the precipitation processes" *J. Mater. Sci. 25* 970-976 (1990)
101. X. Turrillas, P. Barnes, D. Häusermann, S.L. Jones and C.J. Norman, "Effect of chemical and heat treatment on the tetragonal-to-monoclinic transformation of zirconia" *J. Mater. Res. 8* [1] 163-168 (1993)
102. C. Li and P.C. Stair, "Ultraviolet Raman spectroscopy characterization of sulfated zirconia catalysts: fresh. deactivated and regenerated" *Catalysis Letters 36* 119-123 (1996)

103. G. Štefanić, S. Musić, S. Popović and K. Furić, "Formation of ZrO_2 by the thermal decomposition of zirconium salts" *Croatia Chimica Acta 69* [1] 223-239 (1996)
104. G. Štefanić, S. Musić, S. Popović and A. Sekulić, "FT-IR and laser Raman spectroscopic investigation of the formation and stability of low temperature *t*-ZrO_2" *Journal of Molecular Structure 408/409* 391-394 (1997)
105. R. Srinivasan, B.H. Davis, O.B. Cavin and C.R. Hubbard, "Crystallisation and phase transformation process in zirconia: an in situ high-temperature X-ray diffraction study" *J. Am. Ceram. Soc. 75* [5] 1217-1222 (1992)
106. G. Štefanić, S. Popović and S. Musić, "The effect of mechanical treatment of zirconium(IV) hydroxide on its thermal behaviour" *Thermochimica Acta 259*, 225-234 (1995)
107. G. Štefanić, S. Musić and A. Sekulić, "Influence of precipitation chemistry and ball-milling on the thermal behaviour of zirconium hydroxide" *Thermochimica Acta 273*, 119-133 (1996)
108. P.D.L. Mercera, J.G. van Ommen, E.B.M. Doesburg, A.J. Burggraaf and J.R.H. Ross, "Influence of ethanol washing of the hydrous precursor on the textural and structural properties of zirconia" *J. Mater. Sci. 27* 4890-4898 (1992)
109. X. Turrillas, P. Barnes, S.E. Tarling, S.L. Jones, C.J. Norman and C. Ritter, "Neutron thermodiffractometry and synchrotron energy-dispersive diffraction studies of zirconium hydroxide calcination" *J. Mater. Sci. Lett. 12* [4] 233-226 (1993)
110. E. Crucean and B. Rand, "Calcination of zirconia gels" *Trans. J. Brit. Ceram. Soc. 78* [3] 58-64 (1979)
111. B.H. Davis, "Effect of pH on crystal phase of ZrO_2 precipitated from solution and calcined at 600°C", *J. Am. Ceram. Soc. 67* [8] C168 (1984)
112. T.Y. Tseng, C.C. Lin and J.T. Liaw, "Phase transformations of gel-derived magnesia partially stabilized zirconias" *J. Mater. Sci. 22* 965-972 (1987)
113. R. Srinivasan, C.R. Hubbard, O.B. Cavin and B.H. Davis, "Factors determining the crystal phases of zirconia powders: A new outlook" *Chem. Mater. 5* [1] 27-31 (1993)
114. R. Srinivasan, *Structural development in ultrafine particles of zirconia produced from sol-gel*, Ph.D. Thesis, University of Kentucky (1989)
115. L.M. Zaitsev, "Zirconium hydroxides" *Russ. J. Inorg. Chem. 11* [7] 900-904 (1966)
116. W.B. Blumenthal, *The chemical behaviour of zirconium*, Van Nostrand, Princeton (1958)
117. J. Livage, K. Doi and C. Mazières, "Nature and thermal evolution of amorphous hydrated zirconium oxide", *J. Am. Ceram. Soc. 51* [6] 349-353 (1968)
118. C. Landron, A. Douy and D. Bazin, "From liquid to solid: residual disorder in the local environment of oxygen-coordinated zirconium" *Phys. Stat. Sol. B 184* 299-307 (1994)
119. V.G. Keramidas and W.B. White, "Raman scattering study of the crystallisation and phase transformation of ZrO_2" *J. Am. Ceram. Soc. 57* [1] 22-24 (1974)
119b. J.R. Fryer, J.L. Hutchison and R. Paterson, "An electron microscopic study of the hydrolysis products of zirconyl chloride" *J. Colloid Interface Sci. 34* [2] 238-248 (1970)
120. S. A. Selim and T. M. El-Akkad, "Thermal decomposition, pore structure and heats of immersion of zirconia gel", *J. Appl. Chem. Biotechnol. 27*, 58-66 (1977)
121. H. Th. Rijnten, Thesis, Delft University of Technology (1971)
122. G. Centi, M. Marella, L. Meregalli, S. Perathoner, M. Tomaselli and T. La Torretta, "Gel supported precipitation" *Advanced Catalysis and Nanostructured Materials*, Edited by W.R. Moser, Academic Press, London (1996)
123. J.L. Woodhead, "Gel processing" *Journal de Physique 47* [2] C1-3 - C1-12 (1986)
124. L.G. Karakchiev and N.Z. Lyakhov, "Gelation in the hydrated system Al_2O_3-ZrO_2" *Colloid Journal 58* [1] 36-39 (1996)
125. J.L. Woodhead, "Sol-gel process to ceramic particles using inorganic precursors" *J. Mater. Ed. 6* 887-925 (1984)
126. J.L. Woodhead, *Improvements in or relating to Zirconium Compounds*, United Kingdom Patent No. 1,181,794 (18th Feb., 1970).
127. *a)* E. Sizgek, J.R. Bartlett and M.P. Brungs, "Production of titanate microspheres by sol-gel and spray-drying" *J. Sol-Gel Sci. Tech. 13* 1011-1016 (1998) *b)* W. Zhang and F.P. Glasser, "Condensation and gelation of inorganic ZrO_2-Al_2O_3 sols" *J. Mater. Sci. 28* 1129-1135 (1993)

128. W. Zhang and F.P. Glasser, "The preparation of Al_2O_3-ZrO_2 sol-gels from inorganic precursors" *J. Eur. Ceram. Soc. 11* 143-147 (1993)
129. W. Zhang and F.P. Glasser, "The structure and decomposition of Al_2O_3-ZrO_2 gels" *J. Eur. Ceram. Soc. 11* 149-155 (1993)
130. K. Matsui, H. Suzuki, M. Ohgai and H. Arashi, "Raman spectroscopic studies on the formation mechanism of hydrous-zirconia fine particles" *J. Am. Ceram. Soc. 78* [1] 146-152 (1995)
131. K. Matsui, M. Ohgai and H. Arashi, "Phase change of yttrium-containing hydrous-zirconia fine particles" *J. Ceram. Soc. Japan Int. Ed. 103* 584-588 (1995)
132. B. Mottet, M. Pichavant, J.-M. Bény and J.-A. Alary, "Morphology of zirconia synthesized hydrothermally from zirconium oxychloride" *J. Am. Ceram. Soc. 75* [9] 2515-2519 (1992)
133. H. Vesteghem, A. Lecomte, A. Dauger, "Film formation and sintering of colloidal monoclinic zirconia", *J. Non-Cryst. Sol. 147&148*, 503-507 (1992)
134. E. Kato, M.Hirano, Y. Kobayashi, K. Asoh, M. Mori and M. Nakata, "Preparation of monodisperse zirconia particles by thermal hydrolysis in highly concentrated solutions" *J. Am. Ceram. Soc. 79* [4] 972-976 (1996)
135. K. S. Chan, G.K. Chuah, S. Jaenicke, "Preparation of stable, high surface area zirconia" *J. Mater. Sci. Lett. 13* [21] 1579-1581 (1994)
136. X. Turrillas, P. Barnes, D. Gascoigne, J.Z. Turner, S.L. Jones, C.J. Norman, C.F. Pygall and A.J. Dent, "Synchrotron-related studies on the dynamic and structural aspects of zirconia synthesis for ceramic and catalytic applications" *Radiat. Phys. Chem. 45* [3] 491-508 (1995)
137. M. Shimazaki, K. Hirota, O. Yamaguchi, S. Fujii, M. Tamamaki, S. Inamura, M. Miyamoto and S. Kume, "Metastable zirconia phases prepared from zirconium alkoxide and yttruim acetylacetonate. Part 1: Formation and characterization of metastable zirconia solid solutions" *Mat. Res. Bull. 28* 877-884 (1993)
138. M.J. Torraluo, M.A. Alario and J. Soria, "Crystallisation behavior of zirconium oxide gels" *J. Catal. 86* 473-476 (1984)
139. S. Ramanathan, R.V. Muraleedharan, S.K. Roy and P.K. Krishnan Naya, "Dehydration and crystallisation kinetics of zirconia-yttria gels", *J. Am. Ceram. Soc 78* [2] 429-432 (1995)
140. J. Málek, S. Matsuda, A. Watanabe, T. Ikegami and T. Mitsuhashi, "Crystallisation kinetics of zirconia-yttria gels" *Thermochimica Acta 267* 181-194 (1995)
141. A. Aronne, P. Pernice and A. Marotta, "Crystallisation of gel-derived zirconia glass" *J. Mater. Sci. Lett. 10* 1136-1138 (1991)
142. M. Sorrentino, L. Steinbrecher and F. Hazel, "The glow phenomenon in colloidal hydrous oxides" *Journal of Colloid and Interface Science 31* [3] 307-316 (1969)
144. E. Bernstein, M. G. Blanchin, R. Ravelle-Chapuis and J. Rodriguez-Carvajal, "Structural studies of phase transformations in ultrafine zirconia powders *" J. Mater. Sci. 27* 6519-6524 (1992).
145. P.D. Southon, J.R. Bartlett, J.L. Woolfrey and M.G. Stevens, "Evolution of the structure of aqueous zirconia gels during preparation and heating" *Ceramic Transactions 81* 75-80 (1998)
146. H.-C. Wang and K.-L. Lin, "Characteristics and comparison of metastability of alkoxy-derived tetragonal ZrO_2 powders, gels and films" *Mater. Sci. Eng. A136* 171-178 (1991)
147. D.E. Collins, K.A. Rogers and K.J. Bowman, "Crystallization of metastable tetragonal zirconia from the decomposition of a zirconium alkoxide derivative" *J. Eur. Ceram. Soc. 15*, 1119-1124 (1995)
148. D.E. Collins and K.J. Bowman, "Influence of atmosphere on crystallisation of zirconia from a zirconium alkoxide" *J. Mater. Res. 13* [5] 1230-1237 (1998)
149. M.C. Silva, G. Trolliard, O. Masson, R. Guinebretiere, A. Dauger, A. Lecomte and B. Frit, "Early stages of crystallisation in gel derived ZrO_2 precursors" *J. Sol-Gel Sic. Tech. 8*, 419-424 (1997)
150. M. Jansen and E. Guenther, "Oxide gels and ceramics prepared by a non-hydrolytic sol-gel process" *Chem. Mater. 7* 2110-2114 (1995)
151. N.H. Brett, M. Gonzalez, J. Bouillot, and J.C. Niepce, "Neutron and X-ray diffraction studies on pure and magnesia-doped zirconia gels decomposed in vacuo" *J. Mater. Sci. 19* [4] 1349-1358 (1984)
152. V.B. Glushkova and E.K. Koehler, "X-ray and spectrographic investigations of phase transitions on refractory oxides (ZrO_2 and rare-earth oxides)" *Mat. Res. Bull. 2* [5] 503-513 (1967)
153. G. Katz, "X-ray diffraction powder pattern of metastable cubic ZrO_2" *J. Am. Ceram. Soc. 54* 531 (1971)
154. A. Benedetti, G. Fargherazzi and F. Pinna, *J. Am. Ceram. Soc. 72*, 467 (1989)
155. A. Benedetti, G. Fargherazzi, F. Pinna and S. Polizzi, *J. Mater. Sci 25*, 1473 (1990)

156. R.C. Garvie, "The occurrence of metastable tetragonal zirconia as a crystallite size effect" *J. Phys. Chem. 69* [4] 1239-1243 (1965)
157. R. Srinivasan, R.J. De Angelis, G. Ice and B.H. Davis, "Identification of tetragonal and cubic structures of zirconia using synchrotron x-radiation source" *J. Mater. Res. 6* [6] 1287-1292 (1991)
158. G. Antonioli, P.P. Lottici, I. Manzini, G. Gnappi, A. Montenero, F. Paloschi and P. Parent, "An EXAFS study of the local structure around Zr atoms in Y_2O_3-stabilised ZrO_2 by the sol-gel method" *J. Non-Cryst. Sol. 177* 179-186 (1994)
159. R. Caruso, N. Pellegri, O. De. Sanctis, M.C. Caracoche and P.C. Rivas "ZrO_2 phase structure in coating films and powders obtained by sol-gel process" *J. Sol-Gel Sci. Tech. 3* 241-247 (1994)
160. P.C. Rivas, J.A. Martinez, M.C. Caracoche, A.M. Rodríguez and A.R. Lopez Garcia, "Evolution of the phase content of zirconia powders prepared by sol-gel hydrolysis" *J. Am. Ceram. Soc. 81* [1] 200-204 (1998)
161. C.M. Phillippi and K.S. Mazdiyasni, "Infrared and Raman spectra of zirconia polymorphs" *J. Am. Ceram. Soc. 54* [5] 254-258 (1971)
162. K.S. Mazdiyasni, C.T. Lynch and J.S. Smith, "Preparation of ultra-high-purity submicron refractory oxides" *J. Am. Ceram. Soc. 48* [7] 372-375 (1965)
163. K.S. Mazdiyasni, C.T. Lynch and J.S. Smith, "Metastable transitions of zirconium oxide obtained from decomposition of alkoxides" *J. Am. Ceram. Soc. 49* [5] 286-287 (1966)
164. B.E. Yoldas, "Effect of variations in polymerised oxides on sintering and crystalline transformations" *J. Am. Ceram. Soc. 65* [8] 389-393 (1982)
165. M.L. Rojas-Cervantes, R.M. Martin-Aranda, A.J. Lopez-Peinado and J. De D. Lopez-Gonzalez, "ZrO_2 obtained by the sol-gel method: influence of synthesis parameters on physical and structural characteristics" *J. Mater. Sci. 29* 3743-3748 (1994)
166. H. Preiss, L.-M. Berger and K. Szulzewski, "Thermal treatment of binary carbonaceous/zirconia gels and formation of Z(C,O,N) solid solutions" *Carbon 34* [1] 109-119 (1996)
167. A. C. Geiculescu and H.G. Spencer, "Effect of oxygen environment on the decomposition and crystallisation of an aqueous sol-gel derived zirconium acetate gel" *J. Sol-Gel Sci. Tech. 14* 1-16 (1999)
168. D.N. Wang and K.M. Liang, "The effect of carbon on the phase stability of zirconia" *J. Mater. Sci. Lett. 17* 343-344 (1998)
169. C.L. Ong, J. Wang, S.C. Ng and L.M. Gan, "Effects of chemical species on the crystallisation behaviour of a sol-derived zirconia precursor" *J. Am. Ceram. Soc. 81* [10] 2624-2628 (1998)
170. T. Kosmač, V. Kraševec, R. Gopalakrishnan and M. Komac, "Crystallisation of ZrO_2 from amorphous precipitates and its influence on the microstructure of sintered ceramics" *Advances in Ceramics 24* (Science and Technology of Zirconia III) 167-172 (1988)
171. L.G. Shcherbakova, V.B. Glushkova and R.A. Sapozhnikov, "Preparation of crystallization of solid solutions based on ZrO_2 and HfO_2" *Izv. Akad. Nauk. SSSR, Neorg. Mater. 13* [4] 674-677 (1977)
172. P.E.D. Morgan, "Synthesis of 6-nm ultrafine monoclinic zirconia" *J. Am. Ceram. Soc. 67* [10] C204-C205 (1984)
173. A.J. Allen, S. Krueger, G. Skandan, G.G. Long, H. Hahn, H.M. Kerch, J.C. Parker and M.N. Ali, "Microevolution during the sintering of nanostructured ceramic oxides" *J. Am. Ceram. Soc. 79* [5] 1201-1212 (1996)
174. S. Ardizzone, G. Bassi and G. Liborio, "Preparation of crystalline zirconia powders. Characterisation of the bulk phase and interfacial behaviour" *Colloids and Surfaces 51* 207-217 (1990)
175. M. Li and Z. Chi, "Transformation from a metastable tetragonal structure into as monoclinic structure in zirconia powders" *Advances in Ceramics 24* (Science and Technology of Zirconia III) 243-250 (1988)
176. Y. Murase and E. Kato, "Phase transformation of zirconia by ball-milling" *J. Am. Ceram. Soc. 62* [9-10] 527 (1979)
177. D. Spielbauer, G.A.H. Mekhemer, T. Riemer, M.I. Zaki and H. Knoezinger, "Structure and acidic properties of phosphate-modified zirconia" *J. Phys. Chem. B 101* [23] 4681-4688 (1997)
179. R.C. Garvie, "Stabilisation of the tetragonal structure in zirconia microcrystals" *J. Phys. Chem. 82* [2] 218-224 (1978)

180. J.M. Bell, R.W. Cheary, M. Rice, B. Ben-Nissan, J.L. Cocking and G.R. Johnstone, "Crystal structures of sol-gel deposited zirconia thin films", *Austceram92 - Ceramics: adding the value*, Edited by M. J. Bannister, 765-770, (1992)
181. O. Ruff and F. Elbert, "Refractory Ceramics: I. The forms of Zirconium Dioxide" *Z. Anorg. Allg. Chem. 180*, 19-41 (1929) In German
182. G.L. Clark and D.H. Reynolds, "Chemistry of Zirconium Dioxide - X-ray diffractions studies." *Ind. Eng. Chem. 29* [6] 711-715 (1937)
183. R. Cyprès, R. Wollast and J. Raucq, "Contribution on the polymorphic conversion of pure zirconia." *Ber. Dtsch. Keram. Ges. 40* [9] 529-532 (1963), In German.
184. C.G. Levi, "Metastability and microstructure evolution in the synthesis of inorganics from precursors" *Acta Mater. 46* [3] 787-800 (1998)
185. G. Skandan, C.M. Foster, H. Frase, M.N. Ali, J.C. Parker and H. Hahn, "Phase characteristics and stabilization due to grain size effects of nanostructured Y_2O_3", *Nanostruct. Mater. 1* 313-318 (1992)
186. V. Heine, C. Cheng and R.J. Needs, "The preference of silicon carbide for growth in the metastable cubic form" *J. Am. Ceram. Soc. 74* [10] 2630-2633 (1991)
187. N.G. Bukun, E.A. Ukshe, E.I. Moskvina and T.N. Aleshina, "Reaction with $ZrO(NO_3)_2$ during the synthesis of NASICON solid electrolytes" *Izv. Akad. Nauk SSSR, Neorg. Mater. 23* [8] (1987) 1355-1359
188. M. Amberg and J.R. Günter, "Metastable cubic and tetragonal zirconium dioxide, prepared by thermal oxidation of the dichalcogenides" *Solid State Ionics 84* 313-321 (1996)
189. C.A. Strydom and G. Pretorius, "The thermal decomposition of zirconium sulphate hydrate" *Thermochimica Acta 233*, 223-232 (1993)
190. H.M. Ismail, "Characterisation of the decomposition products of zirconium acetylacetonate: nitrogen adsorption and spectrothermal investigation" *Powder technology 85* 253-259 (1995)
191. M. Osendi, J. Moya, C. Serna and J. Soria, "Metastability of tetragonal zirconia powders", *J. Am. Ceram. Soc. 68* [3] 135-139 (1985)
192. C.Z. Zechmann, K. Folting and K.G. Caulton, "Synthesis of zirconium pinacolate and mechanism of its thermal transformation to ZrO_2: impact of a vicinal diol ligand" *Chem. Mater. 10* 2348-2357 (1998)
193. S. Shimada and T. Ishii, "Oxidation kinetics of zirconium carbide at relatively low temperatures" *J. Am. Ceram. Soc. 73* [10] 2804-2808 (1990)
194. S. Shimada, "Microstructural observation of ZrO_2 scales formed by oxidation of ZrC single crystals with formation of carbon" *Solid State Ionics 101-103* [2] 749-753 (1997)
195. K. Tamura, T. Ogawa and K. Fukuda, "The oxidation behaviour of ZrC coating and powder studied by laser Raman spectroscopy and X-ray diffraction" *Journal of Nuclear Materials 175* 266-268 (1990)
196. M.M. Bućko and K. Haberko, "Crystallisation of zirconia under hydrothermal conditions", *J. Am. Ceram. Soc. 78* [12] 3397-3400 (1995)
197. E. Tani, M. Yoshimura and S. Sōmiya, "Formation of ultrafine tetragonal ZrO_2 powder under hydrothermal conditions" *J. Am. Ceram. Soc. 66* [1] 11-14 (1983)
198. W. Pyda, K. Haberko and M.M. Bućko, "Hydrothermal crystallisation of zirconia and zirconia solid solutions" *J. Am. Ceram. Soc. 74* [10] 2622-2629 (1991)
199. T. Mitsuhashi, M. Ichihara and U. Tatsuke, "Characterisation and Stabilization of metastable tetragonal ZrO_2" *J. Am. Ceram. Soc. 57* [2] 97-101 (1974)
199b. A. Clearfield, "Crystalline hydrous zirconia" *Inorg. Chem. 3* [1], 146-147 (1964)
200. K. Matsui, H. Suzuki, M. Ohagai and H. Arashi, "Size effect in Raman spectra of hydrous zirconia particles" *Seramikkusu Ronbunshi 98* [12] 1302-1306 (1990) In Japanese.
201. J.E. Bailey, D. Lewis, Z.M. Librant and L.J. Porter, "Phase traansformations in milled zirconia" *Trans. J. Brit. Ceram. Soc. 71* [1] 25-30 (1972)
202. G. Michel, E. Muller, C. Oestreich, G. Staupendahl and K.H. Henneberg, "Ultrafine ZrO_2 powder by laser evaporation: preparation and properties" *Materialwissenschaft und Werkstofftechnik 27* [7] 345-349 (1996)
203. G. Skandan, H. Hahn, M. Roddy and W.R. Cannon, "Ultrafine-grained dense monoclinic and tetragonal zirconia" *J. Am. Ceram. Soc. 77* [7] 1706-1710 (1994)

204. R. Nitsche, M. Rodewald, G. Skandan, H. Fuess and H. Hahn, "HRTEM study of nanocrystalline zirconia powders" *Nanostruc. Mater. 7* [5] 535-546 (1996)
205. J. Málek, L. Beneš and T. Mitsuhashi, "Powder diffraction data and Rietveld refinement of metastable t-ZrO_2 at low temperature" *Powder Diffraction 12* [2] 96-98 (1997)
206. C. Landron, "Phase transition investigation of zirconia by synchrotron radiation" *Ceramic Transactions 71* (Mass and charge transport in ceramics) 201-212 (1996)
207. Y. Zeng, G. Fagherazzi and S. Polizzi, "The local structure characterisation and resulting phase-transition mechanism of amorphous ZrO_2" *J. Mater. Sci. 30* 2153-2158 (1995)
208. P. Kountouros and G. Petzow, "Defect chemistry, phase stability and properties of zirconia polycrystals" *Science and Technology of Zirconia V*, Edited by S.P.S. Badwal *et al*., Technomic, Lancaster USA, (1992) 30-48
209. A. Aronne, P.Pernice, A. Marotta, "Crystallisation of gel-derived zirconia glass" *J. Mater. Sci. Lett. 10* 1136-1138 (1991)
210. R.J. Ackermann, S.P. Garg and E.G. Rauh, "High-temperature phase diagram for the system Zr-O" *J. Am. Ceram. Soc. 60* [7-8] 341-345 (1977)
211. E.G. Rauh and S.P. Garg, "The ZrO_{2-x} (cubic) - ZrO_{2-x} (cubic + tetragonal) phase boundary", *J. Am. Ceram. Soc.* 63, 239-240 (1980)
212. R.C. Garvie and M.V. Swain, "Thermodynamics of the tetragonal to monoclinic phase transformation in constrained zirconia microcrystals, Part 1: In the absence of an applied stress field" *J. Mater. Sci. 20* 1193-1200 (1985)
213. A. Krauth and H. Meyer, "Modifications produced by quenching and their crystal growth in the systems containing zirconium dioxide" *Ber. Dtsch. Keram. Ges. 42* [3] 61-72 (1965) In German.
214. G. Cerrato, S. Bordiga, S Barbera and C. Morterra, "Surface characterization of monoclinic ZrO_2 I. Morphology, FTIR spectra features, and computer modelling" *Appl. Surf. Sci. 115* 53-65 (1997)
215. J. Nawrocki, P.W. Carr, M.J. Annen and S. Froelicher, "A TGA investigation of hydrated monoclinic zirconia" *Analytica Chimica Acta 327* [3] 261-266 (1996)
216. R.C. Garvie, "Thermodynamic analysis of the tetragonal to monoclinic transformation in a constrained zirconia microcrystal, Part 2: In the presence of an applied stress" *J. Mater. Sci. 20* 3479-3486 (1985)
217. J.M. Blakely, *Introduction to the properties of crystal surfaces*, Pergamon, Oxford (1973) 21
218. C.R. Aita, M.D. Wiggins, R. Whig and C,M, Scanlan, "Thermodynamics of tetragonal zirconia formation in a nanolaminate film" *J. Appl. Phys. 79* [2] 1176-1178 (1996)
219. M. Winterer, R. Nitsche, S.A.T. Redfern, W.W. Schmahl and H. Hahn, *Nanostruc. Mater. 5* 679 (1995)
220. R. Pascual, M. Sayer, G. Yi and C. Baker, "Phase transformation kinetics in thin film zirconia", *J. Can. Ceram. Soc. 60* [2] 43-46 (1991)
221. P. Bénard, J.P. Affrédic, and D. Louër, "High-temperature X-ray powder diffractometry of the decomposition of zirconium hydroxide nitrates" *Powder diffraction 8* [1] 39-46 (1993)

3. Formation and characterisation of the sol

3.1 Introduction

Sols and gels are prepared from aqueous zirconium salt solutions by forcing hydrolysis to occur in a controlled way, either chemically or thermally, so that colloidal particles of hydroxide or oxide are formed. Various methods for their preparation are discussed in Chapter 2.2.

Woodhead described a simple method of forcing hydrolysis and forming a colloid while remaining well below 100°C.[1-2] This method involves the addition of further zirconium to an acidic zirconyl nitrate solution, in the form of a hydroxide or carbonate, to give a $Zr:NO_3$ ratio of 1:1. The decomposition of the added material consumes acid, promoting hydrolysis and polycondensation to form colloidal particles. The resultant sol gels reversibly when the pH is raised, and irreversibly if the nitrate anions are removed. Woodhead described the method as "deaggregating zirconium hydroxide with nitric acid",[1] the "nitric acid" being present in the acidic salt solution, but to date there has been no evidence published for either the mechanisms for the formation of the colloidal particles, or their size or structure. This method has since been reported occasionally in the literature,[3-5] and is referred to here as the 'standard' route.

This route is attractive for industrial applications for a number of reasons:

1. All precursor materials are commercially available and inorganic.
2. The method is simple and rapid, with no hydrothermal processing required.
3. All processing is water-based, with no organic liquids required or produced.*
4. The sol produced is stable indefinitely.

* Organic liquids may be used for any subsequent solvent-extraction stage to form micro-spheres.

5. Gelation, by either removal of water or increase in pH, is completely reversible. This provides an extra degree of control over the gelation process; mis-shaped products may be redispersed, and sols may even be gelled in bulk for storage and redispersed for processing.[1]
6. Gelation may be controlled to apply a shaped gel product, such as microspheres, films, or fibres. This is a characteristic that is shared by some non-reversible metal-organic processes, but such shaping is impossible for aqueous precipitation-based routes.
7. The sol can remain fluid with an oxide (ZrO_2) content as high as 500 g/L (~ 30 wt %), which is considerably higher than sols prepared by hydrothermal processing.

These features result in simplicity, ease of scale-up, low cost, and minimal environmental impact of the process, making it potentially a much less expensive and more convenient process than others used to produce zirconia precursor sols. For these reasons, the route described by Woodhead for the preparation of aqueous 'zirconia' sols has been chosen as the route to be studied in this thesis.

However, there are a number of features of this route that are disadvantages for a sol-gel process:

1. The sol produced is highly acidic, with a pH of 0.5 - 1.5 depending on the sol concentration.
2. Gelation cannot be controlled to the same degree that polymerisation of alkoxides can be controlled.
3. The presence of nitrate may cause some problems during calcination and firing.
4. The sol particles are amorphous zirconium hydroxide, not crystalline zirconia as can be produced by hydrothermal routes.

To develop applications for this route, improve the process, and overcome some of these disadvantages, it is important to understand in detail the reactions that occur as the sol is prepared, and the structure of the sol particles. To date, no other published work has studied these aspects of this route.

The characteristics of the sol that will be investigated can be divided into three broad categories: the nature of the hydrolysis and condensation reactions; the size and shape of the resulting particles; and the location of nitrate anions around the particles. These characteristics have been investigated during the formation process, and also any changes that occur after ageing.

As in all investigations in this thesis, a broad range of characterisation techniques have been used. The measurement of pH and use of ^{1}H NMR have provided an insight into the hydrolysis and condensation reactions. Raman spectroscopy has been a particularly useful technique, characterising both the nature of the Zr–O bonds and the symmetry of the nitrate anions. Small-angle X-ray scattering (SAXS) gives information on the shape of the particles, while dynamic light scattering (DLS) provides a size-distribution for the particles.

This chapter is divided into a number of self-contained sections, most of which deal with data from a particular characterisation technique. To assist the discussion of the results, in two sections major work is briefly described, and a full treatment deferred to later chapters. This includes the assignment of the Raman spectrum for zirconyl nitrate in Section 3.5, and the full analysis of the SAXS data in Section 3.6. In Section 3.9 the results presented in the previous sections will be summarised, discussed, and the conclusions presented.

3.2 Preparation of solutions and sols

3.2.1 Reagents

The zirconium carbonate was obtained as a white powder.* It is not a stoichiometric compound and is also hygroscopic. Before each batch of sol was prepared the oxide content of the powder was determined by calcination, and the average content was found to be 44.2 ± 0.5 wt. %. In the following discussion the formula is assumed to be '$ZrOCO_3$', although the presence of water is likely, $ZrOCO_3 \cdot xH_2O$, and the presence of hydroxy groups is also quite possible, $Zr(OH)_2CO_3 \cdot xH_2O$. Neither of these are likely to have an important effect on the dissolution and decomposition of the carbonate in nitric acid.

A sample of the carbonate was calcined at 900°C and the elemental composition determined by X-ray fluorescence spectroscopy. The following impurities were found: HfO_2 1.67 %, P_2O_5 0.16 %, Na_2O 0.15 %, TiO_2 0.15 %, lanthanides 0.11 %, CaO 840 ppm, S 350 ppm. XRF of unheated powder gave similar results. Hafnium (Hf) is chemically nearly identical to zirconium, and is frequently a major impurity in zirconium compounds. It is not anticipated that the presence of a small fraction of hafnia (HfO_2) has a significant effect on the results in this thesis.

The nitric acid use for preparation of the sol was reagent grade, initially 70 wt. %, and diluted when required. The water used in all experiments was research grade.†

3.2.2 Preparation method

A 'standard' sol was prepared according to the following two-stage method.[2] One mole of zirconium carbonate is first dissolved in two moles of nitric acid, producing a clear, acidic zirconyl nitrate solution, $Zr(OH)_2(NO_3)_2$. A second 'additional' mole of zirconium carbonate is mixed with water to form a slurry, which is then slowly added to the solution with stirring over a period of approximately 15 minutes. The mixture is maintained at 70°C for one to two hours, forming a nearly transparent sol with $Zr:NO_3$ ratio of 1:1. Further water is added to the sol to achieve the desired concentration, usually 1.0 M.

---

* Magnesium Elektron, UK.

† All water was taken from a *Modulab Analytical* Laboratory Research Grade Water System, with a 0.1 µm filter.

Several series of sols/solutions were prepared with a range of $Zr:NO_3$ ratios, by varying the amount of 'additional' carbonate. The maximum $Zr:NO_3$ ratio that formed a clear sol was approximately 1.3:1. The main reason for these series was to investigate the evolution of structure between the $Zr(OH)_2(NO_3)_2$ solution and the sol, whilst the 'additional' carbonate is being added. It is recognised that these solutions may not actually be completely representative of the intermediate stages between the precursor solution and the sol, but are as close as could be practically achieved.

When composition of a solution or sol is specifically mentioned, it is given a name in the form ZN*x.x*, where *x.x* indicates the number of nitrate anions per zirconium atom, *eg*: the precursor solution is ZN2.0, and the standard sol is ZN1.0.

3.2.3 Concentration and density

The zirconia content of solutions and sols was determined by calcination in a furnace at 900°C for two hours. Thermogravimetric analysis shows no significant mass loss above 900°C, so it is assumed that at this temperature all other components have evaporated or decomposed into volitile products, leaving zirconia (and hafnia). The density of selected sols was measured by a densitometer.* Typical results for a 1 M sol are given in Table 3-1.

Table 3-1

Density:	1.160 kg/L
Zr concentration:	0.929 mol/kg
	1.08 mol/L

If no water is added during preparation, the sol may have an oxide concentration of up to 4 M (500 g/L).

* Anton Paar Density Meter DMA 58, with a precision of 5 decimal places. Calibrated with water and air.

3.3 Changes in pH

3.3.1 Introduction

When zirconium carbonate is added to a zirconyl nitrate solution, two reactions occur that have opposing effects on the pH; hydrolysis releases H^+ ions, and condensation releases OH^- ions. Thus the solution pH plays a very important role in the degree to which the reaction proceeds.

The decomposition of the carbonate consumes H^+, to form polynuclear, aquated-zirconium species, most probably with the zirconium atoms bridged by hydroxy groups:

$$ZrOCO_3 + 2H^+ \rightarrow \left[Zr(OH^b)_2\right]^{2+} + CO_2 \qquad \textbf{Equation 3-1}$$

These species immediately hydrolyse, releasing H^+:

$$\left[Zr(OH^b)_2 \cdot nH_2O\right]^{2+} \; ? \quad \left[Zr(OH^b)_2(OH^t)_n\right]^{(2-n)+} + nH^+ \qquad \textbf{Equation 3-2}$$

Any zirconyl species already in solution also act as a buffer according to Equation 3-2.

The resulting changes in pH and species concentrations trigger further hydrolysis, condensation and oxolation reactions in the zirconium species,* leading to the formation of colloidal particles. From the change in H^+/Zr ratio as the sol is being formed, we can determine the balance between the hydrolysis and condensation reactions (H^+ producing), and the decomposition of carbonate (H^+ consuming). Note, however, that the accurate measurement of pH in concentrated solutions with very low pH and high ionic strength is difficult.[6]

3.3.2 Procedure

Solutions and sols with Zr:NO_3 ratios ranging from 1:2 to 1:1 were prepared, as described in Section 3.2.1. The Zr concentration for all solutions was 1.0 M. The pH of each sample was measured with a normal combined electrode 1 hour after preparation, to allow for full dissolution, and then 3, 14 and 38 days after preparation. From these measurements the H^+/Zr ratio was calculated.

---

* These reactions are discussed in Section 2.2.2.

3.3.3 Results and discussion

The values of pH and H^+/Zr value for samples that are approximately one hour old, with different Zr:NO_3 ratios, are given in Table 3-2 and plotted in Figure 3-1. The change in H^+/Zr value with ageing over 40 days is shown in Figure 3-2.

Table 3-2

Zr:NO_3	pH	H^+/Zr ratio
1:2.0	0.11	0.90
1:1.8	0.15	0.74
1:1.6	0.25	0.61
1:1.4	0.35	0.48
1:1.2	0.51	0.33
1:1.0	0.77	0.18

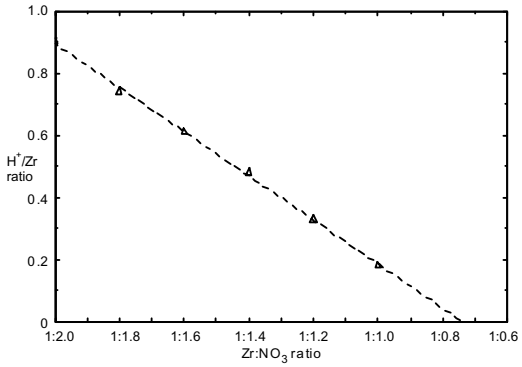

Figure 3-1: The H^+/Zr ratio of sols and solutions one hour after preparation, plotted against Zr:NO_3 ratio.

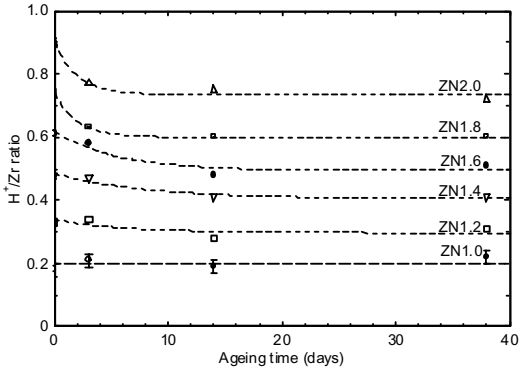

Figure 3-2: The change in H^+/Zr ratio with ageing of sols and solutions. The broken lines indicate trends.

The low pH of the ZN2.0 zirconyl nitrate solution indicated that considerable hydrolysis has already taken place in the precursor solution. Assuming that all zirconium at this point is in the form of polynuclear species with the form $[Zr(OH^b)_2(OH^t)_n]$, at 1 M concentration there are approximately 0.9 H^+/Zr, thus approximately 0.9 terminal hydroxy-groups per zirconium.

The pH increases steadily as zirconium carbonate is added; further hydrolysis occurs but H^+ is consumed at a greater rate. As shown in Figure 3-1, the H^+:Zr ratio of sols/solutions is linearly related to the Zr:NO_3 ratio. The slope of the plot is -0.7, which indicates that under the conditions investigated approximately 0.7 mole of H^+ is consumed for every additional mole of zirconium carbonate added.

The trend in Figure 3-1 has been extrapolated to zero H^+/Zr, representing a neutral solution. Since the dissolution of zirconium carbonate into the zirconyl nitrate solution is dependent on the presence of acid, the corresponding Zr:NO_3 ratio can be regarded as the maximum possible limit for dissolution, and hence further polymerisation. This limit of approximately 1:0.73, or 1.37:1, is close to the practical limit for dissolution of zirconium carbonate into zirconyl nitrate solution, which is approximately 1.3:1. There have been no published studies on this limit.

The pH of the ZN2.0 solution changed considerably over 38 days, rising from 0.1 to 0.2, decreasing the H^+:NO_3 ratio from 0.90 to 0.72. Most of the change occurred in the first five days, but the trend indicated that change was continuing at the end of the period. This observation correlates with many other previously published results, showing that hydrolysis and polycondensation continues in zirconyl salt solutions over an extended period, possibly without reaching an equilibrium state (see Section 2.2.2).

In contrast, the ZN1.0 sols remain at approximately pH 0.7 over 40 days. This indicates that once the solution has been strongly hydrolysed during preparation, little or no further hydrolysis or condensation takes place with ageing over this period. Furthermore, this hydrolysis, and subsequent condensation, has no strong tendency to reverse with time under these conditions.

3.4 ^{1}H nuclear magnetic resonance

3.4.1 Introduction

Nuclear magnetic resonance NMR is a technique used to investigate the immediate environment of atoms of a certain isotope of a particular element. The principles behind the technique and methods of analysis are found in many standard texts.[*]

The ^{1}H isotope is the most commonly used, in a technique sometimes known as 'proton' magnetic resonance. Its use to investigate aqueous solutions is limited by the presence of a very high concentration of hydrogen atoms in the solvent, but it can still provide some useful information on the hydrogen atoms associated with ions or particles.[†] All hydrogen atoms in an aqueous solution exchange with those in the solvent. ^{1}H NMR detects 'slowly-exchanging' hydrogen atoms, but does not detect 'rapidly-exchanging' atoms which exchange at rates similar to those of the operating frequency of the spectrometer (300 MHz).

3.4.2 Procedure

Solutions and sols with Zr:NO_3 ratios ranging from 1:2 to 1:1 were prepared, as described in Section 3.2.1. A solution of tetramethylammonium (TMA) nitrate[‡] was added as an internal standard. The TMA cation possesses 12 structurally-equivalent, non-hydrolysable hydrogen atoms, which give a strong, narrow peak in a ^{1}H NMR spectrum. TMA nitrate was chosen as it is a water soluble salt, and the nitrate anion has a minimal effect on the sol. The final Zr concentration was 0.8 mol/kg and TMA concentration was 0.1 mol/kg.

^{1}H NMR spectra were measured for each sample at ambient temperature.[§] The chemical shift for the TMA peak was determined to be 3.195 ppm using a tetramethyl silane standard, and the chemical shifts for all peaks in the sample spectra were calibrated with respect to the TMA peak.

---

[*] The nucleus of an atom absorbs energy at a certain frequency, which is characteristic of the atom's 'chemical environment'. The frequencies are usually quoted as a 'shift' from a standard frequency, normalised by the operating frequency of the spectrometer, in units of 'parts per million' (ppm).

[†] Note that the 'watergate'-type ^{1}H NMR experiment will suppress the signal from the solvent, allowing greater sensitivity. This approach was not used in these experiments, as it is difficult to accurately quantitate the results.

[‡] Formula $N(CH_3)_4NO_3$, supplied from Fluka, No. 87742.

[§] Bruker-Spectrospin 300 DRX spectrometer.

The areas of each peak in the spectra were measured by curve-fitting. The area was ratioed with the area for the TMA peak to determine the abundance of the hydrogen atoms contributing to that NMR peak. Values for each peak are quoted with respect to the concentration of zirconium, as the value H/Zr.

3.4.3 Results and discussion

Figure 3-3 shows the previously unreported ^{1}H NMR spectrum of the ZN2.0 zirconyl nitrate solution, with a number of distinct peaks.

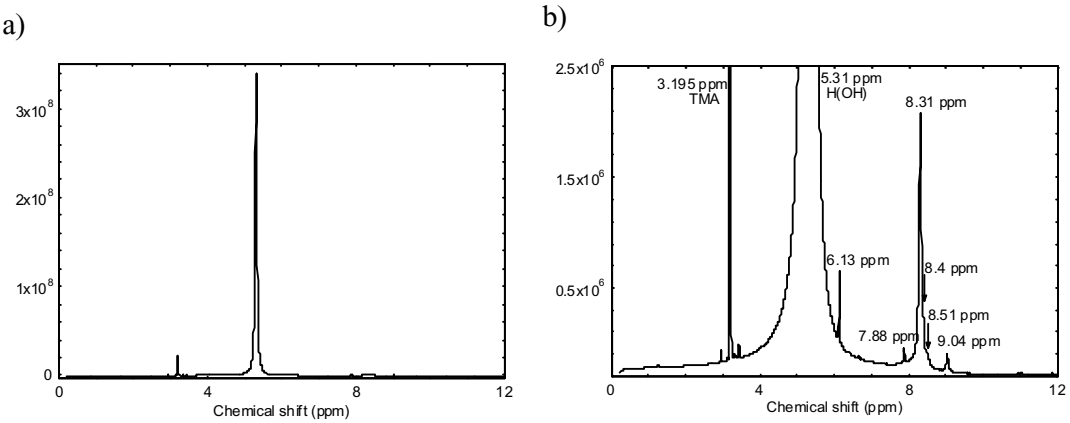

Figure 3-3: ^{1}H NMR spectrum of ZN2.0 solution, a) full scale b) with a magnified intensity scale.

The spectrum is dominated by a broad and very intense peak at 5.31 ppm, which is assigned to the hydrogen atoms in liquid water. The area of this peak corresponds to a hydrogen concentration of 93 ± 5 mol/kg, close to the value for pure water of 111 mol/kg. This peak shifts as the Zr:NO_3 ratio increases, from 5.31 in ZN2.0 to 5.12 in ZN1.0, which is attributed to the accompanying increase in pH.[7] The very sharp peak at 3.195 ppm, and the minor 'satellite' peaks just to either side are assigned to TMA and used to calibrate the other peaks.

The remainder of the peaks, all relatively weak and positioned above 6 ppm, are characteristic of the zirconyl nitrate structure. Six peaks, or shoulders on peaks, can be distinguished and are listed in Table 3-3, along with the corresponding H/Zr value for the peak. The total number of NMR-active hydrogen atoms per zirconium is approximately 1.2. These are all assigned to hydrogen atoms in various structures associated with the zirconyl cation. The peak at 8.31 ppm is by far the most intense, accounting for over 85 % of the hydrogen atoms detected. It is the only peak that has been reported in previous studies of zirconyl perchlorate and chloride solutions,[8-11] and has a H/Zr value of approximately 1.

Table 3-3: Peak positions in the ^{1}H NMR spectrum of ZN2.0.

Position (ppm)	H/Zr
6.13	0.06
7.88	0.03
8.31	1.02
8.4	0.02
8.51	0.03
9.04	0.04
Total	1.19

The 8.31 ppm peak is assigned to slowly-exchanging *water molecules* coordinated around each zirconium cation. This assignment was based on the work by Åberg and Glaser,[8] who reported a combined ^{1}H and ^{17}O NMR study. They observed that the addition of nitrate anions, in the form of HNO_3, to a concentrated zirconyl chloride solution reduced the number of slowly-exchanging hydrogen atoms and slowly-exchanging oxygen atoms from two per zirconium to one. Since the displacement of hydroxy bridges by nitrate is rather unlikely, both the ^{1}H and ^{17}O signals were assigned to slowly-exchanging water molecules coordinated around each zirconium cation. Each of these water molecules has a slowly-exchanging hydrogen atom, presumably with the other hydrogen atoms rapidly-exchanging. The minor peaks above 6 ppm have not yet been assigned.

As the $Zr:NO_3$ ratio increases, the peaks above 6 ppm become less intense and have virtually disappeared when $Zr:NO_3$ reaches 1:1, as shown in Figure 3-4. These peaks are not replaced by any distinct peaks characteristic of the sol. The area of the main 8.3 ppm peak is plotted against the nitrate-to-zirconium ratio in Figure 3-5. The previous studies of zirconyl perchlorate and chloride solutions have also found that the 8.3 ppm peak decreases with intensity as the pH is increased.[9,11]

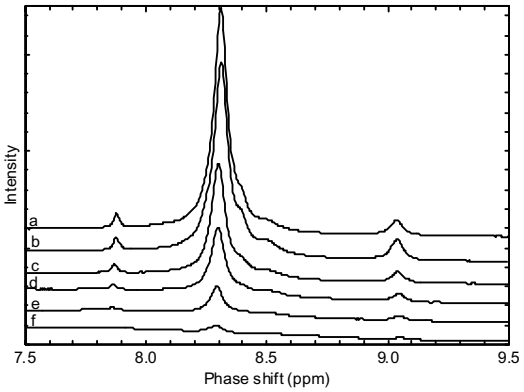

Figure 3-4: Detail of the ^{1}H NMR spectrum for a) ZN2.0, b) ZN1.8, c) ZN1.6, d) ZN1.4, e) ZN1.2 and f) ZN1.0.

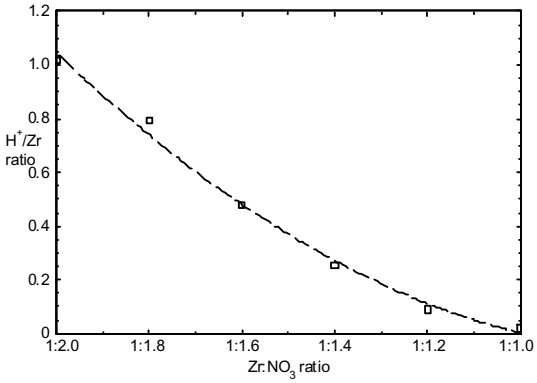

Figure 3-5: Area under the 8.3 ppm peak as $Zr:NO_3$ ratio increases.

The observed decrease from one to zero slowly-exchanging coordinated-water molecules with increase in $Zr:NO_3$ ratio and pH can be attributed to the *hydrolysis* of the coordinated-water molecules around each zirconium atom. In this process, all of the slowly-exchanging hydrogen atoms are progressively removed from the slowly-exchanging water molecules.

$$Zr\cdots OH_2 \;?\; Zr{-}OH^{-} + H^{+}$$

It is evident from the absence of peaks in the ^{1}H NMR spectrum of the ZN1.0 sol that there are no slowly-exchanging water molecules in clearly defined sites coordinated around the sol particles.

No peaks have been assigned to the hydrogen atoms belonging to the bridging hydroxy groups. As suggested by Åberg and Glaser,[8] this may be due to fast quadrupolar relaxation, similar chemical shift to bulk water, or rapid chemical exchange with bulk water.

The position of the 8.31 and 7.88 ppm peaks decrease slightly by 0.02 ppm, while the peak at 9.04 increases in position by 0.02 ppm. These shifts may also be associated with a change in pH, but a definite assignment cannot be made.

In summary, each zirconium atom is coordinated by approximately one slowly-exchanging water molecule, each with a single slowly-exchanging hydrogen atom. Any further coordinated water molecules are rapidly-exchanging, and thus not detectable by NMR. As the $Zr:NO_3$ ratio is increased the slowly-exchanging water molecules are hydrolysed, a process that is virtually complete when the ratio is 1:1. The resulting colloidal particles have no distinct ^{1}H NMR spectrum.

3.5 Raman spectroscopy

3.5.1 Introduction

Vibrational spectroscopy is a characterisation technique that is frequently used to identify the short-range structure of a wide range of materials. In this section it is used to identify the structural changes as the standard sol is prepared from a zirconyl nitrate solution.

The theory and practice of Raman spectroscopy, approaches used for the assignment of Raman bands, and the significance of polarisation and vibration symmetry are all reviewed in Chapter 8. Each spectrum is plotted as Raman-scattering intensity against Raman shift (in cm^{-1}), and each peak, or 'band', in the spectrum can be attributed to a vibration of an interatomic bond or series of bonds, which in turn provides information on the molecular structure.

3.5.2 Procedure

Solutions and sols with $Zr:NO_3$ ratios ranging from 1:2 to 1:1 were prepared, as described in Section 3.2.1, with typical Zr concentrations of 1 or 2 M. Standard sols were aged for periods from several hours to over a year.

The Raman spectrum of each sample was recorded at ambient temperature, using a commercial FT-Raman spectrometer.* Solutions and sols were held in a glass vial, and the horizontal laser beam passed through the wall of the vial into the sample. The Raman spectrum for an empty glass vial and a vial containing only water were also recorded.

Where possible, each band in the Raman spectra has been resolved and its position recorded. Where a number of broad, overlapping bands in a particular region made it difficult to distinguish each band, only the most intense were resolved. There may well be a number of weak or very broad bands, particularly in the 200 - 600 cm^{-1} region, that are concealed by their neighbours and not resolved.

Polarisation measurements were made for ZN1.0 and ZN2.0 samples. A polariser was mounted between the sample and the detector, and Raman spectra were measured with the polariser parallel and perpendicular to the polarisation direction of the incident radiation. The *depolarisation ratio*, ρ, of a particular band is defined as the intensity ratio of radiation

scattered perpendicular and parallel to the incident radiation, and is calculated using Equation 3-3.

$$\rho = \frac{I_{\perp}}{I_{\parallel}} \qquad \textbf{Equation 3-3}$$

Due to the breadth of the overlapping bands, weak signal, and/or uncertain background, it was impractical to precisely measure the depolarisation ratio for many bands, and in most cases the observed bands have only been classified as 'polarised' or 'depolarised'. Bands with $\rho < 0.2$ were classified as polarised, and those with $\rho > 0.7$ were classified as depolarised. (Where the incident radiation is polarised, the theoretical maximum for ρ is 0.75.)

3.5.3 Results and discussion

A typical Raman spectrum of the ZN2.0 zirconyl nitrate solution is shown in Figure 3-6, and the spectrum of the standard ZN1.0 sol in Figure 3-7. The 1000 - 1100 and 250 - 900 cm^{-1} regions are shown in more detail in Figure 3-8 and Figure 3-9, respectively. The spectrum of the zirconyl nitrate solution is discussed fully and assigned in Section 8.3.

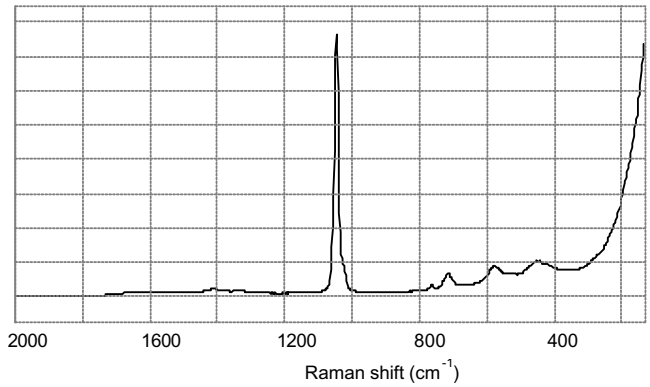

Figure 3-6: Raman spectrum of a zirconyl nitrate solution.

[*] Bio-Rad FT-Raman II, using an excitation line of 1064 nm from a Nd:YAG laser. The effective resolution was 4 cm^{-1}.

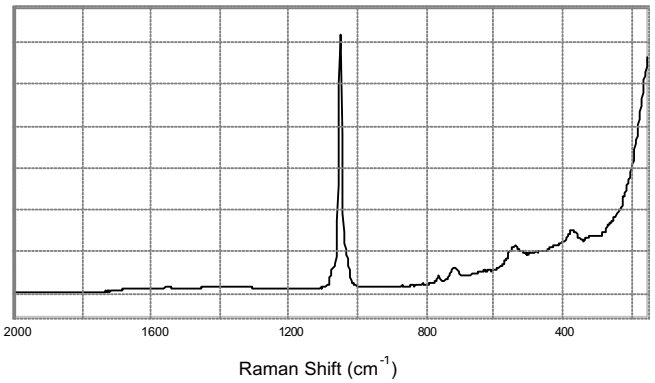

Figure 3-7: Raman spectrum of a standard ZN1.0 sol.

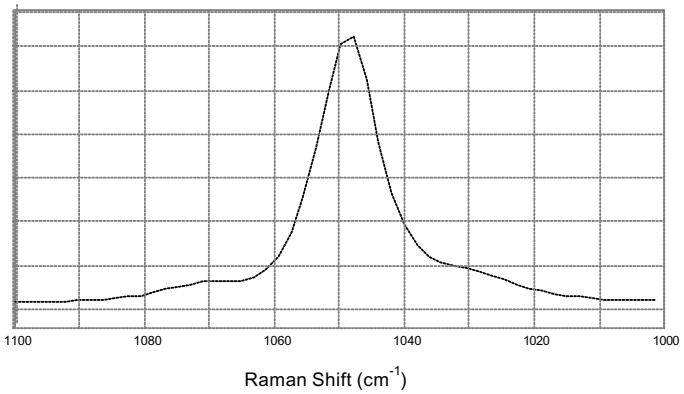

Figure 3-8: Raman spectrum of a standard ZN1.0 sol, 1000 - 1100 cm^{-1}.

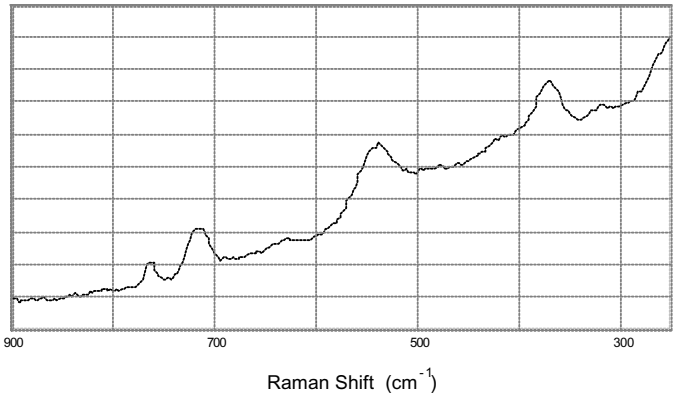

Figure 3-9: Raman spectrum of a standard ZN1.0 sol, 250 - 900 cm^{-1}.

The Raman spectra are presented and discussed in three sections. There is a significant 'background' in each spectrum, due to the water and the glass vial, and this is discussed in Section 3.5.3.1. The Raman spectra of the solutions and sols can be conveniently divided into two regions. The region below 650 cm^{-1} is largely assigned to Zr–O bonds, and is discussed in Section 3.5.3.2. The region above 650 cm^{-1} is largely assigned to the nitrate species, and is discussed in Section 3.5.3.3.

3.5.3.1 The 'background' spectrum

Solutions and sols were held in a glass vial, and the horizontal laser beam passed through the wall of the vial into the sample. The Raman spectrum of the glass vial was thus superimposed over the sample spectrum. The spectrum of an empty glass vial is shown in Figure 3-10, and that of a glass vial containing only water in Figure 3-11. The glass contributes a polarised band ($\rho \sim 0.05$) at approximately 460 cm^{-1}, while the water causes the 'exponential' background that becomes very intense at low Raman-shift. Unfortunately, the Raman band from the glass is at a similar position to a number of bands in the sample spectrum. Although the bands in the sample spectrum are generally stronger and narrower than the band in the glass spectrum, the intensity of the bands in the sample spectrum over this region cannot be measured reliably, and analysis is limited to qualitative observations. This is particularly a problem in making the polarisation measurements. The relative intensity of the Raman scattering from the sample, the water, the glass vial and the detector background varied with the concentration of the sample and focussing of the laser, and thus subtraction of the 'background spectrum' from the sample spectrum was found to be impractical.

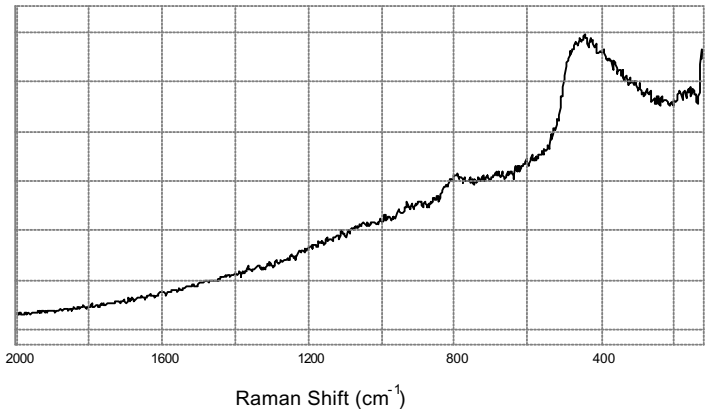

Figure 3-10: Raman spectrum of an empty glass vial.

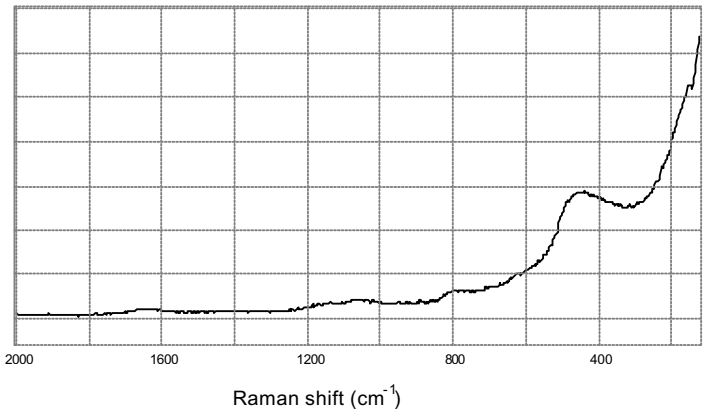

Figure 3-11: Raman spectrum of a glass vial containing water.

It is also probable that, in addition to the 'exponential' background from the water, there is some contribution to the spectrum from the librational modes of the water molecules. The Raman spectrum of liquid water has been previously reported,[12] with three broad librational bands at 425, 550 and 740 cm^{-1}. However, the shape of the resultant 'water' spectrum, shown in Figure 3-12, does not strongly resemble the measured spectrum in Figure 3-11, so we can conclude that the librational spectrum does not greatly contribute to the total spectrum.

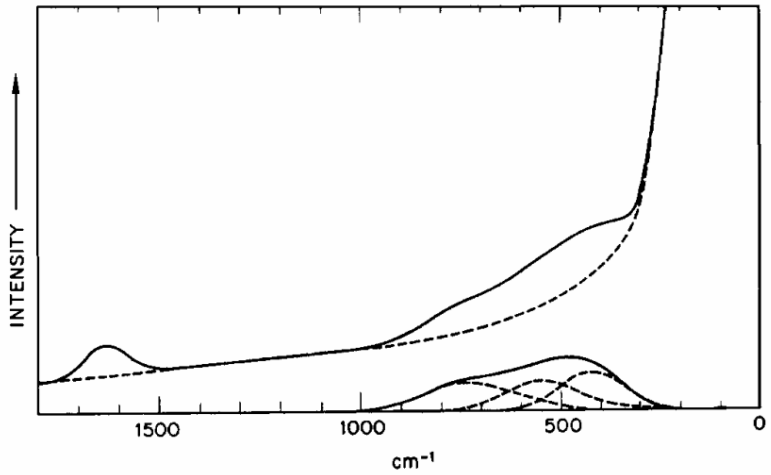

Figure 3-12: Raman spectrum of liquid water, showing the bands due to the librational modes at 425, 550 and 740 cm^{-1}, from Walrafen.[12]

3.5.3.2 Raman spectrum below 650 cm^{-1}

Vibrations of metal-oxygen bonds are generally found in the 200 - 650 cm^{-1} region. Both the standard ZN1.0 sol and the zirconyl nitrate solution have Raman spectra with two main bands in this region, but at quite different positions. The positions and polarisation assignments for all

bands below 650 cm^{-1} are listed in Table 3-4. The difference in the Raman spectra of the solution and the sol indicate that substantial changes occur in the short-range arrangement of the zirconium and oxygen atoms during the formation of the sol.

Table 3-4: Positions of bands observed in Raman spectra < 650 cm^{-1}.

ZN2.0 solution			ZN1.0 sol		
Position (cm^{-1})	ρ	Polarisation assignment*	Position (cm^{-1})	ρ	Polarisation assignment*
			630		*dp*
580	< 0.2	*p*			
			540	< 0.01	*p*
450		*dp*			
			420 sh		*dp*
			375	~ 0.75	*dp*

* *p* = polarised, *dp* = depolarised; Values of ρ were often not able to be determined accurately.

The transformation from solution to sol has been examined by measuring the Raman spectrum of a series of samples with $Zr:NO_3$ ratios ranging from 1:2 to 1:1. The 250 - 900 cm^{-1} sections of these Raman spectra are shown in Figure 3-13. Since scattering intensity varies with focussing and other factors, these spectra had to be normalised. It was observed that the intensity of the band at 1050 cm^{-1} was roughly proportional to the total nitrate content of each sample (which remains constant through the process), so each spectrum was normalised to this band.

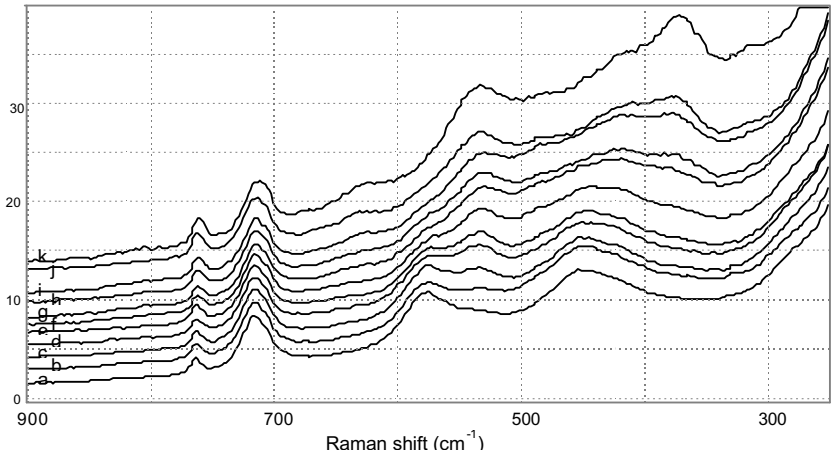

Figure 3-13: Raman spectra of samples with varying $Zr:NO_3$ ratios, over the range 250-900 cm^{-1}: a) ZN2.0 (zirconyl nitrate), b) ZN1.9, c) ZN1.8, d) ZN1.7, e) ZN1.6, f) ZN1.5, g) ZN1.4, h) ZN1.3, i) ZN1.2, j) ZN1.1 and k) ZN1.0 (standard sol). Each spectrum is displaced along the y-axis for clarity.

The transition from the solution spectrum to the sol spectrum is fairly complicated, and a number of bands grow and diminish in intensity, particularly in the region below 650 cm^{-1}. The many overlapping bands makes interpretation difficult, and it is not always possible to identify each band that is contributing to the spectrum.

At least two 'processes' can be clearly distinguished in the spectra as the $Zr:NO_3$ ratio increases from 1:2 to 1:1. The first process is the decrease in the intensity of the polarised band at 580 cm^{-1}, and the concurrent increase in intensity of the polarised band at 540 cm^{-1}. The intensity of these two bands are roughly inversely proportional to each-other, indicating a transition of a certain structure from one state to another. This process appears to take place fairly evenly during the process, being proportional to the amount of additional zirconium added, and is completed in the standard ZN1.0 sol.

The second process identified is the appearance of a depolarised band at 375 cm^{-1}, and the increase in its intensity as the $Zr:NO_3$ ratio increases from 1:1.5 to 1:1.0. The weak band at 630 cm^{-1} also increases in intensity proportionally to the 375 cm^{-1} band. This process clearly does not occur concurrently with the first.

The bands at 450 and 420 cm^{-1} also appear to change with $Zr:NO_3$ ratio. These changes are more difficult to identify due to the breadth of adjacent bands, the contribution from the glass and water spectra, and possibly one or more minor unidentified bands in the sample spectrum. The 450 cm^{-1} band becomes less distinct as the $Zr:NO_3$ ratio increases, while the 420 cm^{-1} band becomes stronger and become a shoulder on the 375 cm^{-1} peak.

Once the standard sol was prepared, very few changes were observed in the Raman spectrum with time. A few minor changes in the region below 650 cm^{-1} were observed over the first week after preparation, mostly sharpening of the existing bands. Spectra of sols aged for over two years showed no further ageing effects in the Raman spectrum.

Comparison with previous studies

It is useful at this point to review previously-published Raman studies that are similar to this one. Hannane, Bertin and Bouix measured the Raman spectrum of the supernatant solution after a base was added to zirconyl chloride solutions at OH:Zr ratio of 0.35:1.[9,13] The bands in the Raman spectrum of the starting solution, at approximately 456 and 580 cm^{-1}, were replaced by bands at 426 and 533 cm^{-1}. With further hydrolysis to a OH:Zr ratio of 1:1, the 426 cm^{-1} band shifted to approximately 400 cm^{-1}. Similar changes to the Raman spectrum of

zirconyl chloride solutions during hydrolysis have been reported elsewhere by Tosan *et al.*,[6] Sharygin *et al.*,[14] and Burkov *et al*.[15]

Various assignments of the Raman spectra, and interpretations of these changes, have already been suggested. Hannane, Bertin and Bouix identified 5 distinct 'species' from the Raman spectra, and suggested that the main change occurring was the oxolation of the bridging hydroxy groups.[9] Sharygin *et al.*,[14] referring to Clearfield's proposed mechanism for polymerisation (Section 2.2.2),[16] maintained that the hydroxy-bridges remained intact during hydrolysis. They instead assigned all the observed bands to the vibrations of coordinated water or terminal hydroxy groups, and interpreted the changes in the spectrum as hydrolysis of the coordinated water groups, and condensation of terminal hydroxy groups.

None of these studies report any strong band below 400 cm^{-1}, and thus the band observed at 375 cm^{-1} in the standard ZN1.0 sol is unusual. Matsui *et al.* have reported a Raman spectrum of 'hydrous zirconia', prepared by boiling 0.8 M zirconyl chloride solution.[17] The reported Raman spectrum of this material was very weak but had bands at approximately 375, 540 and 620 cm^{-1}, very similar to the spectra reported here of the standard sol and gel. The X-ray diffraction pattern of this material was also very similar to that of the standard ZN1.0 gel, as discussed in Chapter 4. Matsui *et al.* made no attempt to assign the spectrum or to speculate on the short-range structure of this material.

Assignments

The best point at which to begin assigning the Raman spectra is with the zirconyl nitrate solution, for which the short-range structure is already known. Chapter 8 is dedicated to this stage, and the conclusions are only summarised here.

The two main bands at 580 and 450 cm^{-1} were both assigned to vibrations of the double hydroxy-bridge structure Zr–$(OH)_2$–Zr. The polarised 580 cm^{-1} band was assigned to the hydroxy groups symmetrically stretching away from and towards each other, as illustrated in Figure 8-11. The depolarised 450 cm^{-1} band was assigned to an antisymmetric stretch of the same group, as was the minor band at 430 cm^{-1}.

The 'new' bands observed in the spectrum of the ZN1.0 sol must be of a vibration that was not Raman-active in the solution. For example, a new species, a change in the frequency or symmetry of vibration of an existing species, or a lattice mode of a newly-formed structure.

The highly polarised band at 540 cm^{-1} is clearly related to the band at 580 cm^{-1}, which it replaces as the Zr:NO_3 ratio increases. Two explanations for the shift from 580 to 540 cm^{-1} have been considered. The Zr–O bond length or bond angles in the hydroxy bridges could have changed in the transition from the polynuclear cation to a 'continuous' network in the sol particles. Alternatively, the hydroxy bridges could have been converted to *oxo* bridges by an oxolation reaction, as in Equation 3-4.

$$Zr–(OH)_2–Zr \;?\; Zr–O–Zr + H_2O \qquad \textbf{Equation 3-4}$$

The range of symmetric vibrations of a Zr–O–Zr bridge is limited to stretching along the axis of the bridge, and in a polynuclear species each bond would have to stretch in-phase to maintain symmetry, *i.e.* an A_1' 'breathing mode'. In a species with more than ~ 10 zirconium atoms, such a symmetric vibration is unlikely to occur, and only antisymmetric vibrations would be possible. Hence the first explanation is favoured; *the 540 cm^{-1} band is assigned to the same vibration as the 580 cm^{-1}, with each frequency characteristic of a certain 'environment' of the bridging hydroxy group.* For example, the bond lengths may change slightly. This suggestion is supported by the EXAFS study of the gel, discussed in Section 4.3.4, which shows that the double hydroxy bridges are preserved in the gel, with slightly shorter Zr–O and Zr–Zr distances than found in the 'cyclic-tetramer' zirconyl species.

We now turn to the depolarised band at 375 cm^{-1}. This band is characteristic of the particles found in the sol, and is not previously reported in the Raman spectra of any zirconyl salt, hydrolysed salt solution, or amorphous 'zirconium hydroxide', except in the single case reported by Matsui *et al.* (see above). The intensity of the band is not directly related to that of the 540 cm^{-1} band, appearing only at Zr:NO_3 > 1:1.5. *The most probable assignment is to a lattice mode* that is inactive in very small species with only a few zirconium atoms, but becomes active once the sol particles have reached a certain size. The above-mentioned EXAFS study of the gel also indicates that a regular $Zr(OH)_4$ lattice is formed in the gel (and presumably also in the sol particles), but the frequencies of the vibrational modes of such a lattice have not been calculated.

Other assignments for the 375 cm^{-1} band are possible. The band could be assigned to a Zr–O–Zr bridge, as we cannot rule out the possibility that a fraction of the hydroxy-bridges have undergone oxolation. It would be difficult to test this hypothesis, but it should be noted that the 375 cm^{-1} band broadens and diminishes considerably when the gel is heated to 300°C, the

point at which oxolation is thought to occur (see Chapter 5), making this assignment unlikely. Alternatively, the band at 1070 cm^{-1} (see Section 3.5.3.3) appears at about the same stage, and assignments to coordinated nitrate or even carbonate have been considered. If this were the case, the 375 cm^{-1} band could conceivably be assigned to a Zr–O(N) or Zr–O(C) stretching mode. However there are several arguments against this assignment. Firstly, either a unidentate or bidentate-coordinated species would have at least one *symmetric* Zr–O stretching mode, which would give rise to a strong, polarised band in the Raman spectrum, and no corresponding band has been observed. Secondly, there is little change in the relative intensity of this band with gelation (see Section 4.3.3), which involves a considerable fraction of the non-coordinated nitrate anions becoming bound to the particles. The intensity of a Zr–O(N) mode would be expected to become much stronger with gelation. Thirdly, microanalysis of the gel (see Section 4.3.2) indicated that there is no significant amount of carbon present, so an assignment to carbonate can be eliminated. Overall, the available evidence favours the assignment of the 375 cm^{-1} band to a lattice mode.

The weak, depolarised band at 630 cm^{-1} changes in intensity in a manner similar to that of the 375 cm^{-1} band. Based on this observation, this band is also assigned to a weak lattice mode. The depolarised band at 430 cm^{-1} is given the same assignment as for the zirconyl nitrate salt, that of antisymmetric vibrations of the bridging hydroxy groups.

3.5.3.3 Raman spectrum above 650 cm^{-1}

The region above 650 cm^{-1} in the Raman spectrum of the zirconyl nitrate solution is fully discussed and assigned in Section 8.3. The positions and assignments for all bands between 650 and 1100 cm^{-1} for both the ZN2.0 solution and ZN1.0 sol are given in Table 3-5.

Table 3-5: Bands in the Raman spectrum of the ZN2.0 solution and ZN1.0 sol.

ZN2.0 Position (cm^{-1})	ZN1.0 Position (cm^{-1})	ρ	Polarisation assignment*	Assignment
	1070	0.2	*p*	unknown
1050	1050	0.09	*p*	D_{3h} aquated nitrate ion
1025	1030	0.14	*p*	C_{2v} bidentate nitrate
766	763	~ 0.75	*dp*	C_{2v} bidentate nitrate
720	715	~ 0.75	*dp*	D_{3h} aquated nitrate ion

* *p* = polarised; *dp* = depolarised.

The most abundant nitrate species in the solution is the *fully-aquated* (ionic) species. This species possesses D_{3h} symmetry, with oxygen atoms evenly distributed around the central nitrogen atom in a triangular plane, undistorted by any nearby molecules. A minor nitrate species, with C_{2v} symmetry, is symmetrically bidentate-coordinated (chelated) to a zirconium atom.

Comparing Figure 3-6 and Figure 3-7, the spectrum above 650 cm^{-1} changes very little as the $Zr:NO_3$ ratio increases. As mentioned above, the major 1050 cm^{-1} band maintains a constant intensity, and the relative intensities of the bands assigned to the two nitrate species also remain constant. *The implication is that the symmetry of the nitrate groups is not affected by the formation of the colloidal particles*. The location and bonding of the nitrate species is further discussed in this chapter in Section 3.8.

The only significant change in the region above 650 cm^{-1} with the increase in $Zr:NO_3$ ratio is the appearance of a new band at 1070 cm^{-1}, as a minor shoulder on the 1050 cm^{-1} peak. As shown in Figure 3-14, this band is almost unnoticeable until the $Zr:NO_3$ ratio reaches 1:1.5, then grows steadily as the $Zr:NO_3$ ratio increases further. A number of assignments have been considered for the band at 1070 cm^{-1}. It is difficult to assign it to the $\nu_2(A_1)$ mode of any coordinated-nitrate species, as this mode has not been previously reported at a frequency above 1040 cm^{-1} for any nitrate compound.[18] There are also no new bands in other regions of the spectrum that would correspond to the other modes of a new nitrate species, except possibly for the very broad and weak 630 cm^{-1} band. The $\nu_2(A_1)$ mode of a C_{2v} coordinated-carbonate species has been reported at 1070 cm^{-1},[18] and it is conceivable that carbonate anions may remain in the sol from incomplete decomposition of the carbonate, or adsorption on the surface of the particles. However, the other polarised (A_1) bands for this species are expected at ~1400, 760 and 360 cm^{-1}, and no new polarised bands are observed at these positions. Furthermore, the highly acidic conditions in the sol would make the survival of the carbonate species unlikely, and the microanalysis of the gel, reported in Section 4.3.2, also indicated that there is no significant amount of carbon present. A further assignment that was considered was the δ(ZrOH) bending mode of a hydroxy group, which is frequently found below 1200 cm^{-1}.[18] However, bands from this vibration are not usually found in Raman spectra,[19] and are expected to be depolarised. No similar bands are observed at all in the spectra of zirconyl chloride or nitrate solutions, which are known to contain both bridging and terminal hydroxy groups. Therefore this band must remain unassigned.

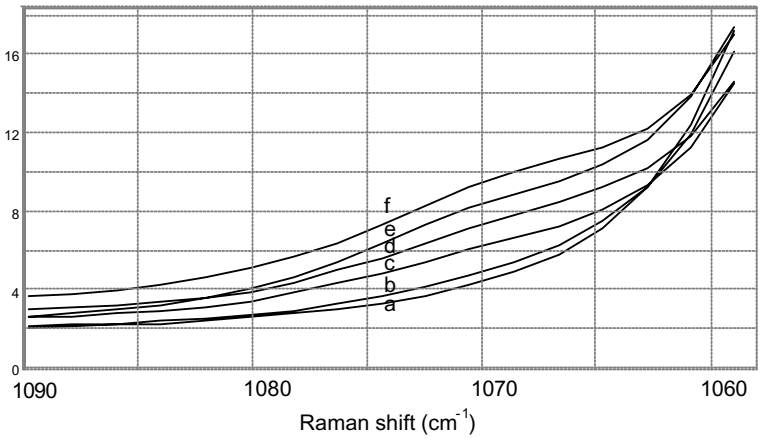

Figure 3-14: Raman spectra of samples with varying Zr:NO_3 ratios, over the range 1060-1090 cm^{-1}: a) ZN2.0 (zirconyl nitrate), b) ZN1.6, c) ZN1.3, d) ZN1.2, e) ZN1.1, f) ZN1.0 (standard sol). The y axis is uniform.

3.5.4 Summary

The following major points can be made from the study of the Raman spectrum:

- In the Raman spectrum of the zirconyl nitrate solution a symmetric vibration at 580 cm^{-1} has been identified as characteristic of the bridging hydroxy group in the zirconyl species. As the colloidal particles are formed, the characteristic vibration changes in frequency to 540 cm^{-1} but remains symmetric, strongly indicating that the group remains intact and does not undergo oxolation. The observed change in frequency was attributed to a change in Zr–O(H)–Zr bond length.
- The 375 cm^{-1} band characteristic of the ZN1.0 sol was tentatively assigned to a lattice mode of the colloidal particles.
- The symmetry of the nitrate groups is not affected by the formation of the colloidal particles.
- A minor band at 1070 cm^{-1} appears with the formation of the colloidal particles, but cannot be unambiguously assigned.

3.6 Small-angle X-ray scattering

The size and shape of colloidal particles is often characterised by studying the way that the particles scatter incident radiation. One of the most widely used techniques is that of small-angle X-ray scattering (SAXS), which is suitable to study particles that are at several tens to several hundred times the X-ray wavelength. In addition to average particle size, the particle shape can also be determined by fitting suitable models to the scattering data.

This section summaries the results from a SAXS study of the standard sol. The full details of the study are contained in Chapter 9, including the procedure and full results, along with a discussion of the theory and various experimental difficulties. Only the main conclusions are given here. Note that all dimensions quoted are 'average' values for the particles, and only for the Zr–O 'core' of the particle. Any bound water or associated nitrate groups are not detected by SAXS, as these molecules have very similar scattering characteristics to the surrounding water matrix.

The samples examined were a ZN2.0 zirconyl nitrate solution and several standard ZN1.0 sols, all with a Zr concentration of 1.0 M and aged for approximately 5 days after preparation. To determine any effects of aging, the scattering profile of one of the ZN1.0 sols was measured again after 6 months. The scattering profile of a ZN1.0 sol diluted to 0.2 M was also measured to determine the effect of dilution. The latter is particularly important, as all dynamic light scattering studies (Section 3.7) were carried out using diluted samples.

Results

Low aspect-ratio particles with radius of gyration of 0.40 ± 0.04 nm dominate the scattering profile of the precursor zirconyl nitrate solution ZN2.0. The size and shape of these particles is close to that previously reported for the 'cyclic-tetramer' species $Zr_4(OH)_8(H_2O)_{16}$ (see Section 2.2.1).[20,21] The scattering profile also indicates the presence of a small fraction of substantially larger particles, which are approximately 14 nm in diameter.

The particles in the 1.0 M ZN1.0 sol are plate-shaped, with average dimensions of 2.8 ± 0.4 nm across and 0.5 ± 0.1 nm thick. This morphology corresponds well with the short-range structure of the particles found by the EXAFS study (Section 4.3.4), and will be discussed in full in Section 3.9. In brief, it is thought that the particles are composed of one or two layers of partially-ordered $Zr(OH)_4$ sheets.

The small population of larger particles, identified in the precursor solution, is also identified in the sol, although it is not practical to compare the volume fraction taken up by these larger particles.

There is very little change in the shape or size of the primary particles during ageing over 6 months. The contribution of the larger (~ 14 nm) particles towards the scattering curve appears to increase a little with ageing.

Dilution of the sol from 1.0 M to 0.2 M increases the average particle diameter to approximately 4.0 ± 0.4 nm,* equivalent to the plate surface area increasing by 80 %. The thickness also appears to decrease slightly to 0.35 ± 0.1 nm.

The results of this study can be compared with previous studies of the formation of particles in zirconyl salt solutions during aging at between 80 and 100°C over periods between 10 and 100 hours.[22,23] These studies found that the initial particles formed were rod-shaped, but this is clearly not the case here. It is evident that different polymerisation mechanisms predominate with different reaction-rates, and possibly at different temperatures. It is suggested that oxolation may play a greater role over longer periods at elevated temperatures, leading to the formation of semi-ordered ZrO_2, rather than $Zr(OH)_4$.

Summary

1. The SAXS profile for the ZN2.0 zirconyl nitrate solution is consistent with the presence of 'cyclic-tetramer' species.
2. The particles in the 1.0 M ZN1.0 sol are plate-shaped, with dimensions approximately 2.8 nm across and 0.5 nm thick (excluding bound water and associated nitrate anions). Ageing over 6 months does not appear to affect the size and shape of these particles.
3. The scattering profile of both ZN2.0 and ZN1.0 indicates the presence of a small fraction of substantially larger particles, which are approximately 14 nm in diameter. Ageing of the sol over 6 months appears to increase the fraction of the particles, due to aggregation.
4. Dilution of the sol from 1.0 M to 0.2 M promotes growth of the sol particles at the edges.

---

* Although it is possible that this apparent increase in size is simply due to the reduction of inter-particle effects, this is not thought to be the case for this set of data. Precautions were taken to exclude from analysis the section of the scattering profile that is most sensitive to inter-particle effects. Further details are given in Chapter 9.

3.7 Dynamic light scattering

3.7.1 Introduction to dynamic light scattering

Dynamic light scattering (DLS), also known as *photon correlation spectroscopy*, is a technique to determine the *size distribution* of colloidal particles in a liquid, using fluctuations in scattered light caused by the *Brownian motion* of the particles. Brownian motion is the erratic motion of colloidal particles in a liquid, in this case water, caused by the collision of the particles with water molecules. The frequency of the motion is dependent on the *diffusion coefficient* of the particles in water, which is inversely proportional to both the *equivalent hydrodynamic diameter* of the particles and the viscosity of the liquid. The hydrodynamic dimensions of a particle are those of the entire entity that is displaced in Brownian motion. This includes the 'double-layer' of water surrounding the particle, which can be many Ångstroms thick. The shape of the particle cannot be inferred from the diffusion coefficient, so the particle is assumed to be spherical and an 'equivalent diameter' is calculated.

The scattering of radiation by colloidal particles is discussed in Section 9.2. If a strong beam of light is passed through a colloidal dispersion and the scattered light measured at a fixed angle, the intensity of the light is found to fluctuate with time due to the Brownian motion of the particles. The characteristic lifetime of these fluctuations is inversely proportional to the diffusion coefficient, and thus proportional to the size of the particles. The *autocorrelation function* of the fluctuating intensity is calculated, to obtain a decaying exponential curve in time. From the decay constant the diffusivity can be calculated, and thus the hydrodynamic diameter. The practical lower size-limit for this technique is approximately 2 nm.

Where there is a distribution of particle sizes, the distribution function is convoluted with the autocorrelation function. There are a number of methods of deriving the particle-size distribution from the autocorrelation function. The simplest method is to assume a simple Gaussian distribution of particle size, fitting only the mean diameter and distribution half-width, which requires relatively little data.

This Gaussian assumption is insufficient when the colloid contains particles with a more complex distribution of particle sizes, such as two distinct 'populations' of particles with different sizes. The NICOMP method is a proprietary method for calculating complex particle-size distributions from the autocorrelation function.[24] No *a priori* assumptions about the shape of the distribution function are made. This method also indicates the relative proportions of each population. The intensity of light scattered from a particle is proportional to its average

cross-section, so the technique is much more sensitive to larger particles than to smaller particles. The NICOMP particle-size distribution can correct for this by weighting the data to indicate the *volume fraction* of each population of particles.

The NICOMP method has some limitations. In practice, the actual plots obtained from the distribution analysis represent very simplified versions of whatever the true particle-size distribution may be. However, it usually turns out that the resolution and accuracy of the NICOMP algorithm are sufficient to yield a meaningful *representation* of the true particle size distribution for many systems of practical significance.[24]

DLS is usually carried out by measuring the scattered light at only one angle. The instrument used in these experiments measures the light fluctuations simultaneously at two angles, and the autocorrelation functions from each angle are analysed independently. This allows data to be double-checked to ensure its validity. If the two angles are widely separated, the time-scale of the measured fluctuations are also considerably different, which adds a further double-check. If similar results are given for each angle, there is a high probability that the results are characteristic of the size-distribution of the scattering particles.

3.7.2 Procedure

The ZN1.0 sols examined were prepared by the standard method described in Section 3.2. The effects of aging were determined by measuring the particle-size distribution for a series of sols ranging in age from 1 day to 22 months. The light scattering intensity was also measured for a solution of zirconyl nitrate solution, ZN2.0.

Samples were first diluted in water to approximately 0.4 M, to minimise multiple scattering and inter-particle effects. This increases the pH, but keeps the $Zr:NO_3$ ratio constant.* The sample was then filtered through several 0.45 μm PTFE filters to remove any large particles.

For the DLS measurements the sample was contained in an insulated vial sitting on a heating block, maintained at 30.0°C. Laser light (488 nm) was passed through the vial, and the intensity of the scattered light detected simultaneously at scattering angles of 39.8° and 79.5°. The signal from each detector was processed by an autocorrelator† and monitored on a

---

* Dilution with other solutions was considered. Dilution with weak nitric acid could be used to maintain the pH, but would greatly change the $Zr:NO_3$ ratio. Weak hydrochloric acid would maintain both the pH and $Zr:NO_3$ ratio, but would also introduce Cl^- anions.

† NICOMP Autocorrelator Model 370, Pacific Scientific Instrument Division.

computer. The particle-size distribution was calculated using both the Gaussian assumption and the NICOMP algorithm. Data collection continued until the calculated distribution was stable, and satisfactory fit-errors were obtained. Data collection periods ranged from 20 to 40 hours.* The instrument was calibrated with a standard dispersion of 19 nm latex spheres, and was found to be accurate within ± 0.5 nm (± 3 %).

3.7.3 Results and discussion

The zirconyl nitrate ZN2.0 solution gave negligible scattering intensity, indicating the absence of any scattering particles. This shows that the ~ 14 nm particles observed by SAXS in a similar solution must have a very low concentration.

The ZN1.0 sols scattered light sufficiently for the particle size distribution of each sample to be determined. In all cases the 'Gaussian' mean diameters calculated from data collected at the two scattering angles agreed within 2 nm, and often with 0.2 nm. The calculated NICOMP distributions for each angle were also very similar. This strongly indicates that the data is characteristic of the size distribution of the scattering particles. In general the results measured at 39.8° had much lower fit-errors, and it is these results that are quoted.

The unweighted distribution plot for two samples, aged for 1 day and 8 months, are presented in Figure 3-15 and Figure 3-16, respectively. Each peak represents a 'population' of particles with a certain range of particle sizes. The intensity of each peak indicates the intensity of the light scattered by each population. Since the intensity of light scattered by a particle is proportional to its average cross-section, a large particle will scatter light much more strongly than a small particle, even when corrected for the particle volume. Consequently, the observed intensities must be weighted to provide an equivalent 'volume fraction' for each population.

* Except for the sol that was one day old, for which the data collection period was 3 hours 20 min. The large particles present in this sol gave a much stronger signal, leading to a low fit-error, but the uncertainties in the size distribution for the smaller particles remains quite high.

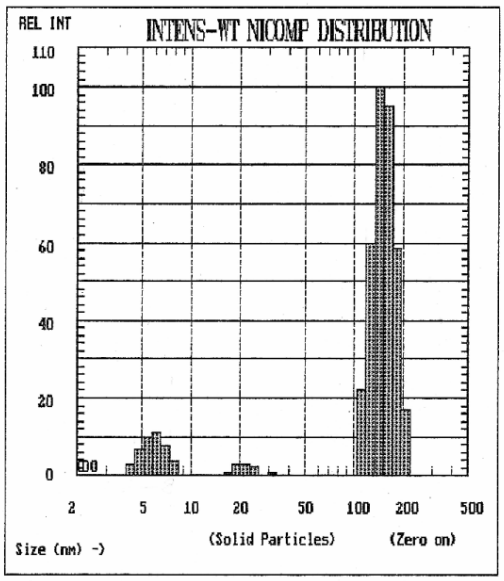

Figure 3-15: NICOMP particle size distribution (intensity weighted) for a ZN1.0 sol aged for 1 day.

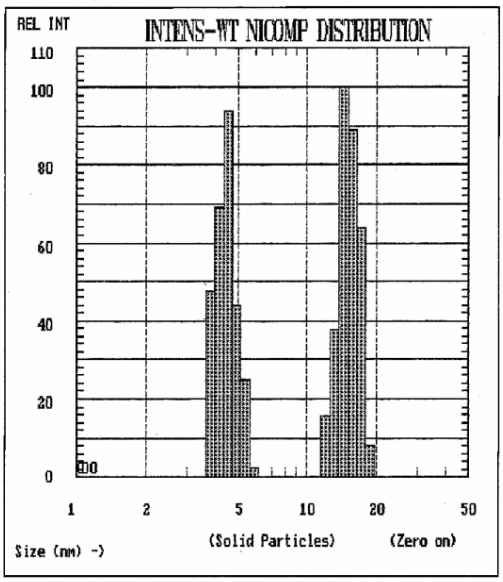

Figure 3-16: NICOMP particle size distribution (intensity weighted) for a ZN1.0 sol aged for 8 months.

The NICOMP distributions for all six ZN1.0 sol samples are summarised in Table 3-6. Each sample is shown to contain up to three 'populations' of particles. The table quotes the 'size range', determined from the width of the peaks in the intensity-weighted distribution.* Also given in the table is the fraction of scattered light attributed to each population, and the calculated volume fraction of each population. Although particle size distributions based on complex models must be treated with caution, a clear pattern can be observed in the results.

Table 3-6: Summary of NICOMP distributions for ZN1.0 sols aged for up to 22 months.

Age	Population 1			Population 2			Population 3		
	size range (nm)	intensity fraction	volume fraction	size range (nm)	intensity fraction	volume fraction	size range (nm)	intensity fraction	volume fraction
1 day	4.5 - 7.0	10 %	99.2 %	18 - 25	3 %	0.7 %	120 - 200	88 %	0.1 %
7 days	3.0 - 5.0	*n.a.*	> 99 %	12 - 18	*n.a.*	< 1 %			
7.5 months	4.0 - 5.0	100 %	100 %						
8 months	3.6 - 5.1	48%	97 %	13 - 18	52 %	3 %			
18 months	3.5 - 4.5	50 %	97 %	11 - 18	50 %	3 %			
22 months	4.0 - 6.5	> 99 %	100 %	~ 22	< 1 %	< 0.1 %			

n.a.: Some 'fraction' values were not able to be calculated from the results

* Although the NICOMP method is not particularly good at determining the true *range* of particle diameters in a particular population, the size range was chosen as a more appropriate way of expressing the results than the peak position.

In all cases the vast majority (> 97 vol %) of the colloidal particles have an equivalent hydrodynamic diameter of approximately 4 nm. In this discussion these referred to as the *primary particles*. The calculated 'size range' varies somewhat, but considering that detecting particles of this size is pushing the limits of the DLS technique, and the uncertainties in the NICOMP method, the results are remarkably consistent. Figure 3-17 plots the 'size range' as a function of the age of the sol, and *no aging effects can be discerned*.

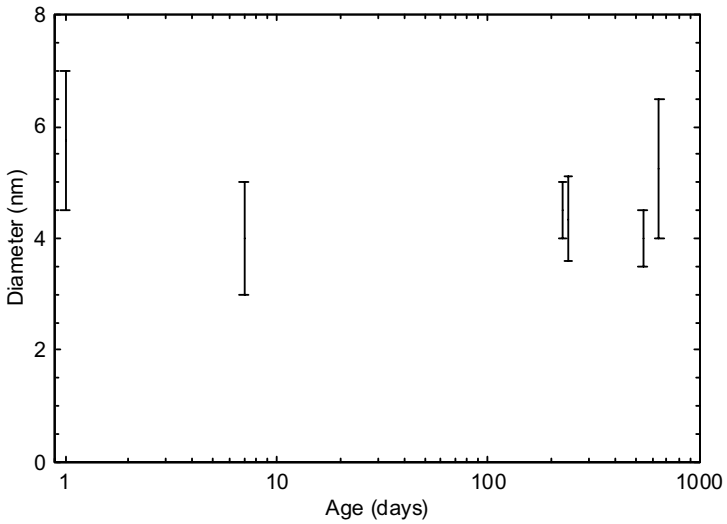

Figure 3-17: Plot of the 'primary particle' size, as determined by DLS, against ageing time. The bars indicate the width of the distribution peak.

The measured size of the primary particles for the sol aged for only one day is a little larger than measured for sols aged for longer periods. However, this measurement is subject to much greater uncertainties than the other measurements; not only was the collection time much shorter, but the signal from the primary particles constituted only 10 % of the total signal.

The SAXS study of sols with 1 M and 0.2 M concentration, summarised in Section 3.6, found 'primary particles' in 1 M sols to be plate-shaped, with approximate width 2.8 nm and thickness 0.5 nm. When diluted to 0.2 M the particles grew to be approximately 4.0 nm wide and 0.4 nm thick. To allow comparison with the DLS results, these dimensions can be converted to an 'equivalent spherical diameter'[*]: 2.6 nm for the 1 M sol and 3.4 nm for the 0.2 M sol.

[*] This value is calculated by substituting the values for the radius if gyration from Table 9-1 into Equation 9-3.

The difference between the 'diameter' values determined by SAXS and DLS can be entirely attributed to the different way that the 'particle' is defined and detected by the two techniques. SAXS detects only the 'Zr–O backbone' of each particle, which scatters X-rays more strongly than the surrounding water. On the other hand, DLS detects any coordinated nitrate and water groups, as well as the *hydration sphere*, a layer of water that moves with the particle in Brownian motion. A layer of nitrate/water approximately 0.3 - 0.5 nm thick is a reasonable value and completely consistent with the results.

Most samples also contained a small population of particles with hydrodynamic diameters of 10 - 20 nm. These particles accounted for up to 50 % of the scattered light, but were calculated to make up less than 3 % of the scattering-particle volume. They clearly correspond with the ~ 14 nm particles observed by the SAXS study. There is no clear trend in the volume fraction with ageing, and the presence of these particles probably depends on minor processing parameters.

In the sol aged for only a day, a very small population of particles with hydrodynamic diameter of 120 - 200 nm was found, which accounts for most of the scattered light. This is probably a minor residue from the decomposition of zirconium carbonate to form the sol, and is not present after ageing for 7 days.

In summary, the vast majority of the particles present in the ZN1.0 sol have an equivalent hydrodynamic diameter of approximately 4 nm, which does not change with ageing over many months. This value is consistent with the SAXS measurements of the same particles, including a hydration layer that is approximately 0.3 - 0.5 nm thick.

3.8 Location of the nitrate anions

The previous sections have discussed the size, shape and structure of the colloidal particles, but made little reference to the nitrate anions that are also present in the sol. It is of interest to determine the location of these anions, whether they are disassociated ions or closely bound to the particles, as they probably play a role in preventing the aggregation of the particles. The techniques used to determine the location of the nitrate are ^{14}N NMR and Raman spectroscopy, the results from which will be presented here in turn, followed by a comparison and discussion.

In this discussion reference will be made to the location of nitrate groups with respect to the zirconium 'cation'. Note that this cation may be located in a small species, such as in the zirconyl nitrate solution, or as part of a larger colloidal particle.

3.8.1 ^{14}N nuclear magnetic resonance

^{14}N NMR was used to determine how the environment of the nitrate anions change as the $Zr:NO_3$ ratio increases and the colloidal particles are formed. ^{14}N NMR spectra were measured* for the ZN2.0 zirconyl nitrate solution and the ZN1.0 sol, each at 0.2 M concentration, and are presented in Figure 3-18. The spectrum of ZN2.0 shows a single, broad peak at approximately -6 ppm, while no ^{14}N peak is detected at all in ZN1.0.

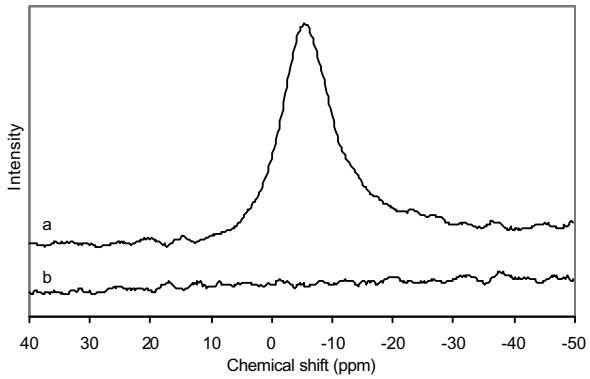

Figure 3-18: ^{14}N NMR spectra of a) ZN2.0 and b) ZN1.0.

There are two mechanisms by which the signal from the ^{14}N nuclei could 'disappear' without their actual removal from the system. The first involves a change in the molecular rotation rate

* Bruker-Spectrospin 300 DRX spectrometer. Spectra were recorded at 21.69 MHz and 27°C. The pulse width was 17.4 μs, and sweep rate 9470 Hz. Shifts were measured with respect to the position of the NH_4^+ peak at –359.6 ppm in a saturated aqueous solution of ammonium nitrate (NH_4NO_3).[7]

of the nitrate anions. For the NMR technique to characterise the chemical environment of a particular atom, the species (or sample) that it is part of must be rotating very rapidly. A 'free' nitrate anion in solution rotates rapidly enough for the ^{14}N NMR signal to be detected, but when it become strongly associated with, or bound to, a larger species then its rotation rate decreases. This decrease in rotation rate is manifested in the NMR spectrum as 'quadrupolar broadening', in which the observed peak or peaks are broadened; if the rotation rate decreases sufficiently then the corresponding peak will broaden out to be indistinguishable from the background.[25]

The second mechanism by which the NMR signal may disappear involves an increase in the NMR spin-lattice relaxation rate of the ^{14}N nucleus, which is caused by the close association of the nitrate anion with the surface of a particle.[26] If the relaxation rate is increased beyond a certain limit, then the NMR signal will no longer be detected by the instrument. Although further experiments would be able to distinguish between these two mechanisms, it is clear at this point that both involve an increased association between the nitrate anions and the zirconyl species or particles.

The above data thus shows a change in the location of at least some of the nitrate groups with respect to the zirconium cation and/or particles. In the ZN2.0 solution at least some of the nitrate groups present are spinning freely, and thus unassociated with the zirconium cations. Although quantitative measurements were not made here, a previous quantitative ^{14}N NMR study of zirconyl nitrate solution by Livage *et al.* found that only about 50% of the nitrate anions in solution were detected.[25] This means that for every zirconium atom, one nitrate anion was sufficiently close to the zirconium atom to be undetectable due to quadrupolar broadening, while the other nitrate anion was sufficiently isolated to be detected. The authors suggested that the former species was directly bound to the zirconium atom, but the evidence from Raman spectroscopy (Section 3.8.2) suggests otherwise.

When the sol particles have formed, all of the nitrate anions have their spin restricted by association with the particles. This 'association' could be either a direct bond to the surface or presence within the hydration sphere; evidence to distinguish between these options is provided in the next section by Raman spectroscopy.

3.8.2 Raman spectroscopy

The detailed Raman spectroscopy study is reported in Section 3.5, with the results relating to the nitrate anion discussed in Section 3.5.3.3. The Raman spectrum of the zirconyl nitrate solution is discussed and assigned in Section 8.3.

The Raman spectrum of the ZN2.0 solution identified two nitrate species, each with a different symmetry. The dominant nitrate species in the solution is the *fully-aquated* (ionic) species. This species possesses D_{3h} symmetry, with oxygen atoms evenly distributed around the central nitrogen atom in a triangular plane, undistorted by any nearby molecules. A minor nitrate species, with C_{2v} symmetry, is symmetrically bidentate-coordinated (chelated) to a zirconium atom.

Unlike the ^{14}N NMR results, there was very little change observed in the transition from solution to sol. The ZN1.0 sol has a very similar proportion of fully-aquated and bidentate-coordinated anions, with the former greatly outnumbering the latter.

3.8.3 Discussion

The two complementary techniques employed investigate the environment of the nitrate anions on different scales, and thus provide a fuller picture of the reactions. Raman spectroscopy shows whether nitrate anions are distorted by coordination to the zirconium atom, while ^{14}N NMR detects only nitrate anions that are outside of the hydration layer of a cation or particle.

Three generalised 'types' of nitrate anion can then be defined. Those that are sufficiently isolated from zirconium-containing cations or particles to rotate freely in solution can be regarded as being *'free*', although in practice some association is likely due to electrostatic attraction. '*Associated*' nitrate groups are located within the hydration sphere of a particle or cation and have their rotation restricted, although they are not directly bound to any cations and maintain their D_{3h} symmetry. Nitrate anions that are *'bound*' to a zirconium, probably covalently, are distorted and possess C_{2v} symmetry. The characteristics of these three types are summarised in Table 3-7 and illustrated in Figure 3-19.

Table 3-7: Types of nitrate anion observed by ^{14}N NMR and Raman spectroscopy

Nitrate type	Symmetry (from Raman)	^{14}N NMR signal
'free'	D_{3h}	6 ppm peak
'associated'	D_{3h}	no signal
'bound'	C_{2v}	no signal

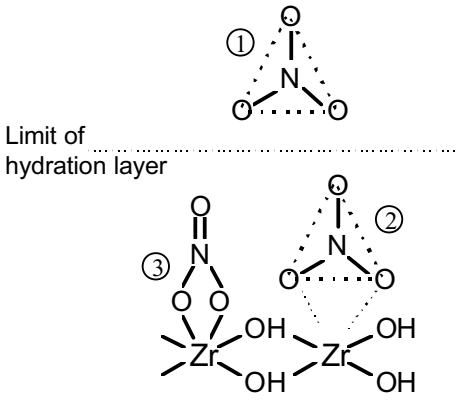

Figure 3-19: Schematic illustration of a section of zirconyl cation or particle, with the three types of nitrate anion: ① 'free', ② 'associated' and ③ 'bound'.

Using this data we can now obtain a fairly complete picture of the location of the nitrate anion with respect to the zirconium cation or colloid. The estimated relative abundance of each type of nitrate in the ZN2.0 solution and ZN1.0 sol is listed in Table 3-8, assuming that the fraction of C_{2v} 'bound' nitrate is approximately 20 %. Included in the table is the crystalline form of zirconyl nitrate, the structure of which is known from diffraction studies, and is described in Section 2.2.1.

Table 3-8: Estimated relative abundance of nitrate types.

Nitrate type	ZN2.0 zirconyl nitrate solution	ZN1.0 sol	Crystalline $Zr(OH)_2(NO_3)_2$
'free'	50 % *	–	–
'associated'	30 %	80 % †	50 % ‡
'bound'	20 % †	20 % †	50 % ‡

* From Livage *et al*.[25]
† Estimated from Raman spectrum
‡ From crystalline structure and Raman spectrum

As the colloidal particles are formed, all of the nitrate anions become either 'associated' with or coordinated to the zirconium atoms. The bound nitrate ions can be assumed to be located

entirely at the 'surface' of the particle, since from the size and shape of the particles, discussed in previous sections, just about all zirconium atoms are likely to be located at, or close to, the surface.

It is interesting to note that as zirconium carbonate is added to the solution to increase the $Zr:NO_3$ ratio from 1:2 to 1:1, the ratio of bound or associated nitrate species to zirconium atoms remains constant at 1:1.

3.9 Summary and discussion

The results presented in this chapter can now be brought together and the structures occurring in the solutions and sols discussed. The reader is also referred to the discussion of the aqueous chemistry of zirconium in Section 2.2.

Formation and structure of ZN2.0 zirconyl nitrate solution

The dissolution of one mole of zirconium carbonate in two moles of nitric acid forms a stoichiometric solution of zirconyl nitrate $Zr(OH)_2(NO_3)_2$, according to Equation 3-5.*

$$ZrOCO_3 + 2\ HNO_3 \rightarrow Zr(OH^b)_2{}^{2+} + 2\ NO_3^- + CO_2{}^{\uparrow} \qquad \textbf{Equation 3-5}$$

Zirconium is predominantly present as aquated cations containing no more than several zirconium atoms, and the SAXS study has shown that the average cation dimensions are similar to those of the 'cyclic-tetramer' structure. These cations will be referred to in this discussion as 'zirconyl' species. Each zirconium atom is connected to neighbouring zirconium atoms by four hydroxy-bridges (OH^b).

The water molecules associated with these cations hydrolyse very readily, in a reaction shown in Equation 3-6. This leads to the formation of reactive terminal-hydroxy groups (OH^t) on the cations, and a highly acidic solution.

$$\left[Zr(OH^b)_2 \cdot nH_2O\right]^{2+} \ ? \ \left[Zr(OH^b)_2(OH^t)_n\right]^{(2-n)+} + n\ H^+ \qquad \textbf{Equation 3-6}$$

According to the pH measurements, each zirconium atom in a 1 M solution is coordinated by an average of approximately one terminal hydroxy group. On a cyclic tetramer species this would lead to a cation charge of 4+.

The ^1H NMR study shows that each zirconium atom in a 1 M solution is also coordinated by one slowly-exchanging water molecule. The coordination number for zirconium in solution is usually eight, so there may be up to two further rapidly-exchanging water molecules, not detectable by ^1H NMR, to make up the coordination number (*ie* 4 OH^b + OH^t + 1 slow-ex H_2O + 2? fast-ex H_2O).

---

* Although most reactions in this discussion involve polynuclear cations, in the interests of simplicity all formula have been expressed in terms of one zirconium atom only.

A small fraction of the nitrate groups are bound to the zirconium atoms, while the remainder are located either in within (^{14}N NMR inactive) or without (^{14}N NMR active) the hydration sphere of the cations.

Reactions on addition of further carbonate

The formation of the colloidal particles from the zirconyl nitrate solution involves a complex combination of reactions. The carbonate essentially acts as a base to cause controlled polycondensation between the zirconyl species in the nitrate solution.

The additional mole of zirconium carbonate is fully dissolved in the highly acidic zirconyl nitrate solution. The decomposition of the carbonate consumes H^+ and forms more polynuclear zirconyl species, most probably with the same initial structure as the cations already present.

$$ZrOCO_3 + 2\ H^+ \rightarrow \left[Zr(OH^b)_2\right]^{2+} + CO_2 \qquad \textbf{Equation 3-7}$$

This reaction increases the pH which promotes hydrolysis of the coordinated water molecules, pushing the equilibrium of Equation 3-6 to the right. Condensation between the terminal-hydroxy groups is promoted by the increased abundance of these groups, the reduced average charge on the zirconyl species, and the increased concentration of the zirconyl species. The net result is to convert coordinated-water molecules into hydroxy bridges between zirconyl species.

$$2\left[Zr(OH)_2(H_2O)_6\right]^{2+} \rightarrow \left[(H_2O)_6Zr(OH)_2Zr\left(H_2O\right)_6\right]^{6+} + 2\ OH^- \qquad \textbf{Equation 3-8}$$

The polycondensation mechanism

Condensation of the cations continues, forming entities that are large enough to be regarded as colloidal particles. There are two main lines of evidence that clearly indicate the mechanism for polymerisation, neither of which have been previously reported. The first line is the plate-like dimensions of the particles formed, with the thickness of approximately 0.5 nm and the width 3 - 4 nm, depending on the sol concentration.

The second line of evidence is provided by an EXAFS study of the short-range structure of the air-dried gel, which is reported in Section 4.3.4. The short-range structure was found to be made up of 'sheets' of zirconium atoms, arranged in a two-dimensional square grid, and joined by double hydroxy bridges. Since there is no evidence for any chemical reactions occurring

during gelation, as discussed in Chapter 4, it is very likely that this structure is also found in the sol particles.

The probable polycondensation process can be easily illustrated if we assume that all of the initial cations present are cyclic-tetramers. These cations may condense to form an 'oligomer' cation, in which the zirconium atoms line up in a square lattice, as shown in Figure 3-20. The zirconium atoms in the center are valance-satisfied and eight-coordinated, and so are relatively unreactive and unlikely to be involved in further hydrolysis. However, the water molecules at the edges of the oligomer continue to hydrolyse, and further condensation occurs at the edges. In this way the oligomer will grow as a sheet to form plate-like particles with the short-range structure reported by EXAFS. If the zirconium atoms do not hydrolyse completely, the particles retain some positive charge. This polycondensation mechanism was first suggested by Clearfield in 1964,[16] but until now there has been very little evidence published to indicate that it actually takes place.

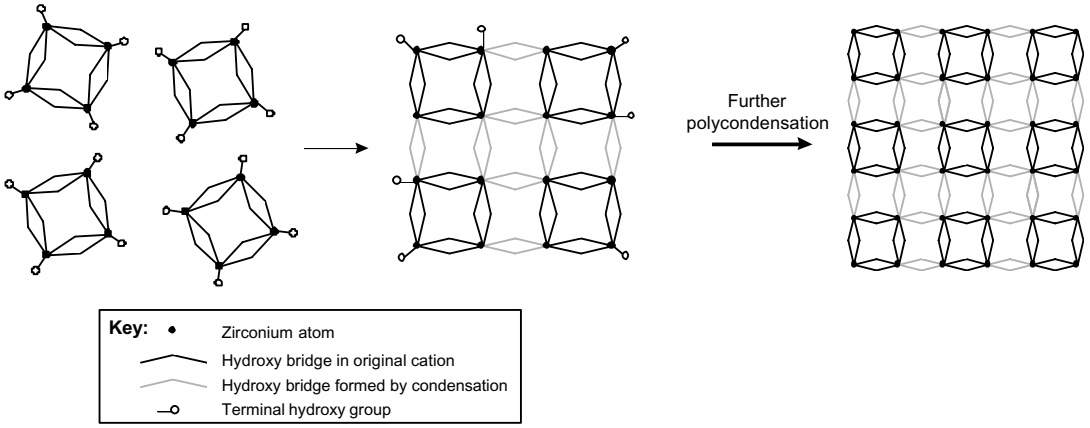

Figure 3-20: Schematic illustration of the condensation of four 'cyclic tetramers' into an oligomer, then a plate-like particle.

The scheme illustrated here is only indicative, and other processes may take place alongside the mechanism described. For instance, cyclic-tetramer cations may not necessarily polymerise in the ordered structure illustrated above, leading to disruptions in the two-dimensional lattice. Further disruptions would be caused by the addition of zirconyl monomers, dimer, *etc*. to the growing oligomer, or the joining of two growing oligomers.

The only previously-reported evidence for a similar mechanism is in the TEM study of precipitates from zirconyl chloride solution by Fryer *et al*.[27] The transmission images of these

precipitates gave evidence for a very thin, coherent, amorphous film, consisting of structural units 5-10 Å in diameter. See Section 2.2.3 for a further discussion.

Calculations, based on the reported size of the particles and a Zr–Zr spacing of 0.354 nm, indicate that there are approximately 50 zirconium atoms in each two-dimensional 'sheet' for the 1 M sol, and approximately 100 zirconium atoms for the 0.2 M sol. Each particle may contain, on average, one or two such sheets. These sheets would be largely bound by hydrogen-bonds between hydroxy-groups in adjacent layers. Some direct bonding, via hydroxy groups, is also possible between the layers.

The hydroxy-bridges in the particle are not identical to those in the tetramer and smaller zirconyl cations, as is shown by the Raman spectroscopy study. In the tetramer the zirconium atom is restrained on only two sides, whereas in the two-dimensional lattice it is restrained on all four sides. This will naturally lead to different Zr–O bond lengths and vibrational frequencies.

The extent of the reaction, and the size of the particles, is limited by the pH in two ways. Firstly, the polymerisation reaction is driven by the 'additional' zirconium dissolved in the solution from the carbonate, which in turn is limited by the maximum pH at which the carbonate dissolves. Secondly, the pH also controls the hydrolysis and formation of reactive terminal-hydroxy groups. The actual location of these limits has not been investigated in detail, although sols with $Zr:NO_3$ ratios of up to 1.3:1 have been prepared.

The rate-limiting reaction in the polymerisation process is most probably the decomposition of the zirconium carbonate. Because this is a relatively slow reaction, and the carbonate is evenly dispersed in the solution as it decomposes, the hydrolysis and polycondensation reactions also occur homogenously through the solution, so that colloidal particles are formed instead of a hydroxide gel precipitating out of solution.

Overall structure of the particle

A small fraction of the nitrate species are directly bound to zirconium atoms on the surface of the particles. The remainder act as counter ions to the charged particles, located within the hydration layer. Water molecules are likely to be coordinated to at least some of the zirconium atoms, particularly those at the edge, but the absence of a characteristic ^1H NMR spectrum

means that any such molecules must be rapidly exchanging with their surroundings. Surrounding the particle is an approximately 0.3 - 0.5 nm hydration layer, associated with the electrical double-layer around the particle, that moves with the particle in Brownian motion. These features are shown schematically in Figure 3-21.

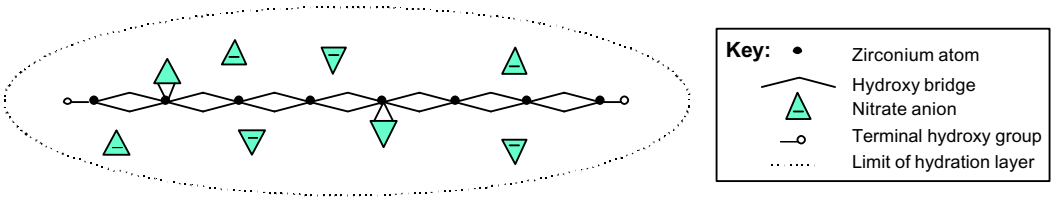

Figure 3-21: Schematic cross-section of a typical particle in the sol.

Reaction on dilution

The increase in the width of the particles with dilution of the sol, observed by SAXS, is fully explained by the polymerisation mechanism described above. The increase in particle size with dilution is attributed to the accompanying rise in pH. This promotes the formation of more terminal-hydroxy groups at the edges of the particles, and further condensation at the edges, either with residual zirconyl cations or other particles.

In opposition to the rise in pH, the dilution of the sol increases the separation of the particles, and so should *decrease* the tendency to aggregate by electrostatic forces. Thus the electrostatic driving force to aggregation is decreased while the chemical driving force is increased. This may cause particles that consist of two or more sheets, bound either by hydrogen-bonds or van der Waal's forces, to split apart, leading to the slight decrease in average thickness with dilution found by the SAXS study.

Stability mechanisms

The mechanisms by which the colloidal particles are stabilised have not been investigated in this thesis, but we will briefly discuss them here.

According to conventional colloid-stability theory, colloids of this size in solution containing 1 M electrolyte are most unlikely to repel each other sufficiently to remain dispersed. One of the reasons is the 'screening' of the repulsive charge surrounding the particles by the electrolyte in the intervening solution. However, it is important to note that the ^{14}N NMR shows that there is no significant number of nitrate anions that are isolated from the particles;

all ions are present within the electrical 'double-layer' around the particles, and the liquid between the particles is essentially pure water. This may allow the charged double-layers around each particle to repel each-other sufficiently to oppose the attractive van der Waals forces.

A more detailed discussion would require the calculation of the interaction potentials between the particles. The conventional approach would use the standard Deryagin-Landau-Verwey-Overbeek (DLVO) theory, but the calculation of the double-layer interaction energies would be difficult, and lie outside the scope of this thesis. Firstly, the Stern potential at the particle surface and the Hamaker constant for the van der Waals forces are unknown, and secondly, conventional calculations for the double-layer interaction-energies assume a finite concentration of electrolyte in the surrounding solution.

Ageing

Once formed, the size and shape of the colloidal particles are fairly stable. None of the characterisation techniques discussed in this chapter have detected any significant changes in structure during ageing of the primary particles over periods ranging between one day to over a year. There is some increase in the volume of particles with sizes of 10 - 20 nm, but these particles do not make up more than 3 vol % of the total particles.

It would thus be easy to claim that no ageing effects occur take place. However, Chapters 4 and 5 describe a number of effects that are strongly connected to the ageing of the sol, attributed to the way that the particles pack together during gelation. This effect is discussed further in the relevant chapters.

3.10 Conclusions

The conclusions from this chapter are:

1. The highly acidic zirconyl nitrate solution, prepared by dissolving zirconium carbonate in nitric acid, contains aquated, partially-hydrolysed 'zirconyl' cations, similar in size to the 'cyclic-tetramer' previously reported.
2. The addition of further carbonate to the zirconyl nitrate solution causes condensation reactions between the 'zirconyl' cations, leading to the formation of plate-shaped, nanoscale particles in a stable dispersion. Growth of these particles occurs at the edge of the plates. This mechanism has not been previously shown to occur in zirconyl solutions.
3. The nitrate anions are all closely associated with the particles, although most anions are not directly bound to them. The absence of any anions in the solution between the particles may play a role in the stabilisation of the sol.
4. None of the characterisation techniques discussed in this chapter have detected any significant changes in the size or shape of the primary particles over ageing periods ranging between one day to over a year.

3.11 References

1. J.L. Woodhead, "Sol-gel process to ceramic particles using inorganic precursors" *J. Mater. Ed. 6* 887-925 (1984)
2. J.L. Woodhead, *Improvements in or relating to Zirconium Compounds*, United Kingdom Patent No. 1,181,794 (18th Feb., 1970).
3. E. Sizgek, J.R. Bartlett and M.P. Brungs, "Production of titanate microspheres by sol-gel and spray-drying" *J. Sol-Gel Sci. Tech. 13* 1011-1016 (1998)
4. W. Zhang and F.P. Glasser, "Condensation and gelation of inorganic ZrO_2-Al_2O_3 sols" *J. Mater. Sci. 28* 1129-1135 (1993)
5. W. Zhang and F.P. Glasser, "The preparation of Al_2O_3-ZrO_2 sol-gels from inorganic precursors" *J. Eur. Ceram. Soc. 11* 143-147 (1993)
6. J.-L. Tosan, B. Durand, M. Roubin, F. Chassagneux, L. Mosoni, F. Bertin and B. Moraweck, "pH-metric and Raman investigations of zirconium aqueous solutions and gels submitted to a reflux" *J. Non-Cryst. Sol. 160* 167-176 (1993)
7. *Multinuclear NMR*, Edited by Joan Mason, Plenum Press, New York (1987) 336
8. M. Åberg and J. Glaser, "^{17}O and ^{1}H NMR study of the tetranuclear hydroxo zirconium complex in aqueous solution" *Inorg. Chim. Acta 206* 53-61 (1993)
9. S. Hannane, F. Bertin and J. Bouix, "Etude de l'hydrolyse de Zr(IV) par spectrométrie Raman et RMN du proton. I. Mise en évidence et formation des espèces en solution" *Bull. Soc. Chim. Fr. 127* 43-49 (1990)
10. K.I. Arsenin, L.A. Malinko, I.A. Sheka, I. Ya Pishchai and A.N. Antishko, "The ^{1}H NMR spectra of aqueous solutions of zirconium and hafnium hydroxide chlorides" *Russ. J. Inorg. Chem. 36* [10] 1496-1500 (1991)
11. R. Claude and D. Vivien, "Solvation de sels de zirconium en solution aqueuse. Étude RMN" *Bulletin de la Société Chimique de France* (1974) [1-2] 65-66 (in French)
12. G.E. Walrafen, "Raman and infrared spectral investigations of water structure", Chapter 5 in *Water: A Comprehensive Treatise*, Edited by F. Franks, Plenum Press, New York (1972)
13. S. Hannane, F. Bertin and J. Bouix, "Etude de l'hydrolyse de Zr(IV) par spectrométrie Raman et RMN du proton. II. Influence de l'acidité et du vieillissement des solutions sur les proportions des espèces formées" *Bull. Soc. Chim. Fr. 127* 50-56 (1990)
14. L.M. Sharygin, V.M. Galkin, S.M. Vovk and A.V. Korenkova, *Colloid Journal of the USSR 47* 95-99 (1985)
15. K.A. Burkov, G.V. Kozhevnikova, L.S. Lilich and L.A. Myund, "The vibrational spectra of the tetrameric hydroxo -complex of zirconium (IV)" *Russ. J. Inorg. Chem. 27* [6] 804-802 (1982)
16. A. Clearfield, "Structural aspects of zirconium chemistry" *Rev. Pure and Appl. Chem. 14* 91-108 (1964)
17. K. Matsui, H. Suzuki, M. Ohgai and H. Arashi, "Raman spectroscopic studies on the formation mechanism of hydrous-zirconia fine particles" *J. Am. Ceram. Soc. 78* [1] 146-152 (1995)
18. K. Nakamoto, *Infrared and Raman spectra of inorganic and coordination compounds*, 4th Edition, Wiley-Interscience, New York (1986)
19. G.V. Kozhevnikova, L.A. Myund and K.A. Burkov, "Raman spectra of zirconium oxyxhloride crystalline hydrate and solutions" *Izvestiya Akademii Nauk SSSR, Neorganicheskie Materialy 24* [3] 470-473 (1988)
20. A. Singhal, L.M. Toth, J.S. Lin and K. Affholter, "Zirconium(IV) tetramer/octomer hydrolysis equilibrium in aqueous hydrochloric acid solution" *J. Am. Chem. Soc. 118* [46] 11529-11534 (1996)
21. L.M. Toth, J.S. Lin and L.K. Felker, "Small-angle X-ray scattering from zirconium(IV) hydrous tetramers" *J. Phys. Chem. 95* 3106-3108 (1991)
22. A. Singhal, L.M. Toth, G. Beaucage, J. Lin and J. Peterson, "Growth and structure of zirconium hydrous polymers in aqueous solutions" *Journal of Colloid and Interface Science 194* 470-481 (1997)
23. J.A. Jutson, R.M. Richardson, S.L. Jones and C. Norman, "Small angle X-ray scattering studies of polymeric zirconium species in aqueous solution" *Mat. Res. Soc. Symp. Proc. 180* 123-128 (1990)
24. NICOMP Model 370 Submicron Particle Sizer Instruction Manual, Pacific Scientific Instrument Division (1987)

25. J. Livage, M. Chatry, M. Henry and F. Taulelle, “Complexation of Zr(IV) precursors in aqueous solutions” *Mat. Res. Soc. Symp. Proc 271* 201-212 (1992)
26. I.S. Pronin and A.A. Vashman, “^{14}N nuclear magnetic relaxation in aqueous and nitric acid solutions of zirconium nitrate” *Russ. J. Inorg. Chem. 32* [3] 338-341 (1987)
27. J.R. Fryer, J.L. Hutchison and R. Paterson, “An electron microscopic study of the hydrolysis products of zirconyl chloride” *J. Colloid Interface Sci. 34* [2] 238-248 (1970)

4. Structure of the gel

4.1 Introduction

The gel is an important stage in the sol-gel-oxide process. Studying the gel structure gives us a range of information on the structure and properties of the sol particles, and the processes that take place during gelation. A knowledge of the structure of the gel also gives us a starting point for understanding the thermal decomposition and crystallisation reactions.

Two main kinds of structural information are studied in this chapter. Firstly, the short-range structure of the particles has been investigated. Since the structure of the particles is not affected by the physical gelation process, it is much more convenient to study their structure in the 'solid state' rather than in the sol. Secondly, the arrangement of the particles in the gel has been studied.

As is the case throughout this thesis, a detailed study of the structure of the gel requires a range of complimentary characterisation techniques. Elemental analysis is useful for confirming the composition of the gel. X-ray absorption spectroscopy, in particular the extended X-ray absorption fine structure (EXAFS) technique, has played a critical role in determining the short-range structure of the gel. Raman spectroscopy also provides information on the short-range structure, and is particularly useful for comparing the gel with the sol and examining the coordination of the nitrate groups. X-ray diffraction and small-angle scattering provide further information on the structure of the gel, covering a length scale from several Ångstroms to tens of nanometres.

4.2 Procedure

Air-dried gels were prepared by evaporation of most of the water in the sol. Small amounts of standard ZN1.0 sols were placed in a glass dish and left under an air-flow for several days, to produce a hard, brittle and transparent solid. A range of ZN1.0 sols were dried, with concentrations ranging between 1 and 3 M, and aged for periods up to 50 months. A ZN2.0 zirconyl nitrate solution was also dried by the same method, to form a hard, brittle and opaque solid.

The ability of a gel to disperse in water and ethanol was tested by adding a small quantity of the ground gel to a few mL of water. Dispersal was characterised by the disappearance of the gel in the liquid, and re-gelation upon evaporation of the liquid.

Samples from a number of standard ZN1.0 gels were analysed for carbon, nitrogen and hydrogen content.[*] Zirconium content was measured by weighing a sample before and after calcination at 950°C for two hours, and assuming that it was pure ZrO_2. The oxygen content was calculated from the zirconium, nitrogen and hydrogen content, assuming that the composition can be described in terms of $a(ZrO_2)\cdot b(HNO_3)\cdot c(H_2O)$.

The short-range structure around the zirconium atoms in the ZN1.0 gel was characterised by extended X-ray absorption fine structure (EXAFS) spectroscopy. EXAFS spectra were measured between 10 and 290 K, and full details of the sample preparation, equipment, data collection and data treatment are given in Chapter 10. The short-range structure was determined by comparing the measured EXAFS spectrum with a model, and this procedure is also discussed fully in Chapter 10.

Portions of all dried samples were ground finely, and the powder diffraction pattern measured.[†] Peak positions were determined with a peak-fitting routine.[‡]

---

[*] C-H-N microanalysis performed using a Carlo Erba Elemental Analyser (Model 1106) at the Research School of Chemistry, Australian National University. Accuracy of results was ± 0.3 % absolute.

[†] Two diffractometers were used, a Siemens Kristalloflex D500 using Co K_α radiation, and a Scintag X1 Advanced Diffraction System using Cu K_α radiation. All low-angle ($2\theta < 15°$) measurements used the Scintag with a narrowed divergence slit to increase resolution.

[‡] Peak-fitting routing from *Grams/32*, Galactic Industries Corporation.

The Raman spectra of selected gel samples was measured at room temperature.[*] The Raman spectra of a ZN1.0 gel and ZN2.0 solid were also measured at –195°C in a cooling stage.[†]

The small-angle X-ray scattering (SAXS) profile of the ZN1.0 gel was measured.[‡] The sample was ground finely and loaded into a 0.3 mm capillary. The scattering profile of the sample and capillary was recorded, then the powder was removed from the capillary, the capillary rinsed several times, and filled with water. The scattering profile from the water-filled capillary was used as the background profile.

---

[*] Bio-Rad FT-Raman II, using an excitation line of 1064 nm from a Nd:YAG laser. The effective resolution was 4 cm^{-1}.

[†] Linkam (UK) FTIR 600 heating-cooling stage. Approximately 20 mg of sample was held in a shallow platinum tray on a silver heating block. A thermocouple was embedded in the block immediately underneath the tray.

[‡] SAXS instrument with a focussed Cu K_α incident beam and a 0.9 m Huxley-Holmes camera, at the Research School of Chemistry, Australian National University. This instrument is described in more detail in Section 9.3.

4.3 Results and discussion

4.3.1 Dispersibility

The ZN1.0 gel dispersed in water over a period of several minutes, and in ethanol over a period of several hours. There was no evident ageing effect on dispersibility, and even gels that were over two years old readily dispersed in water. This clearly shows that no irreversible chemical reactions occur in the gelation of the sol, such as condensation between particles, and that gelation is largely a physical process.

4.3.2 Chemical composition

The 'oxide' content of a standard ZN1.0 gel was typically between 55 and 60 wt %, depending on the water content. From the zirconium, carbon, nitrogen and hydrogen analysis of samples of a range of gels, a typical composition can be expressed as $ZrO_2 \cdot 0.9(HNO_3) \cdot 2.2(H_2O)$.* According to this composition, nitrate groups make up more than a quarter (28 %) of the mass of the gel. The approximately 18 wt % 'H_2O' includes bridging and terminal hydroxy groups, any oxo bridges, as well as water molecules. It is estimated from the proposed structure for the colloidal particles (see Section 4.3.4) that just over half of this mass, approximately 10 wt %, is composed of water molecules.

As expected, the elemental analysis found no carbon present in the gel. This result confirms that the zirconium carbonate decomposes completely when dissolved in the zirconyl nitrate solution.

* Despite the high precision of the measurements, the weight percentage for each element summed to only approximately 95 %, and so these values can only be quoted to single significant figure. The reasons for this discrepancy were investigated but no particular cause was identified. The value of microanalysis is therefore limited until this problem is rectified.

4.3.3 Raman spectra

A typical Raman spectrum of a ZN1.0 gel is shown in Figure 4-1. This spectrum did not change significantly with the age or concentration of the sol before gelation, nor with the age of the gel. Three other Raman spectra are given for comparison. The spectrum of the ZN1.0 sol is given in Figure 4-2, and is assigned in Section 3.5. Figure 4-3 shows the Raman spectrum of the crystalline material dried from a ZN2.0 solution. This material has been identified as $Zr(OH)_2(NO_3)_2 \cdot 5H_2O$ from its XRD pattern in Section 4.3.5, and its Raman spectrum is assigned in Section 8.3.

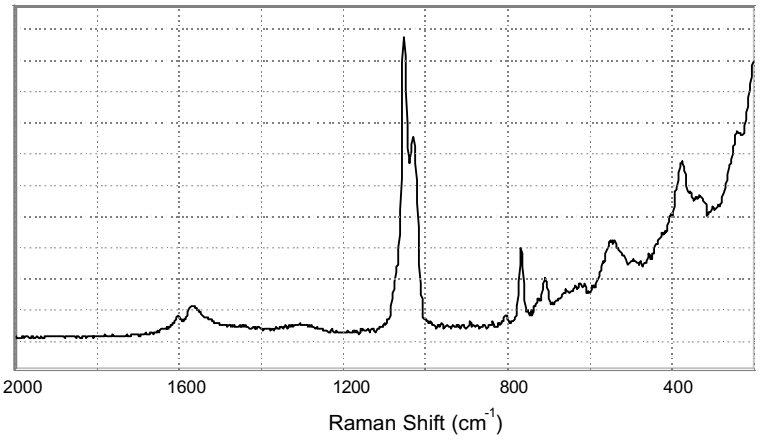

Figure 4-1: Raman spectrum of a ZN1.0 gel.

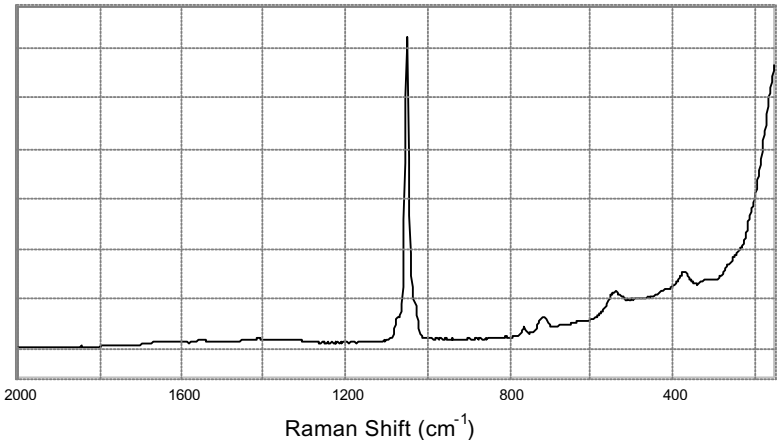

Figure 4-2: Raman spectrum of a ZN1.0 sol.

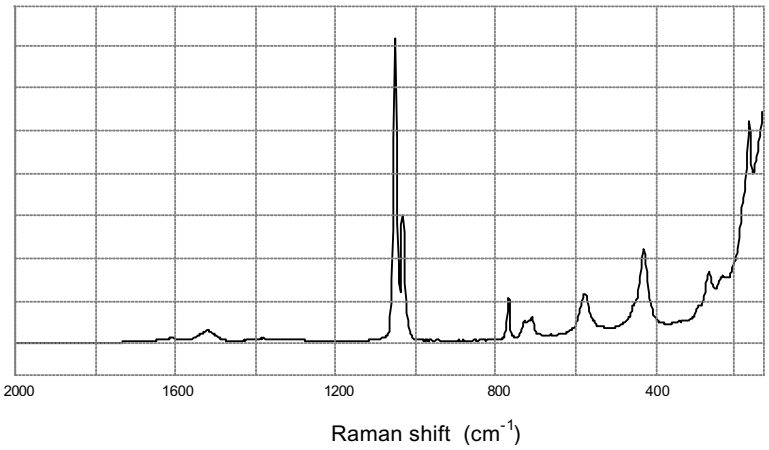

Figure 4-3: Raman spectrum of crystalline $Zr(OH)_2(NO_3)_2 \cdot 5H_2O$

The bands assigned to the vibrations of the Zr–O bonds are below 650 cm^{-1}. A comparison of the spectra for the sol and gel shows little difference in the position or relative intensity of the bands in this region. This indicates that no significant change occurs in the Zr–O bonding of the sol particles during gelation. The main bands at 375 and 545 cm^{-1} are more distinct after gelation, due to the reduction of the water 'background' and the absence of the 450 cm^{-1} band from the glass vial containing the sol (these 'background' features are discussed in Section 3.5.3.1). Shoulders at approximately 240 and 320 cm^{-1} have become clearly defined. The assignments for these latter two bands are uncertain, but they are at appropriate frequencies for lattice modes and only a detailed knowledge of the short-range structure would allow specific assignments to be made.

The major difference in the Raman spectra of the sol and the gel is due to a large fraction of the nitrate species changing from the 'undistorted' D_{3h} symmetry to the 'distorted' C_{2v} symmetry of the bidentate-coordinated nitrate. The bands at 715, 1050 and 1415 cm^{-1} (the latter being quite weak) assigned to the species with D_{3h} symmetry become much less intense with gelation, while the 766, 1030, 1300 and 1565 cm^{-1} bands assigned to the species with C_{2v} symmetry increase in intensity. The 1050 cm^{-1} band, the most intense for the species with D_{3h} symmetry, is reduced to approximately 25 % of the original intensity with respect to the bands below 650 cm^{-1}. Referring to the model presented in Section 3.8, this change can be described as the D_{3h} 'associated' nitrated groups, located in the hydration layer surrounding the particles, becoming directly coordinated to zirconium atoms at the surface of the particles and adopting C_{2v} symmetry. The unassigned band at 1072 cm^{-1} remains relatively constant in intensity with respect to the bands below 650 cm^{-1}.

The relative abundance of nitrate species with D_{3h} and C_{2v} symmetry in the gel is difficult to determine accurately from the Raman spectrum, due to the different Raman-activity for each mode of each species. For instance, the 1050 cm^{-1} band for the D_{3h} 'undistorted' species is much more intense, with respect to the abundance of the species, than the 1030 cm^{-1} band of the C_{2v} bidentate-coordinated species.[1] However, a good estimate of the relative abundance can be obtained by comparing the Raman spectra of the ZN1.0 gel and the $Zr(OH)_2(NO_3)_2 \cdot 5H_2O$ crystalline salt. From studies of the diffraction pattern, discussed in Section 4.3.5, the nitrate anions in the salt are known to be evenly divided between D_{3h} 'undistorted' and C_{2v} bidentate-coordinated species. The ratio of the peak areas (determined by peak-fitting) of the 1050 and 1030 cm^{-1} bands in the spectrum of $Zr(OH)_2(NO_3)_2 \cdot 5H_2O$ is 63:37, while the corresponding ratio for the ZN1.0 gel is very similar at approximately 60:40. This shows that the nitrate species in the gel are also close to evenly divided between 'associated' and coordinated nitrate groups.

Another point to note is that the Raman bands in the spectrum of the ZN1.0 gel are considerably broader than those in the spectrum of the $Zr(OH)_2(NO_3)_2 \cdot 5H_2O$ crystalline salt, for bands assigned to both the Zr–O bonds and the nitrate groups. The frequency at which an interatomic bond or species vibrates is dependent on the energy or length of the vibrating bonds. A broad Raman band indicates that the bonds in question do not all vibrate at the same frequency, an indication of inhomogenous bond lengths and short-range disorder. This disorder can be due to thermal vibration, which increases with temperature, or static variations in the structure. The Raman spectra of a ZN1.0 gel and the crystalline salt were measured at –195°C to minimise the thermal disorder component, and hence distinguish between the two types of disorder. The bands in the spectrum of the salt were substantially narrower at low temperature, particularly for those bands below 650 cm^{-1}, but those in the spectrum of the gel did not change at all. This clearly shows that the disorder of the Zr–O bonds in the gel is predominantly *static* rather than thermal. This result is confirmed by the disorder parameters for the Zr–O distance from the EXAFS study in Section 4.3.4.

4.3.4 Extended X-ray absorption fine structure

Extended X-ray absorption fine structure (EXAFS) spectroscopy is a technique that reveals the average local structure around the atoms of a certain element in a material. The EXAFS spectrum for a ZN1.0 gel was recorded at 10, 80, 180 and 290 K. A full discussion of the EXAFS results can be found in Chapter 10. In this section the main results are presented, along with a discussion of their significance.

A useful way to graphically display the information in the EXAFS spectrum is to Fourier-transform the spectrum, to produce a profile herein referred to as the 'FT'. The FT is effectively an average *pseudo-radial distribution function* of the atoms surrounding each zirconium atom. It generally consists of a series of peaks, each representing a group of atoms roughly the same distance from the 'central' zirconium atom. The position of each peak in the FT is equal to the interatomic distance, r, shifted by a phase shift, α, while the width and intensity is determined by the number and type of the surrounding atoms, their distribution, disorder, etc. The FT for the ZN1.0 gel is shown in Figure 4-4. The first peak, at approximately 1.6 Å, is assigned to the 'nearest-neighbour' oxygen atoms immediately adjacent to the zirconium atom. The peaks at 3.2 and 4.7 Å are largely due to nearby zirconium atoms. Oxygen atoms scatter X-rays weakly, and those that are greater than 2 Å from the central zirconium atom make little contribution to the EXAFS spectrum.

Much further information can be obtained by fitting the EXAFS spectrum with a model. A 'one-dimensional' model is postulated, consisting of a central atom (in this case zirconium) surrounded by 'groups' or *shells* of N atoms of a particular element, at a certain distance r. The number or atoms in a shell is also referred to as the *coordination number*. The variance (assuming a Gaussian distribution) in r for each shell is σ^2, which represents the *thermal or structural disorder*. It can also be regarded as the mean square relative-displacement of the atoms in the shell from the central zirconium atom. The σ^2 parameter is comprised of a static (structural) component, σ^2_{stat}, which remains constant with temperature, and a vibrational (thermal) component, which increases approximately linearly with temperature. The dependence of the vibrational component on temperature can be modelled by one of a number of models, the most frequently used being the Einstein-correlated model, and the Debye-correlated model. For both of these models, the dependence of the vibrational component on temperature is determined by a constant θ, known as the Debye or Einstein temperature, θ_D or

θ_E. A high value of θ (*eg* > 600 K) indicates a small vibrational component, while a low value indicates a large vibrational component. For this work the Einstein model has been used for oxygen shells, while the Debye model has been used for zirconium shells. A more complete treatment of these models can be found in Section 10.2.4.

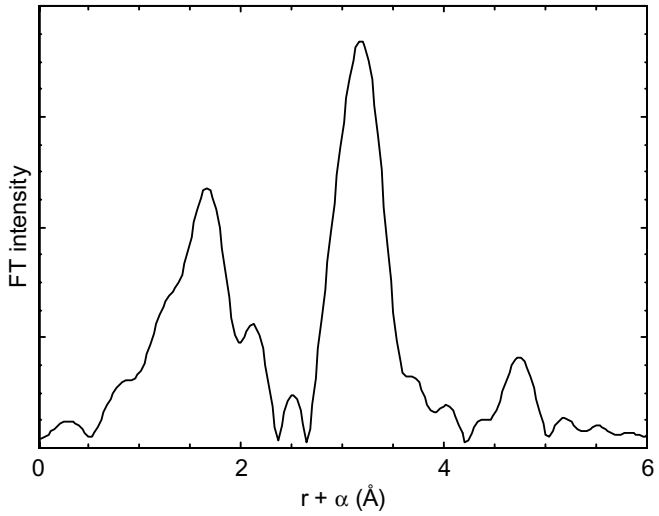

Figure 4-4: Fourier-transformed EXAFS spectrum of a ZN1.0 gel, measured at 10 K.

The theoretical EXAFS spectrum is predicted from the postulated structure, and compared with the experimental spectrum. The model is then recursively adjusted to achieve the 'best fit' between the theoretical and experimental spectra. The refined structural model should then be indicative of the average short-range structure around the zirconium atom.

The EXAFS spectrum of the ZN1.0 gel was best described by a model in which each zirconium atom is coordinated by two 'shells' of oxygen atoms as nearest neighbours, and two shells of zirconium atoms at a further distance. The modelled interatomic distances, coordination numbers and disorder parameters for each shell are listed in Table 4-1. The temperature dependence of the disorder parameter, σ^2, is shown in two different ways. First, values of σ^2 are listed for measurements made at 10 and 290 K, and second, the σ^2_{stat} and θ values are also given. From these parameters the short-range structure of the particles in the gel has been determined.

Table 4-1

Shell	Distance from Zr atom (Å)	Coordination number	σ^2_{10K} ($Å^2\times10^{-3}$)	σ^2_{290K} ($Å^2\times10^{-3}$)	σ^2_{stat} ($Å^2\times10^{-3}$)	$\theta^{\dagger}$ (K)
O1	2.106(9)	7.6(6)	11(2)*	12(2)*	8.5(1.3)*	700(200)*
O2	2.579(14)	4.2(6)	11(2)*	12(2)*	8.5(1.3)*	700(200)*
Zr1	3.539(3)	3.8(2)	3.6(3)	5.6(3)	1.9(3)	470(20)
Zr2	4.995(9)	1.9(8)	5(2)	8(2)	3(2)	380(100)

Note: The uncertainty in the last one or two digits is indicated in parentheses.

* Disorder parameters for O1 and O2 were set to be equal to reduce the number of modelling parameters. See comments in Section 10.3.2.

† The Einstein-correlated model was used for the oxygen shells, and the Debye correlated model for the zirconium shells.

The parameters for the zirconium shells indicate the nature of the Zr–Zr framework. Each zirconium atom is coordinated by approximately four other zirconium atoms at a distance of 3.54 Å. The next shell of zirconium atoms is at 5.00 Å, which is exactly $\sqrt{2}$ times the first-shell distance. *This is strong evidence that the zirconium atoms are positioned in a square, two-dimensional lattice*, in which the Zr–Zr distance for the second shell of zirconium atoms represents the 'diagonal' distance across the 'square', as shown in Figure 4-5.

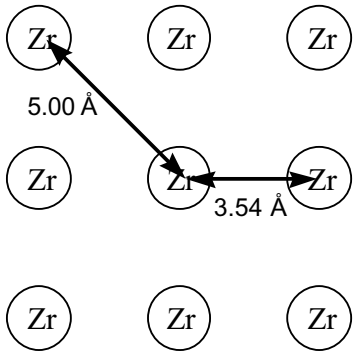

Figure 4-5: Schematic illustration of the arrangement of Zr atoms in a square lattice.

The σ^2 values for the zirconium shells, which are much lower than σ^2 for the oxygen shells, are very similar to the corresponding values for phases of crystalline zirconia (see Section 10.3.7). This indicates that there is relatively little static disorder in the overall lattice structure. Another point to note is that if the Zr atoms are in a square lattice, then σ^2_{stat} for the second Zr shell should be approximately *twice* σ^2_{stat} for the first Zr shell.

Another important question to resolve was the nature of the zirconium-oxygen-zirconium bonds. Double hydroxy-bridges Zr–$(OH)_2$–Zr are known to predominate in the aqueous

precursor solutions. The Raman spectroscopy study in Section 3.5 has identified the 'symmetric' vibration of double hydroxy-bridges in the sols, and the characteristic Raman peaks are largely unchanged in the spectrum of the gel, as discussed in Section 4.3.3. However, measuring bond lengths and coordination numbers by EXAFS is a more direct method of identifying the type of bonding. There are two pieces of evidence that are useful. Firstly, to satisfy valency, a zirconium atom can be coordinated by either eight bridging hydroxy groups, four terminal hydroxy groups, four oxo bridges, eight oxygen atoms from four bidentate-nitrate groups, or a weighted combination of these. The coordination number of 7.6(6) for the first oxygen shell indicates that hydroxy bridges predominate, and allows for the presence of coordinated-nitrate groups. Secondly, where zirconium atoms are joined by *double* hydroxy bridges, as opposed to single hydroxy bridges, each Zr–O(H)–Zr bond must be at a considerable angle to keep the hydroxy groups separated. As a result, each Zr–O(H) distance is considerably greater than half of the Zr–Zr distance. This is also supported by the modelled bond lengths. Thus we can assign the first modelled shell of oxygen atoms largely to bridging hydroxy groups between neighbouring zirconium atoms.

The presence of coordinated nitrate will also contribute oxygen atoms to the first shell. The Raman study in Section 4.3.3 has shown that approximately 0.5 nitrate groups per zirconium are directly bidentate-coordinated to zirconium atoms, thus an average of one oxygen atom out of the approximately eight observed will belong to a nitrate group.

The disorder parameters for the oxygen shells are much larger than those for the zirconium shells, and a comparison of σ^2 for 10 and 290 K shows that this disorder is dominated by the *structural disorder* component. This disorder is caused by a range of Zr–O bond lengths, with an *average* variation of ± 0.05 Å. At least part of this structural disorder is attributed to the different kinds of oxygen-containing species that are coordinated around the zirconium atom, each with its own equilibrium Zr–O bond-length.

A structural model can now be proposed, in which zirconium atoms are arranged in a square lattice, each connected by double hydroxy-bridges. A 'perfect' lattice would have a stoichiometric formula of approximately $Zr(OH)_4$, with each zirconium atom coordinated by eight oxygen atoms, four nearest zirconium atoms, and four more zirconium atoms at the diagonal distance as illustrated in Figure 4-6 and Figure 4-7. Sheets of this zirconium hydroxide may be stacked together to form particles, and would be coordinated by water molecules and nitrate groups.

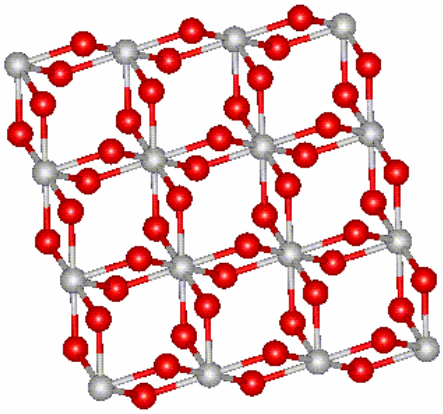

Figure 4-6: 'Ball & stick' representation of an ordered $Zr(OH)_4$ sheet. Grey circles = Zr; Red circles = OH.

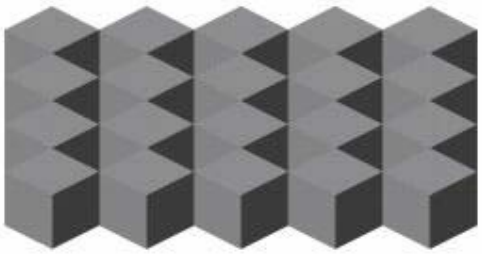

Figure 4-7: Polyhedral representation of an ordered $Zr(OH)_4$ sheet, showing how the cubic ZrO_8 octahedra are arranged.

The second 'oxygen' shell, at a distance of 2.58 Å from the central atom, could be assigned to hydroxy groups in adjacent layers, coordinated water molecules, or nitrogen atoms in the coordinated nitrate groups; probably a combination of all three.

In practice this sheet structure is not perfect, as evidenced by the lower-than-expected coordination numbers. Note that the difference between measured and predicted coordination numbers increases with distance from the central atom. This is most likely due to the small size of the $Zr(OH)_4$ sheets, since zirconium atoms at the edge have a reduced number of zirconium neighbours[*]. There may be other structural reasons for lower than expected coordination numbers. Any vacancies or disruption of the lattice would decrease the measured coordination number, and any fraction of oxo bridges would decrease the average number of oxygen neighbours.

The nearest *known* structure to that proposed is the cyclic-tetramer cation, $[Zr_4(OH)_8{\cdot}16H_2O]^{8+}$, described in Section 2.2.1, which should have similar distances for Zr–O(H), Zr–$(OH)_2$–Zr, and the diagonal Zr–Zr pair. The tetramer exists as a discrete cation in crystalline $Zr(OH)_2Cl_2$,[2] and interatomic distances from diffraction measurements are compared with the modelled distances in Table 4-2. Small differences in interatomic distances

[*] In principle it would be possible to calculate the average size of the sheets from the coordination numbers, but in practice the uncertainties are too large, and best left to other techniques such as SAXS (see Chapter 9).

can be expected between the tetramer, bound by chloride ions into an ionic crystal, and a continuous $Zr(OH)_4$ lattice. This is consistent with the observed change in the vibrational frequencies for the Zr-O bond during the formation of the sol particles.

Table 4-2

	modelled interatomic distance (Å)	interatomic distance for $Zr(OH)_2Cl_2$ (Å), from Mak[2]
Zr–O(H)	2.106(9)	2.14*
Zr–O(H_2)	2.58(2)	2.27*
Zr–Zr (1st neighbour)	3.539(3)	3.558
Zr–Zr (diagonal)	4.995(9)	5.03

*averaged values

The $Zr(OH)_4$ structure identified in the gel is very similar to a model proposed by Clearfield,[3] who suggested that the ordered polymerisation of $[Zr_4(OH)_8{\cdot}16H_2O]^{8+}$ cyclic-tetramer species would form a two dimensional $Zr(OH)_4$ sheet. However, *until now there has been no conclusive evidence for its existence*. An ambient-temperature EXAFS study of an amorphous zirconia precursor by Turrillas *et al*. found similar interatomic distances for the first shells of oxygen and zirconium that were consistent with a partially oxolated version of this structure,[4] *but did not find the characteristic 5.0 Å Zr–Zr diagonal distance*. This diagonal distance has only been reported once before, in a EXAFS study of an inorganic sol with a $Zr:NO_3$ ratio of 1:1,[5] but very little detail accompanied this report. *The results presented here provides the first detailed evidence for the occurrence of $Zr(OH)_4$, in a square, two-dimensional lattice.*

4.3.5 X-ray diffraction pattern of zirconyl nitrate

The X-ray diffraction pattern of the solid material dried from the ZN2.0 solution, shown in Figure 4-8, corresponded to the pattern reported for $Zr(NO_3)_2(OH)_2{\cdot}5H_2O$, or more precisely $Zr(OH)_2(NO_3)_2{\cdot}(4+x)H_2O$ ($x \leq 1$), as one of the lattice water sites may be vacant. This structure was recently solved from the powder diffraction pattern by Bénard, Louër and Louër.[6]

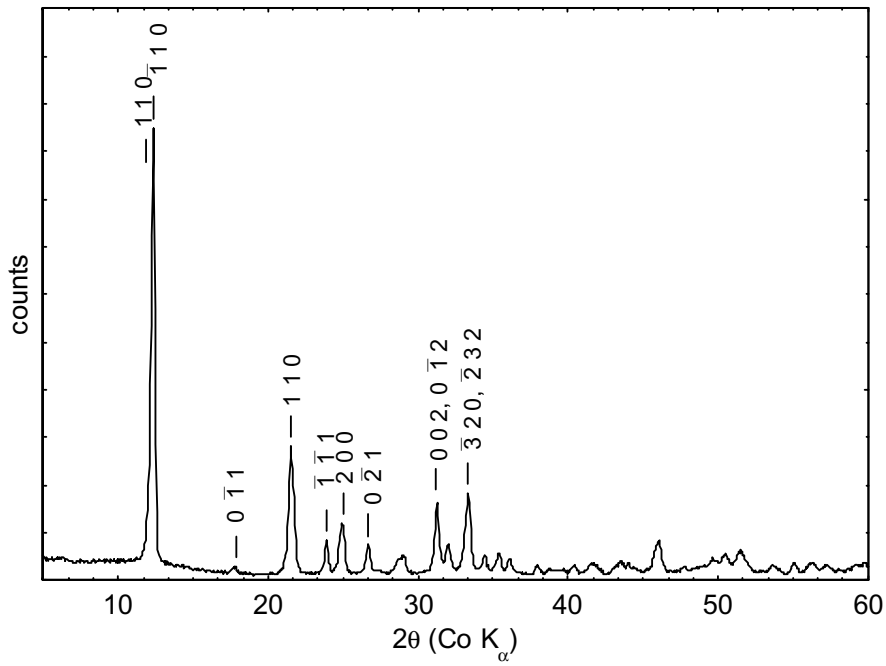

Figure 4-8: X-ray diffraction pattern of $Zr(NO_3)_2(OH)_2{\cdot}5H_2O$, dried from ZN2.0 solution.

The main structural units are parallel, cationic chains, with the repeating unit $[Zr(OH)_2(NO_3){\cdot}2H_2O]^+_n$. The zirconium atoms within each chain are linked by double hydroxy-bridges, and each zirconium is coordinated by four bridging-hydroxy groups, two water molecules, and a bidentate nitrate group (with C_{2v} symmetry). For each repeating unit there are also 2 - 3 water molecules and an additional nitrate group (with D_{3h} symmetry) that is ionically bound in the crystal lattice between the chains.

Note that there are a number of other crystal structures identified for 'zirconyl nitrate', including several polymorphs of $Zr(OH)_2(NO_3)_2{\cdot}H_2O$ and one of $Zr(OH)_2(NO_3)_2$.[7] All references here to the crystalline zirconyl nitrate salt are to the $Zr(OH)_2(NO_3)_2{\cdot}5H_2O$ structure only.

4.3.6 X-ray diffraction pattern of the gel

A typical diffraction pattern of a ZN1.0 gel is given in Figure 4-9.* Although there are no sharp diffraction peaks corresponding to a fully-crystalline phase, there are a number of broad peaks in the pattern that are reproducible and characteristic. All attempts to gel the sol in such away as to sharpen the diffraction pattern were unsuccessful.

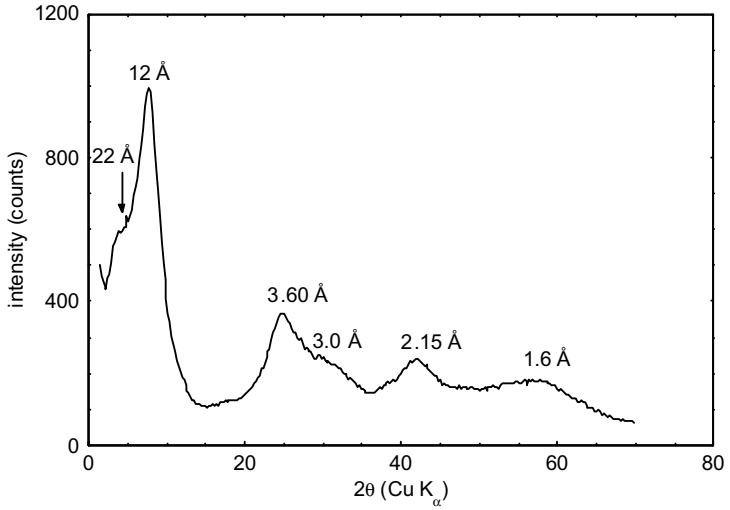

Figure 4-9: X-ray diffraction pattern of the Woodhead-type gel

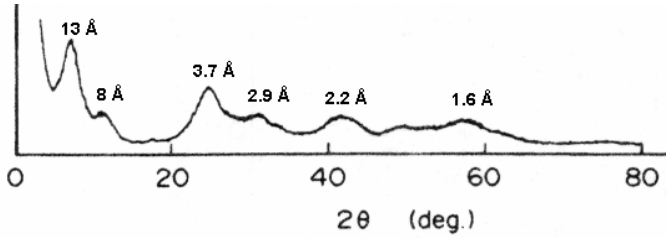

Figure 4-10: X-ray diffraction pattern of a gel prepared from boiling concentrated zirconyl chloride solution, from Matsui *et al.*[11] The approximate *d* spacings for each peak have been calculated and marked on the pattern.

Where XRD patterns are reported in other studies of 'amorphous' zirconia or zirconium hydroxide the patterns generally contain some broad peaks, but these peaks are generally not as distinct as those observed for the ZN1.0 gel.[8-10] The diffraction pattern most similar to the observed pattern is that measured from a gel prepared by refluxing a concentrated zirconyl chloride solution, reported by Matsui *et al.*[11] and shown in Figure 4-10.

---

* The term 'diffraction pattern' will be used throughout, even though certain features may be due to scattering rather than diffraction.

There are no peaks in the measured diffraction pattern that correspond to the crystalline zirconyl nitrate, indicating that at least most of the oligomeric cations have been reacted to form the particles, which themselves have a distinctive diffraction pattern. The pattern can be conveniently divided up into the low-angle region ($2\theta < 15°$; $d > 6$ Å) and the high-angle region ($2\theta > 15°$; $d < 6$ Å); these two regions are discussed separately below. The low-angle region provides information on the arrangement of the particles, and is affected by the aging of the sol; the high-angle region provides information on the short-range order.

The high-angle region

The high-angle region of the diffraction pattern is shown in Figure 4-11. There are three broad peaks, with approximate *d* spacings at 3.60, 2.15 and 1.60 Å. The 3.60 Å peak is the most intense of these, and has a shoulder at 3.0 Å. The relative intensity and position of these peaks are not affected by the concentration or ageing of the sol, but the peak-width does vary a little.

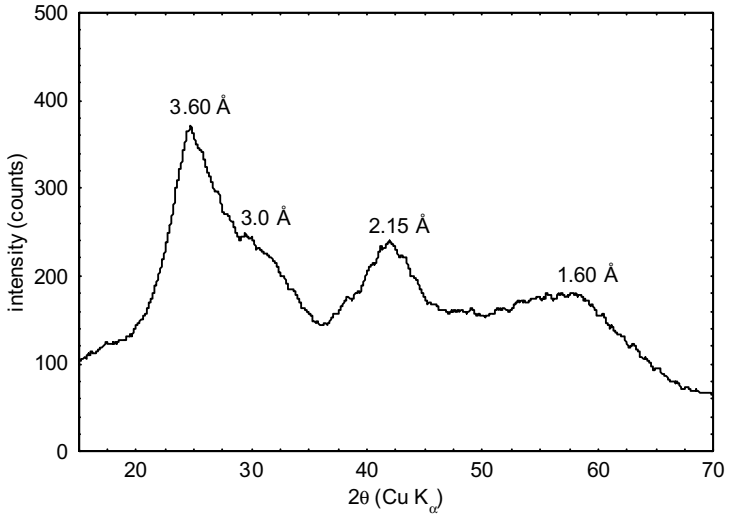

Figure 4-11: Typical X-ray diffraction pattern of the ZN1.0 gel over the 2θ range 15 - 70°.

Several ways of interpreting the high-angle pattern have been considered. The simplest approach is to treat it as a conventional diffraction pattern, but there are two difficulties with this approach. Firstly, the observed peaks are too few and too broad for any kind of *ab initio* indexing, and all attempts to index the pattern on the basis of the structure elucidated in Section 4.3.4 have failed. Secondly, it is doubtful that Figure 4-11 is a true diffraction pattern, as the sol particles are too small to diffract X-rays. The observation of any true diffraction peaks below 6 Å would mean that the individual particles would be 'stacked' in a regular

array to form a continuous Zr–O(H) lattice structure, which is unlikely considering that within the structure is a considerable amount of water and both coordinated and non-coordinated nitrate anions.

It is interesting to note the striking resemblance between the diffraction pattern of the ZN1.0 gel and the diffraction patterns for both the cubic and tetragonal zirconia phases. The diffraction pattern of the cubic phase is shown in Figure 4-12. The diffraction peaks for the gel are much broader, but the positions and relative intensities are fairly similar. Previous studies of 'amorphous' zirconia or zirconium hydroxide precipitate have also noted this similarity, and it has been interpreted as indicating the presence of very small cubic/tetragonal crystallites.[8,12] This assignment has been considered for the present study, but is inconsistent with the EXAFS evidence.*

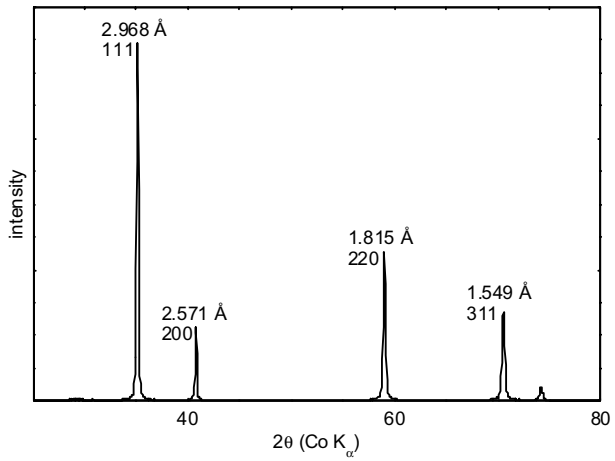

Figure 4-12: X-ray diffraction pattern of cubic yttria-stabilised zirconia, $Zr_{0.85}Y_{0.15}O_{1.93}$.

The most useful approach to interpret the high-angle pattern is to treat it as a result of *scattering*, rather than diffraction, so that the peaks represent 'average' interatomic-distances

* There are similarities in the structure of the cubic zirconia phase and the proposed structure of the gel. The 001 plane in the cubic and tetragonal structures consists of zirconium atoms in a square lattice approximately 3.6 Å apart. This bears a close resemblance to the arrangement of zirconium atoms in the gel structure, as determined by the EXAFS spectrum of the gel, discussed in Section 4.3.3. (The implication of this similarity to the crystallisation mechanism is discussed in Section 5.3.2.) Thus the diffraction pattern of the gel may be interpreted to indicate that the $Zr(OH)_4$ layers are stacked in such a way so that the zirconium atoms have the same arrangement as in the cubic phase. However, there are some difficulties with this interpretation. In the cubic phase the shortest Zr–Zr distance is approximately 3.6 Å, and the 111 peak is at 3.0 Å. If the 3.6 Å peak in the gel pattern is assigned to the 111 reflection, the Zr–Zr distance would be approximately 4.4 Å, which is much greater than the distance measured by EXAFS or reported

rather than planes in the structure. This approach can be confirmed by comparison with the EXAFS results, as shown in Table 4-3, and is rather more successful than the two approaches discussed previously. *The Zr–Zr and the Zr–O(H)^{br} distances determined by EXAFS are within a few percent of the two strongest peaks in the high-angle diffraction pattern.* The Zr–O distance for the 'second oxygen shell' does not correlate as well with any diffraction peak, but this shell most likely represents a *range* of Zr–O distances. However, even with this approach the assignment of the 1.61 Å peak is not certain, as there is no known corresponding interatomic distance. The expected O–O distance for the paired hydroxy groups is expected to be approximately 2.3 Å. It may be possible that the observed pattern is a combination of scattering and diffraction.

Table 4-3

Atomic pair	Distance determined by EXAFS (Å)	Corresponding peak in diffraction pattern (Å)
Zr–Zr	3.54	3.60
Zr–O *	2.60	2.99
Zr-O(H)^{br}	2.11	2.15
	?	1.61

* Assigned to oxygen atoms in adjacent $Zr(OH)_4$ sheets, coordinated water, or nitrate groups.

In summary, the high-angle 'diffraction' pattern of the gel is most easily interpreted in terms of scattering, which indicates average interatomic distances that confirm the measurements made by EXAFS.

The low-angle region

In the low-angle region of the diffraction pattern one or two peaks are observed. The number and position of these peaks was found to depend upon the *age* of the sol at the time of gelation. Figure 4-13 shows the low-angle diffraction patterns of six gel samples, each dried from sols that had been aged for different periods. The positions of the observed peaks above 6 Å are listed in Table 4-4.

---

for any zirconium compound. Furthermore, the arrangement of the zirconium atoms in a cubic-like structure would not leave sufficient space for the hydroxy bridges.

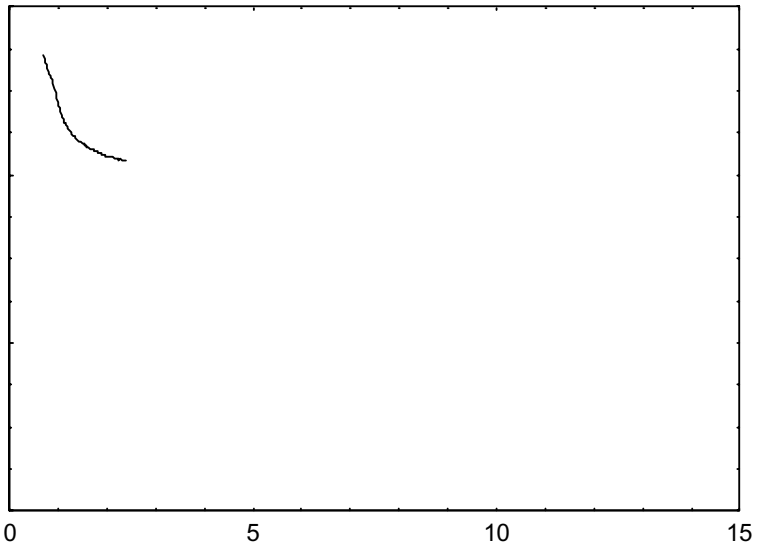

Figure 4-13: Low-angle diffraction patterns of gels dried from sols of different ages: a) 2 hours, b) 2 days, c) 15 days, d) 7 months, e) 14 months, and f) 50 months.

Table 4-4

Age of sol	Peak positions (Å)	
2 hours	12.0	
2 days	12.1	
15 days	12.8	
7 months	12.1	23
14 months	11.5	22
50 months	11.5	22

The gel formed from a sol only hours old has a broad diffraction peak corresponding to a *d*-spacing of 12.0 Å. The position of this peak increases slightly with ageing of the sol up to 15 days. Unfortunately no data points are available between 15 days and 7 months. The diffraction pattern of gel from the 7 month old sol has two peaks, the strongest at 12.1 Å with another at 23 Å. The peaks become more distinct and shift slightly with ageing to 50 months. Note that the peak at the lower angle also increases in relative intensity with ageing. The position of these peaks was not greatly influenced by the concentration of the sol or the age of the gel.

It is most probable that the peaks are the result of X-ray scattering rather than diffraction, and are indicative of the average distance between particles in the gel. Such peaks are commonly

found in the diffraction patterns of aggregates of colloidal particles. If significant diffraction were taking place then higher order peaks would be expected.*

The size and shape of the particles in the sol has been investigated in Chapter 3. A 1 M sol was found to contain unaggregated plate-shaped particles, with average dimensions approximately 28 Å across and 5 Å thick, not including coordinated nitrate or water groups. The Raman spectrum of the gel also shows that roughly one nitrate group for every two zirconium atoms is bidentate-coordinated to the particles.

Figure 4-13 clearly shows that ageing of the sol over several months causes a large change in the way that the plate-shaped sol particles are arranged after gelation. This would most easily be explained by changes in the particle size or shape, but the SAXS and DLS results presented in Chapter 3 give no indication of any such change over the same period. Note also that DLS would detect any aggregation of particles.

It is proposed that there are two packing 'phases' that may be formed by the particles. In phase A, illustrated in Figure 4-14a, the 5 Å thick particles are stacked face-to-face to form a 'layered' structure. The average distance separating the particles is 12 Å, which allows for an approximately 3 to 4 Å layer of coordinated water and nitrate anions around each particle. The stacking arrangement is not ordered enough to give rise to second- or third-order diffraction peaks. In phase B, illustrated in Figure 4-14b, the particles are predominantly stacked edge-to-face, to give a less-ordered 'house of cards' structure. The average distance separating the particles is considerably greater, approximately 22 Å, and a wider range of interparticle distances lead to a significantly broader peak.

* Note that where two peaks are present the peak at higher angle has a *d*-spacing of slightly more than half of the *d*-spacing of the other peak. The possibility that the former peak is a second-order reflection of the latter was considered, but several observations argued against this assignment. First, the relative intensities of these two peaks varied independently with ageing of the sol and heating of the gel (see Section 5.3.3). Secondly, there is no indication of any third order peak.

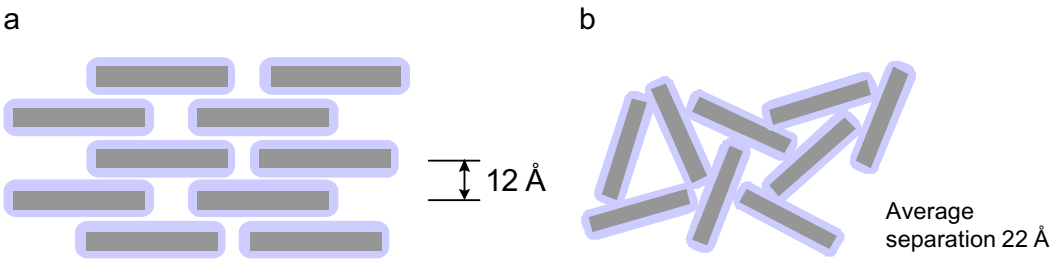

Figure 4-14: Two-dimensional representation of two possible stacking arrangements of plate-shaped particles: a) phase A and b) phase B (see text). The particles are 30 Å wide by 5 Å thick, with a ~ 3 Å surrounding layer of coordinated water and nitrate groups.

The primary characteristic leading to the different particle arrangements is proposed to be the difference in surface charge between the 'face' and the 'edge' regions. If the charge is relatively uniform over the entire particle, then the particles will stack face-to-face and phase A will predominate. If the charge on the edge and faces are considerably different, particularly if the signs of the charge are different, then the edges will be attracted to the face as the water is removed and phase B will predominate.

The implication is thus that the charge distribution on the particles changes over a period of months, even though the size and shape does not. A comprehensive mechanism for this change has not been developed, but it is speculated that it may be associated with slow changes in the hydrolysis of the water groups at the 'edge' of the particle, and possibly also partial oxolation of the hydroxy-bridges on the 'face' of the particles.

4.3.7 Small-angle X-ray scattering profile

The small-angle X-ray scattering profile for the ZN1.0 gel is shown in Figure 4-15 and Figure 4-16. A full discussion of the SAXS technique is provided in Chapter 9.

The log I vs. log Q plot of the scattering profile gives a straight line between 0.013 and 0.06 $Å^{-1}$, with a slope of –2.9. The absolute value of this slope indicates the *fractal dimension* of the gel over the range 50 - 10 nm. A fractal dimension of approximately 3 indicates a closed, tightly-packed structure, with negligible fractal component. The 'house-of-cards' packing in phase B, discussed previously in Section 4.3.6, would lead to some fractal structure but at a length-scale considerably less than 10 nm.

At high Q there is a broad peak in the profile, centred at around 0.32 $Å^{-1}$. This is assigned to a diffraction/scattering peak, corresponding to a d-spacing of 20 Å. This compares well with one of the low-angle X-ray diffraction peaks reported in Section 4.3.6.

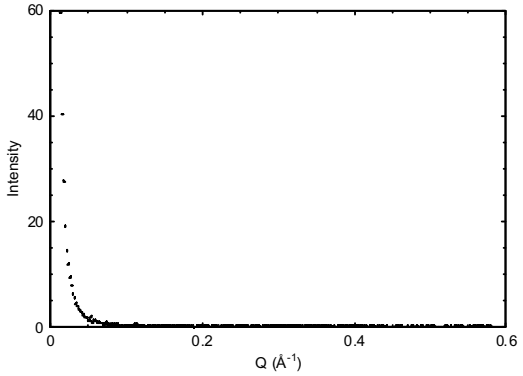

Figure 4-15: Scattering profile of a ZN1.0 gel, plotted on linear axes.

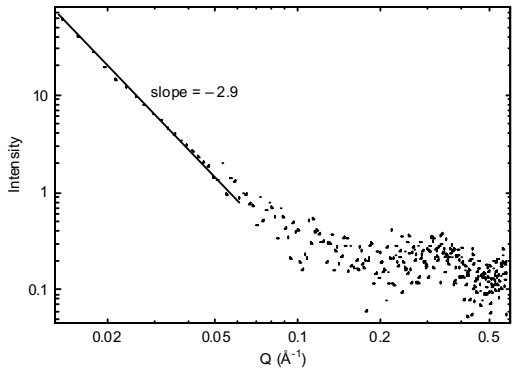

Figure 4-16: Scattering profile of a ZN1.0 gel, plotted on logarithmic axes.

4.4 Conclusions

The gelation process is largely a physical aggregation of the particles in the sol. There is no indication of chemical condensation or any changes in the Zr–O structure of the particles during gelation. During gelation approximately half of the 'associated' nitrate groups in the water layer around the particle become directly coordinated to the zirconium atoms.

The short-range structure of the particles has been investigated. The zirconium atoms are arranged in a regular planar square lattice, at a distance of 3.6 Å, with little disorder in the framework. The zirconium atoms are joined by double hydroxy-bridges. The results presented here provide the first detailed evidence that $Zr(OH)_4$, in a square, two-dimensional lattice, exists in the solid state. Low-temperature EXAFS and Raman show that there is a considerable degree of static disorder in the Zr-O bonds. The interatomic distances measured by EXAFS are supported by the X-ray 'diffraction' pattern.

The arrangement of the particles in the gel is dependent on the age of the sol. In a gel prepared from an 'unaged' sol (< 1 month old) the 5 Å thick plate-shaped particles are stacked face-to-face at intervals of approximately 12 Å, separated by a layer of water, and coordinated and non-coordinated nitrate groups. With aging of the sol over several months the relative charge on the 'edge' and 'face' of the particle changes, favouring a less-ordered 'house-of-cards' structure in the gel. At a length-scale greater than 10 nm the gel is closely packed, with negligible fractal component.

4.5 References

1. K. Nakamoto, *Infrared and Raman spectra of inorganic and coordination compounds*, 4th Edition, Wiley-Interscience, New York (1986)
2. T. C. W. Mak, "Refinement of the crystal structure of zirconyl chloride octahydrate" *Can. J. Chem. 46* 3493-3497 (1968)
3. A. Clearfield, "Structural aspects of zirconium chemistry" *Rev. Pure and Appl. Chem. 14* 91-108 (1964)
4. X. Turrillas, P. Barnes, A.J. Dent, S.L. Jones and C.J. Norman, "'Hydroxide' precursor to zirconia: Extended X-ray absorption fine structure study" *J. Mater. Chem. 3* [6] 583-586 (1993)
5. J.D.F. Ramsay, "EXAFS study of polynuclear ions in solution" *Synchrotron radiation, Appendix to the Daresbury annual report 1988/89*, Compiled by C. Nave *et al*., Science and Engineering Research Council 38-39 (1989)
6. P. Benard, M. Louër and D. Louër, "Crystal structur determination of $Zr(OH)_2(NO_3)_2{\cdot}4.7H_2O$ from X-ray powder diffraction data" *J. Solid State Chem. 94*, 27-35 (1991)
7. P. Bénard, J.P. Affrédic, and D. Louër, "High-temperature X-ray powder diffractometry of the decomposition of zirconium hydroxide nitrates" *Powder diffraction 8* [1] 39-46 (1993)
8. V.G. Keramidas and W.B. White, "Raman scattering study of the crystallisation and phase transformation of ZrO_2" *J. Am. Ceram. Soc. 57* [1] 22-24 (1974)
9. D.A. Ward and E.I. Ko, "Synthesis and structural transformation of zirconia aerogels" *Chem. Mater. 5* 956-969 (1993)
10. X. Turrillas, P. Barnes, D. Häusermann, S.L. Jones and C.J. Norman, "Effect of chemical and heat treatment on the tetragonal-to-monoclinic transformation of zirconia" *J. Mater. Res. 8* [1] 163-168 (1993)
11. K. Matsui, H. Suzuki, M. Ohgai and H. Arashi, "Raman spectroscopic studies on the formation mechanism of hydrous-zirconia fine particles" *J. Am. Ceram. Soc. 78* [1] 146-152 (1995)
12. P. Kountouros and G. Petzow, "Defect chemistry, phase stability and properties of zirconia polycrystals" *Science and Technology of Zirconia V*, Edited by S.P.S. Badwal *et al*., Technomic, Lancaster USA, (1992) 30-48

5. Decomposition and crystallisation with heating

5.1 Introduction

Once a zirconia-precursor has been prepared from a sol or solution, the conventional method to convert it to a pure oxide is by heating, during which crystallisation also usually occurs. The decomposition reactions are important to understand for two reasons. Firstly, they provide information on the original structure of the gel; secondly, decomposition reactions may be able to be controlled through processing conditions to obtain certain structures, control crystallisation, promote the loss of volitile components, *etc*. This chapter examines how the semi-ordered structure in the gel decomposes and loses mass with heating, and also the crystallisation of the amorphous oxide into the 'metastable' tetragonal phase at approximately 450°C.

The crystallisation of the tetragonal phase is of particular interest. Many theories have been proposed to account for the formation of the metastable phase, and the principle theories are reviewed in Section 2.4.2. It has been suggested that the short-range structure of the amorphous oxide promotes the crystallisation of the tetragonal phase, and this idea is investigated using the EXAFS technique.

The main experimental approach has been to heat samples to a certain temperature for a short period, before cooling to ambient temperature. The structure of the heat-treated samples was then characterised by a range of techniques. Brief heating times were chosen so that the samples would roughly correspond to the stages found during constant-rate heating. The characterisation techniques were chosen to investigate structure on a range of scales, from the short-range structure (EXAFS, Raman) to the arrangement of the particles (low-angle XRD).

In many other studies in which a material is characterised after heating and cooling, an implicit assumption is made that no significant change occurs during cooling. This is not always the case, so it is also useful to characterise the material *in-situ* during heating. Raman spectroscopy and EXAFS were used for these studies, in addition to differential thermal and thermogravimetric analysis.

The decomposition of precipitated oxy-hydroxides has not been widely studied, and reports of *in-situ* studies are particularly rare. Those reports found in the literature are described in

Section 2.3.1. The decomposition process is generally assumed to involve gradual loss of terminal water and hydroxyl groups, and oxolation of hydroxy bridges.

5.2 Experimental procedure

Samples of standard ZN1.0 gels were ground finely, heated in static air at 10 or 20°C/min to a specified 'treatment temperature' between 150 and 500°C, held at this temperature for 5 minutes, then air-cooled.* One further sample was heated to 470°C for an hour. Unless otherwise specified, the gel used was formed from a sol that was less than two days old, in order to avoid ageing effects. During heating a type-K thermocouple was placed as close as practical to the sample to record and control the temperature. The uncertainty of the sample temperature was less than ± 3°C.

For comparison with the standard gel, a "zirconium hydroxide" was prepared. A zirconyl nitrate solution (ZN2.0) was prepared, and an excess of ammonia added rapidly. The resulting precipitate was washed four times with deionised water and dried at 110°C to leave a white powder. The Raman spectrum indicated that this material contained much less nitrate than the standard gel (approximately 10 % of the amount in the gel).

The Raman spectrum of each heat-treated sample was measured under ambient conditions using a FT-Raman spectrometer.† The position of selected bands was determined by a peak-fitting routine.

The thermal decomposition and crystallisation of the gel was characterised by *in-situ* Raman spectroscopy, while the sample was heated in a hot-stage containing a static air atmosphere.‡ Three experiments were carried out, covering different temperature intervals. For the first experiment the sample was held at 100°C and 200°C, while spectra were collected by the FT-Raman spectrometer with a 20 minute acquisition time.

In the second experiment the gel sample was heated at a constant rate of 2°C/min from 300°C to 550°C, with a spectrum collected every 50°C using a conventional Raman spectrometer.§

---

* In some cases sample were heated in flowing air, but this made no observable difference to the results. 'Dwell times' of up to 10 minutes at the treatment temperature also made little difference.

† Bio-Rad FT-Raman II, using an excitation line of 1064 nm from a Nd:YAG laser. The effective resolution was 4 cm^{-1}.

‡ Linkam FTIR 600 hot stage. Approximately 20 mg of sample was held in a shallow platinum tray on a silver heating block. A thermocouple was embedded in the block immediately underneath the tray.

§ Dilor XY 600 spectrometer, using an excitation line of 514.5 nm from an Ar^+ laser, focused onto the sample through a ×10 objective lens. The effective resolution was 1.5 cm^{-1}. One limitation of a FT-Raman spectrometer is that it uses a infrared laser, so that infra-red radiation emitted from a hot sample (above approximately 250°C) swamps the very weak Raman signal. Conventional Raman spectrometers generally use a visible laser, so this problem does not occur until the sample becomes much hotter.

The acquisition time was 5 minutes, so that spectra were collected over an interval of 10°C. The laser was focused onto a single fragment of the sample, and as the temperature increased the fragment shifted and contracted in size due to the decomposition reactions, so that it was necessary to refocus the laser before each spectrum was collected. This means that the absolute intensity of each peak can not be reliably compared between spectra, only the relative intensities within a spectrum. The third *in-situ* Raman experiment investigated the isothermal crystallisation process. Gels were rapidly (130°C/min) heated to 400 or 450°C, and held at this temperature for 20 minutes. Raman spectra were collected with the conventional Raman spectrometer every minute, with a 20 s acquisition time.

The X-ray diffraction pattern of heat-treated samples was measured with a laboratory diffractometer* over the 2θ range 2 - 80°, and again over the range 0.7 - 15° with a narrowed divergence slit for improved resolution. Where several diffraction patterns are displayed together on a graph, the intensity is normalised by the collection time. Peak positions were determined with a peak-fitting routine.

The short-range structure of selected heat-treated samples was studied by measuring the extended X-ray absorption fine structure (EXAFS) spectrum at the Zr K-edge. Spectra were measured at a range of temperatures between 10 and 290 K. Full details of the sample preparation, equipment, data collection and data treatment are given in Chapter 10. The short-range structure was determined by comparing the measured EXAFS spectrum with a model, and this procedure is also discussed fully in Chapter 10.

The decomposition and crystallisation processes were characterised *in-situ* by time-resolved EXAFS, using an energy-dispersed beam. A wafer containing a sample of ZN1.0 gel was heated at 5°C/min in a custom-made furnace, while the EXAFS spectra were measured every 25°C. Full details of the sample preparation, equipment, data collection and data treatment are given in Section 10.4.

The ability of heat-treated samples to redisperse in water was tested by adding a small quantity of the ground material to a few millilitres of water. Dispersal was characterised by the disappearance of the gel in the liquid, and re-gelation upon evaporation of the liquid.

The mass loss and heat flow during decomposition and crystallisation of the ZN1.0 gel were measured by simultaneous differential thermal analysis and thermogravimetric analysis

(DTA/TGA).[†] A number of gel samples were examined, derived from sols aged for periods between 1 day and 50 months. Each sample was heated at 10°C/min in dry, flowing air.

Attempts were made to measure the porosity of a range of heat-treated samples by N_2 adsorption, but all of the amorphous samples were very difficult to completely de-gas. The results were not satisfactory, and will not be discussed further.

---

[*] Scintag X1 Advanced Diffraction System using Cu K_α radiation.

[†] Setaram TAG 24 simultaneous DTA/TGA instrument.

5.3 Results and discussion

5.3.1 Raman spectroscopy

Figure 5-1 shows the Raman spectra, measured under ambient conditions, of samples of gel that have been heated and cooled. Changes in the short-range structure are reflected in the changes in the Raman spectrum.

One difficulty in quantifying these changes is that the absolute intensity of the bands in one spectrum cannot be compared with those of other spectra. The intensity of each band is directly proportional to the ability of the powder to scatter light, which varies as the sample is dried and heated. The intensity of each of the spectra in Figure 5-1 has therefore been normalised so that the region below 650 cm^{-1} is approximately the same average intensity.

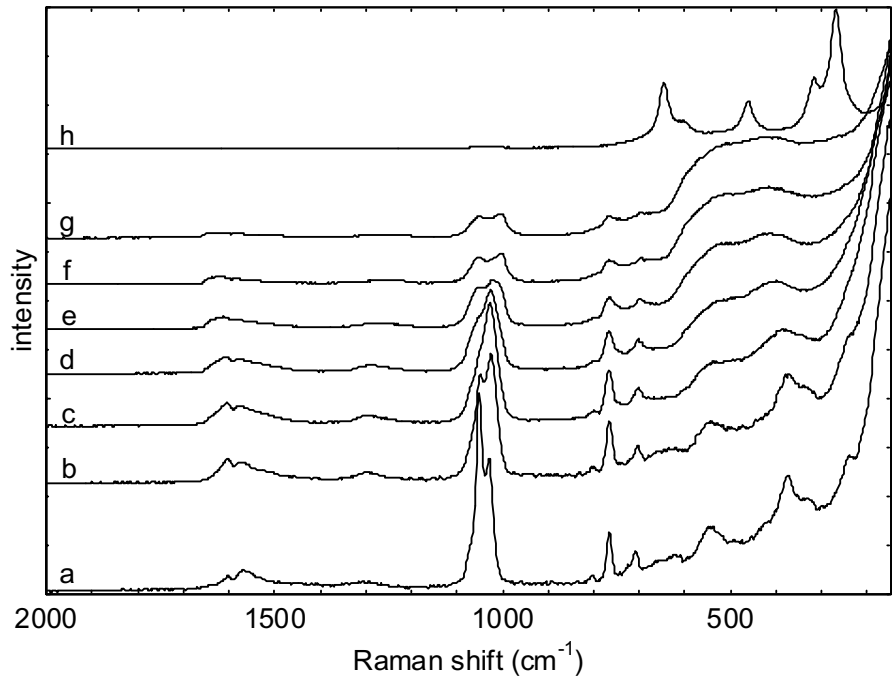

Figure 5-1: FT-Raman spectra of a) unheated gel, and gel heated for 5 minutes at b) 150°C, c) 200°C, d) 250°C, e) 300°C, f) 350°C, g) 400°C, and h) 500°C. The intensity scale of each spectrum is adjusted so that the region below 650 cm^{-1} is approximately the same intensity.

Figure 5-2 shows *in-situ* FT-Raman spectra of a gel when heated at 100 and 200°C. Figure 5-3 shows *in-situ* conventional-Raman spectra of a gel when heated at 300 to 550°C. Both of these sets of results have been reported previously.[1,2]

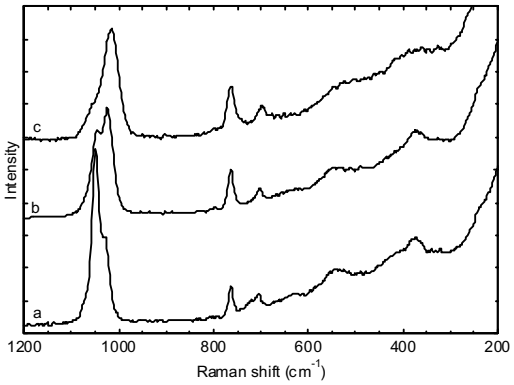

Figure 5-2: *In-situ* FT-Raman spectra of a) the unheated gel, and heated at b) 100°C and c) 200°C.

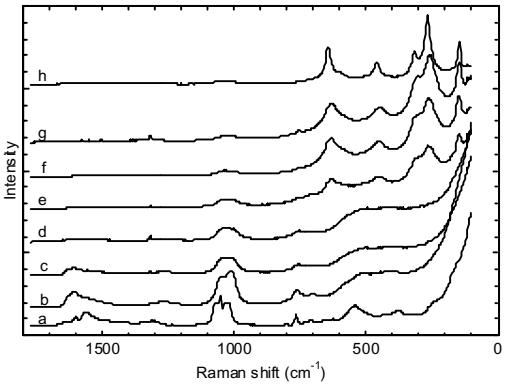

Figure 5-3: *In-situ* conventional-Raman spectra of a) unheated gel (truncated between 1015 and 1080 cm^{-1}), and heated at b) 300°C, c) 350°C, d) 400°C, e) 450°C, f) 500°C and g) 550°C, and h) after cooling back to 20°C.

The following discussion is divided into two parts; the spectrum below 650 cm^{-1} will be discussed first, followed by the spectrum above 650 cm^{-1}.

The spectrum below 650 cm^{-1}

The bands in the spectrum below 650 cm^{-1} are assigned to Zr–O vibrations. The main bands in the spectra of the unheated gel, and sol, have been assigned in Section 3.5. The band at 540 cm^{-1} was assigned to a symmetric stretch of the paired hydroxy-bridges, and the band at 375 cm^{-1} was tentatively assigned to a lattice mode of the $Zr(OH)_2$ network.

Heating the gel to 150°C leads to only a slight broadening of the bands. Between 150°C and 300°C considerable peak-broadening progressively takes place, indicating a large increase in the short-range disorder of the material. The bands also change position, and after heating to 300°C are at approximately 415 and 530 cm^{-1}. It is difficult to interpret these changes in terms of the previous assignments. At this point the most that these observations can be used for is to indicate change and disorder in the short-range structure.

There is little change in the Raman spectrum in this region above 300°C until crystallisation occurs, indicating that there is little change in the Zr–O bands over this interval.

It is important to note that there is no particular similarity between the spectrum of the material at 400°C and the spectrum of the crystalline tetragonal phase (discussed below). As discussed in Section 2.4.2.1, it has been previously suggested that X-ray 'amorphous' zirconia contains 'nano-crystals' of the tetragonal phase,[3-5] although no direct evidence has been published to support this proposition. If such crystallites were present the Raman spectrum of the material

should also contain peaks characteristic of the tetragonal phase, since Raman spectroscopy can distinguish between crystalline and amorphous zirconia regardless of the 'crystal size'. We can conclude that the 'amorphous' material studied here does not contain such 'nano-crystals'.

For the amorphous samples, the Raman spectrum (below 650 cm^{-1}) that was measured *in-situ* at a certain temperature is very similar to the spectrum measured after cooling from that temperature. Of particular interest is the early stages of heating up to 150°C, as certain decomposition processes such as oxolation may be reversible, and thus measuring the spectrum after cooling would give the illusion that no change was occurring. Although the *in-situ* data in this temperature region (Figure 5-2) is limited, there is no evidence here that there are any reversible processes that affect the Raman spectrum. The implication of this observation is that the Zr–O(H) structure that gives rise to the spectrum below 700 cm^{-1} is stable to at least 150°C.

Crystallisation takes place between 400 and 500°C, as shown by the appearance of intense Raman bands characteristic of the crystalline phases in the region between 100 and 700 cm^{-1}. The Raman spectra of the monoclinic and tetragonal phases are well-known and can be very clearly distinguished.[6,7] Although most reported spectra of the tetragonal phase are of various *stabilised* structures (*i.e.* 'doped' with other oxides),[7-9] or of pure zirconia at high temperature,[6,10] the crystal structures are very similar and the main features of the spectrum are expected to be the same as for the 'metastable' phase. A number of Raman spectra of the metastable tetragonal phase have been published, mostly with poor signal-to-noise.[3,11-14] The Raman spectrum of the stabilised-cubic phase is known,[7] and is quite distinguishable from that of the tetragonal phase, but no spectrum has been reported for the pure cubic phase.

Figure 5-4 shows the Raman spectra of the material heated to 500°C. The six strong bands are all assigned to the tetragonal zirconia phase. Table 5-1 lists the observed band positions (determined by band fitting), and compares them with those reported for the metastable tetragonal phase and the stabilised tetragonal phase. The conventional assignments for these bands are also listed.* Two very weak bands at 177 and 193 cm^{-1} can be assigned to the

* While these assignments are widely accepted,[6,7,15] a recent lattice-dynamical study has indicated that the symmetry selection rules are significantly violated in tetragonal zirconia, and that the observed Raman spectrum comes to a great extent from the phonon-density distribution over the Brillouin zone.[16]

monoclinic phase. This spectrum of pure, metastable zirconia is one of the clearest reported to-date, with very high signal-to-noise.

Note that the Raman bands are broadened considerably at elevated temperatures; compare spectra **g** and **h** in Figure 5-3.

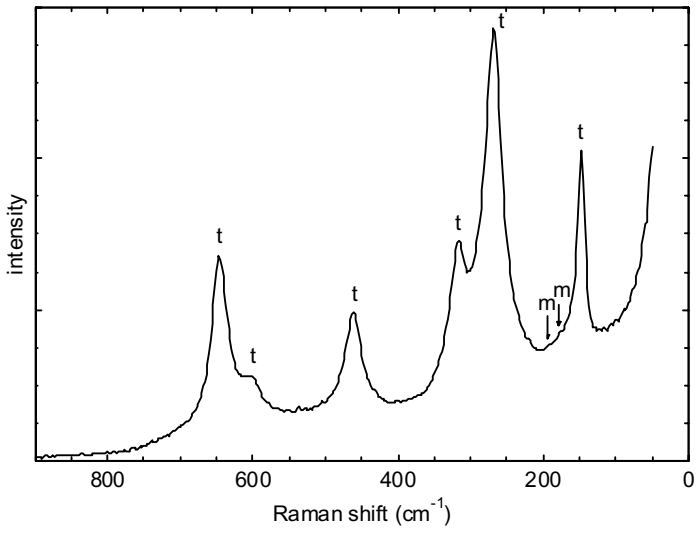

Figure 5-4: FT-Raman spectrum of material heated to 500°C for 5 minutes, with the bands assigned to the tetragonal (t) or monoclinic (m) phases.

Table 5-1: Raman band positions observed for tetragonal zirconia, compared with previously reported spectra.

Observed (cm^{-1})	Reported [14] for metastable t-ZrO_2 (cm^{-1})	Reported [7] for t-ZrO_2 stabilised by 4.6 mol% Y_2O_3 (cm^{-1})	Raman-active mode [7]
646	642	645	E_g
602		616	A_{1g}
462	463	474	E_g
317	314	326	B_{1g}
269	267	266	E_g
148	147	155	B_{1g}

Yashima *et al*. studied the Raman spectra of a large series of stabilised-tetragonal zirconia samples, with varying quantities of trivalent $RO_{1.5}$ dopant (R = Nd, Sm, Y, Er, Yb).[8] They observed that the intensity ratio of the bands at approximately 460 and 640 cm^{-1} increases

from zero at 20 mol % dopant (cubic phase), to approximately 0.35 at 6 mol %.* This change is attributed by the authors to be a function of oxygen displacement along the *c*-axis in the unit cell, which increases with decreasing dopant.† If the trend in intensity ratio is extrapolated to zero dopant, the ratio is approximately 0.50 ± 0.05. The intensity ratio for the spectrum in Figure 5-4, calculated by the same method, is also 0.50. Thus we can state that the oxygen displacement in the metastable tetragonal phase is large in comparison to the stabilised phase, and is consistent with the trend observed by Yashima *et al*.[8]

Crystallisation has also been observed *in-situ* by Raman spectroscopy. Samples of ZN1.0 gel were heated rapidly (130°C/min) and held at 400 and 450°C. At 400°C, no crystallisation was observed after 20 minutes. At 450°C, peaks assigned to t-ZrO_2 were observed after 1 minute, and increased in intensity over a period of 10 minutes. Ideally this technique could be used to study the kinetics of crystallisation, but changes in focussing as the grains shift and shrink make it difficult to consistently compare absolute intensities of consecutive spectra.

The Raman spectrum above 650 cm^{-1}

The changes in the Raman spectrum above 650 cm^{-1} are best illustrated in Figure 5-1. The bands in this region are mostly due to various 'nitrate' species.‡ These bands occur in three regions: 700-800, 1000-1100, and 1500-1700 cm^{-1}. In this discussion we will concentrate on the 1000-1100 cm^{-1} region. Each nitrate species has a single band in this region, which is relatively intense.[17]

As discussed in Chapter 4.3.3, two nitrate species are identified in the ZN1.0 gel. The first is not directly bound to the surface of the particles, has an 'undistorted' D_{3h} symmetry, and to which is assigned the 1050 cm^{-1} band. The second species identified is bidentate-coordinated to the surface zirconium atoms, has a 'distorted' C_{2v} symmetry, and to which is assigned the 1030 cm^{-1} band. The relative abundance of these two species was determined to be approximately 1:1.

---

* Kim *et al*. have found a similar trend in the ratio of the bands at approximately 640 and 610 cm^{-1}.[9]

† The oxygen displacement, represented by the lattice parameter *z*, is further discussed in Section 2.1.1. The correlation between oxygen displacement and the Raman spectrum may potentially lead to a simple method to determine the value of *z* without resorting to diffraction with a neutron or synchrotron source.

‡ In this discussion, both nitrate and nitrato species are referred to as 'nitrate' for convenience.

As the gel is heated a number of changes occur in the bands assigned to nitrate species, and three trends are identified. First, the intensity of the bands, with respect to the intensity of the < 700 cm^{-1} region, decreases very substantially. This decrease in intensity indicates a loss of nitrate groups, however as discussed above it is difficult to be quantitative due to differences in scattering intensity of samples and Raman-activity of different species.

The second trend is that the position of the bands shifts slightly, and the third is that the relative intensity between bands changes. Table 5-2 shows the band positions and the approximate *relative* peak area with respect to the other bands in the 1000-1100 cm^{-1} region. Note that this value does not equal the relative abundance, as the Raman-activity for each vibrational mode of each species is different, but it does indicate the *changes* in relative abundance.

Table 5-2

Treatment temperature	Band position (cm^{-1}) and relative peak area.		
Unheated *	1051 (60 %)	1029 (40 %)	
150°C *	1049 (40 %)	1023 (60 %)	
200°C	1056 (30 %)	1025 (70 %)	
250°C	1061 (30 %)	1025 (70 %)	
300°C	1055 (50 %)	1020 (30 %)	1001 (20 %)
350°C	1053 (50 %)	~ 1023 (10 %)	1002 (40 %)
400°C	1052 (50 %)	~ 1021 (10 %)	1001 (40 %)

* A minor peak at 1070 cm^{-1} was also fitted in the spectrum of the unheated and 150°C samples, but was excluded from the calculations as it remains unassigned.

In the early stages of heating up to 200°C there is a clear decrease in the intensity of the 1050 cm^{-1} band, while the 1030 cm^{-1} band remains relatively constant. This clearly indicates that most of the nitrate groups with D_{3h} symmetry are being coordinated or lost. These nitrate groups may be coordinating to the surface of the particles and adopting C_{2v} symmetry, or converted to NO_x gas. The DTA/TGA data discussed in Section 5.3.5 suggests that nitrate is lost in this temperature interval, so the latter mechanism is more likely.

A band at 1052-1061 cm^{-1} remains in the spectrum of samples heated to 250°C and above, which is an appropriate position for D_{3h} nitrate. However, since this species would not be bound to the surface of the particles it is uncertain whether it is likely to still be present after heating at these temperatures. One likely explanation is that when the powder is cooled, rehydration of the surface takes place, and some of the coordinated-nitrate species lose their coordination to the surface. The corresponding bands of the *in-situ* Raman spectra (Figure 5-

3) are quite broad, but no distinct band is observed at ~ 1050 cm^{-1} which is consistent with the above interpretation.

Between 200 and 300°C the intensity of the 1030 cm^{-1} band decreases very strongly. This indicates that the coordinated-nitrate groups with C_{2v} symmetry are being lost, most probably also converted to NO_x gas. After heating to 300°C and beyond, this band becomes quite weak in comparison to the other two bands observed.

After heating to 300°C, the appearance of a new kind of nitrate group can be distinguished, characterised by a band at ~ 1000 cm^{-1}. This band has not been unambiguously assigned, as there is no previous report of a nitrate group coordinated to zirconium with an A_1 Raman band at a position lower than 1020 cm^{-1}. This species could possibly be one in which the nitrogen is directly bound to the zirconium atom, *e.g.* Zr–N=O.

Virtually all of the nitrate/nitrato groups remaining at 400°C are lost in the crystallisation stage. In the spectrum of the crystallised oxide the bands observed above 650 cm^{-1} are very weak, with some very minor bands in the 980 - 1100 cm^{-1} region that may be assigned to residual nitrate groups.

5.3.2 Extended X-ray absorption fine-structure spectroscopy

The short-range structure around the zirconium atoms in gels heated to various temperatures has been studied using the EXAFS technique. The analysis of the results is fully described in Chapter 10; in this section the main results are presented, along with a discussion of their significance. A brief introduction to the interpretation of EXAFS spectra and modelling is given in the previous chapter in Section 4.3.4.

Along with an unheated gel sample, four heat-treated samples were examined. The first two were heated to 150 and 300°C for five minutes, chosen to represent points between the main stages in the decomposition process. The third sample was heated to 400°C for five minutes, chosen to represent the structure immediately before crystallisation. The final sample was heated at 470°C for an hour, to produce a sample largely composed of the metastable tetragonal phase.

Figure 5-5 compares the Fourier-transformed spectra of the samples listed, along with the spectrum of pure monoclinic zirconia for comparison. The first peak, at approximately 1.6 Å, is due to the 'nearest-neighbour' oxygen atoms immediately adjacent to the zirconium atom. The rest of the peaks are largely due to neighbouring zirconium atoms. In comparing the spectra there are two obvious transitions. The first is between 150 and 300°C, in which there is a sharp drop in the intensity of the second peak. The second transition is between 400 and 470°C, in which the material crystallises.

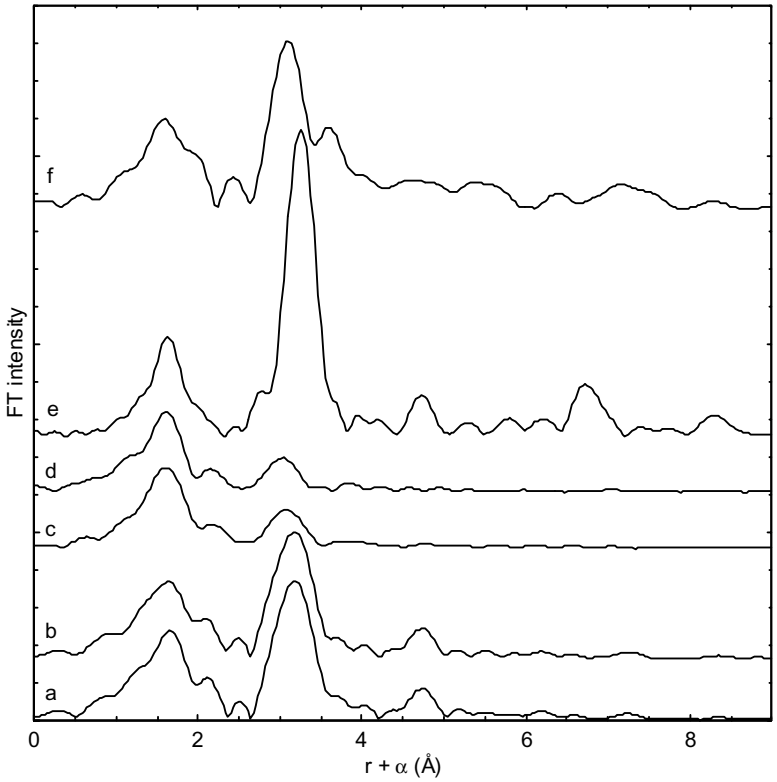

Figure 5-5: Fourier-transformed EXAFS spectra of a) ZN1.0 gel, and the same gel heated for 5 minutes at b) 150°C, c) 300°C, and d) 400°C. e) Heated at 470°C for 1 hour and f) pure monoclinic phase zirconia. All spectra measured at 10 K.

The following discussion is divided into three parts. The first part will deal with the decomposition reactions up to 300°C, while the second will discuss the crystallisation mechanisms. The third part will briefly discuss a further experiment, in which the short-range structure of the material is characterised *in-situ* during heating.

Decomposition

The spectra of the amorphous materials is best described by a model in which each zirconium atom is coordinated by two 'shells' of oxygen atoms as nearest neighbours (O1 and O2), and one or two shells of zirconium atoms at further distances (Zr1 and Zr2). The modelled interatomic distances and coordination numbers for these shells are listed in Table 5-3, and the disorder parameters in Table 5-4. Uncertainties in the last one or two decimal places are indicated in parenthesis. The modelled interatomic distances are plotted as a function of treatment temperature in Figure 5-6.

Table 5-3: Modelled interatomic distances and coordination numbers for amorphous samples.

Treatment temperature	O1		O2		Zr1		Zr2	
	r (Å)	N	r (Å)	N	r (Å)	N	r (Å)	N
Unheated	2.106(9)	7.6(6)	2.579(14)	4.2(6)	3.539(3)	3.8(2)	4.995(9)	1.9(8)
150°C	2.092(6)	6.6(4)	2.583(9)	4.9(4)	3.535(2)	3.6(2)	4.984(7)	1.4(5)
300°C	2.070(6)	5.1(4)	2.547(14)	1.6(2)	3.412(12)	4.1(8)	-	-
400°C	2.067(5)	4.8(3)	2.563(19)	0.9(2)	3.371(11)	2.9(5)	-	-

Values in parentheses represent the uncertainty in the final one or two significant figures.

Table 5-4: Modelled disorder parameters for amorphous samples.

Treatment temperature	O			Zr1			Zr2	
	σ^2_{stat} ($Å^2\times10^{-3}$)	θ_E (K)	σ^2_{10K} $Å^2\times10^{-3}$	σ^2_{stat} ($Å^2\times10^{-3}$)	θ_D (K)	σ^2_{10K} $Å^2\times10^{-3}$	σ^2_{stat} ($Å^2\times10^{-3}$)	θ_D (K)
Unheated	8.5(1.3)	700(200)	11(2)	1.9(3)	470(20)	3.6(3)	3(2)	380(100)
150°C	8.3(1.0)	700(200)	11(1)	2.1(2)	470(20)	3.8(2)	1(2)	330(60)
300°C	*n.a.*	*n.a.*	8.1(6)	11.2(1.5)	485(100)	13(2)	-	-
400°C	4.5(7)	575(70)	7.6(7)	9.8(1.3)	500(120)	11.4(1.5)	-	-

n.a.: Values not available, See Chapter 10.

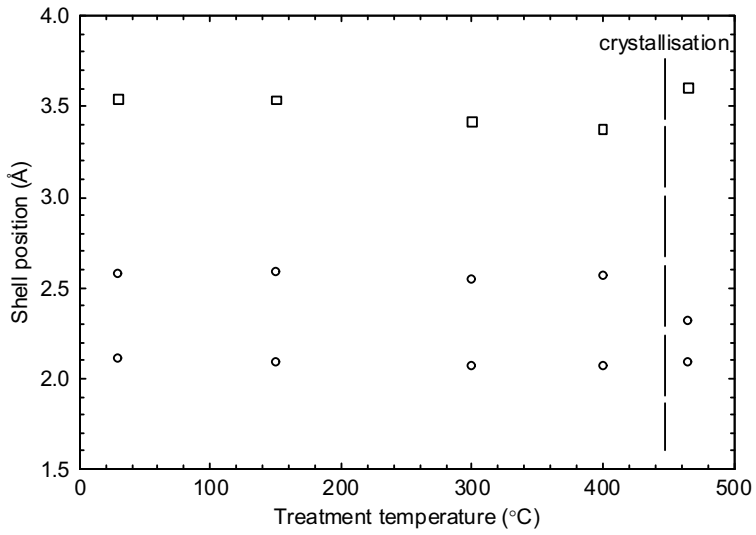

Figure 5-6: Modelled positions for the two oxygen shells (○) and the first zirconium shell (□).

The EXAFS spectrum for the unheated gel is discussed in Section 4.3.4. It was concluded that the zirconium atoms are arranged in a regular square lattice, at a distance of 3.6 Å. The zirconium atoms are joined by hydroxy bridges, with a considerable degree of static disorder in the Zr–O bonds. 'Sheets' of this two-dimensional structure may be stacked together in individual particles. The first oxygen shell at 2.11 Å is assigned to mainly bridging hydroxy groups, and possibly some nitrate groups coordinated to the surface. The second oxygen shell

at 2.58 Å is assigned to water groups, nitrogen atoms in coordinated-nitrate groups, and/or the oxygen atoms in adjacent sheets. The first zirconium shell is assigned to the four closest zirconium atoms, which are joined to the central zirconium atom by the hydroxy bridges. The second zirconium shell is assigned to those zirconium atoms that are diagonally across the lattice square. The high value of θ_E (and high uncertainties) means that the σ^2 value does not change very much with measurement temperature, so it is difficult to separate out the small thermal component from the static component.

The modelled parameters for the sample heated to 150°C are very close to those for the unheated gel. The only significant difference is the decrease in coordination-number for the first oxygen shell from 7.6 to 6.6. The loss of nearest-neighbour oxygen atoms is most probably associated with the partial *oxolation* of hydroxy bridges, as in Equation 5-1, and possibly associated with the loss of coordinated-nitrate groups.

$$Zr–(OH)_2–Zr \rightarrow Zr–O–Zr + H_2O \qquad \textbf{Equation 5-1}$$

Much greater change in structure takes place between 150°C and 300°C. The coordination number for the first oxygen shell has been reduced further to 5.1, and the number of atoms in the second oxygen shell has been greatly reduced. Both Zr–O distances have decreased slightly. Interestingly, the value of σ^2_{stat} for the oxygen shells has substantially decreased, indicating that the complexity in the Zr–O structure that was represented by the large σ^2_{stat} values is no longer present. Heating to 300°C also greatly reduces the intensity of the peak representing the nearest Zr neighbour. The modelled parameters show that the coordination number remains roughly constant at 4, and that the loss in intensity of the corresponding FT peak is essentially peak-broadening, due to a large increase in structural disorder. The FT peak for the second-nearest Zr neighbour has disappeared completely.

These changes are explained by the oxolation of most of the hydroxy bridges between 150 and 300°C, and the distortion of the ordered sheet structure. While the number of oxygen neighbours greatly decreases with oxolation, the number of zirconium neighbours will remain the same. As each double-hydroxy bridge undergoes oxolation the average Zr–Zr distance also decreases, distorting the regular structure of the sheet and increasing disorder. This disorder will decrease the contribution of the first shell to the EXAFS spectrum, making the corresponding peak in the FT broader and less intense. This disorder is multiplied in the second Zr shell, and the ‘diagonal’ Zr–Zr distance now varies too much to contribute towards

the EXAFS spectrum. This distorted sheet structure is schematically illustrated in Figure 5-7, assuming complete oxolation and neglecting the presence of residual nitrate.

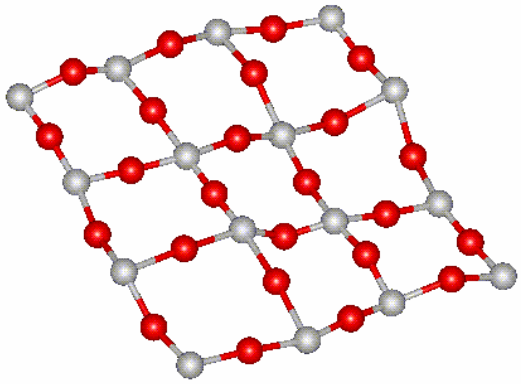

Figure 5-7: Representation of distorted ZrO_2 sheets. Zirconium atoms are grey, and oxygen atoms red.

The change in modelled Zr–Zr bond length from 3.54 to 3.37 Å is very similar to that found by an EXAFS study of the calcination of zirconyl chloride-exchanged clay, in which the Zr–Zr distance decreases from 3.59 to 3.38 Å.[18]

The assignment of the second oxygen shell at 2.6 Å is not certain, so the large decrease in coordination number could be due to a number of processes. If the shell is to assigned to water or nitrate groups, then the loss of these groups is consistent with DTA/TGA data in Section 5.3.5, showing that these groups are lost in the temperature range 150 - 300°C. If the shell is to be assigned to adjacent sheets, then the distortion of the sheets with oxolation will disrupt any regular spacing between them.

Crystallisation

As discussed in Section 2.4, there is a continuing debate over the mechanisms for the formation of the 'metastable' tetragonal phase. One theory often referred to is the 'structural similarity' theory: the short-range structure of the amorphous material closely resembles the structure of the tetragonal phase, so when crystallisation occurs the tetragonal structure requires less energy to form than the monoclinic structure. In principle, EXAFS is an ideal method to test this theory, although there have been no published reports of any attempts to do so.

The main limitation of conventional EXAFS analysis is that the structure is only expressed in one dimension, as a radial distribution of shells around a central atom. Table 5-5 lists the *r* and *N* values for shells fitted for the gel heated to 400°C. These values are compared with the equivalent values for the short-range structure of the metastable-tetragonal and monoclinic phases, calculated from previously published diffraction data for pure zirconia.[19,20] Values are also given for a hypothetical 'room-temperature cubic' phase, with the same unit-cell volume as the tetragonal phase.

Table 5-5: Short-range structure around the Zr atom in a range of materials

	amorphous sample		metastable t-ZrO_2 (from Igawa [19])		m-ZrO_2 (from Hill [20])		hypothetical c-ZrO_2	
	r (Å)	*N*	*r* (Å)	*N*	*r* (Å)	*N*	*r* (Å)	*N*
O	2.067(5)	4.8(3)	2.082	4	2.15-2.28	7	2.212	8
	2.563(19)	0.9(2)	2.359	4				
Zr	3.371(11)	3.9(5)	3.591	4	3.334	1	3.612	12
			3.623	8	3.47*	5		
					3.580	1		

* averaged value

The main Zr–O distance and coordination number of the amorphous material is similar to that for the first oxygen shell in the tetragonal structure, however there is no correlation with the second oxygen shell. The Zr–Zr distance is closer to the average distance in the m-ZrO_2 structure than in the t-ZrO_2 structure. Using this approach, it would appear that there is no particular similarity between the short-range structure of the 'amorphous' material, just before crystallisation, and the short-range structure of the 'metastable' tetragonal (or cubic) phase.

However, a three-dimensional approach can be made to this problem, using the structural model developed above. The tetragonal structure can be visualised as a series of layers parallel to the 001 plane, as shown in Figure 5-8. Each layer consists of zirconium atoms arranged in a square lattice, with adjacent zirconium atoms bridged by an oxygen atom that lies either above or below the plane, as shown in Figure 5-9. In contrast, the monoclinic phase has a much more complicated structure, and a plane of zirconium atoms as described here is not easily distinguished.

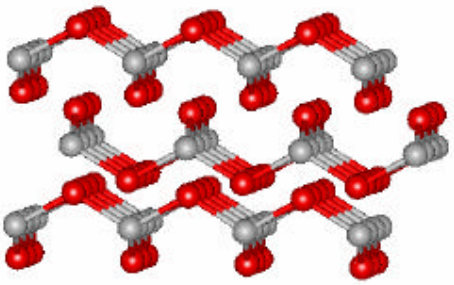

Figure 5-8 (above): Illustration of the tetragonal zirconia structure, showing the layers parallel to the 001 plane. Zirconium atoms are grey, and oxygen atoms red.

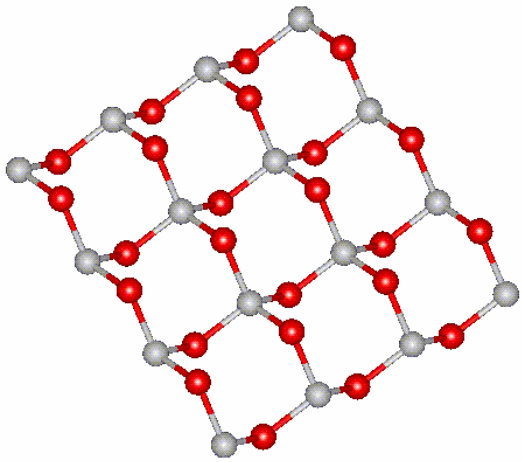

Figure 5-9 (at right): Illustration of a single 'layer' out of the tetragonal structure. Compare with Figure 4-6 and Figure 5-7.

Assuming that the structure of the material heated to 400°C is similar to that illustrated in Figure 5-7, it is simple to envisage how topotactic crystallisation into the tetragonal phase may take place. If these sheets are stacked in an appropriate way, then very little rearrangement is required to nucleate the tetragonal phase. One complicating factor is the Zr–Zr distance in the sheet, which is 3.37 Å for the amorphous material and 3.59 Å for the tetragonal phase, so some expansion will occur on crystallisation.

The EXAFS data thus provides some supporting evidence for the 'structural similarity' theory, at least for the material examined here. A much more extensive study, examining a range of amorphous zirconia precursors, would be required to establish a good case for the general occurrence of this mechanism.

The crystallised material was also examined by EXAFS. Figure 5-5e shows the Fourier-transformed EXAFS spectrum of a gel that has been heated to 470°C for an hour. The Raman spectrum and XRD pattern (Figure 5-15c) indicate that this material consists of crystalline tetragonal zirconia, and the FT profile is similar to that previously reported for yttria-stabilised tetragonal zirconia by Li *et al.*.[21]

The modelled parameters in Table 5-6 are fairly similar to those reported by Li *et al.*, except for a large discrepancy in the coordination number for the zirconium shell. This discrepancy is discussed in more detail in Section 10.3.7, and may be due to the presence of a fraction of amorphous material (see the TEM image in Section 6.3.3). Note, however, that Li *et al.* fixed

the coordination numbers, so that a direct comparison may not be valid. The uncertainties in the values found for the coordination numbers for the oxygen shells are also quite high, which is unfortunate in view of the debate on the role of vacancies in the stabilisation of pure tetragonal zirconia at low temperatures (discussed in Section 2.4.2.2).

Table 5-6: Comparison of EXAFS models for tetragonal zirconia.

	O_I		O_{II}		Zr	
	r (Å)	N	r (Å)	N	r (Å)	N
Modelled values	2.085(4)	3.5(4)	2.317(10)	3.5(4)	3.606(2)	8.1(4)
Reported by Li *et al*.[21]	2.10	4†	2.33	4†	3.62	12†

† Fixed

In-situ EXAFS

A further EXAFS study was carried out, measuring the EXAFS spectrum of the gel *in-situ* as it was heated. This study is fully discussed in Section 10.4, and only the main conclusions will be given here. The decomposition and crystallisation reactions were clearly observed, demonstrating the potential of the technique for such studies. However, the amount of information available was limited by a number of experimental difficulties. Most observations are consistent with the previous EXAFS study and other studies described in this chapter. There is an indication that the decomposition occurs in two stages, in which the Zr–Zr distance first increases, then decreases. The changes in short-range structure associated with crystallisation take place within a 40°C interval. Improvements in spectrum quality, and reduction of the time between collection of sample spectra, are necessary to make full use of this technique's potential.

5.3.3 X-ray diffraction

The X-ray diffraction patterns of a series of heat-treated samples are given in Figure 5-10.* The diffraction pattern for the unheated gel is discussed in Section 4.3.6. As done previously, the pattern can be divided into a low-angle region ($2\theta < 15°$) and a high-angle region ($2\theta > 15°$) for discussion.

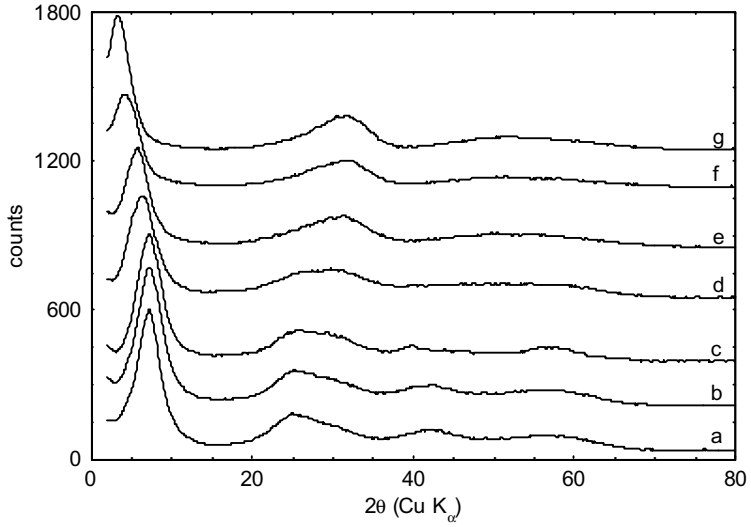

Figure 5-10: XRD patterns of a) an unheated gel, and gel samples heated for 5 minutes at b) 150°C, c) 200°C, d) 250°C, e) 300°C, f) 350°C and g) 400°C.

The low-angle region

The effect of the age of a sol on the low-angle region of the diffraction pattern has been discussed in Section 4.3.6. Gels that are formed from sols that are less than one month old have a single peak at approximately 12 Å, while gels formed from sols that have been aged for at least 7 months have two peaks at approximately 12 and 22 Å. Both peaks are attributed to the 'average' distance between the plate-shaped particles in the gel. The 12 Å peak is assigned to a phase in which the particles are arranged face-to-face in layers (phase A). The 22 Å peak is assigned to a phase in which the particles are arranged face-to-edge, in a 'house of cards' structure (phase B).

Figure 5-11 expands the low-angle region of the diffraction patterns given in Figure 5-10. The original gel was formed from a sol that had been aged for two days, and so has only a single

peak at low-angle. For selected samples this region was measured again with a narrower divergence slit for improved resolution, and these patterns are given in Figure 5-12. The positions of the peak, which are very similar for both sets of measurements, are listed in Table 5-7.

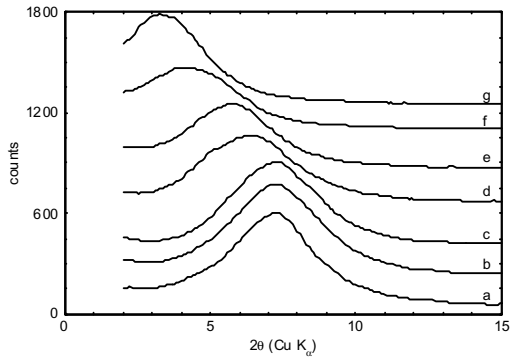

Figure 5-11: Low-angle XRD patterns of a) an unheated gel, and gel samples heated for 5 minutes at b) 150°C, c) 200°C, d) 250°C, e) 300°C, f) 350°C and g) 400°C.

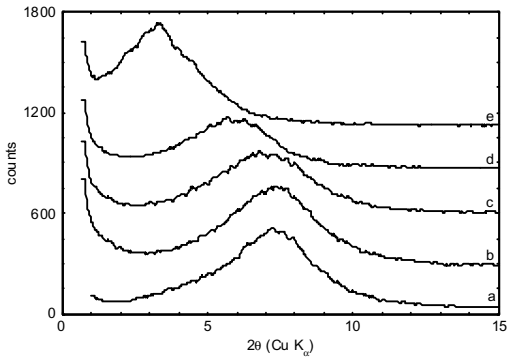

Figure 5-12: Low-angle XRD patterns of a) an unheated gel, and gel samples heated for 5 minutes at b) 150°C, c) 200°C, d) 300°C and e) 400°C. The divergence slit has been narrowed for better resolution but less intensity.

Table 5-7

Treatment temperature	$2\theta^*$	d^* (Å)
unheated	7.32°	12.1
150°C	7.30°	12.1
200°C	7.00°	12.6
250°C	(6.4°)	(13.9)
300°C	6.0°	14.7
350°C	(4.2°)	(21)
400°C	3.3°	27

* Values in parentheses are from wide-divergence slit measurement.

The peak remains at 12 Å up to 150°C. Above this temperature the peak shifts to a higher position, with a small shift to 15 Å by 300°C, and a much larger shift to 27 Å by 400°C. Between 150 and 350°C the intensity of the peak also decreases, but it becomes much greater after heating to 400°C.

---

* Note that the term 'diffraction pattern' will be used throughout, even though certain features may be due to scattering rather than diffraction.

The shift in peak position with heat-treatment is attributed to an increasing distance between the particles in phase A. The most probable mechanism, at least up to 300°C, is the distortion of the particles, which may cause them to 'buckle' or 'curl', and thus increase in average separation. Note that beyond 300°C the low-angle peak shifts considerably, while the short-range structure, as characterised by EXAFS, does not change. Over this temperature range the distorted particles may be coalescing, increasing the particle size and the average distance between particles.

Figure 5-13 shows changes in the low-angle region when there are two peaks in the pattern of the unheated gel. In this case the gel was dried from a sol that was 50 months old. The peak positions are listed in Table 5-8. The peak at 12 Å behaves in a similar way to that of the equivalent peak in the previous sample, decreasing in intensity and shifting to a higher *d*-spacing. The peak at 22 Å becomes stronger, and shifts to a slightly lower *d*-spacing. By 300°C these two peaks have merged, and the diffraction patterns of samples heated to higher temperatures are similar to the equivalent for the previous sample.

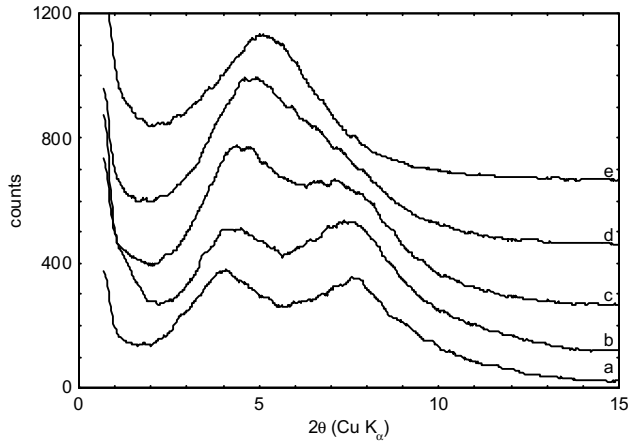

Figure 5-13: Low-angle XRD patterns of a) an unheated gel, from a sol aged 50 months, and the same gel heated for 5 minutes at b) 150°C, c) 200°C, d) 250°C, and e) 300°C.

Table 5-8

Temperature (°C)	2θ	*d* (Å)	2θ	*d* (Å)
unheated	4.0	22	7.7°	11.5
150	4.2°	21	7.6°	11.6
200	4.6°	19	7.3°	12
250	4.9°	18		
300	5.2°	17		

The shift in the 22 Å peak characterises the changes in phase B with heating. The average distance between particles decreases, which implies that the 'house of cards' structure is at least partially collapsing, probably also due to the distortion of the particles mentioned above. Comparing the patterns in Figure 5-12**d** and Figure 5-13**e,** it appears that the differences in the medium-range order of phase A and phase B are largely eliminated after heating to 300°C.

High-angle region

Figure 5-14 expands the high-angle region of the diffraction patterns shown in Figure 5-10. Very similar results to Figure 5-14 were obtained for heated samples from a gel which had two low-angle diffraction peaks. As determined previously in Section 4.3.6, ageing of the sol had no effect on this region of the diffraction pattern.

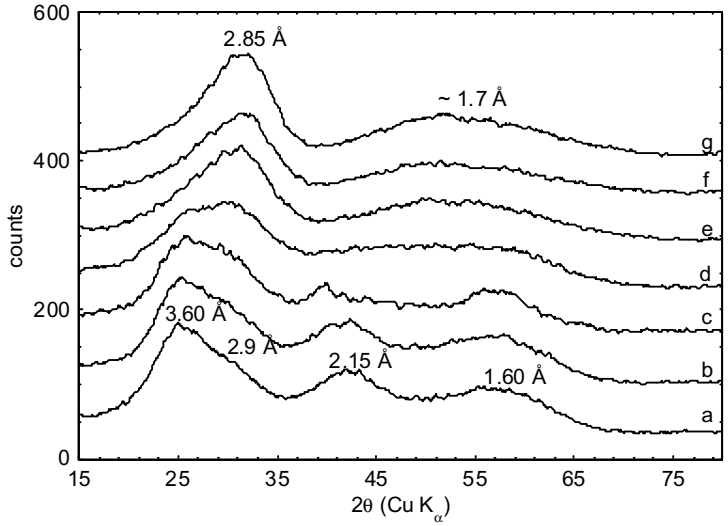

Figure 5-14: High-angle XRD patterns of a) an unheated gel, and gel samples heated for 5 minutes at b) 150, c) 200, d) 250, e) 300, f) 350 and g) 400°C.

There are strong changes in the shape and position of the peaks between 150 and 300°C. The strongest peak at 3.6 Å becomes weaker and disappears by 300°C, while the shoulder at ~ 2.9 Å increases in intensity and becomes the dominant peak. The 2.15 and 1.6 Å peaks become much less distinct, and are replaced by a very broad 'peak' centred at approximately 1.7 Å.

The decrease in intensity of the peaks at 3.6 and 2.15 Å can be interpreted on the basis of the changes in the short-range structure, as elucidated by the EXAFS study in Section 5.3.2. The 3.6 Å peak in the diffraction pattern of the unheated gel has been assigned to scattering from the Zr–Zr interatomic distance, and the EXAFS study found that between 150 and 300°C the disorder in this distance greatly increases. Thus it is expected that the equivalent peak in the XRD pattern would also diminish over the same interval. Similarly, the 2.15 Å peak in the diffraction pattern is assigned to the principle Zr–O distance, and this peak disappears as the number of oxygen atoms coordinated around the zirconium atom decreases.

The assignment for the 2.85 Å peak is more difficult. It cannot be assigned to an interatomic distance, as the Zr–Zr distance, even for crystalline phases, is always greater than 3.3 Å, and the Zr–O distance is always less than 2.3 Å. The similarity in the position of this peak with the primary peak in the tetragonal phase (see Figure 5-15) may suggest that very small crystals of tetragonal phase are present, but the absence of any bands characteristic of the tetragonal phase in the corresponding Raman spectrum argues strongly against this assignment. This peak must therefore remain unassigned.

The high-angle pattern changes very little above 300°C until crystallisation at 450°C. This observation, consistent with the EXAFS results, indicates that the short-range structure does not change over this interval, even though the medium-range structure is evolving.

The crystallised material

Diffraction is the most direct method of identifying crystallisation. Figure 5-15 shows the diffraction patterns of three samples, the first two heated to 400 and 500°C for 5 minutes, and the third heated to 470°C for an hour. Clearly crystallisation has taken place between 400 and 500°C, and virtually all of the diffraction peaks in the crystalline samples can be assigned to the tetragonal zirconia phase. The tetragonal phase can be clearly distinguished from the cubic phase by the characteristic 'peak splitting'. Two minor peaks in the sample heated to 500°C are assigned to the two strongest peaks in the diffraction pattern of monoclinic zirconia. Aside

from these two peaks, the diffraction patterns in Figure 5-15**b** and **c** are virtually identical. The positions of the peaks assigned to the tetragonal phase are listed in Table 5-9.

A discussion of crystal size, lattice parameters, phase transformations *etc*, can be found in Chapter 6.

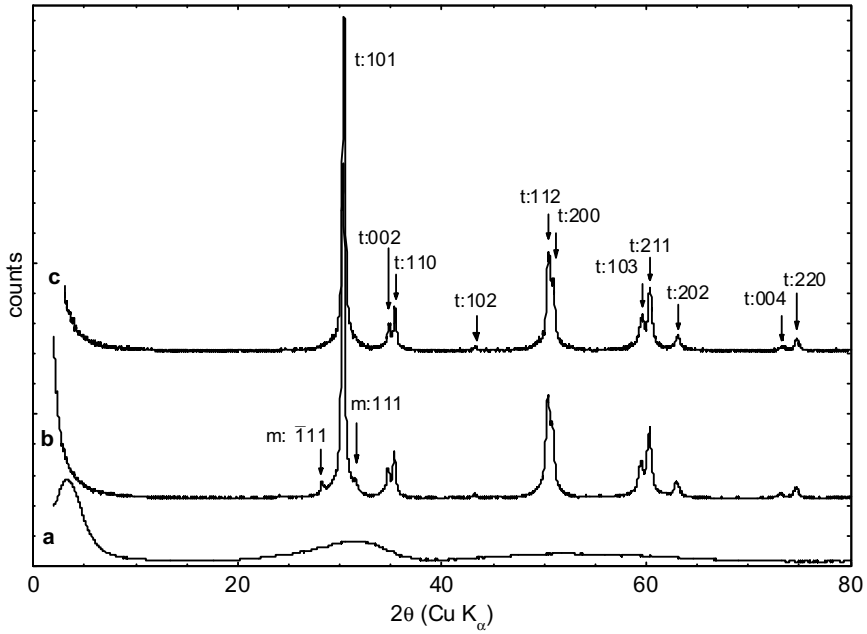

Figure 5-15: Diffraction patterns of standard gels heated at a) 400°C for 5 min, b) 500°C for 5 min, and c) 470°C for 1 hour. Peaks are assigned to either the tetragonal (t) or monoclinic (m) zirconia phase.

Table 5-9

2θ (°)	*d* (Å)	*h k l*
30.42	2.938	1 0 1
34.86	2.574	0 0 2
35.43	2.534	1 1 0
43.26	2.090	1 0 2
50.46	1.809	1 1 2
50.92	1.795	2 0 0
59.56	1.551	1 0 3
60.38	1.534	2 1 1
63.10	1.474	2 0 2
73.30	1.292	0 0 4
74.70	1.270	2 2 0

5.3.4 Dispersibility

A striking characteristic of this system is that gels can be redispersed in water even after substantial heating. Table 5-10 shows the results of dispersibility tests on samples that had been heated for five minutes at a range of temperatures. A 'redispersible' gel dispersed quite quickly, and when the water dried a transparent gel remained. A 'non-dispersible' material did not disperse, and only a white powder remained when the water dried. There is a clear distinction between dispersible and non-dispersible materials; a gel heated briefly to 200°C remains completely dispersible, while a gel heated to 250°C is unable to be dispersed. It was also found that the gel is dispersible after 48 hours at 150°C.[2]

Table 5-10

Treatment temperature	Result
150°C	dispersible
200°C	dispersible
250°C	non-dispersible
300°C	non-dispersible

The most likely reason for the loss of dispersibility is that the surface characteristics of the particles have changed. Two mechanisms could be at work here, and it is probably that both contribute in some way. First, the loss of nitrate groups that can be readily converted to aqueous anions could prevent dispersal of the particles, since dispersal requires sufficient counter-ions to balance the charge on the dispersed particles. From the discussion in Section 5.3.1, and the Raman spectrum in Figure 5-1, the number of D_{3h} aquated nitrate groups and the C_{2v} bidentate-coordinated nitrate groups decrease in number significantly between 200 and 250°C, possibly beyond a critical point at which dispersal cannot take place.

The second mechanism by which the surface could be altered is through the oxolation of the Zr–$(OH)_2$–Zr bridges, which will greatly change the surface potential. EXAFS spectroscopy at finer temperature intervals would be the best method to test this mechanism.

A further way in which the particles could become non-dispersible is if they were cross-linked together, for example by the condensation of terminal hydroxy-groups at the surface to form Zr–O–Zr bonds. The condensation of only a fraction of the hydroxy groups would be necessary, and it would be very difficult to characterise this process by either vibrational spectroscopy or EXAFS.

5.3.5 DTA/TGA

A typical DTA/TGA trace for a ZN1.0 gel is given in Figure 5-16. The top trace shows the heat-flow to and from the sample, indicating endothermic and exothermic reactions. The lower traces show the mass loss during heating, and the rate of mass loss. Three main stages can be distinguished. The first two stages are endothermic decomposition reactions, peaking at approximately 120 and 280°C, during which approximately 40 % of the mass is lost, depending on the water content. Although these two stages peak at different temperatures, they overlap somewhat and cannot be fully separated. The third stage is a complex exothermic reaction at approximately 460°C.

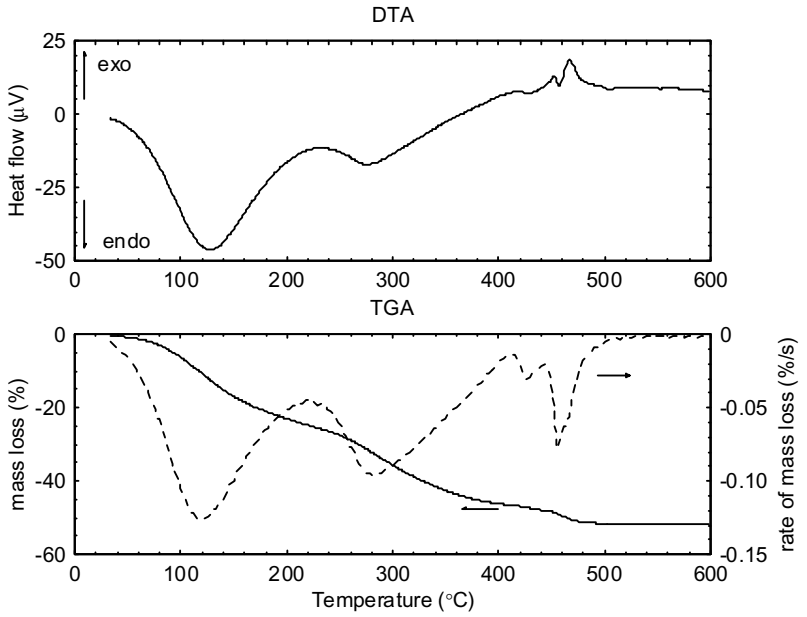

Figure 5-16: Typical set of DTA/TGA traces for a standard gel. The small arrows on the thermogravimetric trace indicate the appropriate axis.

For comparison, Figure 5-17 shows the DTA/TGA traces for the 'zirconium hydroxide' material, which was precipitated from a zirconyl nitrate solution. The traces up to 400°C are very similar, while the exothermic reaction at 455°C causes a much sharper peak in the DTA trace, and a much smaller mass-loss.

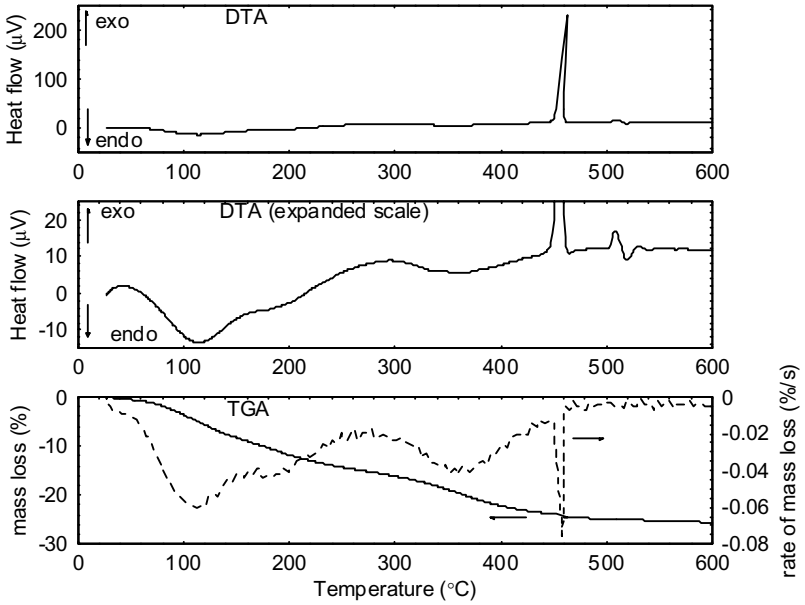

Figure 5-17: DTA/TGA trace for precipitated zirconium hydroxide. The strong exothermic peak is 'tilted' due to the sample temperature increasing rapidly during the reaction, then being allowed to cool slightly before the heating ramp continues. The feature in the DTA trace at approximately 510°C is probably an instrumental artefact. The small arrows on the thermogravimetric trace indicate the appropriate axis.

Decomposition reactions

Knowing the original structure of the gel, the nature of the first two stages of decomposition can be determined with the help of the Raman and EXAFS data. The chemical analysis of the gel, discussed in Section 4.3.2, showed that the gel contains approximately 10 wt % water, 8 % hydroxy groups and 28 wt % nitrate (as HNO_3).

It is interesting to note that the traces for the standard ZN1.0 gel and the precipitated hydroxide are very similar up to 400°C, although the magnitude of the mass-losses are quite different. While over a quarter of the mass of the standard gel is nitrate, the nitrate content of the precipitated hydroxide is much smaller. From a comparison of the two sets of traces, the decomposition and loss of the nitrate is clearly not the sole cause for any of the major features of the trace up to 400°C.

The first stage of decomposition takes place largely between 80 and 200°C, peaking at approximately 120°C, and is strongly endothermic. It involves the loss of approximately 20 % of the original mass, with the peak mass-loss rate coinciding with the endothermic peak. It can be assumed that during this stage all free water present in the gel is removed, and probably most water molecules coordinated to the surface of the particles. However, water can only

account for approximately 10 % of the original mass, so another component must also be lost in this stage. The XRD, Raman and EXAFS data discussed in previous sections show that the Zr–O structure of the gel does not change significantly after heating at 150°C for 5 minutes, so permanent oxolation of the hydroxy bridges is unlikely to occur at this stage, although limited reversible oxolation may occur. The loss of nitrate groups is the main alternative. The Raman spectra discussed in Section 5.3.1 show that after heating to 150°C much of the original non-coordinated nitrate anions are no longer present, either converted to coordinated-nitrate groups or to NO_x, and this process is nearly completed by 200°C. The most likely conclusion is that during the first stage of decomposition a majority of the non-coordinated nitrate anions are converted to NO_x.

The second stage of decomposition takes place largely between 230 and 350°C, peaking at approximately 280°C, and is more weakly endothermic. It also involves the loss of approximately 20 % of the original mass. According to Raman, XRD and EXAFS characterisation this temperature range corresponds with substantial changes in the short-range structure of the material, most probably oxolation of the hydroxy bridges. The Raman spectra also show that much of the nitrate is also lost in this region.

Reactions associated with crystallisation

The DTA/TGA traces give evidence of a complex series of reactions between 400 and 500°C, and a detail of this region is given in Figure 5-18. The clearest features in the DTA trace are two exothermic peaks, at approximately 453 and 467°C. There is also a sharp mass-loss of approximately 5 %, peaking at 456°C, in between the two exothermic peaks. A small, endothermic mass-loss at ~ 430°C precedes the main reaction, and a slightly exothermic reaction with no associated mass-loss follows at ~ 495°C. Table 5-11 lists the activation energy values for each of the main exothermic peaks and the main mass-loss, which were determined in a previous study.[2] *

* Activation energies were determined by the Ozawa method,[22] which assumes a simple Arrhenius relationship between the 'peak' temperature and the heating rate. Hayward *et al.* showed that where surface crystallisation dominates, as is expected in high-surface-area gels, no modification is required to this method.[23]

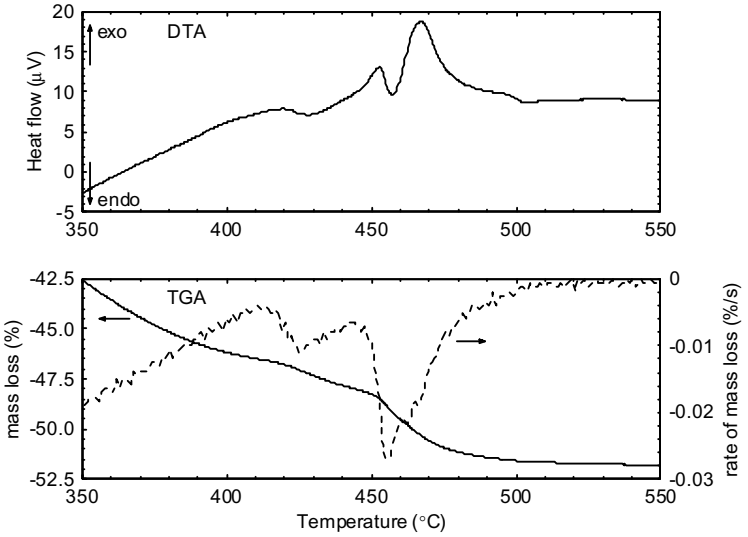

Figure 5-18: Typical set of DTA/TGA traces for a standard gel, between 350 and 550°C.

Table 5-11

Reaction	Activation energy (kJ/mol)
First exothermic peak	335
Second exothermic peak	340
Main mass loss	390

XRD and Raman evidence discussed in previous sections strongly suggests that the crystallisation of the tetragonal zirconia phase occurs at a similar temperature to the reactions observed in the DTA/TGA trace, but these reactions are more complex than would be expected for a simple crystallisation reaction. Previous studies of the crystallisation of amorphous zirconia have been reviewed in Section 2.3.2. In all cases where pure, 'amorphous' zirconia is heated at a constant rate, a strong, sharp exotherm occurs concurrently with crystallisation. This is sometimes termed the 'glow' exotherm, and a good example is shown in Figure 5-17. This peak is generally attributed to the heat released during a transformation from a high-entropy amorphous state to a crystalline state, but some studies have presented evidence that suggests that the exotherm is instead due to a rapid decrease in surface area, which may not occur concurrently with crystallisation for certain mixtures of zirconia with other oxides.

Regardless of the actual assignment of the glow exotherm, there is no report of two closely-spaced exothermic peaks in the literature. Another point to note is that the intensity of the

exotherm with respect to the decomposition endotherms is much less in the ZN1.0 gel than for the precipitated hydroxide.

Although the 'double peak' can be interpreted as two separate exothermic reactions, a more satisfactory approach is to treat it as *a combination of a rapid endothermic reaction occurring nearly simultaneously with a less-rapid exothermic reaction*. The resultant DTA trace would be that of a narrow endothermic peak superimposed on a broad exothermic peak, leading to two minor exothermic peaks as illustrated in Figure 5-19. Furthermore, the main mass-loss can be associated with the endothermic reaction, as the peak mass-loss occurs at the same temperature that the DTA trace reaches a minimum between the two exothermic peaks. This interpretation is consistent with the measured activation energies, which indicate that the two exothermic peaks are closely related, while the higher activation energy for the mass-loss is indicative of a reaction that is more independent.

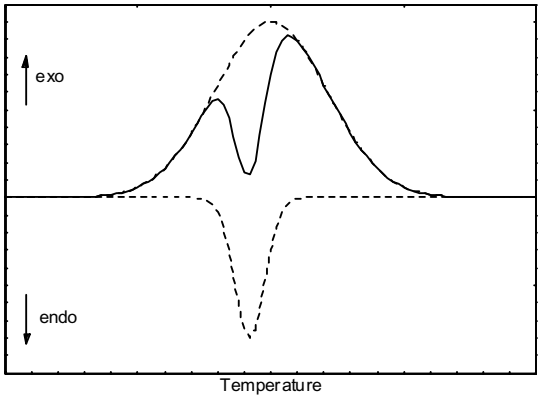

Figure 5-19: Illustration of how superimposed exothermic and endothermic peaks can lead to two exothermic peaks.

If we interpret the DTA/TGA trace as a combination of an exothermic and an endothermic peak, then we can reasonably assume that the exothermic component is the 'glow' exotherm associated with crystallisation. However, we must still identify the nature of the endothermic mass loss. The two candidates for this process are the removal of remaining nitrate groups to form NO_x gas, and the final oxolation of residual hydroxy groups. The evidence available points towards the former process. The Raman spectrum of the standard ZN1.0 gel heated to 400°C indicates that there is a significant quantity of residual nitrate present. Although it is difficult to make a comparison of the intensities of Raman bands in the spectra of different materials, the spectra discussed above in Section 5.3.1 indicate that a substantial quantity of

the residual nitrate is lost between 400 and 500°C. Furthermore, the hydroxide precipitated from a nitrate solution contains much lesser quantities of nitrate, and gives a single sharp exothermic peak at 455°C. There is a sharp mass-loss at this temperature, but of only 0.6 % of the original sample mass. Given these observations, it is reasonable to assign the endothermic peak to the conversion of residual nitrate groups to NO_x, although a small amount of oxolation may take place concurrently.

Without more detailed data on the structure during this process, the mechanism by which the loss of nitrate is linked to the crystallisation can only be speculated on. Three possible contributing factors are:

1. The nitrate groups are probably mainly located on the surface of the particles, and crystallisation is likely to be accompanied by a rapid loss of surface area.
2. The nitrate groups are too large to be incorporated into the crystalline lattice.
3. As indicated by the exotherm, the crystallisation/surface-area-reduction process is accompanied by a considerable release of heat, which could provide activation energy for the endothermic loss of nitrate.

A surprising observation was that the ageing of the sol not only affects the structure of the gel, but also the crystallisation reaction. Figure 5-20 shows sample DTA traces of batches of gel, each dried from a sol aged for a period between one day and 50 months.

In all cases the original exothermic ‘double peaks’ are still observed, although in general they become weaker with increasing age of the sol. The most prominent change is the appearance of a DTA peak at approximately 495°C, which is not associated with any mass loss, and becomes stronger with increasing age of the sol.

It is proposed that the changes in the DTA trace are associated with the two ‘phases’ found in the gel, discussed in Section 4.3.6. While the exothermic ‘double peaks’ are assigned to the crystallisation of ‘phase A’, the new exothermic peak is attributed to the crystallisation of ‘phase B’. The thermal decomposition of the two phases is studied by XRD in Section 5.3.3, which shows that the arrangement of the particles in the two phases are similar after heating to 300°C. However, the DTA results show that sufficient difference remains between the structures to inhibit crystallisation in phase B, so that it lags approximately 40°C after crystallisation in phase A. The nature of this difference in structure remains uncertain.

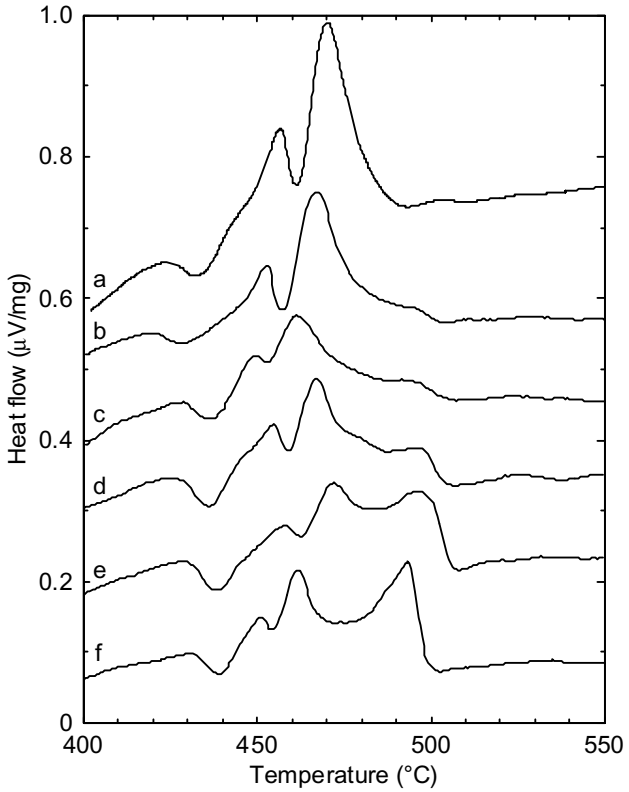

Figure 5-20: DTA traces of gels from sols that have been aged for a) one day, b) 2 days, c) 15 days, d) 2 months, e) 8.5 months, and f) 50 months. The heat-flow scale has been normalised by the original mass of the sample.

A further point to note is that there is no mass-loss associated with the crystallisation of phase B. This could be attributed to the fact that the packing of the particles in phase B is much more open than in phase A, at least up to 150°C, so the nitrate anions are more easily removed.

The temperatures at which the DTA peaks in Figure 5-20 occur vary up to 10°C between samples. This variation could be at least partially due to variation in size of the gel fragments after grinding, as it is known that fragment size can affect the temperature of reactions in DTA.[24]

5.4 Summary and conclusions

From the studies discussed in this chapter the decomposition of the gel and crystallisation of the oxide have been investigated. Three distinct stages of decomposition have been identified. The stages can be summarised as follows:

First stage

During heating up to 150°C there is very little change in the short-range structure of the particles. Any water contained in the gel, including pore water and structural water, is lost. Much of the non-coordinated nitrate (second-sphere) is also lost, probably mostly converted to NO_x gas. The material remains dispersible in water after cooling.

Second stage

- Between 150 and 300°C a comprehensive decomposition of the Zr–OH framework of the particles take place, leading to distortion of the structure and a large increase in disorder. The principle reaction taking place is oxolation of hydroxy bridges.
- Where the particles are packed in a layer structure, the distance between them increases, probably due to distortion (warping) of the particles.
- Most of the coordinated-nitrate groups (first sphere) are lost between 200 and 300°C, and the material becomes non-dispersible after heating to 250°C.

Third stage

- The decomposition is largely complete by 300°C, leaving zirconium oxide. Little further change occurs in the short-range structure until crystallisation.
- Above 300°C the average distance between particles increases substantially, and this is attributed to particle growth.
- The Raman and EXAFS spectra show that the amorphous oxide does *not* contain nano-sized, non-diffracting crystals.

Crystallisation

- Pure, tetragonal phase crystallises from the amorphous oxide at approximately 450°C, and a high-quality X-ray diffraction pattern and Raman spectrum are reported.
- The crystallisation process was found to involve two near-simultaneous reactions: the exothermic crystallisation of the amorphous material into the tetragonal phase, and the endothermic conversion of residual nitrate groups to NO_x gas.
- A structural mechanism for crystallisation has been proposed, based on similarities between the tetragonal crystal structure and the disordered sheet structure in the amorphous material just prior to crystallisation.

5.5 References

1. P.D. Southon, J.R. Bartlett, J.L. Woolfrey and M.G. Stevens, "Evolution of the structure of aqueous zirconia gels during preparation and heating" *Ceramic Transactions 81* 75-80 (1998)
2. P.D. Southon, "Evolution of the structure of zirconia gels during preparation and heating" B. Appl. Sc. (Hons) Thesis, UTS (1995)
3. V.G. Keramidas and W.B. White, "Raman scattering study of the crystallisation and phase transformation of ZrO_2" *J. Am. Ceram. Soc. 57* [1] 22-24 (1974)
4. R. Srinivasan, B.H. Davis, O.B. Cavin and C.R. Hubbard, "Crystallisation and phase transformation process in zirconia: an in situ high-temperature X-ray diffraction study" *J. Am. Ceram. Soc. 75* [5] 1217-1222 (1992)
5. W. Stichert and F. Schüth, "Influence of crystallite size on the properties of zirconia" *Chem. Mater. 10* [7] 2020-2026 (1998)
6. M. Ishigame and T. Sakurai, "Temperature dependence of the Raman spectra of ZrO_2" *J. Am. Ceram. Soc. 60* [7-8] 367-369 (1976)
7. A. Feinberg and C.H. Perry, "Structural disorder and phase transitions in ZrO_2-Y_2O_3 system" *J. Phys. Chem. Solids 42*, 513-518 (1981)
8. M. Yashima, K. Ohtake, M. Kakihana, H. Arashi and M. Yoshimura, "Determination of tetragonal-cubic phase boundary of $Zr_{1-x}R_xO_{2-x/2}$ (R = Nd, Sm, Y, Er and Yb) by Raman scattering" *J. Phys. Chem. Solids 57* [1] 17-24 (1996)
9. D.-J. Kim, "Effect of tetravalent dopants on Raman spectra of tetragonal zirconia" *J. Am. Ceram. Soc. 80* [6] 1453-1461 (1997)
10. G.A. Kourouklis and E. Liarokapis, "Pressure and temperature dependence of the Raman spectra of zirconia and hafnia" *J. Am. Ceram. Soc. 74* [3] 520-523 (1991)
11. R. Srinivasan, S.F. Simpson, J.M. Harris and B.H. Davis, "Discrepancies in the crystal structures assigned to precipitated zirconia" *J. Mater. Sci. Lett. 10* [6] 352-354 (1991)
12. D.A. Ward and E.I. Ko, "Synthesis and structural transformation of zirconia aerogels" *Chem. Mater. 5* 956-969 (1993)
13. M.J. Paterson and B. Ben-Nissan, "Multilayer sol-gel zirconia coatings on 316 stainless steel" *Surfaces and Coatings Technology 86-87* 153-158 (1996)
14. G. Štefanić, S. Musić, S. Popović and A. Sekulić, "FT-IR and laser Raman spectroscopic investigation of the formation and stability of low temperature *t*-ZrO_2" *Journal of Molecular Structure 408/409* 391-394 (1997)
15. D. Michel, M.T. Van Den Borre and A. Ennaciri, "Vibrational spectra and force fields of tetragonal zirconia and zirconium germanates" *Advances in Ceramics 24* (Science and Technology of Zirconia III) 555-562 (1988)
16. A.P. Mirgorodsky, M.B. Smirnov and P.E. Quintard, "Lattice-dynamical study of the cubic-tetragonal-monoclinic transformation of zirconia" *Phys. Rev. B 55* [1] 19-22 (1997)
17. K. Nakamoto, *Infrared and Raman spectra of inorganic and coordination compounds*, 4th Edition, Wiley-Interscience, New York (1986)
18. J. Miehebrendle, L. Khouchaf, J. Baron, R. Ledred and M.H. Tuilier, "Zr-exchanged and pillared beidellite - preparation and characterization by chemical analysis, XRD and Zr K EXAFS" *Microporous Materials 11* (3-4) 171-183 (1997)
19. N. Igawa, Y. Ishii, T. Nagasaki, Y. Morii, S. Funahashi and H. Ohno, "Crystal structure of metastable tetragonal zirconia by neutron powder diffraction study" *J. Am. Ceram. Soc. 76* [10] 2673-2676 (1993)
20. R.J. Hill and L.M.D. Cranswick, "International Union of Crystallography Commission on Powder Diffraction Rietveld round robin. II. Analysis of monoclinic ZrO_2" *J. Appl. Cryst. 27*, 802-844 (1994)
21. P. Li, I.W. Chen and J.E. Penner-Hahn, "X-ray absorption studies of zirconia polymorphs. I. Characteristic local structures" *Phys. Rev. B 48* [14] 10063-10073 (1993)
22. T. Ozawa, "A modified method for kinetic analysis of thermoanalytical data" *J. Thermal Anal. 9*, 369-373 (1976)
23. P.J. Hayward, E.C. Vance and D.C. Doern, "DTA/SEM study of crystallisation in sphene glass-ceramic" *Ceram. Bull. 66* [11] 1620-1626 (1987)
24. R. F. Speyer, *Thermal Analysis of Materials*, Marcel Dekker, New York, 1994

6. Structure of the crystallised oxide

6.1 Introduction

This chapter investigates the microstructural changes that occur in the crystalline zirconia during heating to temperatures between 450 and 1100°C. The microstructure of the oxide is important, as it determines the processing properties such as the ability to sinter. It is also of interest to investigate the relative stability of the tetragonal and monoclinic phases in the nanocrystalline zirconia. The structural features of most interest in this study are phase composition, crystal size and morphology, and porosity.

Two experimental approaches were used. The first approach was to heat samples of the standard gel to temperatures between 450 and 1100°C for an hour, cool to ambient temperature, and characterise the structure by a range of techniques. The second approach was to characterise the changes in structure *in-situ* during heating

The primary characterisation techniques used were Raman spectroscopy, X-ray diffraction (XRD), differential thermal and thermogravimetric analysis (DTA/TGA) transmission electron microscopy (TEM) and N_2 sorption. The characterisation techniques complement each other in investigating different aspects of the structure, as illustrated in Figure 6-1.

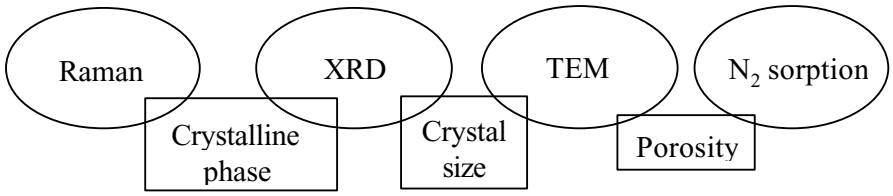

Figure 6-1: Schematic illustration of the applicability of various characterisation techniques to characterisation of various properties of the zirconia powders.

Five main topics are examined in this chapter; some are focussed on a particular property, and others on a particular technique. Section 6.3.1 discusses the phase composition of the crystalline powders, while the lattice parameters of the tetragonal phase are discussed in Section 6.3.2. Results concerning the size and shape of the crystals are given in Section 6.3.3, along with a discussion on the relationship between crystal size and crystalline phase. The loss of residual volatile components is covered briefly in Section 6.3.4. Porosity is examined in Sections 6.3.5 and 6.3.6, the first with TEM, and the second with nitrogen adsorption. Finally, a summary of the results and conclusions is given in Section 6.4.

6.2 Procedure

Samples of standard ZN1.0 gels were ground finely, heated in static air in a laboratory furnace at 10°C/min to a temperature between 450 and 1100°C, held at the maximum temperature for one hour, then furnace-cooled. Unless otherwise specified, the gel used was formed from a sol that was less than two days old.

The X-ray diffraction pattern of samples was measured with a laboratory diffractometer over the 2θ range 2 - 80°.* The samples were not ground or crushed before packing into the sample holders, in order to prevent any mechanically-induced phase transformation. Where several diffraction patterns are displayed together on a graph, the intensity is normalised by the collection time.

The phase ratios of tetragonal and monoclinic phase were calculated from the diffraction patterns. The *integrated intensities* of the 101 peak of the t-ZrO_2 phase and the 111 and $\bar{1}11$ peaks of the m-ZrO_2 phase were measured by fitting a mixed Lorentzian-Gaussian curve to each peak, with a baseline. Peak-broadening effects were large enough to render any asymmetry in the peaks negligible. The volume fraction of monoclinic phase (neglecting any amorphous component), f_m, was calculated in two stages: first a parameter representing the relative intensities of the major lines of the tetragonal and monoclinic phases was calculated using Equation 6-1, and then f_m was calculated using a calibration curve (Equation 6-2) developed by Toraya, Yoshimura and Sōmiya.[1]

$$X_m = \frac{I(\bar{1}11)_m + I(111)_m}{I(\bar{1}11)_m + I(111)_m + I(101)_t} \qquad \textbf{Equation 6-1}$$

$$f_m = \frac{1.311 \cdot X_m}{1 + (0.311 \cdot X_m)} \qquad \textbf{Equation 6-2}$$

The position of each peak was determined by a peak-fitting routine, and from these the lattice parameters for the 'metastable' tetragonal phase were determined from the peak positions with a computer program. This program fitted the observed peak positions to those predicted from the space group, taking into account a zero shift, and with various option for 'weighting' the value of each peak position.

---

* Scintag X1 Advanced Diffraction System, using Cu K_α radiation.

The peak half-width was measured for either the 101 peak of the t-ZrO_2 phase or the 111 and $\bar{1}11$ peaks of the m-ZrO_2 phase. The peak half-width due to crystal-size broadening, β, was calculated, assuming no significant contribution from strain and an instrumental peak-width of 0.07°. The average 'diffraction size' of the crystals, *D*, and was then calculated using the Scherer equation, given in Equation 6-3 (where β is given in radians). The value of *K* was fixed at a standard value of 0.89 radians.

$$D = \frac{K\lambda}{\beta \cos\theta} \qquad \textbf{Equation 6-3}$$

The Raman spectrum of each heated sample was measured under ambient conditions using a FT-Raman spectrometer.* The spectra were normalised, since scattering intensity is dependent on crystallinity, particle size, and various other properties of the sample.

Selected samples were deposited on a 'holey carbon' film and examined in a transmission electron microscope.† Parallel electron energy-loss spectroscopy was carried out with a scanning transmission electron microscope.‡

The mass loss and heat flow during heating was measured by simultaneous differential thermal analysis and thermogravimetric analysis (DTA/TGA)§. A number of gel samples were examined. Each sample was heated at 10°C/min in dry, flowing air to 1000°C, then maintained at 1000°C for 30 minutes.

The surface area, pore volume and pore distribution was determined from the nitrogen adsorption and desorption isotherm.** The equilibration interval for each point was varied from 20 s for samples with little porosity to 50 s for samples with high porosity, and in one case was increased to 90 s to ensure that the measured isotherm was reproducible.

---

* Bio-Rad FT-Raman II, using an excitation line of 1064 nm from a Nd:YAG laser. The effective resolution was 4 cm^{-1}.

† The two instruments used for this work were a JEOL 2000 FX analytical TEM and a JEOL 2000 FXII analytical TEM, the latter equipped with an Oxford Link ISIS energy dispersive spectroscopy (EDS) attachment. The accelerating voltage for both instruments was 200 kV.

‡ Vacuum Generators HB601 STEM, with accelerating voltage 100 kV.

§ Setaram TAG 24 simultaneous DTA/TGA instrument.

** Micromeritics ASAP 2010.

6.3 Results and discussion

6.3.1 Crystalline phase composition

The presence and relative abundance of crystalline zirconia phases have been determined from the X-ray diffraction pattern of each sample. Raman spectroscopy is also shown to be useful for determining phase composition.

When the standard gel is heated to just beyond the crystallisation temperature and cooled the resulting crystalline oxide is composed almost entirely of the 'metastable' tetragonal phase (t-ZrO_2), sometimes with a very small fraction of monoclinic phase present. When samples are heated beyond 500°C and cooled, the fraction of the monoclinic phase increases. The only crystalline phases identified in this study were the tetragonal and monoclinic phases of zirconia.

The X-ray diffraction patterns of samples heated to temperatures between 470 and 1100°C are shown in Figure 6-2. From these patterns the relative abundance of the tetragonal and monoclinic phases has been calculated, and expressed as volume fraction monoclinic in Table 6-1, neglecting any amorphous component. These values are plotted against treatment temperature in Figure 6-3.

Table 6-1

Treatment temperature (°C)	Volume fraction monoclinic phase
470	0 %
600	4 %
800	6 %
900	7 %
950	93 %
1000	98 %
1100	100 %

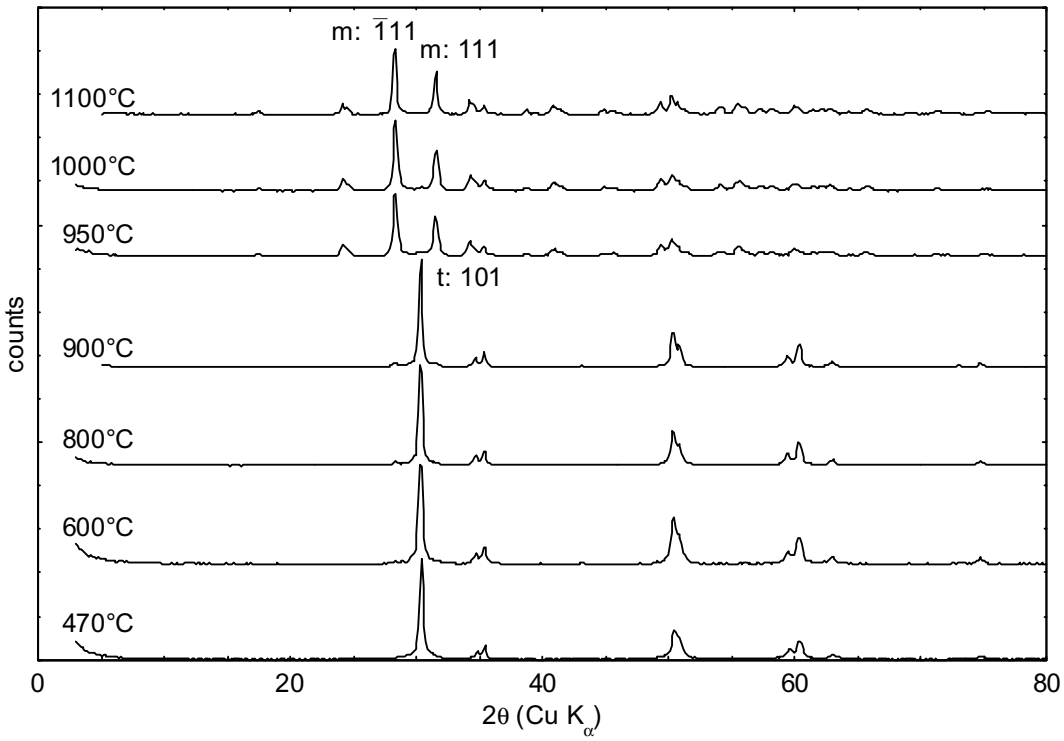

Figure 6-2: X-ray diffraction patterns for samples heated for one hour at the temperature indicated. The strongest diffraction peaks of the tetragonal (t) and monoclinic (m) phases are marked. The y-axis is displaced for clarity.

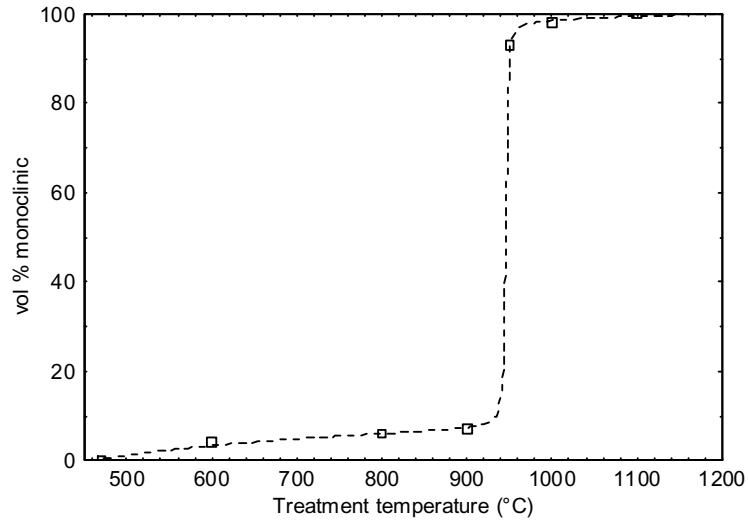

Figure 6-3: Volume fraction monoclinic phase after heating for one hour.

Up to 900°C the fraction of monoclinic phase remains below 7 vol %. After heating to 950°C or above the material has almost entirely converted to the monoclinic phase. Two processes can be inferred from this plot. The first involves a gradual increase of the fraction of

transformed monoclinic phase from crystallisation up to 900°C. The second stage involves the transformation of the majority (> 80 %) of the material to the monoclinic phase. This stage appears to be a discrete 'event' that occurs after heating to a 'threshold temperature' between 900 and 950°C, rather than a continuous process. Three factors that may be related to the threshold are discussed in the following Sections: the lattice parameters of the tetragonal phase in Section 6.3.2, the crystal size in Section 6.3.3, and the loss of surface species in Section 6.3.4. The t → m transformation, and the link with these factors, will be examined in more detail in Chapter 7.

Raman spectroscopy has previously been used to determine the phase composition of zirconia in a wide range of studies, for example to study structural changes at high temperatures [2,3] and pressures,[2] to monitor phase transformations in partially stabilised zirconia under loading,[4,5] to investigate structures in high-dopant zirconia,[6,7] and to identify the initial phase crystallised from zirconia gels.[8-11] Its major advantages over diffraction techniques is that it is very rapid, and that very little sample or sample preparation is required. The Raman spectra of samples heated to temperatures between 470 and 1000°C are shown in Figure 6-4. These spectra correlate with the results from XRD, and quantitative determination of phase ratios are very similar to those listed in Table 6-1. Raman spectroscopy is thus a useful method for quickly determining the phase composition of zirconia, and will be used in the next chapter for time-resolved studies.

Note that the bands assigned to the tetragonal phase become narrower with increasing treatment temperature, particularly for the band at 269 cm^{-1}. This attributed to increased crystallinity and homogeneity in the tetragonal crystals.

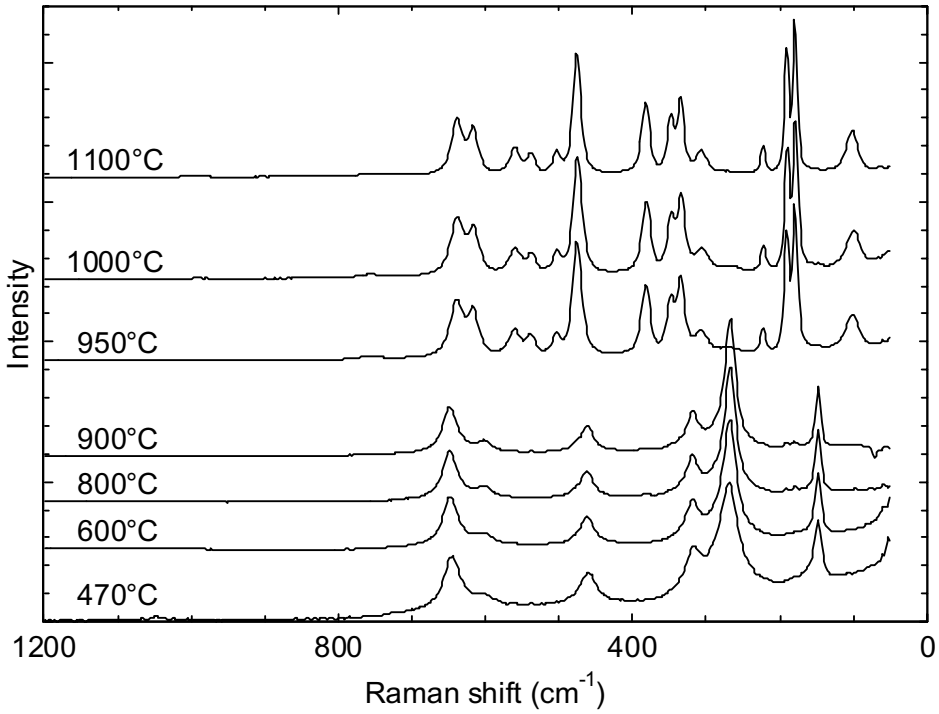

Figure 6-4: Raman spectra of standard gels heated for one hour at the temperatures indicated. All bands below 900 cm^{-1} in spectrum **a** are assigned to the tetragonal phase, and all bands in spectrum **g** are assigned to the monoclinic phase. The spectra of samples heated 470 - 900°C are normalised to the intensity of the 269 cm^{-1} band. The y-axis is displaced for clarity.

6.3.2 Lattice parameters of the tetragonal phase

The lattice parameters a and c for the tetragonal phase have been calculated from the diffraction patterns shown in Figure 6-2, and are listed in Table 6-2. For comparison, Table 6-3 lists the equivalent values reported by diffraction previous studies, using CuK_α [12] and neutron [13] radiation. As discussed in Section 2.1.1, the lattice parameter a can be calculated for either the primitive $P4_2/nmc$ unit cell, a_p, or for the near-cubic $P\bar{4}m2$ 'super-cell', a_s, where $a_s = \sqrt{2} \cdot a_p$. While the primitive unit cell is usually used to calculate the lattice parameters, the value a_s is used to calculate the c/a_s value, or *tetragonality*. This value is found to be between unity and 1.020 for a wide range of stabilised-tetragonal zirconia structures.[6,14-18] The displacement of the oxygen atoms along the c-axis, z, is difficult to determine from X-ray diffraction without very high quality data and Rietveld analysis, and was not calculated for the data presented here.

Table 6-2

Treatment temperature (°C)	a_p (Å)	a_s (Å)	c (Å)	c/a_s
470	3.5970(15)	5.087(2)	5.172(2)	1.0167(8)
520	3.5978(15)	5.088(2)	5.179(2)	1.0179(8)
600	3.5958(15)	5.085(2)	5.183(2)	1.0192(8)
800	3.5949(15)	5.084(2)	5.185(2)	1.0198(8)
900	3.5932(15)	5.082(2)	5.183(2)	1.0199(8)

Table 6-3

Source	a_p (Å)	a_s (Å)	c (Å)	c/a_s
Málek *et al.*[12]	3.5984(5)	5.0889(7)	5.152(1)	1.012
Igawa *et al.*[13]	3.591(1)	5.078(1)	5.169(1)	1.018

It is observed that the value of a decreases slightly with heating, while the value of c increases strongly in the early stages of heating. The c/a_s value increases correspondingly from 1.017 to 1.020. The lattice parameters are plotted against treatment temperature in Figure 6-5. It is likely that this change in the lattice parameters is driven by thermal annealing of some kind.

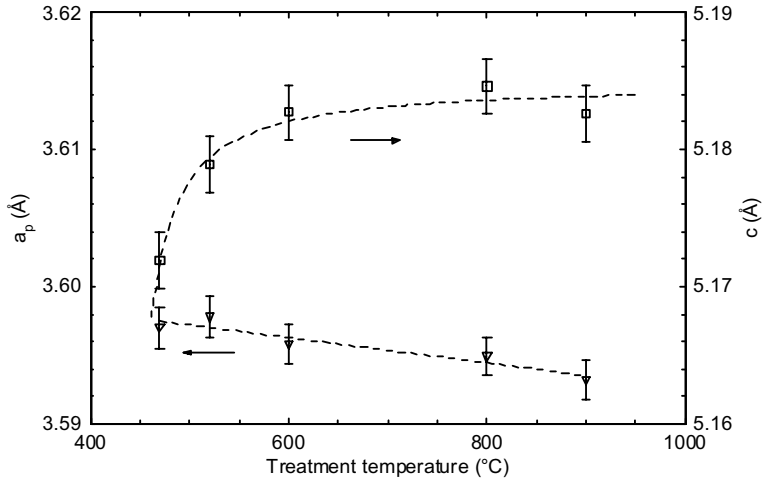

Figure 6-5: Calculated values of the lattice parameters *a* (∇) and *c* (□) for the metastable tetragonal phase.

Relationship between lattice parameters and stability

We now will consider the relationship between the lattice parameters and stability of the tetragonal phase. At this stage it is useful to review some results from 'doped-zirconia' systems. As discussed in Section 2.1.2, the tetragonal phase can be fully or partially stabilised by the addition of small quantities of a wide range of trivalent and tetravalent 'dopant' cations, and these materials have been very extensively studied. The *tetragonality* of the unit cell, expressed as c/a_s, is often closely associated with the stability of the tetragonal phase,[14-17] and generally does not exceed 1.020. However, this link is sometimes questioned,[16] and it certainly is not the only factor affecting stability. In the most widely-studied system of Y_2O_3-stabilised zirconia, an increasing Y^{3+} content decreases the c/a_s value and increases the stability of the tetragonal phase,[17] although tetragonal $Zr_{1-x}Y_xO_{2-x/2}$ is still regarded as thermodynamically metastable. If enough Y^{3+} is substituted into the lattice, the c/a_s value decreases to unity and a thermodynamically-stable *cubic* phase is formed.

The results from several studies on the variation of the lattice parameters with dopant in four "stabilised zirconia" systems [18,19] are plotted in Figure 6-6 as a 'lattice parameter plot', with a_s on one axis and c on the other.* The data covers the approximate range 2 - 7 mol % dopant. These trends can be extrapolated to zero dopant (pure zirconia), and the corresponding lattice

* The conventional method of presenting this data is to plot each lattice parameter against the dopant quantity, which provides no information on the relationship between the two lattice parameters. As far as the author is aware, the approach used in Figure 6-6 to plot changes in lattice parameters has not been used previously for tetragonal zirconia.

parameters are plotted as a single point. The data for the metastable tetragonal phase from Table 6-2 is also plotted on the Figure.

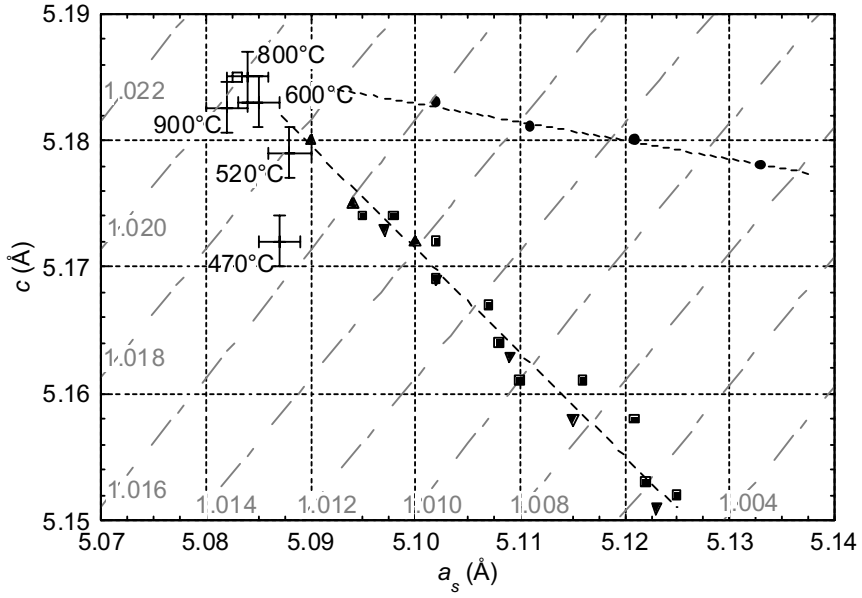

Figure 6-6: Measured lattice parameters for the metastable tetragonal phase (crosses with error bars), and previously reported values for various stabilised-tetragonal systems: Y_2O_3 (■),[18] Er_2O_3 (▼),[18] Sm_2O_3 (●),[18] and CeO_2 (▲).[19] The trends have been projected to a point for pure zirconia (□). Grey diagonal lines mark contours for the c/a_s value.

This plot leads to a number of interesting observations. The first is that in the 'doped-zirconia' systems the increase in a is inversely linear to the decrease in c, a result that is implied in the work by Scott.[20] This relationship could be justified in terms of the displacements in the unit cell caused by the substitution of the dopant cation and resultant oxygen vacancies, and is worth further investigation. This is in contrast to the trend for the pure metastable phase, in which value of c changes with heating while a remains relatively constant. The second observation, which is more relevant to the subject at hand, is that the lattice parameters of the metastable phase converge with the trend lines for the doped-zirconia phases, and the 'limit to stability' points for all of the series coincide.

The relationship between lattice parameters and stability can now be applied to the pure metastable phase. There appears to be a 'zone of metastability' within which the tetragonal phase can exist at low temperature. The limit of this zone could be expressed as approximately $c \approx 5.185$ Å or $c/a_s \approx 1.020$, beyond which the tetragonal phase will transform to the thermodynamically-stable monoclinic phase. The material crystallised at 450°C is well within the 'zone of metastability'. As the material is heated further the lattice parameters change to

bring the structure closer to the limit of metastability, via a thermal annealing mechanisms as discussed above. This limit is almost reached after heating to 800 and 900°C, and is passed after heating to 950°C, leading to the tetragonal-to-monoclinic transformation.

Mechanisms

The structural mechanism that leads to these changes in lattice parameters is yet to be identified with certainty. The most likely candidates at this stage are lattice strain or defects of some kind (vacancies, impurities) within the crystal. Both structures have also been previously associated with the stability of the tetragonal phase (See Section 2.4.2), but no definite link has been shown. Either strain or defects could be incorporated into the crystal lattice during the rapid crystallisation process, would be expected to have an effect on the lattice parameters, and would be 'annealed' out during further heating.

The effect of crystal size on the lattice parameters has also been considered. It may be possible that a small crystal may allow some 'relaxation' in the lattice parameters, increasing the stability of the tetragonal phase. However, based on the available evidence this scenario is unlikely, as the largest change in the lattice parameters is between 450 and 600°C, while the crystal size only increases beyond 900°C.

Conclusion

Evidence for a link between the stability of the pure, metastable zirconia phase and its lattice parameters has been reported for the first time. This hypothesis requires more extensive experimental work to be proven, but the evidence provided here provides a starting point and may lead to a better understanding of the metastability mechanisms for pure tetragonal zirconia.

6.3.3 Crystal size and morphology

Results from two complimentary techniques are reported in this section: transmission electron microscopy (TEM) and X-ray diffraction peak-broadening.

Transmission electron microscopy

The size and morphology of crystals and aggregates in a material can be directly determined from a transmission electron micrograph. A number of micrographs were taken of each sample, and in each micrograph crystals have been identified and their approximate diameter measured. For a number of samples bright-field and dark-field images were compared, and the average 'crystal size' identified in each image was approximately the same. [*] All micrographs shown here are 'bright-field' images.

TEM micrographs of the sample heated at 470°C for an hour are shown in Figure 6-7 and Figure 6-8. These show crystals of zirconia in a matrix of material with lower density, which is presumably amorphous. The crystal size ranges between 15 and 60 nm across, with an average size of approximately 35 nm, and there are no clear facets. The volume fraction of the amorphous component could possibly exceed 50 %, although it is difficult to estimate the mass fraction from the micrographs. Clearly crystallisation is not complete at this stage. Also observed in these micrographs are many 'low-density' features, approximately 5 to 10 nm in size. These features are thought to be pores, and are discussed in detail in Section 6.3.4. The presence of the amorphous component does not greatly affect the diffraction pattern and Raman spectrum, but it does affect the EXAFS spectrum significantly, as discussed in Section 10.3.7.

Figure 6-9 through to Figure 6-12 show the changing morphology as the treatment temperature is increased to 900°C. The fraction of amorphous material decreases, and the sample heated to 700°C appears to be completely crystalline. The angularity and faceting of the crystals also increases, as diffusion within each crystal allows low-index planes to

[*] TEM has two modes of imaging: bright-field and dark-field. Bright-field imaging uses direct transmission to show all of the features of the sample. Crystal boundaries can usually be seen as slightly darker against the background. Dark-field imaging collects only light that is scattered or diffracted in a certain direction. If crystals are oriented randomly only a few will be visible in a dark-field image, but their dimensions may be more accurately determined.

predominate on the surface. However, the average observed crystal size does not change significantly, remaining below 40 nm.

Figure 6-7: TEM image of a gel heated to 470°C for an hour.

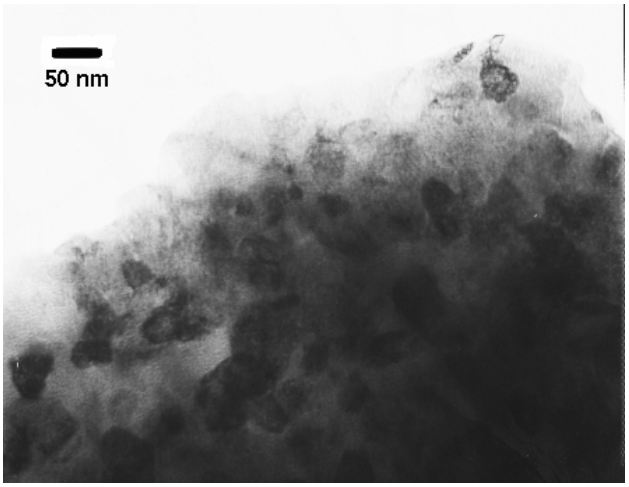

Figure 6-8: TEM image of a gel heated to 470°C for an hour.

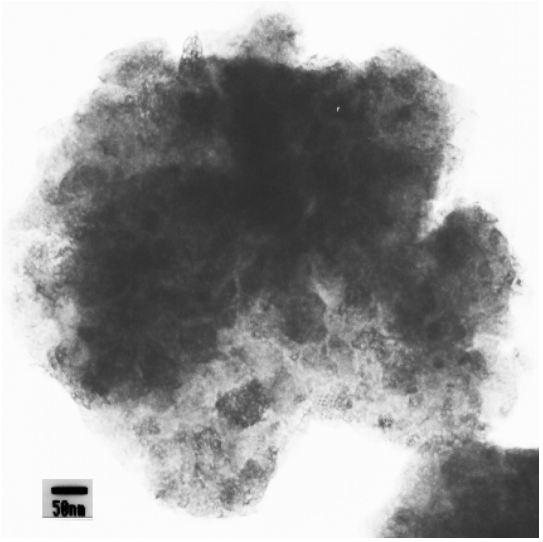

Figure 6-9: TEM image of a gel heated to 520°C for an hour.

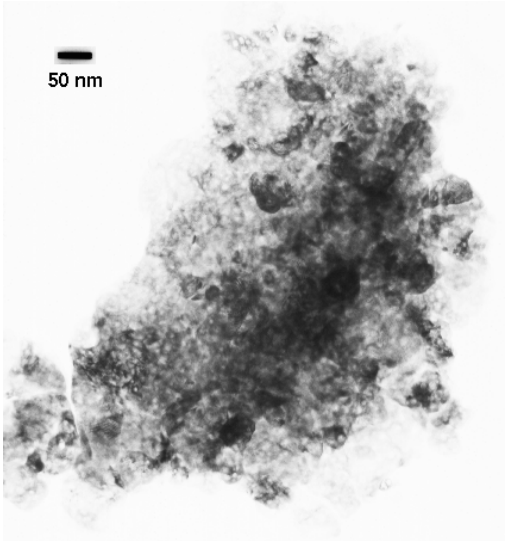

Figure 6-10: TEM image of a gel heated to 600°C for an hour.

Significant crystal growth occurs once the treatment temperature reaches 1000°C, and crystals up to 100 nm across are observed in Figure 6-13. Figure 6-14 shows the micrograph of a sample heated for an hour at 1100°C, showing that very extensive crystal growth and

consolidation has taken place. The average crystal size in this sample is approximately 120 nm.

Another feature to notice is the twinning bands in the crystals, marked by arrows in Figure 6-13 and Figure 6-14. These samples are monoclinic phase, having transformed from the original tetragonal phase, and the occurrence of twinning during the martensitic tetragonal-to-monoclinic transformation is well documented.[21-23]

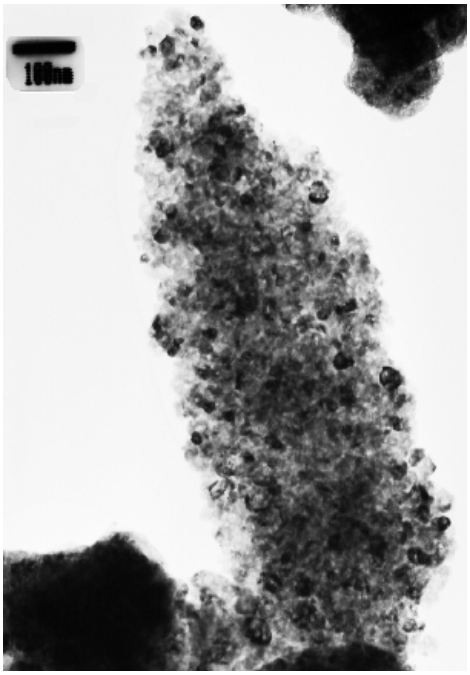

Figure 6-11: TEM image of a gel heated to 700°C for an hour.

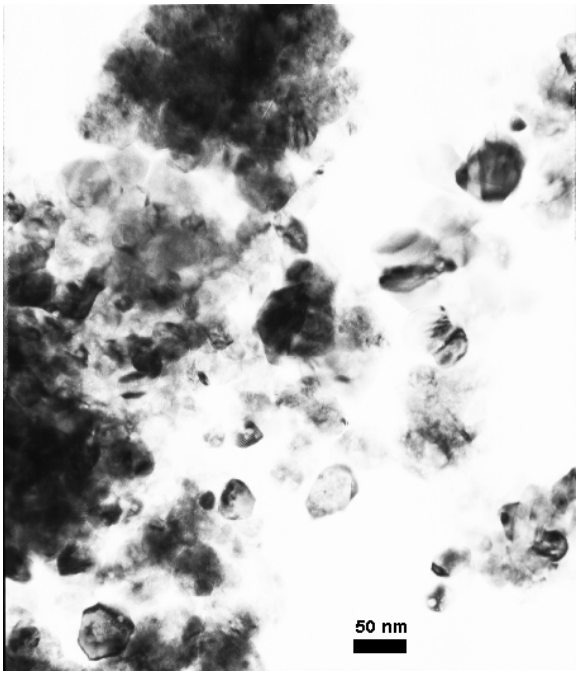

Figure 6-12: TEM image of a gel heated to 900°C for an hour.

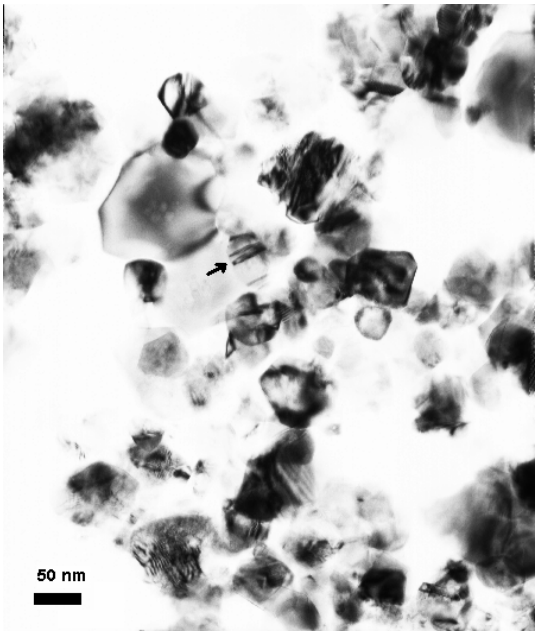

Figure 6-13: TEM image of a gel heated to 1000°C for an hour.

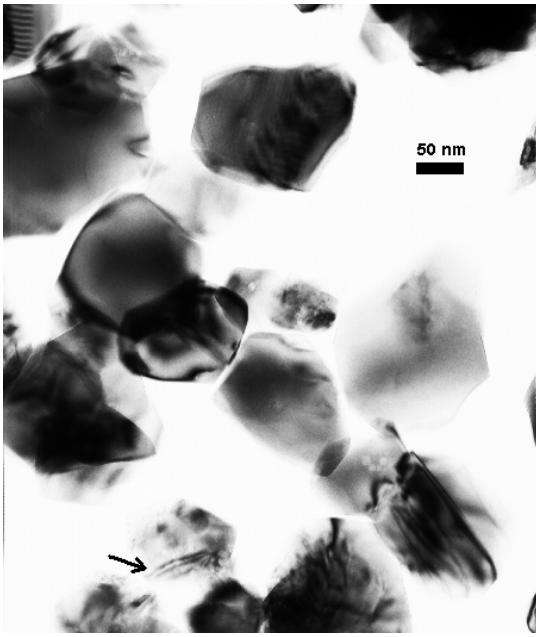

Figure 6-14: TEM image of a gel heated to 1100°C for an hour.

The average observed crystal size, the approximate range of particle sizes, and morphology observations are summarised in Table 6-4.*

Table 6-4

Treatment temperature (°C)	Average crystal size (nm)	Crystal size range (nm)	Morphology comments
470	35	15 - 60	Crystals in an amorphous matrix
520	~ 30	20 - 40	Increased crystallinity
600	~ 40	20 - 60	Increased crystallinity & faceting
700	25	8 - 50	Fully crystalline, faceted crystals.
900	37	20 - 60	Fully crystalline, faceted crystals.
1000	60	25 - 100	Faceted crystals, twinning bands
1100	120	80 - 170	Faceted crystals, twinning bands

The determination of crystal size from TEM micrographs has a few limitations. The procedure is time-consuming and only a very small part of the sample can be examined. The accuracy of the 'average' crystal size determined from TEM images is limited by the number of images

* In some cases the average crystal size was difficult to determine as agglomerates were not broken up sufficiently for many individual crystals to be distinguished. No statistical methods have been applied to the measured crystal sizes; a smaller range may simply reflect a smaller sample.

collected, the number of crystals observed in each image, and whether the small section examined is representative of the whole sample.

X-ray diffraction line-broadening

Another method for determining the crystal size is to use the broadening of the peaks in the diffraction pattern. It is known that when the diffracting crystal size is less than approximately 100 nm, the breadth of the diffraction peak is related to the size of the diffracting crystal. The primary difficulty with this technique is that peak-broadening is also caused by instrumental factors and crystal strain. In this study the peak half-width has been corrected for instrumental broadening, but we have initially assumed that no significant broadening is caused by strain.

The peak half-widths have been measured for the diffraction patterns shown in Figure 6-2. Where the tetragonal phase dominates the 101 peak was used, and where the monoclinic phase dominates the 111 and $\bar{1}11$ peaks were used. The calculated average 'diffraction size' values are listed in Table 6-5, and plotted in Figure 6-15 alongside the size ranges determined by TEM.

Table 6-5

Treatment temperature (°C)	phase and peak	uncorrected half-width, β (°)	Calculated crystal size (nm)
470	tetragonal 101	0.326	32
520	tetragonal 101	0.330	31
600	tetragonal 101	0.352	29
800	tetragonal 101	0.332	31
900	tetragonal 101	0.300	35
950	monoclinic $\bar{1}11$	0.350	29
	monoclinic 111	0.438	22
1000	monoclinic $\bar{1}11$	0.330	31
	monoclinic 111	0.388	26
1100	monoclinic $\bar{1}11$	0.284	38
	monoclinic 111	0.304	35

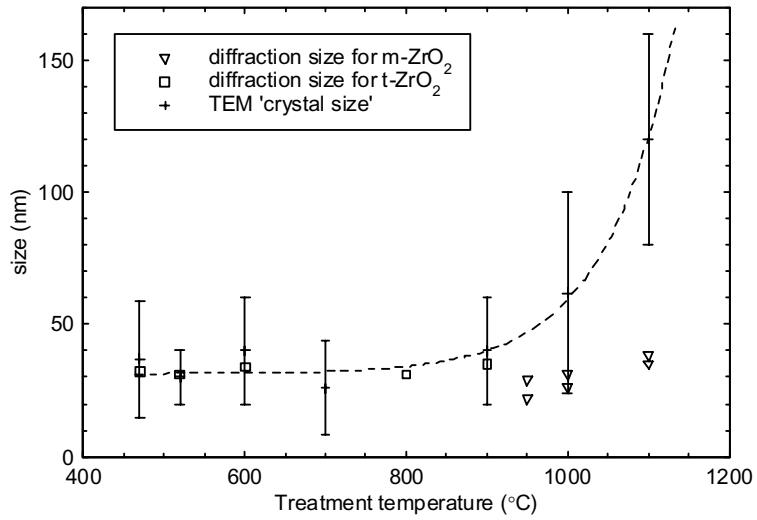

Figure 6-15: Plot of 'crystal size' as determined by TEM imaging and XRD. Bars are not 'error bars', but indicate the range of sizes observed in the TEM micrographs.

For samples heated up to 900°C the average 'crystal size' calculated from the diffraction line-width was quite consistent with the crystal size observed by TEM. This indicates that any strain in the crystals does not contribute significantly to the calculated values. However, for the samples heated to 950°C or above, there is a large discrepancy between the crystal size values observed by TEM and calculated from the monoclinic phase diffraction peaks. The most likely cause for this discrepancy is the previously-mentioned twinning in the crystal. A twinned crystal appears in a TEM image as a single crystal, but diffracts as if it were composed of two different crystals. Furthermore, a crystal containing a number of twinning bands diffracts as many crystals, thus substantially decreasing the average 'crystal size' calculated from the diffraction pattern.

From Figure 6-15 it is clear that virtually no crystal growth occurs at temperatures below 900°C over the period of an hour, but that the crystal size will increase substantially after heating to above 1000°C. The simplest explanation is that the rate of the mass-transport mechanisms is limited below 900°C. An *in-situ* TEM study of the sintering of zirconia at 890°C found surface diffusion to be the most probable mass-transport mechanism, and that

the neck growth between particles would begin but not continue beyond a certain size.[24] Heating to higher temperatures is evidently required for consolidation of crystals.*

The relationship between crystal size and the phase transformation

A comparison of Figure 6-3 and Figure 6-15 shows a clear correlation between the temperature at which the average crystal size starts increasing, between 900 and 1000°C, and the 'critical temperature' beyond which the majority of the tetragonal phase transforms to monoclinic, between 900 and 950°C. In light of the many previous publications that have reported on this correlation, it is reasonable to consider the possibility that these two observations are linked by a microstructural mechanism. As discussed in Sections 2.3.3 and 2.4.2.6, there have been many studies that purport to show the existence, or non-existence, of this correlation in various nanocrystalline zirconia systems. Generally these studies have been dealing with the hypothesis that an increase in crystal size leads to the tetragonal-to-monoclinic transformation, often based on the 'surface energy' theory which is discussed in full in Section 2.4.2.6.

However, a closer examination of the data shows a more complicated situation. Figure 6-15 also shows the *range* of crystal sizes observed by TEM. There is a large overlap between the crystal size range observed in the sample heated to 900°C, which is mostly tetragonal phase, and the size range observed in the sample heated to 1000°C, which is nearly completely monoclinic phase. The observed size ranges are too broad, and transformation too sharp, to sustain an causal link between the crystal size and the transformation. Furthermore, there is very little difference in the measured surface area of the material heat-treated at 800 and 1000°C (See Section 6.3.6 and Figure 6-22).

It is worthwhile to consider the proposition of the reverse relationship - that the free energy released by the t → m transformation promotes crystal growth. Although there has been some suggestion that metastable-to-stable transformations strongly promote crystal growth,[25] a recent paper claims that there is little evidence for such transformations having any effect on microstructural development.[26] In any case, as shown in Chapter 7, the t → m transformation

* It could be suggested that the presence of the intracrystalline pores, discussed in Section 6.3.4, will inhibit crystal growth. However, at the stages of heating covered in this study most of the crystal growth takes place by mass transport, not migration of crystal boundaries, so it is unlikely that the pores have a significant effect on crystal growth.

occurs during cooling at below 400°C, under which conditions it is unlikely that there is sufficient thermal energy to permit any significant crystal growth.

Therefore, although there is a correlation with average crystal size, we cannot say that the increase in crystal size directly causes the t→ m transformation, nor vice-versa. The most likely link between the two is that both are caused by changes in the structure due to the thermal treatment, possibly associated with the activation of mass-transport mechanisms above 900°C.

This conclusion has important implications for the 'surface energy' theory of tetragonal phase stability, in that crystal size (or surface area) in itself does not seem to be a dominant factor in the phase stability of these nanocrystals. If this theory is valid, then *changes in the actual surface energy must be more important that changes in the surface area*. This possibility will be explored in Section 6.3.4.

6.3.4 Loss of volatile species

Although most of the non-oxide material has been lost from the material either before or during crystallisation, a small amount of mass is lost during the heating stage between 500 and 1000°C.

A typical thermogravimetric analysis trace for a standard gel is shown in Figure 6-16. Only the region above 500°C is shown, as the mass losses are very small compared to those that occur below 500°C. The heating profile was 10°C/min to 1000°C, then the temperature was maintained at 1000°C for 30 minutes.* For this reason the data is plotted against time rather than against temperature.

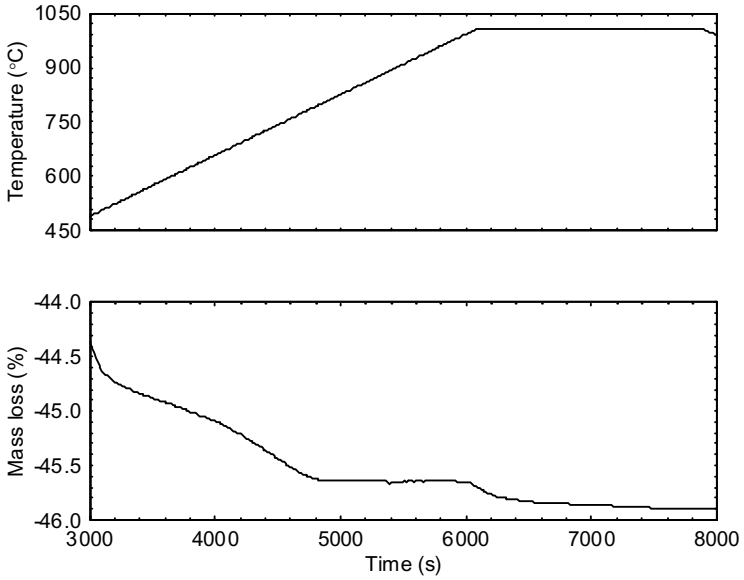

Figure 6-16: Typical thermogravimetric trace for a standard gel, heated at 10°C/min to 1000°C, then held at 1000°C for 30 minutes.

The sample continues to lose a small amount of mass during heating, particularly over the range 650 - 800°C during which approximately 0.37 % of the original mass is lost. Between 820 and 990°C there is very little change in mass, but at 990°C a further mass-loss reaction begins, and continues during the hold at 1000°C. In this stage a further 0.17 % of the original mass is lost.

* The data reported here was part of the series of experiments discussed in Section 7.3.2.

The material lost is most probably nitrate or nitrato groups desorbed from the surface of the crystals. It may also be gas from the intracrystalline pores as they are eliminated from the crystals (see Section 6.3.5).

A change in mass of this magnitude would normally be regarded as insignificant, except that the mass-loss at approximately 1000°C corresponds fairly closely with the 'critical temperature' identified in Section 6.3.1. Note that the reaction observed to begin at 990°C during a constant heating ramp could well occur during holding at 950°C. The surface energy of zirconia crystals has been suggested to play a role in the relative stability of the tetragonal and monoclinic phases (See Section 2.4.2.6), and the loss of surface nitrate species could be an important mechanism in the 'destabilisation' of the 'metastable' tetragonal phase.

Unfortunately, proof that the phase stability is sensitive to such small traces of surface species would require an inordinate amount of work, and is not attempted in this thesis. Nevertheless, it remains a strong possibility that merits further investigation.

6.3.5 TEM observations of intracrystalline porosity

Section 6.3.2 has already discussed the TEM imaging of the zirconia crystals, which range in size between 10 and 100 nm. One unusual observation, discussed in detail in this section, is of many distinct 'spots' on the image of the crystals, indicating discrete regions of significantly higher electron transparency. The size of these spots ranges from 0.5 nm (the limit at which features can be resolved with the microscopes used) up to 30 nm, and they appear to be entirely contained within, or on, individual crystals. Analysis of the TEM images and comparison with the nitrogen sorption results in Section 6.3.6 strongly indicates that these features are pores within the crystals, which may be open or closed. There have been two previous reports of similar features in nanocrystalline zirconia observed by HREM, but with only very brief discussion and no suggestion of their origin.[27,28]

A range of evidence shows that the observed features are definitely not solid inclusions. Energy dispersive spectroscopy (EDS) on the nano-scale and large-scale X-ray fluorescence do not indicate the presence of any significant impurities, and neither XRD or Raman spectroscopy identify any material other than zirconia.

Figure 6-17*a*, which is a magnification of the region shown in Figure 6-7, shows a micrograph of the standard gel after heating to 470°C for an hour. Dense crystals are located in a matrix of less-dense material, most probably amorphous. Both the crystals and the amorphous material are thickly covered with the 'spots' identified as pores, although they are more clearly identified in contrast against the crystals. This micrograph gives an important clue to the origins of the pores, as they are observed in the amorphous material before the crystallites are formed. These pores are most likely initially formed by the decomposition of nitrate species in the gel to form nitrous oxide gas, NO_x, which is trapped in the amorphous material to form 'bubbles'. Possible mechanisms by which these bubbles are incorporated into the crystals will be discussed later.

Changes in morphology with heating

The size, number, shape and location of the pores changes with the thermal treatment of the material. Figure 6-17 gives sample bright-field micrographs of the pores after different thermal treatments. A number of processes were identified: consolidation of the pores, faceting, and crystal growth around the pores.

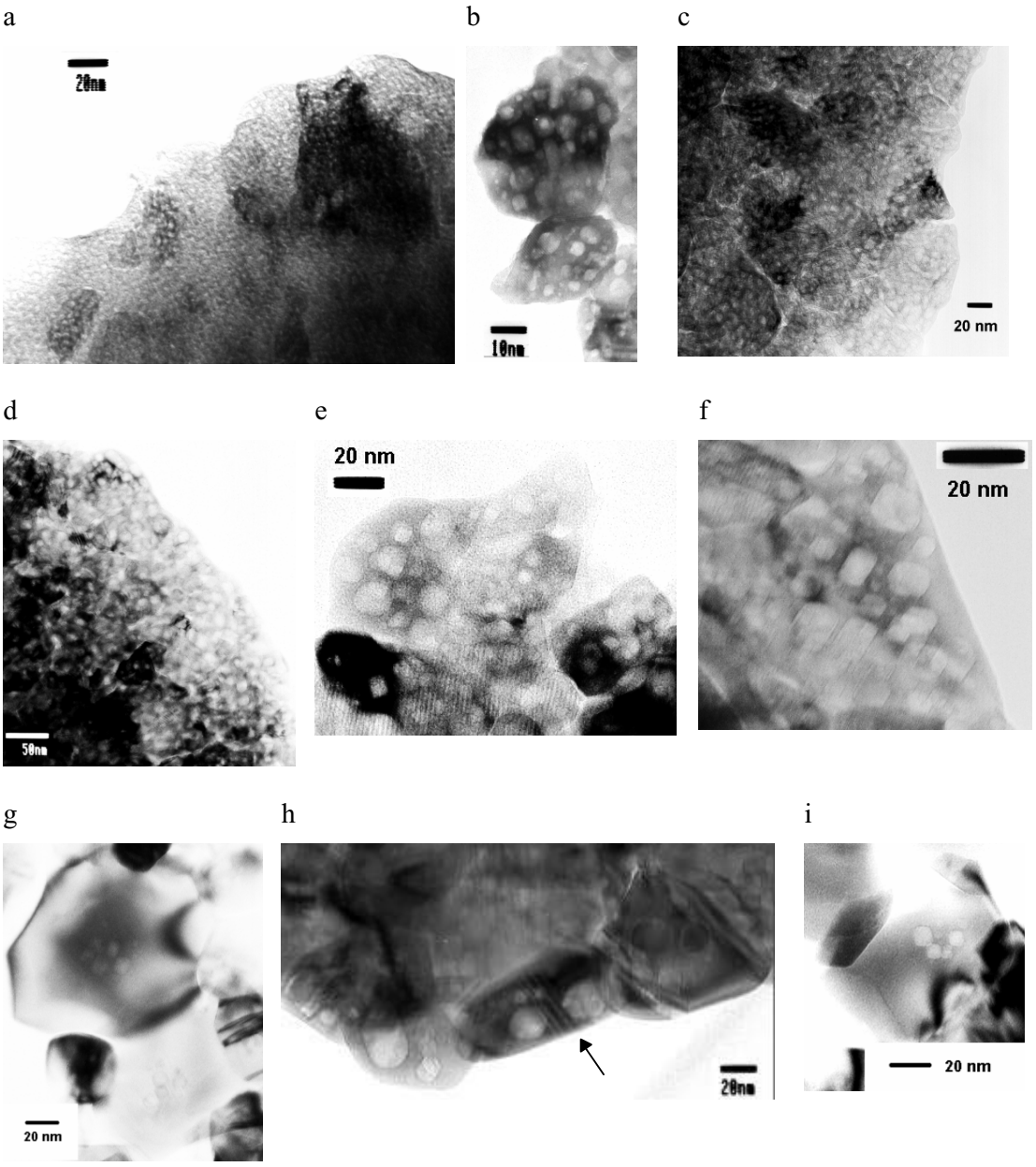

Figure 6-17: Transmission electron micrographs of samples heated to a) 470°C, b and c) 500°C, d and e) 600°C, f) 700°C, g and h) 1000°C, and i) 1100°C. The arrow indicates twinning bands.

In the sample heated to 470°C the pore size is generally 2 - 5 nm, with some as small as 0.5 nm or as large as 7 nm. After heating to 600°C the *average* size increases to 5 - 10 nm, but remains roughly stable with further heating. However, the *range* of sizes observed in each sample increases with treatment temperature, with pores up to 30 nm in diameter observed in samples heated to 1000°C. In all samples a large number of very small pores (< 5 nm) are observed. The most likely mechanism for the increase in size is consolidation of the pores, in which two or more adjacent pores merge to become one. However, given that the average

size of the pores changes very little, and the close proximity of the pores to each other, their mobility in the crystal must be quite low.* This correlated with the observation in Section 6.3.3 that mass-transport is slow below 1000°C.

Note that if the pores contained no gas their size would be expected to *decrease* with further heating, as they would shed vacancies into the surrounding crystal and eventually disappear altogether. Instead, the observed behaviour supports the proposition that the majority of the observed pores are closed, and contain some gas which prevents their elimination.

The micrographs in Figure 6-17 show that there are usually many pores in a single crystal, frequently overlapping on the image, giving some crystals a 'sponge-like' appearance. It is not clear if they are touching either each other or the crystal surface. The 'number-density' of the pores decreases a little with heating up to ~ 600°C, due to the above-mentioned consolidation process. With heating beyond 900°C there is a strong decrease in the number of pores observed, corresponding with an increase in the observed crystal size (see Section 6.3.3). At this stage there is also a change in the location in which they are observed; Figure 6-17*g* and *i* show good examples of large crystals (~ 100 nm) which contain pores only in the *centre* of the crystal. This is caused by the mechanism of crystal growth, in which mass is transported from smaller crystals to larger crystals. A non-porous crystal will grow around a porous core at the expense of surrounding crystals. The elimination of the pores is thus largely achieved by the diffusion of material from porous crystals to form non-porous crystals. Those pores that are trapped in the center of the crystals will remain until a much later stage of sintering, when they may be concentrated at grain boundaries, possibly 'pinning' them.

In the samples heated to 470°C the pores are roughly ovoid or spherical, and it is difficult to distinguish the edges of the pores. With heating to higher temperatures the pores become easier to distinguish, and some faceting becomes evident. Faceting is quite clear after heating to 700°C, as the external surfaces of the crystals also become faceted. The facets of pores with the same crystal are generally are aligned with each-other, most probably along a low-index crystalline plane such as 001, 111, etc. Some observations indicate that the facets of the pores are also aligned with the external surface facets of the crystal, as would be expected.

---

* A secondary mechanism for the increase in pore size may be that raising the temperature will increase the internal pressure of any gas present. This effect will be relatively small (pressure increase from 460 to 600°C is 17 % at constant volume) and will only result in a *uniform* increase in particle size.

This tendency towards faceting is consistent with energy minimisation of a 'free' crystalline surface, and would be opposed by the internal pressure of any gas in a closed pore.

Note in Figure 6-17*h* that a highly porous crystal contains twin-bands, indicating that it has transformed to the monoclinic phase. This shows that the presence of the pores does not prevent the t → m transformation, though it is speculated that it may inhibit it.

PEELS experiments

A VG TEM, equipped with a parallel electron energy-loss spectroscopy (PEELS) facility, was used in two experiments to further characterise the pores in a sample heated at 1000°C for an hour.

In the first experiment, a 'thickness profile' of two crystals containing pores was determined by measuring the electron absorption along a line through each crystal, and from the absorption calculating the thickness.* Each pore corresponds with a decrease in electron absorption of 10 - 30 %. The calculated thickness of each pore was approximately the same as the measured width, indicating a roughly spherical shape that was indicated from the micrographs discussed above. The thickness profiles are shown in Figure 6-18 and Figure 6-19, compared with a transmission micrograph of the corresponding area..

In the second experiment the PEELS facility was used to measure the elemental composition of a section of crystal, approximately 5 nm across, that included a pore. No nitrogen could be unambiguously detected above the background zirconium signal.

* The thickness was calculated using an estimate of the mean-free-path of a 100 keV electron through zirconia, λ, assuming that whatever material may be in the pores has a negligible electron adsorption. The λ value was calculated to be 104 nm from an equation published by Malis, Cheng and Egerton,[31] which is estimated to be accurate ± 20 %.

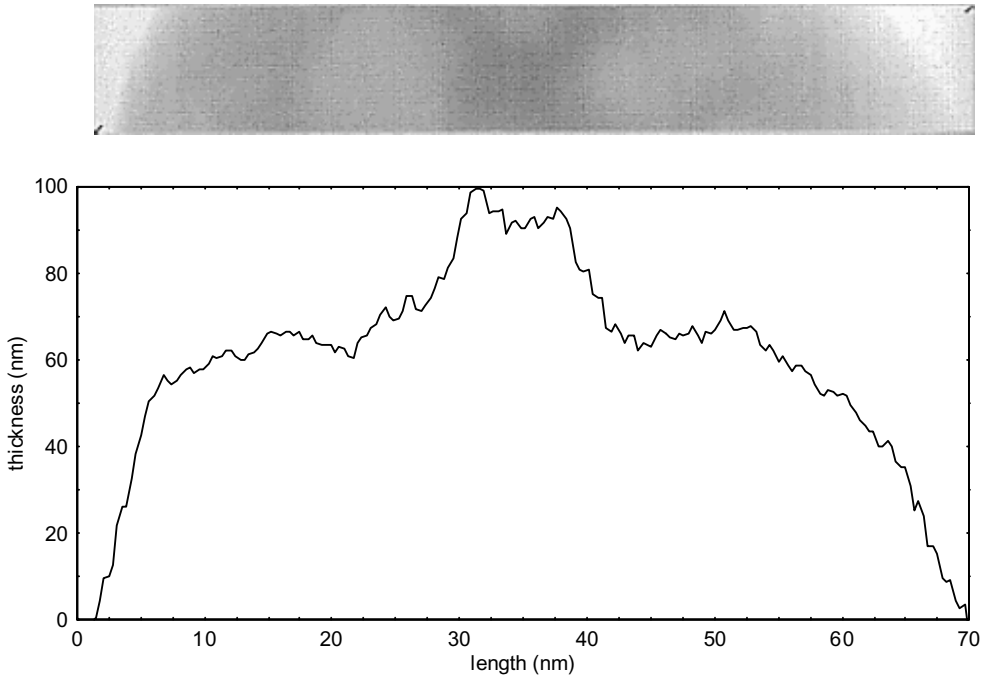

Figure 6-18: Thickness profile and corresponding transmission electron micrograph of a crystal containing three pores.

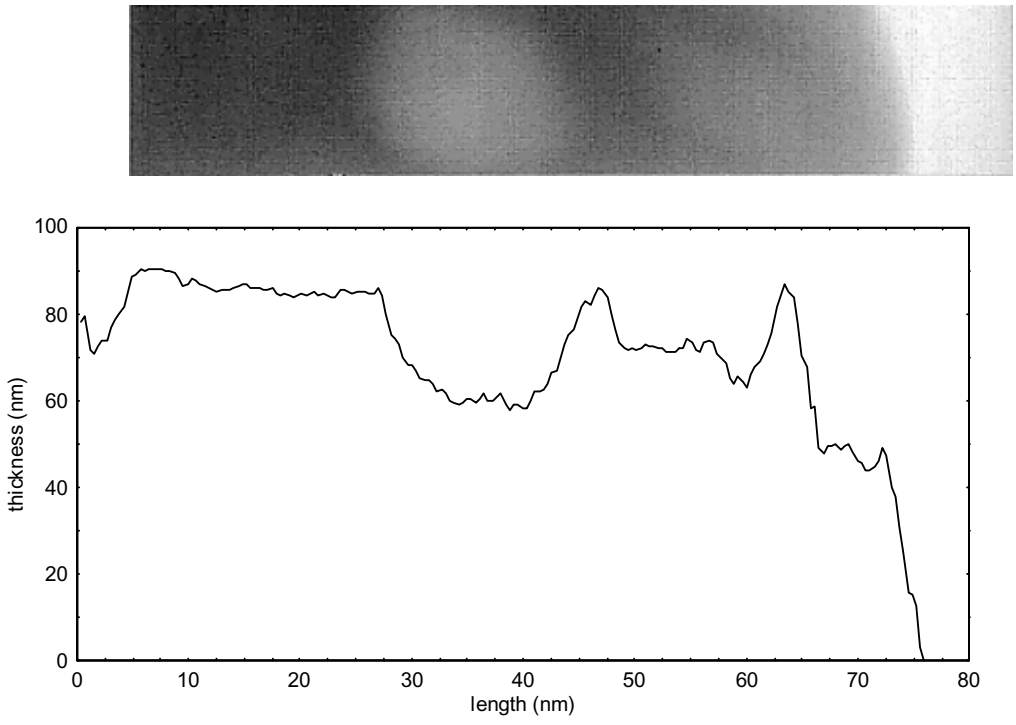

Figure 6-19: Thickness profile and corresponding transmission electron micrograph of part of a crystal containing two pores.

Mechanisms of formation

Three possible mechanisms for the formation of the pores within the crystals are proposed. Evidence discussed above indicates that the pores are initially present as gas bubbles in the amorphous material before crystallisation, and this is taken as the starting point for the mechanisms. In the first route a crystalline nucleus forms in the amorphous material, then grows progressively around each bubble. In the second mechanism a region of partially-ordered material containing several bubbles may rapidly and topotacticly transform into a single crystal. This may be possible since the short-range order of the amorphous material bears some resemblance to the tetragonal phase, as discussed in Chapter 5.3.2. In the third mechanism many crystallites may form in a region around the bubbles, and then align to form a single porous crystal. These three mechanisms are schematically illustrated in Figure 6-20.

A much more extensive study is required to choose between these routes, preferably with *in-situ* observation of crystallisation by high-resolution TEM. At present the second route is favoured, considering the rapid crystallisation reaction, and that evidence already exists that a topotactic transformation may occur in the material studied.

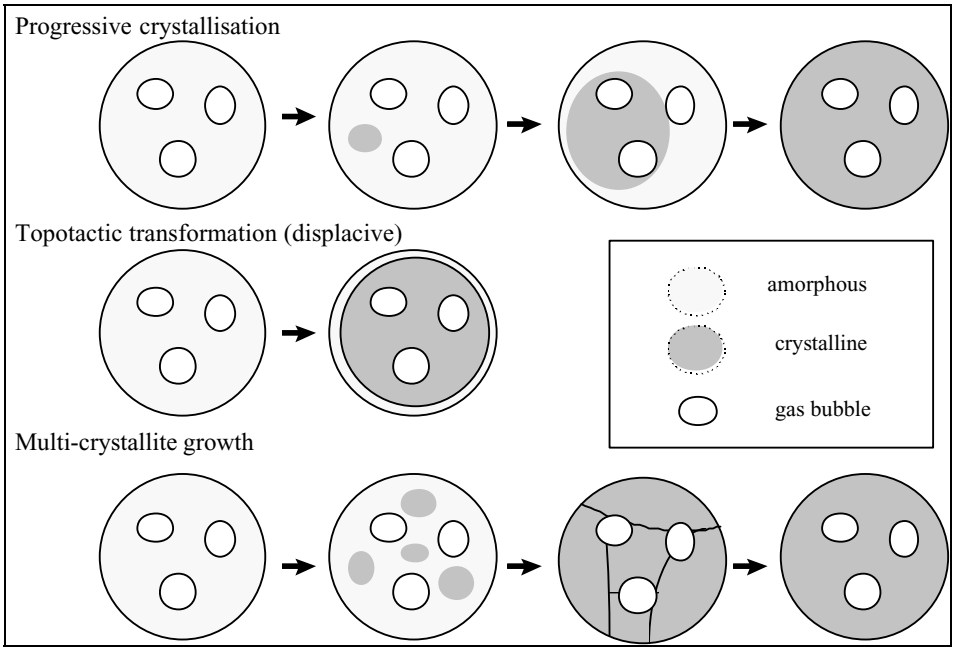

Figure 6-20: Schematic illustration of three possible routes for the crystallisation of zirconia around gas bubbles in the amorphous material, to form porous crystals.

6.3.6 Nitrogen adsorption/desorption

Gas adsorption measurements are frequently used for determining the surface area and pore-size distribution of a wide variety of solid materials. The processes involved in the physical adsorption (physisorption) of gas onto a surface, and the effect of porosity adsorption characteristics, is well established and will not be discussed here.[29]

The general approach to characterise the surface of a material by gas adsorption involves the controlled adsorption and desorption of a gas, usually nitrogen, onto the surface of a sample.[29,30] First, all molecules adsorbed on the surface of the sample are removed by applying a vacuum and heat. A controlled quantity of gas is then incrementally added to the sample chamber and allowed to adsorb onto the surface of the sample. The chamber pressure, P, is monitored until saturation occurs at P_0. At this point the process is reversed, and the gas pressure is incrementally decreased to remove the adsorbed molecules from the surface. The volume of gas adsorbed is plotted against the relative pressure, P/P_0, in the sample chamber to give the adsorption/desorption *isotherm*. A number of theories have been developed to determine information on the surface area, pore volume, pore-size distribution and other properties from the measured isotherm. The lower limit for the detection of pores is dependent on the gas used; for nitrogen it is approximately 2 nm. It is important to keep in mind that only *open* porosity can be characterised by this method, not closed porosity (for example shown in Figure 6-17***i***).

Figure 6-21 shows the isotherms for the adsorption and desorption of nitrogen on the surface of a range of standard samples, heated to between 470°C and 1000°C. These isotherms show the adsorption curve as a solid line and the desorption curve as a broken line. All of the isotherms display some degree of *hysteresis*, in which the adsorption and desorption curves do not completely overlap. Hysteresis in the isotherm is associated with capillary condensation in mesopores, and is used to characterise the presence of mesoporosity.[*] The desorption curve is indicative of the minimum pore diameter, while the adsorption curve is indicative of the maximum pore diameter.

---

[*] A widespread convention has been established in which pores are classified into three types according to their size: pores with widths exceeding about 50 nm are called *macropores*; pores of widths between 2 nm and 50 nm are called *mesopores*; and pores with widths not exceeding about 2 nm are called *micropores*.[30]

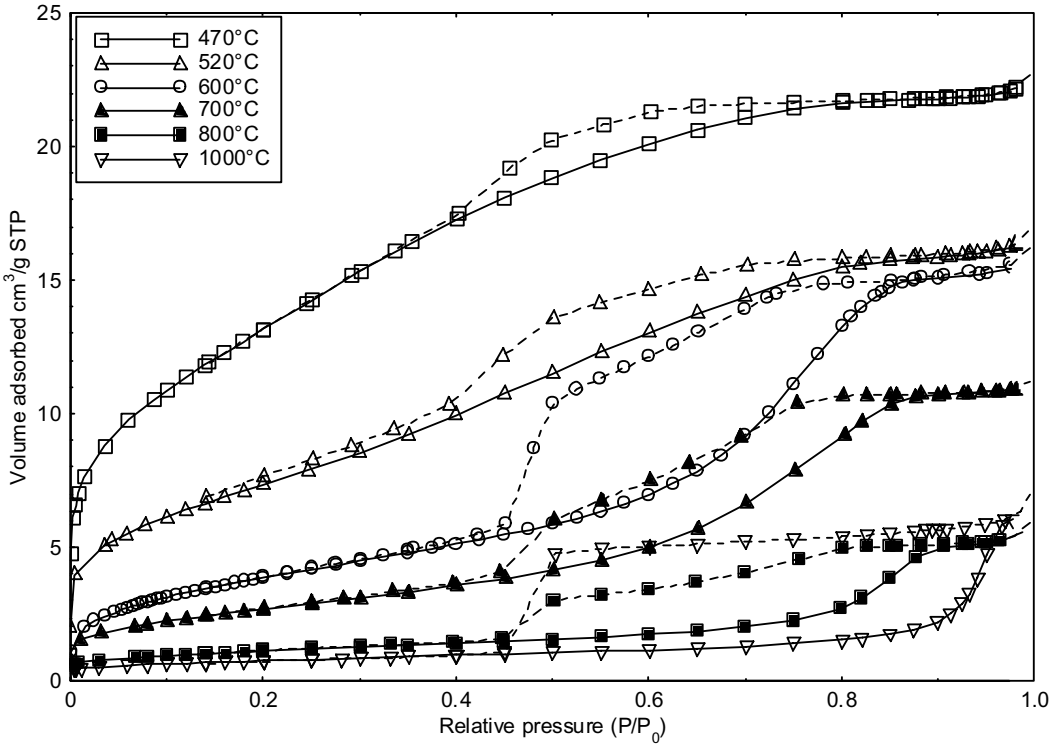

Figure 6-21: Nitrogen adsorption/desorption isotherms for samples heated for one hour at the temperatures indicated on the key. Solid lines indicates the adsorption curve, and broken lines indicate the desorption curve.

The first point to note is that the total volume of gas adsorbed decreases considerably with treatment temperature. This is due to decreasing surface area, both open porosity and external surfaces of the crystals.

Isotherm types

A range of standard IUPAC isotherm 'types' have been defined, from Type I to Type VI, as well as types of hysteresis loops, H1 to H4.[30] Each of these types is associated with particular structures or adsorption/desorption mechanisms.

The isotherms for all samples indicated that virtually all gas adsorption was due to micro- and mesoporosity. The samples heated to 470 and 520°C gave composite Type I/Type IV isotherms. These isotherms are largely concave, indicating that the samples are mostly microporous (pores <2 nm). The comparatively small hysteresis loops, which are close to Type H4, indicate that some mesopores are present. The samples heated to 600, 700 and 800°C gave Type IV isotherms, indicating that most adsorption is due to mesoporosity. These isotherms have a 'distorted' hysteresis loop that could not be readily classified, but which may indicate the presence of slit-shaped mesopores. The shape of this isotherm does not change

with increasing equilibrium times (up to 90 s per point), and so is judged to be valid. The sample heated to 1000°C gave a classical Type IV isotherm, with a large hysteresis loop and virtually all adsorption attributed to microporosity. In all samples, the small upturn of the curve at the high-pressure end of the isotherm indicates that a small fraction of macropores (> 50 nm) are present.

Surface area

The most commonly used method for determining the total surface area from the isotherm is the Brunauer-Emmett-Teller (BET) method, although it is based on an oversimplified model.[30] Figure 6-22 plots the calculated BET surface area for each sample as a function of treatment temperature. The calculated surface area of the powders decreases strongly and exponentially with increasing treatment temperature, from 50 m^2/g to less than 5 m^2/g. However, the value of 'surface area' for largely microporous materials, such as those samples heated to 470 and 520°C, has little physical significance, as adsorption is limited by the accessible micropore volume rather than the total internal surface area.

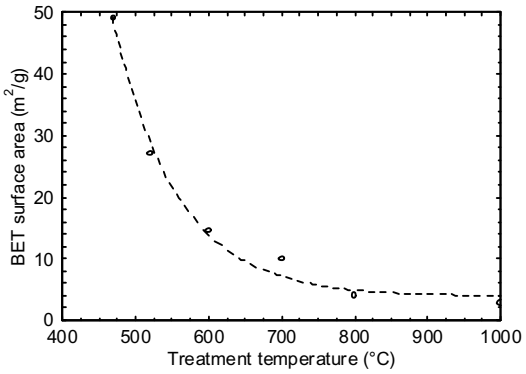

Figure 6-22: BET surface area of samples plotted against treatment temperature.

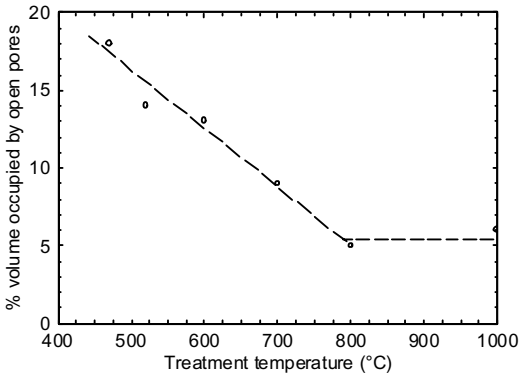

Figure 6-23: Volume occupied by open pores in samples, plotted against treatment temperature.

Pore volume and size distribution

The total open-pore volume per unit mass for each sample was determined by the 'single point' method.* From this value the volume fraction of open porosity was calculated, assuming that the remainder of the material is of theoretical density for zirconia and neglecting any closed porosity. The volume fraction, plotted against treatment temperature in Figure 6-23, decreases linearly with treatment temperature from 18 % to 5 % at 800°C, then remains constant.

The pore-size distribution was determined using the Barrett, Joyner and Halenda (BJH) method. Two pore-size distributions were calculated for each sample, one from the adsorption curve and the other from the desorption curve. The 'pore size' values calculated from the desorption curve are indicative of the minimum pore diameter, and are generally the most reliable, while the values calculated from the adsorption curve are indicative of the maximum pore diameter. The distribution is determined by calculating the volume of gas, V, adsorbed by pores of a particular size range, with an average diameter D. The plot of V/D against D gives an effective pore-size distribution. Examples of this distribution are given in Figure 6-24. Note that micropores below 2 nm cannot be included in the distribution.

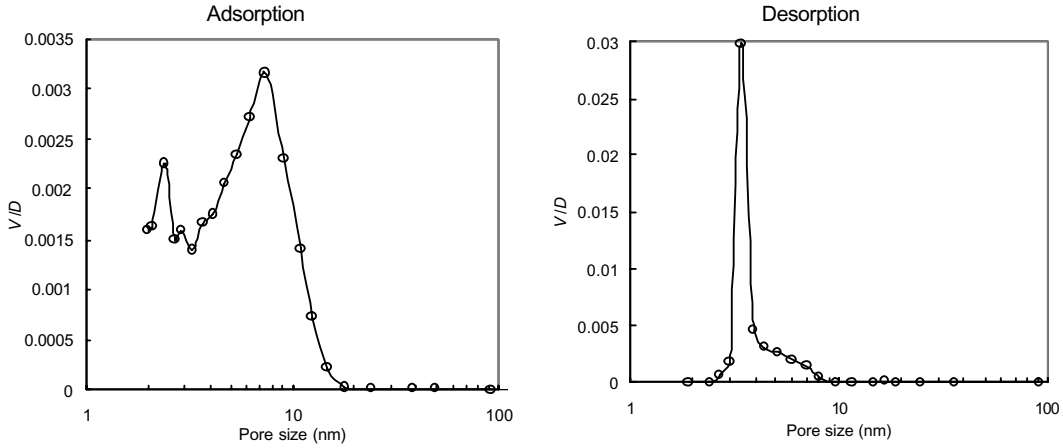

Figure 6-24: BJH pore-size distributions from adsorption and desorption curves for the sample heated to 600°C.

The pore-size distribution graph calculated from the adsorption curve always contained a single broad peak, while the distribution calculated from the desorption curve usually contained two peaks, one very sharp and the other broad. The pores belonging to the sharp peak accounted for 50 - 70 % of the total volume measured, with this proportion decreasing with increasing treatment temperature.

The pore-size range for each peak was measured, corresponding approximately to the peak's half-width, and these values are listed in Table 6-6 and plotted in Figure 6-25 and Figure 6-26. Only a single value is given for the very narrow peak from the desorption curve. Where the distribution continues substantially into the sub-2 nm region, this was interpreted as indicating that a high degree of microporosity was present.

---

[*] For the single point method, the intercept of the BET equation is taken as zero or a small positive value,

Table 6-6

Treatment temperature (°C)	Adsorption	Desorption		Comments
		Narrow peak	Broad peak	
470	< 5	~ 3.5	~ 2 - 4	High degree of microporosity
520	< 6	~ 3.5	~ 3 - 5	High degree of microporosity
600	5.2 - 13	~ 3.5	3.5 - 7.7	No microporosity indicated
700	4.5 - 13	~ 3.5	4.5 - 8.2	No microporosity indicated
800	9.5 - 18	n/a	4 - 9.5	No microporosity indicated
1000	23 - 43	n/a	n/a	No microporosity indicated

n/a: Some values were not available due to lack of data points.

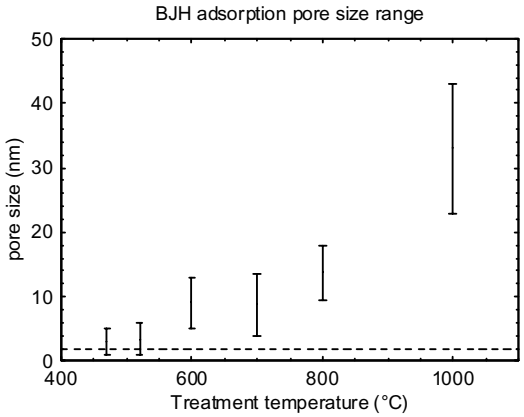

Figure 6-25: Approximate size-range for the pores, determined from the adsorption curve using the BJH method, plotted against treatment temperature. The dotted line indicates the lower limit of valid measurement (~ 2 nm).

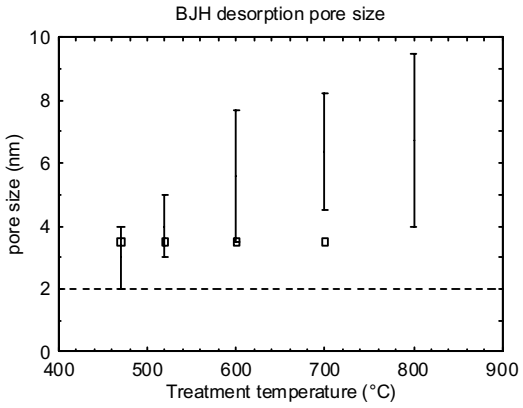

Figure 6-26: Approximate size-range for the pores, determined from the adsorption curve using the BJH method, plotted against treatment temperature. The points (□) indicates the position of the sharp peak in the size distribution. The dotted line indicates the lower limit of valid measurement (~ 2 nm).

The size distributions determined from the adsorption and desorption curves give similar size ranges for the sample heated to 470 and 520°C, but they diverge in the samples heated to 600°C or above. This is because, as mentioned above, the adsorption mechanism is largely determined by the 'maximum' pore size, while the desorption mechanism is largely determined by the 'minimum' pore size.

The pore-size range indicated from the desorption curve corresponds closely with the size of the *intracrystalline* pores observed by TEM, which are described in Section 6.3.4. Clearly there is a fraction of these pores that are open to the surface of the crystal. Pores of this size are not detected in the sample heated to 1000°C, and the micrographs shown in Figure 6-17

and the slope from the BET plot used to calculate the surface area.

show that the intracrystalline pores are mainly present in the center of crystals, and therefore closed.

The sharp peak in the desorption size-distribution corresponds to a large population of uniform pores, approximately 3.5 nm in diameter. Although it is most likely that this observation is related to the intracrystalline pores, a more comprehensive explanation is not yet proposed.

The pore size determined from the adsorption curve remains roughly constant for samples heated to between 600 and 800°C, and increases greatly for the sample heated to 1000°C. This is also the same trend as observed for the crystal size. Comparing Figure 6-25 with Figure 6-15, it can be seen that the 'maximum' pore size is approximately half that of the crystal size. It is likely that the adsorption curve is determined by the presence of *intercrystalline* porosity, which is not easily observed by TEM. Thus the adsorption process is governed by intercrystalline porosity, while desorption is governed by intracrystalline porosity.

Summary of open-porosity observations

Using the above interpretation of the measured isotherms, and in conjunction with the TEM observations in Section 6.3.3, it is possible to give a summary of the way in which the open porosity changes in the oxide with heating.

After heating the standard gel to 470°C, the resulting material contains a very large degree of microporosity (< 2 nm), with a small fraction of slightly larger open pores that are up to 4 nm in size.

Heating to higher temperatures greatly reduces the open microporosity and the BET surface area, and by 600°C most microporosity has been eliminated. Comparison with the micrographs in Section 6.3.3 strongly suggests that the microporosity is associated with the amorphous fraction of the material. The mesopores, at this stage mostly intracrystalline, increase in size from ~ 3 nm to ~ 6 nm.

Between 600 and 800°C the BET surface area and pore volume are halved, while there is little increase in the size of the pores. The dominant mechanism is the elimination of intracrystalline mesopores by diffusion of zirconia from porous crystals to form non-porous crystals. This process is continued to 1000°C, at which point the only open mesoporosity present is intercrystalline, with pore diameters between 20 and 40 nm.

6.4 Summary

This chapter has investigated the changes that occur in the microstructure of nanocrystalline zirconia with heating in the range 450 - 1100°C. The evolution of microstructure can be divided into three stages:

1. As described in Chapter 5, amorphous zirconia heated to approximately 450°C forms crystals of tetragonal phase crystals, with average diameter ~ 30 nm. A fraction of highly microporous, amorphous zirconia remains. The crystals contain many 2 - 5 nm *intracrystalline* pores, derived from NO_x-containing bubbles in the amorphous material. In the first stage of heating, up to 600°C, the residual amorphous material fully crystallises, greatly reducing the BET surface area. The intracrystalline pores increase in size to approximately 5 - 10 nm. While a fraction of these pores are open to the surface and can be detected by nitrogen sorption, the majority are probably closed and remain present up to higher temperatures. The lattice parameters of the tetragonal phase also change significantly during this stage, with the value of c/a_s increasing from 1.017 to 1.019.

2. The microstructure changes very little during the second stage of heating, between 600 and 900°C. The crystal size and intracrystalline pores remain the same size, although faceting of the crystal surfaces develops. A small fraction (4 %) of monoclinic phase is formed after heating to 600°C, and this fraction increases slightly with higher treatment temperature. The material has largely formed a stable microstructure, and at these temperatures the mass-transport mechanisms remain largely inactive.

3. Considerable changes occur in the microstructure during the third stage, at treatment temperatures above 900°C. The crystal size increases strongly, indicating that the mass-transport mechanisms, particularly surface diffusion, have become active. These mechanisms lead to the elimination of most of the intracrystalline pores, as zirconia diffuses from porous crystals to form non-porous crystals, although some pores are trapped at the centre of large crystals. The only open porosity remaining is intercrystalline. The other major change takes place between 900 and 950°C, between which a 'critical temperature' is reached and over 90 % of the tetragonal phase transforms to monoclinic.

This chapter has also reported three important observations relating to the transformation of the 'metastable' tetragonal phase to the monoclinic phase:

1. The transformation is not directly triggered by an increase in the crystal size or a decrease in surface area. Crystalline samples that are composed of almost entirely either tetragonal or monoclinic phase have greatly overlapping crystal size distributions, and very similar surface areas. The effect of surface area on phase stability is minimal.

2. The 'critical temperature' is coincident with the loss of a small amount of mass, probably surface nitrate. This provides a realistic mechanism by which changes in surface energy could alter the stability of the tetragonal phase.

3. A link between the stability of the pure, metastable zirconia phase and its lattice parameters has been reported for the first time. A 'limit of stability' (or metastability) for the tetragonal phase, corresponding to $c/a_s \approx 1.020$, has been identified by comparing the data presented here with previously published data of stabilised zirconia.

6.5 References

1. H. Toraya, M. Yoshimura and S. Sōmiya, "Calibration curve for quantitative analysis of the monoclinic-tetragonal ZrO_2 system by X-ray diffraction" *J. Am. Ceram. Soc. 67* [6] C119-C121 (1984)
2. G.A. Kourouklis and E. Liarokapis, "Pressure and temperature dependence of the Raman spectra of zirconia and hafnia" *J. Am. Ceram. Soc. 74* [3] 520-523 (1991)
3. M. Ishigame and T. Sakurai, "Temperature dependence of the Raman spectra of ZrO_2" *J. Am. Ceram. Soc. 60* [7-8] 367-369 (1976)
4. M. Bowden, G.D. Dickson, D.J. Gardiner and D.J. Wood, "Patterns of stress-induced phase transformation in MgO-stabilized zirconia ceramic revealed using micro-Raman imaging", *J. Mater. Sci. 28*, 1031-1036 (1993)
5. C.S. Lim, T.R. Finlayson, F. Ninio and J.R. Griffiths, "*In-situ* measurement of the stress-induced phase transformations in magnesia-partially-stabilised zirconia using Raman spectroscopy" *J. Am. Ceram. Soc. 75* [6] 1570-1573 (1992)
6. M. Yashima, K. Ohtake, M. Kakihana, H. Arashi and M. Yoshimura, "Determination of tetragonal-cubic phase boundary of $Zr_{1-x}R_xO_{2-x/2}$ (R = Nd, Sm, Y, Er and Yb) by Raman scattering" *J. Phys. Chem. Solids 57* [1] 17-24 (1996)
7. Yu. K. Voron'ko, A.V. Gorbachev and A.A. Sobol', "Raman scattering and the structure of cubic solid solutions based on zirconium and hafnium dioxides" *Phys. Solid State 37* [7] 1055-1062 (1995)
8. R. Srinivasan, M.B. Harris, S.F. Simpson, R.J. De Angelis and B.H. Davis, "Zirconium oxide crystal phase: the role of the *p*H and time to attain the final *p*H for precipitation of the hydrous oxide" *J. Mater. Res. 3* [4] 787-797 (1988)
9. D.A. Ward and E.I. Ko, "Synthesis and structural transformation of zirconia aerogels" *Chem. Mater. 5* 956-969 (1993)
10. V.G. Keramidas and W.B. White, "Raman scattering study of the crystallisation and phase transformation of ZrO_2" *J. Am. Ceram. Soc. 57* [1] 22-24 (1974)
11. G. Štefanić, S. Musić and A. Sekulić, "Influence of precipitation chemistry and ball-milling on the thermal behaviour of zirconium hydroxide" *Thermochimica Acta 273*, 119-133 (1996)
12. J. Málek, L. Beneš and T. Mitsuhashi, "Powder diffraction data and Rietveld refinement of metastable t-ZrO_2 at low temperature" *Powder Diffraction 12* [2] 96-98 (1997)
13. N. Igawa, Y. Ishii, T. Nagasaki, Y. Morii, S. Funahashi and H. Ohno, "Crystal structure of metastable tetragonal zirconia by neutron powder diffraction study" *J. Am. Ceram. Soc. 76* [10] 2673-2676 (1993)
14. M. Yashima, T. Noma, N. Ishizawa and M. Yoshimura "Effects of noncompositional inhomogeneity on $t \rightarrow m$ phase transformation during grinding of various rare-earth-doped zirconias" *J. Am. Ceram. Soc. 74* [12] 3011-3016 (1994)
15. D.-J. Kim and T.-Y. Tien, "Phase stability and physical properties of cubic and tetragonal ZrO_2 in the system ZrO_2-Y_2O_3-Ta_2O_5" *J. Am. Ceram. Soc 74* [12] 3061-3065 (1991)
16. D.-J. Kim, "Effect of tetravalent dopants on Raman spectra of tetragonal zirconia" *J. Am. Ceram. Soc. 80* [6] 1453-1461 (1997)
17. E.H. Kisi and C.J. Howard, "Crystal structure of zirconia phases and their inter-relation" *Key Engineering Materials 153-154* 1-36 (1998)
18. M. Yoshimura, "Phase stability of zirconia" *Bull. Am. Ceram. Soc. 67* [12] 1950-1955 (1988)
19. M. Yashima, M. Kakihana, K. Ishii, Y. Ikuma and M. Yoshimura, "Synthesis of metastable tetragonal (t′) zirconia-calcia solid solution by pyrolysis of organic precursors and coprecipitation route" *J. Mater. Res. 11* [6] 1410-1420 (1996)
20. H.G. Scott, *J. Mater. Sci. 10*, 1527 (1975)
21. N.K. Simha, "Crystallography of the tetragonal → monoclinic transformation in zirconia" *Journal de Physique IV 5* [C8] 1121-1126 (1995)
22. R. Srinivasan, B.H. Davis, L.A. Rice and R.J. De Angelis, "Electron microdiffraction studies of zirconia particles" *J. Mater. Sci. 27* 661-670 (1992)
23. P.M. Kelly, "Martensitic transformations in ceramics" *Mater. Sci. Forum 56-58* 335-346 (1990)
24. J. Rankin and B.W. Sheldon, "In situ TEM sintering of nano-sized ZrO_2 particles" *Mater. Sci. Eng. A204* 48-53 (1995)

25. C.G. Levi, "Metastability and microstructure evolution in the synthesis of inorganics from precursors" *Acta Mater. 46* [3] 787-800 (1998)
26. A.J. Allen, S. Krueger, G. Skandan, G.G. Long, H. Hahn, H.M. Kerch, J.C. Parker and M.N. Ali, "Microevolution during the sintering of nanostructured ceramic oxides" *J. Am. Ceram. Soc. 79* [5] 1201-1212 (1996)
27. E. Bernstein, M. G. Blanchin, R. Ravelle-Chapuis and J. Rodriguez-Carvajal, "Structural studies of phase transformations in ultrafine zirconia powders *" J. Mater. Sci. 27* 6519-6524 (1992).
28. M. Daturi, C. Binet, S. Bernal, J.A. Pérez Omil and J.C. Lavelley, "FTIR study of defects produced in ZrO_2 samples by thermal treatment; residual species into cavities and surface defects" *J. Chem. Soc. Faraday Trans. 98* [8] 1143-1147 (1998)
29. S.J. Gregg and K.S.W. Sing, *Adsoption, Surface Area and Porosity* (second edition), Academic Press, London (1982)
30. K.S.W. Sing, D.H. Everett, R.A.W. Haul, L. Moscou, R.A. Pierotti, J. Rouquérol and T. Siemieniewska, "Reporting physisorption data for gas/solid systems with special reference to the determination of surface area and porosity" *Pure & Appl. Chem. 57* [4] 603-619 (1985)
31. T. Malis, S.C. Cheng and R.F. Egerton, "EELS log-ratio technique for specimen-thickness measurement in the TEM" *Journal of Electron Microscopy Technique 8* 193-200 (1988)

7. The tetragonal-to-monoclinic transformation

7.1 Introduction

The transformations and reactions that occur in a material during a heating-cooling cycle can only be indirectly studied by characterising the material after cooling, and much more valuable information can be provided by *in-situ* characterisation *during* the heating cycle. For example, until recently it was assumed that the transformation of the 'metastable' tetragonal phase to monoclinic occurred at high temperature, during heating or holding at high temperature. As is discussed in Section 2.3.3, a few recent XRD studies have shown that the transformation occurs during cooling, often below 500°C.[1-3] The work described here complements and extends these studies.

The general approach used has been to apply a heat-hold-cool cycle to tetragonal zirconia, in which the sample was heated at a steady rate to the maximum temperature, held at that temperature for a period, and then cooled to ambient temperature. A maximum temperature of 1000°C was chosen for most experiments, as it was found that the transformation would occur upon cooling from this temperature. A number of the previous studies have found that increasing the maximum treatment temperature strongly increased the temperature at which the t ? m transformation was observed, so this experiment was not repeated except for DTA/TGA.

Two *in-situ* techniques have been applied. Conventional Raman spectroscopy was used to characterise the phase composition, while simultaneous DTA/TGA was used to provide information on exothermic and endothermic reactions. *There has been no previous report of the use of either Raman spectroscopy or DTA/TGA to characterise the t ? m transformation during cooling of the metastable tetragonal phase.*

XRD is the most widely used technique for *in-situ* studies of phase composition, but Raman spectroscopy is a far more convenient technique to use with zirconia. A Raman spectrum with a reasonable signal-to-noise ratio could be measured in approximately one minute, much more quickly than a diffraction pattern using a conventional laboratory X-ray source, and from this spectrum the monoclinic and tetragonal phases can be very easily distinguished. The technique also requires much less sample quantity and sample preparation time. The main limitations are that lattice parameters and crystal size cannot be obtained, and a loss of precision in phase-ratio measurements. Experiments with a heating stage on a X-ray diffractometer were also

attempted but were not successful, as the sample chamber had to be evacuated to prevent overheating, and it is known that a vacuum inhibits the t ? m transformation.[4-6]

The starting material chosen was near-pure phase (> 96 %) metastable tetragonal zirconia, prepared by heating a standard gel just past the crystallisation point.* Limited *in-situ* Raman and DTA/TGA experiments using the as-dried gel as a starting material have given very similar results, so it does not appear as if the 'pre-calcine' has greatly affect the major findings.

* This choice of 'pre-calcined' zirconia over the unheated gel was made for a number of practical reasons. Firstly, it was desirable to avoid the release of NO_x gas in sample compartment of the instruments during decomposition of the gel. Secondly, when fine particles of gel were heated in the hot-stage they moved considerably during the decomposition reactions, which made focusing the laser onto the sample very difficult. Thirdly, the mass-loss measurements on the DTA/TGA instrument are most accurate when only a very small mass is lost from the initial sample.

7.2 Procedure

The starting material was prepared by heating a standard gel to 500°C for an hour. The Raman spectrum and the diffraction pattern indicated that the resulting zirconia powder primarily consisted of the tetragonal phase, with less than 4 % monoclinic phase present.

For the *in-situ* Raman experiments, samples were heated and cooled in a hot-stage[*] with static air atmosphere, with Raman spectra recorded periodically with a conventional spectrometer.[†] The volume fraction of monoclinic phase was calculated from each spectrum using the calibration method described in Appendix B.

The mass loss and thermal characteristics were measured by simultaneous differential thermal analysis and thermogravimetric analysis (DTA/TGA)[‡] in dry, flowing air. After the samples were cooled, they were removed from the instrument and their phase composition determined by FT-Raman spectroscopy.[§]

The maximum temperature, dwell time, and cooling rate were varied to investigate their effect on the events observed during cooling. The range of conditions for which results are reported here are given in Table 7-1.

Table 7-1: Variations in heating profile

	Raman	DTA/TGA
Heating rate	20°C/min	10°C/min
Maximum temperature	600, 1000°C	700, 900, 1000, 1100°C
Dwell time	10, 30, 60 min	30 min
Cooling rate	10, 20, 50°C/min	5, 10, 20°C/min

Calibration of instruments

It was important to ensure that the Raman/hot-stage and DTA/TGA systems measured the temperature of the sample consistently. To calibrate the two systems, a standard material with

---

[*] Linkam TS1500 hot stage, capable of reaching 1500°C. Approximately 20 mg of sample was held in a shallow platinum tray within the alumina furnace.

[†] Dilor XY 600 spectrometer, using an excitation line of 514.5 nm from an Ar^+ laser, focused onto the sample through a heat-resistant ×20 objective lens. The effective resolution was 1.5 cm^{-1}. The collection time was typically 60 seconds.

[‡] Setaram TAG 24 simultaneous DTA/TGA instrument.

[§] Bio-Rad FT-Raman II, using an excitation line of 1064 nm from a Nd:YAG laser. The effective resolution was 4 cm^{-1}.

a known, reversible transformation was selected, and the transformation temperature was measured during heating and cooling at several heating/cooling rates. The material selected was cristobalite, a crystalline form of silica, which was prepared at 1540°C. The α ? β transformation of cristobalite at approximately 260°C could be characterised by both DTA and Raman spectroscopy.* It was found that the 'peak' temperatures in the DTA trace corresponded to the transformation temperature determined from the Raman spectra within ± 10°C. It was also found that for both systems the transformation temperature shifted less than 5°C with changes in the heating and cooling rate (*ie* negligible thermal 'lag'). Doubling the laser power from 50 to 100mW made no significant difference to the transformation temperature, so there no evidence for heating from the laser beam.

* The α ? β transformation of cristobalite has been studied extensively with DTA by Hill and Roy.[7] Cristobalite has a α ? β transformation during heating at ~ 270°C, and a β ? α transformation on cooling at ~ 250°C, but the transformation temperature varies with preparation conditions. The Raman spectra of the α and β cristobalite phases have been reported and assigned.[8,9]

7.3 Results and discussion

7.3.1 Raman spectroscopy

Results

Figure 7-1 shows a three-dimensional plot of conventional Raman spectra collected during cooling of tetragonal zirconia from 1000°C. The bands assigned to the tetragonal phase start to decrease strongly in intensity as the temperature falls below 400°C, and the bands assigned to the monoclinic phase correspondingly increase in intensity.

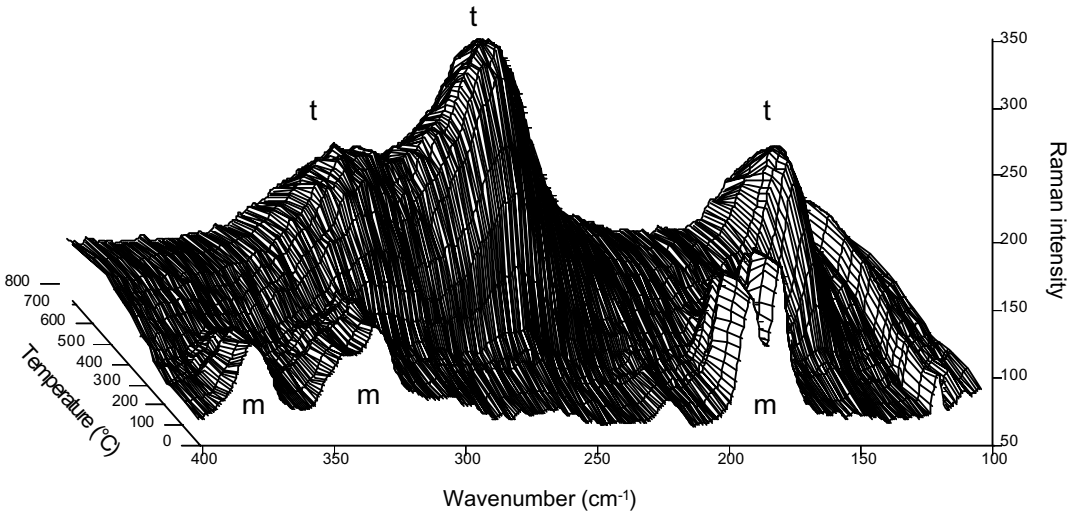

Figure 7-1: Three-dimensional plot of conventional Raman spectra collected during cooling of tetragonal zirconia from 1000°C. The bands assigned to the tetragonal (t) and monoclinic (m) phases are marked. The small peak at approximately 120 cm^{-1} is due to a 'plasma line' from the laser.

Although the Figure 7-1 shows how the Raman spectrum changes with cooling, the data is more clearly expressed by calculating the volume fraction of monoclinic phase, f_m (defined in Appendix B), and plotting it against temperature. Plots of f_m are given in Figure 7-2 for experiments in which the maximum temperature was 1000°C. In most cases a small fraction of monoclinic phase, approximately 10 vol %, has formed after holding at 1000°C, and is present before cooling takes place. Observations indicate that this fraction forms during the holding stage, and not during heating. The remainder of the transformation does not take place until below 400°C, and between 400 and 100°C approximately 70 - 80 vol % of the tetragonal phase transforms to monoclinic.

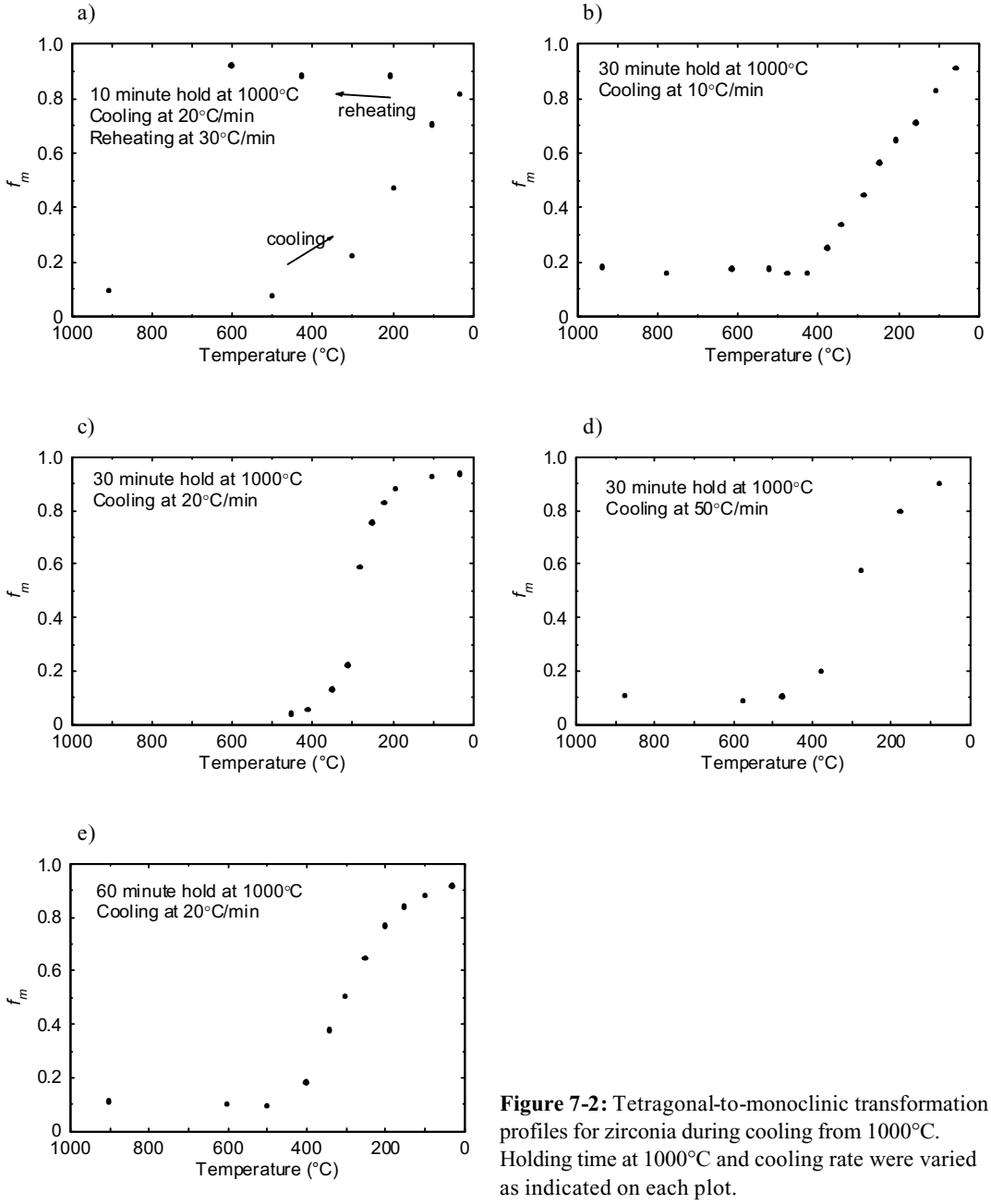

Figure 7-2: Tetragonal-to-monoclinic transformation profiles for zirconia during cooling from 1000°C. Holding time at 1000°C and cooling rate were varied as indicated on each plot.

A further experiment was carried out in which tetragonal zirconia was held at 600°C for an hour before cooling. No transformation was observed, as was expected from the results in Section 6.3.1.

From these profiles, two temperatures have been defined for the following discussion. The first is the *initiation temperature*, T_i, which corresponds to the point at which the transformation begins. This temperature is difficult to measure precisely from the profiles, but is at approximately 500°C, and no lower than 400°C. The second temperature is the '*transformation temperature*', which was defined as the 'midpoint' of the reaction, $f_m = 0.5$,

and generally coincided with the steepest part of the transformation curve (ie the point of most rapid transformation).

Dependence of the transformation temperature on heating profile

The variation of transformation temperature with the holding temperature and cooling rate is shown in Table 7-2. The largest effect is that of holding time, in which the transformation temperature can be increased by over 100°C by increasing the holding time from 10 to 30 minutes. A very similar result has been obtained by a number of other *in-situ* diffraction studies.[1-3,10] There is little further increase in the transformation temperature if the holding time is doubled to 60 minutes.

Table 7-2: Variation of the t ? m 'transformation temperature' with cooling rate and holding time.

Holding time	Cooling rate (°C/min)		
(min)	10	20	50
10		180°C	
30	270°C	290°C	295°C
60		300°C	

The transformation temperature also increases slightly with cooling rate. The measured change is quite small with respect to the total width of the transformation profile, and may be negligible. One earlier study has reported that the onset temperature for the transformation may decrease as cooling rate increases, but that the size of the difference depends on the chemical preparation conditions for the precursor.[11] In any case, it is clear that for the material studied here the cooling rate is not a major factor in determining the transformation temperature.

Reheating

For all experiments a small fraction of tetragonal phase remained after cooling to ambient temperature. In the case in which the sample was cooled after heating for only 10 minutes, the fraction of remaining tetragonal phase was approximately 20 vol %. This sample was then re-heated at 30°C/min and the transformation to monoclinic phase was observed to continue, as shown in Figure 7-2*a*. For another experiment (the data for which is not shown here), in which the holding time at 1000°C was 5 minutes, the fraction of tetragonal phase remaining was

approximately 50 vol %. When this sample was re-heated beyond 200°C the transformation continued, and was almost complete by 1000°C.

These observations, previously unreported, have two important implications. The first is that there is a minimum temperature, T_m, below which the t? m transformation can be 'frozen'. The transformation profiles in Figure 7-2 indicate that T_m is in the vicinity of 100 - 200°C. This means that no particular 'mechanism', such as small particle size, is required to explain the indefinite stability of the tetragonal phase *at ambient temperature*; lack of thermal energy is sufficient. However, a mechanism is required to account for stability at above T_m.

The second implication is that the tetragonal phase is *metastable* immediately before transformation; if it were thermodynamically stable then reheating would reverse the t? m transformation. Although cooling conditions are required to initiate the bulk of the transformation, they are not required to continue the reaction. This is consistent with most theories, but has an important bearing on the 'surface energy' theory, which relies on thermodynamic arguments (see Section 2.4.2.6). Regardless of whether the tetragonal phase is thermodynamically stabilised by a large surface area, it becomes metastable at some point before the t? m transformation. Therefor the 'surface energy' theory is not particularly useful for explaining the effect of heat-treatment conditions on the transformation temperature.

Relating the 'initiation temperature' to the 'critical temperature'

The t? m transformation 'initiation temperature' can be considered to be a particular property of any metastable tetragonal material. If it is above T_m, then the transformation will begin to take place. Depending on the thermal history of the sample, the initiated transformation may then proceed to completion before the temperature falls below T_m. If the initiation temperature is below T_m, then no transformation will take place.

The 'critical temperature' identified in the previous chapter can now be clearly defined as the minimum treatment temperature (all other conditions being equal) that will increase the initiation temperature above T_m, and thus initiate the transformation on cooling. Chapter 6 identified two factors that were likely to contribute to the value of the 'critical temperature': a change in the surface energy of the crystals, and the lattice parameters of the tetragonal phase. However, although these two factors may explain whether the tetragonal phase transforms or not after heating at a certain temperature, they do not provide a mechanism to account for the variation in the actual transformation temperature. The remainder of this section explores the ways by which the thermal treatment might affect the initiation and transformation temperatures.

Hysteresis in the t ? m transformation

It is worthwhile to consider the reversible t ? m transformation at ~ 1100°C, which has been thoroughly studied in the past and is discussed in Section 2.1.3. This transformation is subject to hysteresis, which increases with stress and crystal size.[12] Examples of m ? t temperatures above 1150°C and t ? m temperatures below 800°C have been previously reported,[13] and the t ? m transformation at ~ 300°C reported here could be regarded as an extreme case of hysteresis. This would also explain why the transformation was not reversed on re-heating, as the corresponding m ? t temperature would be well above 1100°C.

Unfortunately, there is no known mechanisms for the degree of hysteresis to be affected by thermal treatment, atmosphere, etc, aside from the crystal size. The results in Section 6.3.3 strongly indicate that crystal size does not have major influence on the transformation.

The 'dynamic embryo' concept

A concept that has been previously proposed, and may yet prove useful, is that of a 'dynamic embryo' site of some kind,[1,14-16] which was introduced in Section 2.4.2.5. The proposed embryo is a nanoscale structure in the tetragonal phase, with a structure either similar to that of the monoclinic phase,[1] or midway between the two phases.[15] The embryo initiates the transformation to the monoclinic phase in a particular crystal when the temperature falls below a certain temperature, which correspond to the 'initiation temperature' as defined above. The initiation temperature *increases* with the size of the embryo. The embryo may grow in size during heating, so that more extensive heat treatment leads to higher transformation temperatures.

Various variations of this theory have been suggested which account for many other observed characteristics of the t ? m transformation. For example, the strong effect of chemical preparation conditions on the transformation temperature may be caused by the number of embryos initially present in the crystalline structure.[1]

Chapter 6 identified a number of factors that may well trigger the t ? m transformation. Two of these can be related to the embryo theory, in that they may promote the growth of the embryos. Firstly, in the case of the change in lattice parameters beyond a 'critical point' of stability, it is quite possible that monoclinic embryos will grow more rapidly in the tetragonal phase if its lattice parameters render it less thermodynamically stable. Secondly, an increase in the diffusion coefficients beyond 900 - 1000°C may also promote the growth of the embryos. A third factor, the surface energy of the nanocrystals, does not directly relate to behaviour of

the embryos, but surface energy is most likely to determine the stable ? metastable transition rather than the metastable ? unstable transformation.

There is only one major difficulty with the embryo concept in explaining the characteristics of the t ? m transformation. It does not explain the effect of atmosphere on the t ? m transformation, which has been reported in many previous studies (see Section 2.3.3). Furthermore, there is no direct evidence for the existence of the proposed embryo structure. Nevertheless, it remains the best available theory at the present.

7.3.2 Thermal analysis

Figure 7-3 shows a typical DTA/TGA trace for a sample heated at 10°C/min to 1000°C, held for 30 minutes, then cooled at the same rate. The main point of interest in the trace is the exothermic peak that is observed during the cooling stage. The exotherm begins at 560°C, peaks at 533°C, and trails off to below 400°C. The main section of the peak spans approximately 540 - 515°C. There is no corresponding change in mass observed.* The Raman spectrum of all samples after cooling from 1000°C or above show them to be composed entirely of the monoclinic phase, as expected from results discussed in Chapter 6 and Section 7.3.1.

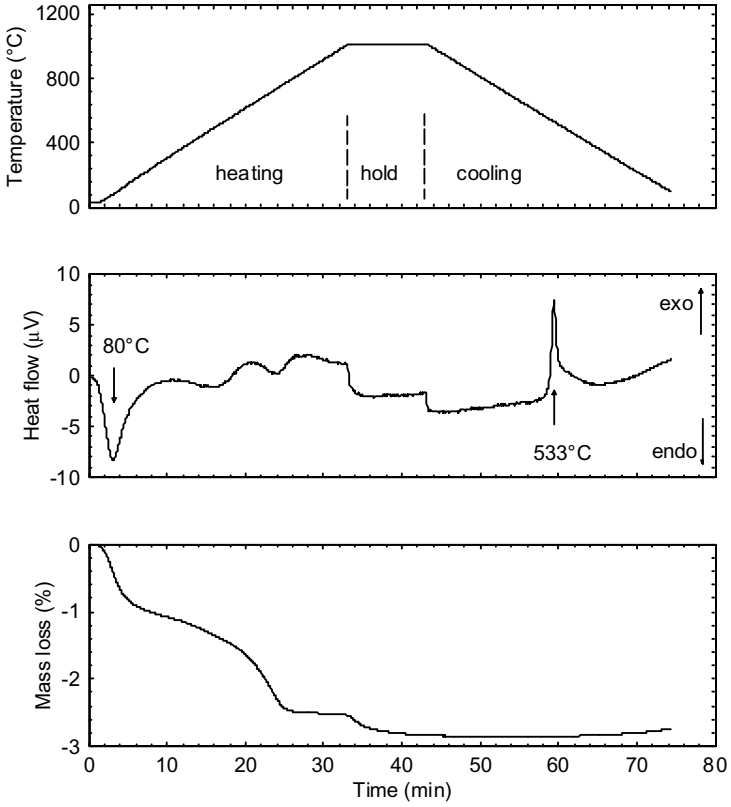

Figure 7-3: DTA/TGA trace for tetragonal zirconia heated to at 10°C/min to 1000°C, held for 30 minutes, then cooled at the same rate.

As the cooling rate was decreased the 'peak temperature' for the exotherm increased slightly, as shown in Table 7-3. Note that this trend is opposite to the minor trend observed in the

* In other heating-cooling experiments, using a different batch of gel, the loss of approximately 0.05 % of the original mass was consistently observed to occur concurrent to the exotherm. The origin of this mass-loss remains uncertain.

in-situ Raman study for the t ? m transformation. The four points measured do not conform to a simple Arrhenius relationship between the 'peak temperature' and the heating rate.

Table 7-3

Cooling rate (°C/min)	Peak temperature (°C)
20	530
10	533
7	537
5	542

In further experiments the maximum dwell temperature was varied. When the maximum temperature was 700 or 900°C no exotherm was observed during the cooling stage, and the sample after cooling consisted largely of the tetragonal phase. When the sample was heated to 1100°C for 30 minutes an exothermic peak was observed at 720°C, and the product was monoclinic phase.

These observations strongly imply that the exothermic reaction observed during cooling is associated with the tetragonal-to-monoclinic transformation. However, it is clear that the temperature at which the exotherm occurs is approximately 250°C *above* the 'midway point' of the transformation as identified by the *in-situ* Raman study. In addition, the exotherm spans approximately 40°C, while 60% of the transformation generally takes place over a range of approximately 200°C. *Thus the exotherm cannot be due to heat released by the t ? m transformation itself, but probably is due to some other process associated with the transformation.* Note that in the DTA/TGA experiment dry air was used, while the stage for the *in-situ* Raman experiment contained static, atmospheric air. However, the presence of moisture is unlike to cause the observed difference in temperatures, as all previous studies have shown that moisture *promotes* the t ? m transformation rather than inhibits it.[4,17-19]

The nature of the process that leads to the exotherm is currently unclear. Comparison of Table 7-3 with Figure 7-2 indicates that the exotherm occurs just before the main transformation begins, and it is suggested that the exotherm may be due to some type of nucleation reaction by which the transformation is rapidly initiated. It remains to be determined whether this exothermic reaction can be related to the formation or growth of monoclinic 'embryo' structures discussed in the previous section.

There are several other minor features of the DTA/TGA trace shown in Figure 7-3, in particular the endothermic loss of small amounts of mass during the heating stage. The first of these, at 80°C, is due to the loss of adsorbed water, while the subsequent reactions are assigned to the loss of residual nitrate and hydroxy groups. Those observed above 500°C correspond to the DTA/TGA trace of the as-prepared gel, discussed in Section 5.3.5. Note the mass loss of 0.2 - 0.3 % that begins just before the hold at 1000°C. The discontinuities in the heat-flow trace at the points at which the heating rate changes are instrumental artefacts, and can be disregarded.

7.4 Conclusions

The work presented in this chapter leads to the following conclusions on the tetragonal-to-monoclinic (t ? m) transformation:

- The t ? m transformation occurs in two stages. In the first stage a small fraction (~ 10 %) of the material transforms to monoclinic during holding at high temperature. In the second stage the majority (> 80 %) of the material transforms during cooling between 400 and 100°C.
- There is insufficient energy for the t ? m transformation to proceed below approximately 100 - 200°C. The transformation may be quenched below this temperature, and will continue if the material is re-heated.
- The tetragonal phase is thermodynamically metastable before it transforms to the monoclinic phase; otherwise re-heating would reverse the transformation.
- Lengthening the dwell time at maximum temperature increases the transformation temperature. The mechanism is not clear, but is consistent with the 'monoclinic embryo' theory, which has been proposed in various forms in previous studies.
- Cooling rate does not have a significant influence on the transformation temperature in this system.
- During cooling, the t ? m transformation is preceded by an exothermic 'reaction'. The nature of this reaction is unclear at present, but it is suggested that the reaction is associated with a nucleation/initiation process.
- Raman spectroscopy is a useful method to rapidly determine the phase composition of zirconia, and is appropriate for time-resolved studies of the t ? m phase transformation.

7.5 References

1. D.A. Ward and E.I. Ko, "Synthesis and structural transformation of zirconia aerogels" *Chem. Mater. 5* 956-969 (1993)
2. R. Srinivasan, C.R. Hubbard, O.B. Cavin and B.H. Davis, "Factors determining the crystal phases of zirconia powders: A new outlook" *Chem. Mater. 5* [1] 27-31 (1993)
3. X. Turrillas, P. Barnes, D. Häusermann, S.L. Jones and C.J. Norman, "Effect of chemical and heat treatment on the tetragonal-to-monoclinic transformation of zirconia" *J. Mater. Res. 8* [1] 163-168 (1993)
4. M.A. Villa Garcia, M.C. Trobajo Fernandez and C. Otero Arean, "Effect of water vapour on the thermal evolution of the metastable phases of zirconium dioxide" *Thermochimica Acta 126* 33-41 (1988)
5. Y. Murase and E. Kato, "Phase transformation of zirconia by ball-milling" *J. Am. Ceram. Soc. 62* [9-10] 527 (1979)
6. J. Livage, K. Doi and C. Mazières, "Nature and thermal evolution of amorphous hydrated zirconium oxide", *J. Am. Ceram. Soc. 51* [6] 349-353 (1968)
7. V.G. Hill and R. Roy, "Silica structure studies: V. The variable inversion in cristobalite" *J. Am. Ceram. Soc. 41* [12] 532-537 (1958)
8. J.B. Bates, "Raman spectra of α and β cristobalite" *J. Chem. Phys. 57* [9] 4042-4047 (1972)
9. J. Etchepare, M. Merian and P. Kaplan, "Vibrational normal modes of SiO_2. II Cristobalite and tridymite" *J. Chem. Phys. 68* [4] 1531-1537 (1978)
10. R. Srinivasan, B.H. Davis, O.B. Cavin and C.R. Hubbard, "Crystallisation and phase transformation process in zirconia: an in situ high-temperature X-ray diffraction study" *J. Am. Ceram. Soc. 75* [5] 1217-1222 (1992)
11. G.T. Mamott, P. Barnes, S.E. Tarling, S.J. Jones and C.J. Norman, "Dynamic studies of zirconia crystallisation" *J. Mater. Sci. 26* 4054-4061 (1991)
12. B.C. Muddle and G.R. Hugo, "Martensitic transformations in ceramics" *Proceedings of the International Conference on Martensitic Transformations, Monterey 1992*, 647-658 (1993)
13. R.N. Patil and E.C. Subbarao, "Monoclinic-tetragonal phase transition in zirconia: mechanism, pretransformation and coexistence" *Acta. Cryst. A26* 535-542 (1970)
14. R.C. Garvie and S.K. Chan, "Mechanism and thermodynamics of the monoclinic-tetragonal transformations of zirconia" *Material Science Forum 34-36* 95-101 (1988)
15. S.-K. Chan, "Theory of the energetics and non-classical nucleation for the tetragonal-monoclinic transformation of zirconia" *Advances in Ceramics 24* 983-995 (1988)
16. C.A. Andersson and T.K. Gupta, "Phase stability and transformation toughening in zirconia" *Advances in Ceramics 3* 184-201 (1981)
17. T. Kosma[illegible], V. Kra[illegible]evec, R. Gopalakrishnan and M. Komac, "Crystallisation of ZrO_2 from amorphous precipitates and its influence on the microstructure of sintered ceramics" *Advances in Ceramics 24* (Science and Technology of Zirconia III) 167-172 (1988)
18. T.Y. Tseng, C.C. Lin and J.T. Liaw, "Phase transformations of gel-derived magnesia partially stabilized zirconias" *J. Mater. Sci. 22* 965-972 (1987)
19. Y. Murase and E. Kato, "Role of water vapor in crystallite growth and tetragonal-monoclinic phase transformation of ZrO_2" *J. Am. Ceram. Soc. 66* [3] 196-200 (1983)

8. Assignment of the Raman spectra of zirconyl salts

8.1 Introduction

The purpose of this chapter is to assign the Raman spectra of zirconyl nitrate and chloride salts. These assignments are used in the assignment of the Raman spectrum of the sol in Section 3.5. Since this chapter contains a considerable amount of detail that is not directly necessary to understanding the structural evolution of the sol and gel, it is placed towards the end of this thesis.

This chapter is divided into three principle parts. Section 8.2 will introduce the principles and practice of Raman spectroscopy. Section 8.3 will assign the Raman spectra of zirconyl salts using the conventional approach of comparing the spectra with the structure of the material, where known, and previous studies of closely-related materials. 'First-principles' theoretical vibrational calculations have been carried out as an additional method to assign the Raman spectra, and the results are presented in Section 8.4.

8.2 Raman spectroscopy: theory and practice

This section briefly introduces vibrational spectroscopy, and Raman spectroscopy in particular. A fuller treatment of the topics covered here can be found in standard texts.[1,2]

Vibrational spectroscopy

All molecules and atomic networks vibrate with thermal energy, through the elasticity of interatomic bonds. Every vibrating structure will vibrate (ie cyclic deformations of the structure) in a several well-defined ways, known as *modes*. Each mode of vibration occurs at a characteristic frequency, which is determined by the mass of the atoms and the strength of the bonds involved. If the frequency and other characteristics of the vibrational modes can be identified, they can be used to obtain a great deal of information about the structure of a material. Molecular vibrations can be characterised by their interaction with electromagnetic radiation, leading to a class of characterisation techniques known as *vibrational spectroscopy*. There are two common approaches: *infrared absorption* and *Raman* spectroscopy.

Infrared absorption spectroscopy makes use of the fact that structures vibrating at a certain frequency will absorb radiation of the same frequency. Electromagnetic radiation in the infrared region is passed through, or reflected off, the sample, and the absorption spectrum is measured. This spectrum will indicate the frequency of each "infrared-active" mode of the structure.

Raman spectroscopy makes use of the Raman phenomenon. When radiation is scattered by a material the vast majority of the radiation is scattered elastically. A very small fraction ($\sim 10^{-6}$) is scattered inelastically, interacting with the vibrations occurring in the material, which either remove or add energy to the scattered radiation. The result is that a very small fraction of radiation scattered by a material will be scattered at wavelengths that are slightly higher or lower than the original wavelength. The energy by which the wavelength has been changed, known as the *Raman shift*, is the same as the vibrational frequency for each of the "Raman-active" modes in the material. The radiation scattered at a lower energy is more intense than that scattered at a higher energy, and in practice the former is most commonly used in Raman spectroscopy. The spectrum of the scattering intensity as a function of the Raman shift is known as the *Raman spectrum*.

These two complementary approaches have various advantages, and are sensitive to different kinds of modes and suitable for different environments. Only Raman spectroscopy has been used for the work in this chapter and elsewhere in this thesis, mainly because infrared absorption spectroscopy is difficult to apply to acidic, aqueous solutions, and requires considerably more sample preparation time.

Vibrational frequencies and Raman shifts are commonly measured in *wavenumbers*, cm^{-1}, which is a convenient unit, although non-SI.

Raman spectroscopy in practice

The excitation source used for Raman spectroscopy is usually a laser, producing polarised, coherent, monochromatic radiation. The laser beam is incident on the sample, which scatters the radiation. Some of the scattered radiation is collected by the spectrometer, and the excitation wavelength is filtered out so that only the Raman-shifted wavelengths are detected. There are two techniques of measuring the Raman scattering spectrum. The conventional technique is to separate the various wavelengths, which are then detected by a scanning photomultiplier tube or a CCD array. A more recent development is the *FT-Raman* technique, by which the wavelengths are separated by an interferometer, and the interferogram is Fourier-transformed to produce a spectrum. FT-Raman allows a spectrum to be measured very rapidly over a very wide frequency range (eg -2000 to 3500 cm^{-1}).

An advantage of Raman spectroscopy is that it only requires the incident radiation to be scattered, not transmitted or reflected as in infrared absorption spectroscopy. This greatly reduces the sample preparation required, and increases the range of samples to which it can be applied.

Water absorbs very strongly in the infrared region below 7400 cm^{-1}, so that samples must be largely free of water in order to measure an infrared absorption spectrum. An important advantage of Raman spectroscopy is that the excitation wavelength can be selected to avoid this region. For example, a Nd^{3+}:YAG laser, commonly used in FT-Raman spectrometers, will radiate at 9398 cm^{-1} (1064 nm), allowing Raman shifts up to 2000 cm^{-1} to be measured without interference from water absorption. A similar advantage applies to glass, so liquid samples can be held in glass cells. In addition to this, the Raman spectrum of water is relatively weak.

Although the Raman spectra of materials can be calculated from first principles, given the precise composition and structure, the procedure is complex and seldom done. In practice the structure of a material cannot be calculated from the raw Raman spectra, and identification is usually by comparison of the sample spectrum with those of model systems and earlier studies. Thus the accurate interpretation of spectra can be time consuming and requires considerable experience.

Raman-activity and symmetry of vibrations

Any particular vibrational mode may be 'active' in either the Raman and/or the infrared spectra, depending on the characteristics of the vibration. When a molecule vibrates it periodically changes in size and/or shape, and the distortion from the equilibrium position can be expressed as the quantity q. The molecular polarisability, α, and the dipole moment, μ, also change with the vibration. A mode is *Raman-active* if the 'rate of change' of polarisability, $d\alpha/dq$, at the equilibrium position of the molecule ($q = 0$) is non-zero. Likewise, a mode is *infrared-active* if the 'rate of change' of the dipole moment, $d\mu/dq$, at the equilibrium position is non-zero.

Another important concept is the *symmetry* of the vibrational mode. A mode is symmetric to the extent that any geometric symmetry present in the equilibrium position is retained throughout the oscillation. Vibrational modes are generally classed as *symmetric* or *antisymmetric*, according to the degree of symmetry present in the vibration. A good way of classifying simple vibrations is to compare the two 'extreme' points of the vibration, q^+ and q^-. If the shape of a molecule at the two extremes is the same, although the size is different, then the vibration can be classed as completely symmetric. If the molecule at q^+ is a mirror image of that at q^-, the mode can be classed as completely antisymmetric. Two simple examples of symmetric and antisymmetric vibrations of a triatomic molecule are given in Figure 8-1.

The symmetry of a mode is closely related to the change in polarisability. Antisymmetric modes generally have a zero value of $d\alpha/dq$ at the equilibrium position, and are thus Raman-inactive.

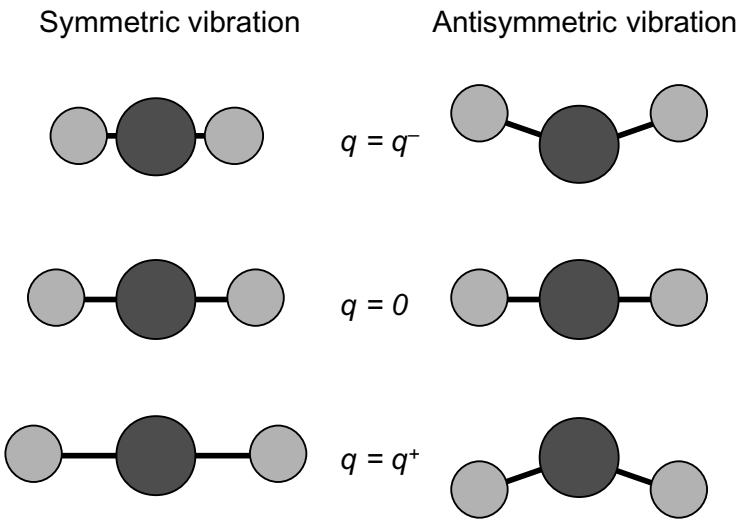

Figure 8-1: Simple examples of symmetric and antisymmetric vibrations of a triatomic molecule.

Polarisation of Raman bands

The symmetry of a vibrational mode will also influence the way that it interacts with the radiation as it is Raman-scattered. When radiation interacts with a completely symmetric vibration, the Raman-scattered radiation will retain its initial polarisation; radiation that is Raman-scattered from an antisymmetric vibration will be randomly polarised, and is said to be *depolarised*.* This effect can be measured using polarisers, and is used to identify the symmetry of each Raman-active vibrational mode that contributes towards a Raman spectrum, and thus help to assign it to particular vibration.

A polariser is mounted between the sample and the interferometer, through which the scattered radiation passes before detection. The Raman spectrum is measured with the polariser in two positions: parallel and perpendicular to the polarisation of the laser. The *depolarisation ratio*, ρ, of a particular line is defined as the intensity ratio of radiation scattered perpendicular and parallel to the incident radiation:

$$\rho = \frac{I_{\perp}}{I_{\parallel}}$$

* This phenomenon is mathematically expressed by the contribution of the polarisability tensor to the vibration. A totally symmetric vibration will contain only contributions from the diagonal component of the tensor, and so will scatter radiation only with the same polarisation as the exciting radiation.

The depolarisation ratio of a line is directly related to the symmetry of the molecular vibration giving rise to that line. When the excitation radiation is polarised, such as for a laser source, completely antisymmetric vibrations will have a depolarisation ratio of ¾. Symmetric (polarised) vibrations have a lower depolarisation ratio, which is often close to zero. In this case, the Raman peaks of polarised vibrations virtually disappear from the spectrum.

Polarisation measurements are only possible in homogenous, continuous materials, such as liquids and glasses. Measurements are not possible in polydomain materials, such as most solids, as the polarisation of the Raman-scattered radiation is scrambled as it is subsequently scattered by multiple boundaries between phases.

8.3 Study 1: Comparison of the Raman spectra of zirconyl salts

8.3.1 Introduction

This section reports and assigns the Raman spectra of zirconyl nitrate and zirconyl chloride, both as hydrated crystals and aqueous solutions. These assignments then assist in the assignment of the spectrum of the sol in Section 3.5.

Assignments for the Raman spectrum of zirconyl nitrate have not been previously published, although the spectrum of $Zr(NO_3)_4$ has been assigned.[3] In a recent infrared spectroscopy study assignments were only given to vibrations of nitrate species.[4] The Raman spectrum of zirconyl chloride has been reported and assigned by Kozhevnikova, Myund and Burkov and others,[5-8] but the assignments are tentative, and as discussed later in Section 8.3.4, may not be correct. Infrared spectra of crystalline zirconyl chloride have also been published.[6,9]

Information on the zirconium-oxygen bonds holds the most clues for determining the structure of zirconyl cations and the particles formed from them. The vibrations of metal-oxygen bonds, including stretching, twisting and bending modes, occur at relatively low frequencies, and we will concentrate primarily on the spectral region 200 to 650 cm^{-1}. Water libration (partial rotation) modes may also be found at these frequencies.

The known structures of the zirconyl salts will first be reviewed in this section. The Raman spectra will then be presented in Section 8.3.3, followed by a discussion and assignment of the observed bands in Section 8.3.4.

Review of structures

The salt crystallised from the zirconyl chloride solution was identified as $Zr(OH)_2Cl_2{\cdot}7H_2O$ by X-ray diffraction. The crystalline structure consists of discrete $[Zr_4(OH^{br})_8{\cdot}16H_2O]^{8+}$ 'cyclic-tetramer' cations, separated from each other in the lattice by chloride anions and water molecules.[10,11*] The structure of the tetramer species is that of four Zr^{4+} ions at the corners of a slightly-distorted square, each joined by two bridging hydroxy-groups (or hydroxy-bridges) along each 'edge'. Four water molecules around each Zr^{4+} ion complete the eight-fold coordination. The tetramer species has *close to* D_{4h} symmetry, but is slightly distorted.

---

* Throughout this thesis, OH^b will refer to hydroxy-bridges, and OH^t to terminal-hydroxy groups.

The cyclic-tetramer species has been shown to predominate in zirconyl chloride solution by ultracentrifugation,[12] wide-angle X-ray scattering,[13] small-angle X-ray scattering,[14] and X-ray absorption spectroscopy.[15] Some of the water molecules coordinated to the zirconium atoms will be hydrolysed, with terminal hydroxy groups which decrease the charge on the species, giving a formula of $[Zr_4(OH^{br})_8(OH^t)_n(16\text{-}n)H_2O]^{(8-n)+}$. The 'core' of the species, excluding the terminal-hydroxy and coordinated-water groups, *could* have a symmetry as high as D_{4h}, but including these groups the symmetry is likely to be much lower.

The structure of the salt crystallised from the zirconyl nitrate solution can be determined from the powder diffraction pattern, which is discussed in Section 4.3.5. This $Zr(OH)_2(NO_3)_2{\cdot}5H_2O$ structure is made up of parallel, cationic chains, with the repeating unit $[Zr(OH)_2(NO_3){\cdot}2H_2O]^+_n$.[16] The zirconium atoms within each chain are linked by double hydroxy bridges, and each zirconium is coordinated by four hydroxy-bridges, two water molecules, and a bidentate nitrate group. For each repeating unit there are also 2 - 3 water molecules and an additional ionic nitrate group located between the chains. Thus, half of the nitrate groups present are coordinated to the zirconium atoms, and the other half are ionically bound in the crystal lattice between the chains. The symmetry of these chains is fairly low.

No previous studies have indicated the size or type of species present in zirconyl nitrate solutions. It is occasionally assumed that the tetramer species will predominate,[14,17,18] although Livage has suggested that the 'chain' structure in the crystalline form may form the basis of the cation in solution.[19] The small-angle X-ray scattering measurements of zirconyl nitrate solutions, described in Chapter 9, provide some further information. The results are not very clear, due to the presence of a small fraction of larger (~140 Å) particles, but the scattering profile does suggest that the predominant species is approximately the size and shape of the tetramer species. The high scattering-angle profile gives no indication of any rod-shaped particles. For the purposes of this chapter, we will assume that the tetramer species predominates in zirconyl nitrate solution.

8.3.2 Procedure

Zirconyl nitrate and chloride salt solutions were prepared by the dissolution of zirconium carbonate in nitric or hydrochloric acid, with a zirconium-to-anion ratio of 1:2. Samples of solutions were dried under an air-flow to form the hydrated crystalline salts. The structure of each crystalline sample was determined by comparing its X-ray diffraction pattern* with previously published patterns.

The Raman spectrum of each sample was recorded at ambient temperature, using a commercial FT-Raman spectrometer.† Where possible, each band in the Raman spectra has been resolved and its position recorded. Where a number of broad, overlapping bands in a particular region made it difficult to distinguish each band, only the most intense were resolved. There may be a number of weak or very broad bands, particularly in the 200 - 600 cm^{-1} region, that are concealed by more intense neighbours and not resolved.

Raman polarisation measurements were made for the solutions. A polariser was mounted between the sample and the detector, and Raman spectra were measured with the polariser at 0° and 90° to the polarisation direction of the incident radiation. Due to the breadth of the overlapping bands, weak signal, and/or uncertain background, it was impractical to precisely measure the depolarisation ratio, ρ, for many bands. In most cases the observed bands have only been classified as polarised or depolarised. Peaks with $\rho < 0.2$ were classified as polarised (*p*), and those with $\rho > 0.7$ (theoretical maximum 0.75) were classified as depolarised (*dp*).

---

* Scintag X1 Advanced Diffraction System, using Cu K_α radiation.

† Bio-Rad FT-Raman II, using an excitation line of 1064 nm from a Nd:YAG (Neodymium-doped Yttrium Aluminium Garnet) laser. The effective resolution was 4 cm^{-1}.

8.3.3 Results

The XRD pattern of the zirconyl nitrate salt, dried from the zirconyl nitrate solution, is reported in Section 4.3.5, and identifies the crystalline structure as $Zr(OH)_2(NO_3)_2 \cdot 5H_2O$. The XRD pattern of the salt dried form the zirconyl chloride solution corresponded very closely with the pattern reported for $Zr(OH)_2Cl_2 \cdot 7H_2O$, which has been reported previously.[10,11]

Examples of the measured Raman spectra are given below. The position and polarisation assignments for all bands observed above 300 cm^{-1} is provided in Table 8-1. In this table, bands that have been assigned to the same vibration are aligned in rows. It was generally found that the concentration of the solution did not affect the band position or relative intensities, but that the Raman spectrum of more concentrated solutions had more intense bands with respect to the background.

It is important to note that both the glass vial containing the sample, and the water in the solution, contribute towards the observed spectra, and these are discussed more fully in Section 3.5.3.1. The most significant contribution is a polarised band at approximately 460 cm^{-1}, from the spectrum of the glass, which overlaps with a number of bands assigned to the vibration of the zirconyl species.

Detailed assignments are given in Section 8.3.4. The bands below 650 cm^{-1} are generally assigned to zirconium-oxygen vibrations, while the bands above 650 cm^{-1} are largely assigned to vibrations of various nitrate species.

Table 8-1: Positions, depolarisation ratios and polarisation assignments of bands in the Raman spectra of zirconyl salts

Zirconyl nitrate				Zirconyl chloride		
Solution			Crystalline	Solution		Crystalline
Position (cm^{-1})	ρ *	Polarisation assignment	Position (cm^{-1})	Position (cm^{-1})	Polarisation assignment*	Position (cm^{-1})
420 sh		*dp*	430			420
450		*dp*	455 sh	450	*dp*	455
535†		*p*				
580	< 0.2	*p*	578	580	*p*	585
720	≥ 0.75	*dp*	710, 718, 729			
766		*dp*	769			
						834
						1023
1025 sh		*p*	1033			
1050	0.05	*p*	1053			
1340		*dp*	1300			
1415		*dp*	1385			
1550		*p*	1522			
1630		*dp*	1610	1650	*dp*	1635

* Values of ρ generally not able to be determined accurately, see comment in Section 8.3.2.

† Sometimes was present as a weak band

Zirconyl nitrate

A typical Raman spectrum of a zirconyl nitrate solution is given in Figure 8-2, with the 300-900 cm^{-1} region detailed in Figure 8-3a.

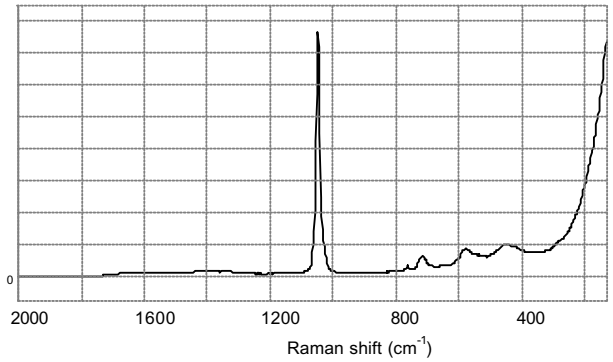

Figure 8-2: Raman spectrum of a zirconyl nitrate solution.

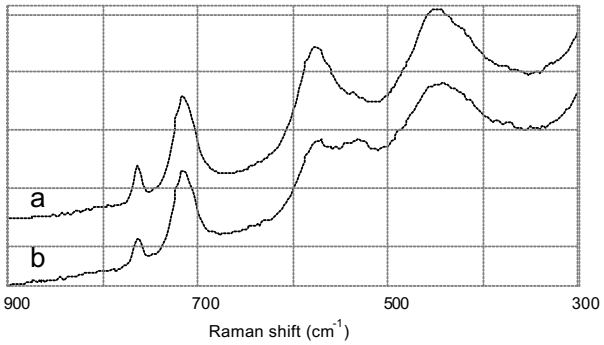

Figure 8-3: a) Raman spectrum of a zirconyl nitrate solution, 300-900 cm^{-1}, and b) the same with a weak band at 535 cm^{-1}.

The Raman spectrum of the zirconyl nitrate solution is dominated by an intense, polarised band at 1050 cm^{-1}. Below 800 cm^{-1} there are two bands at 766 and 720 cm^{-1}, followed by two broader bands at 450 and 580 cm^{-1}, and a minor shoulder at approximately 420 cm^{-1}. A weak band at approximately 535 cm^{-1} is sometimes observed in the spectrum, as shown in Figure 8-3b. The intensity of this band is observed to decrease with ageing over the first week after preparation, particularly in concentrated solutions.

A difficulty in the analysis of this spectrum is the superposition of the broad Raman band at 460 cm^{-1} from the glass spectrum. Comparison of the glass spectrum with the spectra of the salt solutions indicates that this 'glass' band may compose up to half of the observed intensity at 450 cm^{-1}, depending on focussing of the laser and concentration of the solution, but it does not significantly change the position of the observed band. The spectra in Figure 8-3 contain quite a small contribution from the glass spectrum. The presence of this extra polarised band

makes it difficult to determine the depolarisation ratio for the 450 cm^{-1} band in the sample spectrum, but it appears to be depolarised or very weakly polarised.

It was observed that with time the 1028 and 763 cm^{-1} bands decrease in intensity by up to 50 %, with respect to the more intense neighbouring bands at 1050 and 720 cm^{-1}, particularly over the first few days after preparation.

The Raman spectrum of crystalline zirconyl nitrate is given in Figure 8-4, with the 200-900 cm^{-1} region detailed in Figure 8-5. The spectrum is similar to that of the zirconyl nitrate solution, but some significant changes have occurred with drying and crystallisation. All bands have become sharper, and the relative intensities have changed.

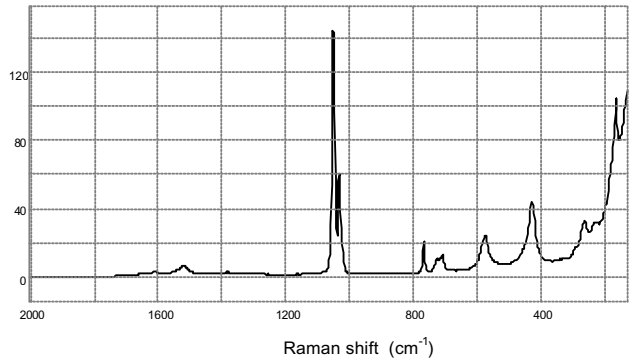

Figure 8-4: Raman spectrum of crystalline $Zr(OH)_2(NO_3)_2{\cdot}5H_2O$

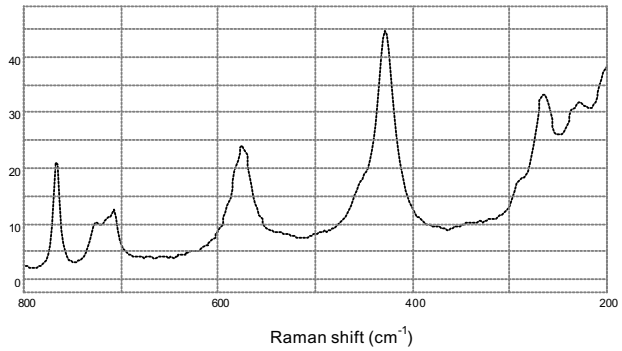

Figure 8-5: Raman spectrum of crystalline $Zr(OH)_2(NO_3)_2{\cdot}5H_2O$, 200 - 800 cm^{-1}.

Some bands have appeared in the spectrum below 300 cm^{-1}. These are assigned to lattice vibrational modes, and will not be considered further. A relatively intense peak has appeared at 430 cm^{-1}. The broad 450 cm^{-1} band that was present in the solution spectrum remains as a shoulder on the new peak. The minor 535 cm^{-1} band, which was sometimes observed in the solution spectrum, is not observed in the spectrum of the crystalline material. The weak band

at 720 cm^{-1} in the solution spectrum has split into at least three overlapping bands with crystallisation, while the minor shoulder at 1025 cm^{-1} has become an intense peak.

Zirconyl chloride

A typical Raman spectrum of zirconyl chloride solution is shown in Figure 8-6, with the 250-900 cm^{-1} region detailed in Figure 8-7. Two broad bands are observed at 450 and 580 cm^{-1}. The superposition of the glass spectrum causes variations in the intensity and symmetry of the 450 cm^{-1} band between spectra, and makes it difficult to accurately determine the depolarisation ratio. However, it seems clear that the 450 cm^{-1} band is not polarised, in agreement with previous observations.[5-7] A third band is observed at 1650 cm^{-1}.

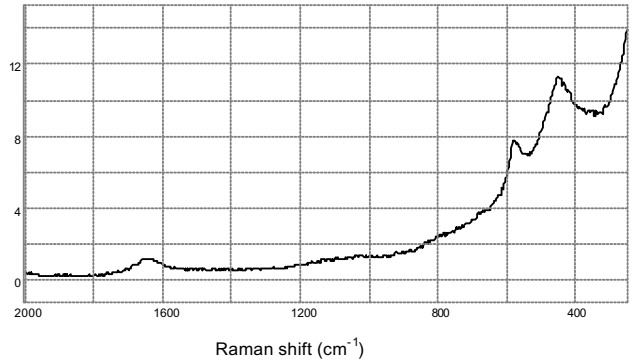

Figure 8-6: Raman spectrum of a $Zr(OH)_2Cl_2$ solution.

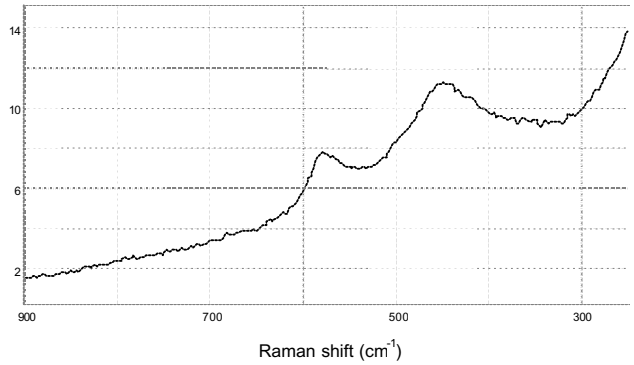

Figure 8-7: Raman spectrum of a $Zr(OH)_2Cl_2$ solution, 250 - 900 cm^{-1}.

The Raman spectrum of crystalline zirconyl chloride is given in Figure 8-8, with the 200-900 cm^{-1} region detailed in Figure 8-9. The observed bands are in the same position as those found in the spectrum of the solution, but are much narrower. A small shoulder at approximately 420 cm^{-1} has emerged, as have a number of minor bands above 650 cm^{-1} and 'lattice modes' below 300 cm^{-1}.

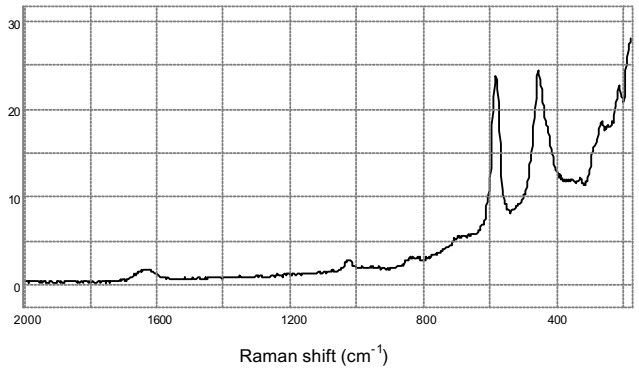

Figure 8-8: Raman spectrum of crystalline $Zr(OH)_2Cl_2 \cdot 7H_2O$.

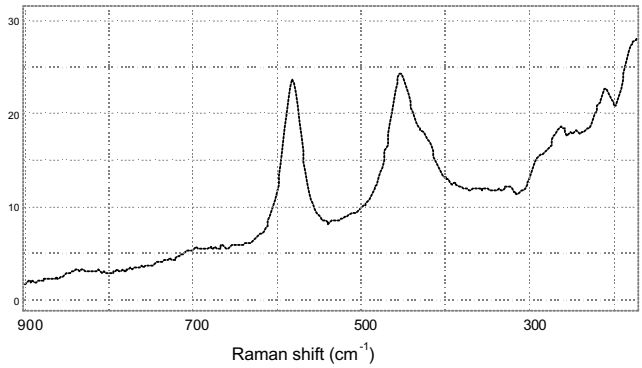

Figure 8-9: Raman spectrum of crystalline $Zr(OH)_2Cl_2 \cdot 7H_2O$, 170 - 900 cm^{-1}.

8.3.4 Discussion and assignments

Spectral region below 650 cm^{-1}

Typical Raman spectra for the zirconyl nitrate and zirconyl chloride solutions and crystals are given in Figure 8-10. Just as there is a similarity in the short-range structure of the cation species, there is also a strong similarity between the spectra in the region below 650 cm^{-1}. Assignments have been made on the assumption that the bands at similar positions in different spectra can be assigned to the same vibration or type of vibration.

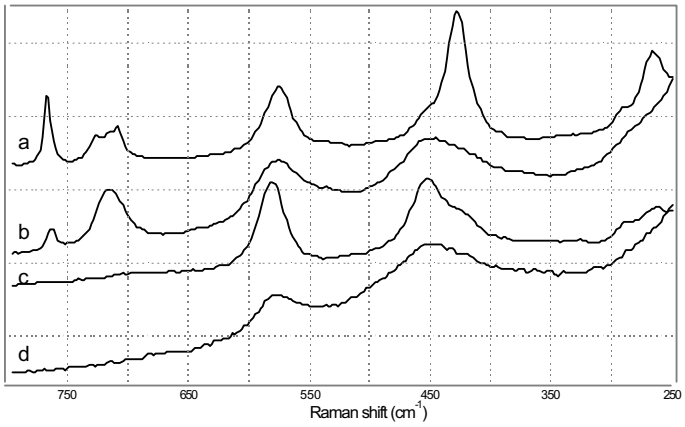

Figure 8-10: Raman spectra of a) zirconyl nitrate, b) zirconyl nitrate solution, c) crystalline zirconyl chloride, and d) zirconyl chloride solution.

The main candidates for assignment of the bands below 650 cm^{-1} are Zr–O modes. These may involve stretches of the bridging or terminal-hydroxy groups, either of individual functional groups or across the whole cation species. Other possibilities for assignment are librational modes or Zr–O(H_2) stretch modes of coordinated-water groups, or Zr–O(N) stretch modes of coordinate-nitrate species. We can eliminate most of these candidates by carefully considering the data presented both here and from previous investigations.

An important tool for the identification of vibrational spectra is the measurement of the shift in frequency when component atoms in the structure are replaced by heavier or lighter isotopes. *Deuteration*, the replacement of H_2O by D_2O, has previously been used to assign the vibrational spectrum of zirconyl chloride. The Raman spectra of zirconyl chloride solutions in D_2O,[6,7] and the Raman[5] and infrared[6,9] spectra of crystalline $Zr(OH)_2Cl_2 \cdot 7D_2O$ have been reported, and the isotopic shift calculated. The shifts for all bands below 700 cm^{-1} were less than 5% (except for an infrared-active band at 510 cm^{-1}, assigned to the coordinated-water

'wag' [9]). The small shift indicates that the species involved in the vibrations at 450 and 580 cm^{-1} are unlikely to be water molecules, and on this basis these vibrations are generally assigned to Zr–OH stretches. It seems reasonable that this conclusion can also be applied to the spectrum of zirconyl nitrate.

The bands at 580 and 450 cm^{-1} are observed in all four of the spectra considered, and on this basis there are some functional groups that cannot be assigned to these bands. There are no terminal-hydroxy groups in the structure of the crystalline salts. There are no Zr-O(N) bonds in the chloride salts, and there is no evidence in the literature for any direct zirconium-chloride bond. These structures therefore cannot make a major contribution to the 580 and 450 cm^{-1} bands.

The 580 cm^{-1} band is strongly polarised, and is observed in the Raman spectrum of zirconyl nitrate and chloride solutions and crystals. The band becomes narrower with crystallisation, but the position does not seem to change significantly. The band must arise from a symmetric vibration of a species that is present in all the cation structures. After the above elimination process, the most likely species is the hydroxy-bridge.

Kozhevnikova, Myund and Burkov have studied the Raman spectra of zirconyl chloride solutions and crystals, and assigned them assuming that the cyclic-tetramer possesses D_{4h} symmetry.[5,8] In principle, molecules with D_{4h} symmetry have three Raman-active modes: the symmetric A_{1g}, and antisymmetric B_{1g} and B_{2g}. The polarised 580 cm^{-1} vibration was thus assigned to the A_{1g} 'breathing' mode, in which the species symmetrically expands and contracts. However, as noted above in Section 8.3.1, diffraction studies show that the tetramer species *is not present* in the crystalline $Zr(OH)_2(NO_3)_2{\cdot}5H_2O$ structure, and the $[Zr(OH)_2NO_3]^+_n$ linear-chain cation certainly does not possess D_{4h} symmetry. This point not only eliminates the A_{1g} 'breathing' mode assignment, but shows that the observed vibrations are *not* determined by D_{4h} symmetry. As also noted above in the same section, in practice the cyclic-tetramer may not possess D_{4h} symmetry.

Vibrations must then be assigned on smaller units within the cation, such as the vibration of individual hydroxy-bridges, or pairs of hydroxy-bridges. A reasonably symmetric vibration is one in which the two hydroxy groups bridging a pair of zirconium atoms move in opposite directions, perpendicular to the plane that passes through the zirconium atoms. This vibration is illustrated schematically in Figure 8-11. Such a vibration may occur in both the cyclic-tetramer species, and in the chain structure of the zirconyl nitrate crystal.

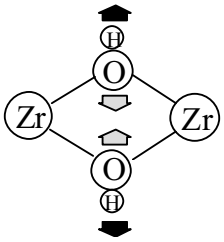

Figure 8-11: Schematic illustration of the vibration assigned to 580 cm^{-1} band.

We now turn to the depolarised bands at 450 cm^{-1} and 420-430 cm^{-1}, remembering that the spectrum of the glass makes it difficult to unambiguously identify the bands from the solution spectra in this region. It may also be possible that there are two or more overlapping bands at this position. The band at 450 cm^{-1} appears to be considerably stronger than the small band at 420 cm^{-1} in all samples considered except the crystalline zirconyl nitrate, in which a peak at 430 cm^{-1} dominates. This suggests that the arrangement of the $[Zr(OH)_2]_n$ structure in the cation affects the frequency of the vibrations.

Kozhevnikova, Myund and Burkov assigned the 450 cm^{-1} band to the antisymmetric B_g vibration of the D_{4h} cyclic-tetramer.[5,6] If, as discussed above, we cannot use the D_{4h} symmetry for assignments, we still can assign the bands in this region to various antisymmetric vibrations of the hydroxy-bridges. At least some of the vibrations of the hydroxy-bridges could be expected to change in frequency with the arrangement of the cations into parallel chains instead of cyclic-tetramers.

Alternatively, the strong 430 cm^{-1} peak in the crystalline zirconyl nitrate may assigned to a different species altogether, such as a Zr–O(N) stretch from the coordinated-nitrate group. This would be consistent with the assignments to the nitrate groups, discussed below, and the known structure of the crystalline salt.

The assignment of the Raman bands below 650 cm^{-1} to the bridging-hydroxy groups is fully supported by the results of *ab-initio* vibrational modelling calculations, described in Section 8.4.

The band sometimes observed at approximately 535 cm^{-1} is characteristic of the hydrolysed sol, and is discussed and assigned in Section 3.5.3.2.

Spectral region above 650 cm^{-1}

Most of the bands observed in the spectra above 650 cm^{-1} have been assigned to two kinds of nitrate group, while the broad band at 1650 cm^{-1} is assigned to the H–O–H bend of the water molecule. The observed frequencies and assignments are listed in Table 8-2.

Table 8-2: Assignments of bands observed above 650 cm^{-1}.

Position (cm^{-1})	Polarisation assignment	Species and mode
720	*dp*	D_{3h} aquated nitrate ion, E′ mode
766	*dp*	C_{2v} bidentate nitrate, B_1 mode
1025	*p*	C_{2v} bidentate nitrate, A_1 mode
1050	*p*	D_{3h} aquated nitrate ion, A_1' mode
1330	*dp*	C_{2v} bidentate nitrate, B_1 mode
1415	*dp*	D_{3h} aquated nitrate ion, E′ mode
1550	*p*	C_{2v} bidentate nitrate, A_1 mode
1650	*dp*	water

The crystalline structure of zirconyl nitrate contains two kinds of nitrate species, in equal numbers. The first is an 'ionic' nitrate species located between the Zr–OH chains, and the second is symmetrically bidentate-coordinated (chelated) to a zirconium atom. The bands in the Raman spectrum have been assigned to these two species, based on their position and polarisability, in accordance with the literature values for other metal-nitrate salts.[1,3,20,21*]

The ionic species possesses D_{3h} symmetry, with oxygen atoms evenly distributed around the central nitrogen atom in a triangular plane, undistorted by any nearby molecules. There are three Raman-active modes ($A_1' + 2\,E'$), all of which are identified in the spectrum of zirconyl nitrate solution. This is the dominant nitrate species in solution, presumably fully aquated.

The bidentate-coordinated nitrate species possesses C_{2v} symmetry,[†] meaning that its symmetry is distorted by proximity to a cation. A C_{2v} species has six Raman-active modes ($3\,A_1 + 2\,B_1 + B_2$), which means that two modes have not been identified. These modes, of A_1 and B_2 symmetry, are both expected at approximately 700-800 cm^{-1},[3] and may overlap with other bands or be too weak to be detected. This assignment agrees with a previous infrared-absorption study of $Zr(OH)_2(NO_3)_2{\cdot}4H_2O$.[4]

---

[*] There is some disagreement over the symmetry assignment of coordinated-nitrate peaks.[1,4,20,21] This discussion has used the assignments of Addison *et al.*,[20] which are based on both infrared and Raman polarisation data.

[†] In addition to the crystal structure data, this species can be distinguished from unidentate-coordinated nitrate by the polarisability of the two bands at the highest frequencies.[20,21] Note that the *chelating* bidentate nitrate species may not be easily distinguished from the symmetric *bridging* bidentate species by Raman spectroscopy.[20] However, there is no indication that bridging nitrate species are formed at any time.

A further confirmation can be made of the assignment to the C_{2v}, symmetric bidentate-coordinated nitrate group by comparison with the Raman spectra of $Zr(OH)_3NO_3$ (see Appendix A) and $Zr(NO_3)_4$.[3] The crystal structures of both these compounds contain only one kind of nitrate group, which is bidentate-coordinated to a single zirconium atom. The bands assigned above to the bidentate-nitrate species are strong and sharp in the reported spectra of these compounds. At this point no firm assignment has been made of Zr–O(N) vibrations, which are expected to be found below 340 cm^{-1}.[3]

Both the 766 and 1025 cm^{-1} bands of the coordinated-nitrate species are very weak with respect to the corresponding bands assigned to the fully-aquated species, indicating that only a small fraction of the nitrate groups in the solution are coordinated. As noted above in Section 8.3.3, these bands in the zirconyl nitrate solution decrease in intensity by up to 50 % with time, particularly over the first few days after preparation. This indicates the conversion of coordinated-nitrate species to ionic.

The minor band at 1023 cm^{-1} in the spectrum of crystalline zirconyl chloride has been previously observed in the Raman spectrum[5] and the infrared spectrum,[6,9] and assigned to the antisymmetric 'bending' δ(ZrOH) mode of the hydroxy bridge. This band is not observed in crystalline nitrate, and is probably hidden beneath the intense 1030 cm^{-1} band of the coordinated-nitrate species.

The minor band at 1650 cm^{-1} is assigned to the H–O–H bending mode of liquid water.

8.3.5 Summary

The following points summarise the findings of this study:

- The Raman spectra of $Zr(OH)_2(NO_3)_2$ solution and $Zr(OH)_2(NO_3)_2{\cdot}4H_2O$ crystalline salt have been reported and assigned for the first time.
- The Raman spectra of zirconyl nitrates and chlorides have been reported together, and assigned based on known crystalline structures. Previous assignments have been shown to be inadequate.
- The principal bands below 650 cm^{-1} are assigned to the symmetric and antisymmetric stretching of bridging hydroxy groups. The overall symmetry of the cation does not affect the spectrum.

8.4 Study 2: Vibrational modelling

8.4.1 Introduction

The Raman spectra of zirconyl salts are discussed and assigned in Section 8.3. These assignments have used the traditional methods of comparing the observed spectra of a range of compounds, making polarisation measurements, and considering the symmetry of the most probable vibrational modes. However, more confident assignments could be made if we took advantage of recent developments in theoretical chemistry and computational power. The availability of software that uses 'first-principles' (*ab initio*) quantum theory allows the properties of a wide range of molecules and species to be calculated.

Density functional theory (DFT) is 'first-principles' procedure which is based on the theorem that all ground state properties are functions of the electron density. In DFT the exchange-correlation energy can be approximated via one-electron integrals involving local spin densities, and hence computational requirements are significantly reduced in comparison with the more conventional Hartree-Fock approach.[22,23] Thus DFT can be applied in large systems for which other first-principles procedures are impractical. Density functional theory has been shown to produce particularly accurate theoretical calculations of vibrational frequencies for small molecules.[24]

The main precedent for this work is the use of molecular orbital theory to predict the theoretical vibrational spectra of metal ions complexed with acetate ions and water molecules.[25,26]

8.4.2 Procedure

The software package used for geometry optimisation and calculation of vibrational spectra was *DMol*,[*] which calculates solutions to the density functional theory equations for a particular molecular model.

Molecular models were formulated, and are described below. The geometry of the model (ie bond lengths and angles) was optimised to the configuration with minimum internal energy. During optimisation the geometry could be constrained to a particular symmetry to reduce computational time. When a minimum energy state was reached, the structure was altered

---

[*] *DMol* Version 960, Density Functional Theory electronic structure program, © 1996 by Molecular Simulations, Inc.

slightly and re-optimised to ensure that the absolute minimum was reached. The vibrational frequencies of the molecule were then calculated, along with the atomic displacements associated with each vibrational mode. Selected modes were graphically animated in order to determine the type of vibration and the symmetry. As this was a time-consuming process, not all the modes were animated.

The numerical basis set used for the calculations was a double-numerical polarisation (DNP) type. Atomic positions were described by Cartesian coordinates, in which the position of each atom was specified in three-dimensional space.*

A simple molecule with a known structure and vibrational spectrum was modelled first. The molecule chosen was titanium tetrachloride, $TiCl_4$, which was constrained to a T_d symmetry.

Several zirconium-containing models were examined. The main desired attributes were simplicity, in order to reduce computation and analysis time, and similarity with 'known' species. Unfortunately there is only one aqueous zirconium species for which the structure and vibrational spectrum are well known, the 'cyclic-tetramer', which is described in Section 8.3.1.

Three models were constructed: the 'monomer' $Zr(OH^t)_4{\cdot}(H_2O)_4$, the 'dimer' $Zr_2(OH^{br})_2(OH^t)_6(H_2O)_6$, and the 'cyclic-tetramer' $Zr_4(OH^{br})_8(OH^t)_8(H_2O)_8$. All zirconium atoms in the models are eight-fold coordinated. No symmetry constraints were imposed on the first two models, while the tetramer model was constrained to D_{4h} symmetry, which reduced the computation time considerably. Each of these species had a net charge of zero, which assisted with geometry optimisation. In aqueous solution these species generally have a positive charge, and thus fewer terminal-hydroxy groups. This would lower the symmetry of the cyclic-tetramer.

8.4.3 Geometry optimisation results

The geometry of the $TiCl_4$ molecule was optimised to give a Ti–Cl bond length of 2.17 Å, which is the same as the published value.[29]

---

* Geometry optimisation is much more efficient and reliable when the structure is instead described by *natural internal coordinates*, in which the position of each atom is specified with respect to neighbouring atoms.[27,28] Unfortunately, the automated method for assigning internal coordinates used by *DMol* could not be applied to atoms with a coordination number greater than 6, or greater than 4 for ring molecules.[27] Since the coordination number for each zirconium atom in the cyclic-tetramer is 8, the program could only use Cartesian coordinates.

During geometry optimisation of the Zr monomer species one water molecule was consistently excluded from the coordination sphere. This molecule was then removed from the model, giving a structure of $Zr(OH^t)_4(H_2O)_3$ and a sevenfold coordination of the zirconium ion. The final interatomic distances are listed in Table 8-3.

Table 8-3: Geometric parameters for the monomer.

Bond	Bond length (Å)
Zr–O(H)	2.01, 2.01, 2.04, 2.19
Zr–O(H_2)	2.33, 2.34, 2.35

The dimer species was found to be geometrically unstable, with a strong tendency to 'bend' in the middle to minimise the Zr^1–OH–Zr^2 angle. The resulting structure was not considered to be useful.

The optimised geometry of the cyclic-tetramer species was remarkably close to the structure reported from a XRD study of crystalline $Zr(OH)_2Cl_2 \cdot 7H_2O$.[11] The structural parameters are compared in Table 8-4. The structure is illustrated in a number of different ways in Figure 8-12, showing the internal structure and the effective external surface of the species.

Table 8-4: Geometric parameters for the cyclic-tetramer.

Atom pair	Modelled	Observed in crystalline salt [11]
Interatomic distance (Å)		
Zr–Zr	3.55	3.56
O^{br}–O^{br}	2.34	2.34
Zr–O^{br}(H)	2.14	2.14*
Zr–O(H)^t	2.14	-
Zr–O(H_2)	2.33	2.21-2.34
Bond angle		
O^{br}–Zr–O^{br}	66.3°	67.2° *

*averaged values

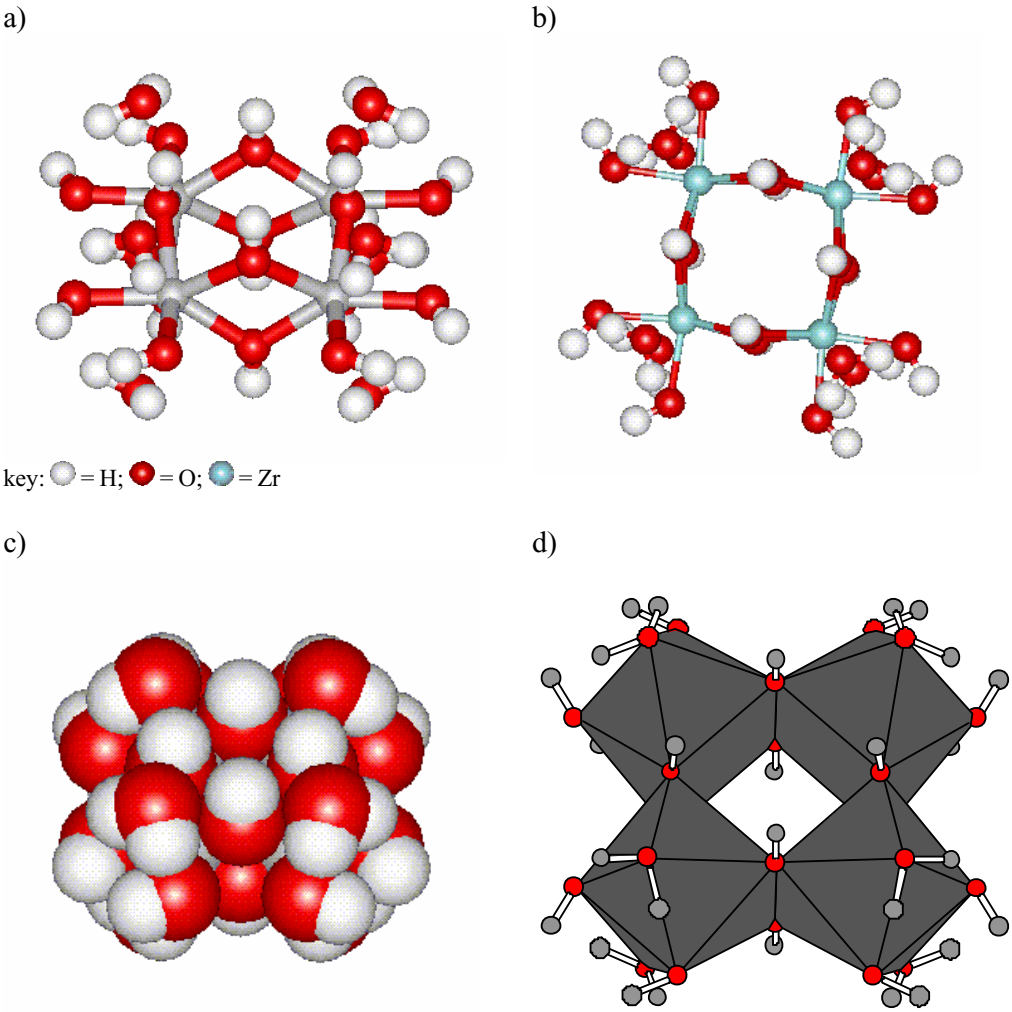

Figure 8-12: Representations of the cyclic-tetramer after geometry optimisation: a) and b) 'ball-and-stick' model, c) 'filled sphere' model, and d) polyhedra model.

8.4.4 Overview of the vibrational modelling results

The vibrational spectrum of the $TiCl_4$ molecule was calculated, and is compared with published assignments for $TiCl_4$ vapour at 65°C in Table 8-5.[29] All the frequencies agree to within 10 cm^{-1}.

Table 8-5: Observed and calculated vibrational frequencies for $TiCl_4$.

Mode	Observed position [29] (cm^{-1})	Calculated position (cm^{-1})	Difference
$\nu_2(E)$	114	124	+ 9 %
$\nu_4(T_2)$	136	145, 146, 146	+ 7 %
$\nu_1(A_1)$	389	379	– 3 %
$\nu_3(T_2)$	509	509	+ 2 %

The vibrational spectrum of the monomer species was calculated, but since there were no bridging Zr–OH–Zr bonds the usefulness of these results was limited, and will not be considered here.

The vibrational spectrum of the tetramer species contained 174 vibrational modes,* each at a unique frequency between 45 and 3800 cm^{-1}. Eight of these modes were predicted at 'imaginary' frequencies, indicating that the structure was not completely minimised. The remaining 166 modes were classified into one of four main groups, listed in Table 8-6. Modes above 1000 cm^{-1} were associated only with the stretching and bending of O–H bonds, and were at frequencies very close to the values expected from the literature.[1] The modes below 1000 cm^{-1} were mostly due to various stretches and deformations of Zr–O bonds, and are of the greatest interest to this study.

The 53 modes in the frequency region 370-730 cm^{-1} were animated and analysed, and the remainder of this discussion will concentrate on this region.

Table 8-6: Main vibration groups for the cyclic-tetramer

Frequency	Number of modes	Assignment
~ 100 - 920 cm^{-1}	126	Zr–O stretching and twisting modes, involving bridging-hydroxy, terminal-hydroxy and coordinated-water groups. Also Zr–O–H bending modes.
1630-1650 cm^{-1}	8	Coordinated-water H–O–H bend
3150-3260 cm^{-1}	16	Coordinated-water O–H stretch
3660-3740 cm^{-1}	16	Bridging and terminal-hydroxy O–H stretch

* The number of possible modes of vibration of a free molecule is given by (3*N*–6), where *N* is the number of atoms, and the 6 modes subtracted correspond to the 6 completely rotatory modes. The tetramer model contained 60 atoms.

8.4.5 Types, symmetry and intensity of the predicted modes 370 - 730 cm^{-1}

The results from *DMol* provide the atomic displacements associated with each mode, and the following discussion will describe vibrations in these terms. However it is important to keep in mind that it is changes in the polarisability of the molecule, caused by these displacements, that lead to the Raman spectrum.

In each predicted mode, most of the atoms in the tetramer are displaced to some extent, and often a considerable fraction are substantially displaced. This makes the description and analysis of the large number of modes very complex, and some form of simplification is required. The simplifying approach used was to divide the molecule up into 'functional groups', such as bridging-hydroxy groups, terminal-hydroxy groups, and coordinated-water molecules. Each of these groups contains an oxygen atom bound to one or two zirconium atoms, and they vibrate in a number of characteristic ways, each referred to as a *displacement type*. Most of the predicted modes between 370 and 730 cm^{-1} have at least several such groups displaced to some extent. The displacement types for each group generally involve stretching or twisting of Zr-O bonds in the structure, and are described in this section.

It is also important to consider the symmetry of a vibration when assigning Raman spectra. The principles used in determining the symmetry of a vibration are discussed in Section 8.2. For a simple molecule, the symmetry of any given vibration can be relatively easily determined. For a large but highly symmetric molecule, such as the modelled tetramer species, the symmetry of each vibration can be considered on several levels:

1. The stretching or distortion of a single bond or group, such as a terminal hydroxy group, involving only a few atoms.
2. The displacement of several groups coordinated around a particular zirconium atom (one corner of the molecule), either pairs of terminal-hydroxy groups, pairs of coordinated water molecules, or two pairs of bridging-hydroxy groups. Pairs of molecules moving together (in-phase) around a zirconium atom may increase the symmetry and also the total change in polarisability. Conversely, if two adjacent groups are stretching symmetrically, but out of phase from each other, the total symmetry of the vibration is reduced. The same principle applies to the displacement of a pair of bridging groups between two zirconium atoms.

3. The symmetry across the whole molecule, if the molecule possesses a significant degree of overall symmetry. This is the level on which symmetry is usually assessed, but is also most sensitive to the total symmetry of the molecule. The discussion in Section 8.3.4 shows that, for large zirconyl species, the symmetry across the whole molecule (or cation) is not likely to be important in determining the Raman-active modes.

Each vibration has a varying degree of symmetry on each of these levels.

Displacement types of the bridging-hydroxy groups

The most important types of displacement are those involving stretching of the bridging Zr–O(H)–Zr bonds. Two types of stretch were identified, classified according to the displacement of the oxygen atoms in relation to the σ_h plane, which is the main plane of symmetry that passes through all the zirconium atoms.

The first type of stretch is where the oxygen atoms are displaced along a line perpendicular to the σ_h plane, known as the *perpendicular-to-plane stretch*, illustrated in Figure 8-13a. Paired oxygen atoms are generally displaced in opposite directions, giving a vibration that is symmetric around the σ_h plane. On average, about half of these stretches are also symmetric around a particular zirconium atom; *ie* when the four bridging-hydroxy groups around a particular zirconium atom oscillate symmetrically around it. The displacements may also be symmetric across the whole molecule .

The second type of stretch is where the oxygen atoms are displaced between the two adjoining zirconium atoms, parallel to the σ_h plane, known as the *parallel-to-plane stretch*. Paired oxygen atoms may move together (in-phase), illustrated in Figure 8-13b, or in opposite directions (out-of-phase), illustrated in Figure 8-13c. These vibrations are generally antisymmetric. Symmetry around a particular zirconium atom is occasionally achieved. It was observed that the oxygen atoms were displaced to a greater extent in the parallel-to-plane stretch than in the perpendicular-to-plane stretch.

There are also two further types of displacement. The *twist*, in which the Zr–O bonds are twisting, and the oxygen is moving in and out of the ring, is largely antisymmetric. The antisymmetric *wag*, in which the oxygen atom stays relatively still while the attached hydrogen moves, can be treated as a Zr-O-H bend.

For two of the predicted modes in the 370 - 730 cm^{-1} region, a number of these types of displacement are combined to give a vibrational mode that is symmetrical across the whole molecule. These modes are at 494 and 568 cm^{-1}.

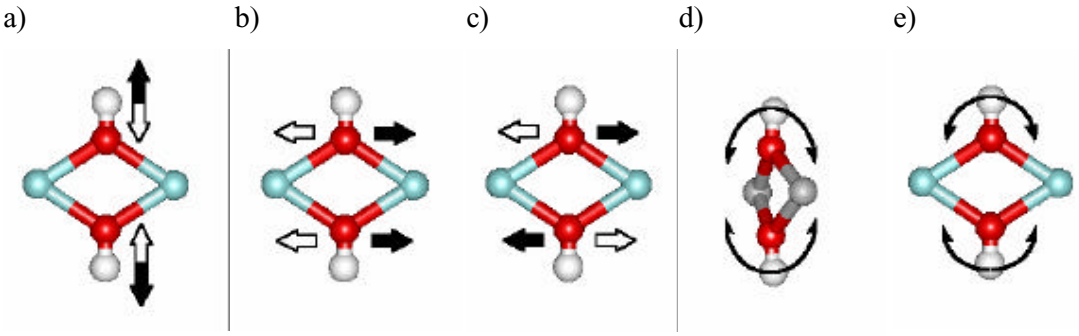

Figure 8-13: Illustration of the displacement 'types' for the bridging-hydroxy groups: a) perpendicular-to-plane stretch, b) parallel-to-plane stretch, in-phase, c) parallel-to-plane stretch, out-of-phase, d) twist, and e) wag. = H; = O; = Zr

Displacement types of the terminal-hydroxy groups

The primary type of displacement of the terminal-hydroxy groups is a combination *stretch/bend*, in which the Zr–O bond stretches while the Zr–O–H angle bends. The stretch component is symmetric, while the bend is antisymmetric. The relative strength of the stretch or bend components vary between modes.

There are two terminal-hydroxy groups bound to each zirconium atom, and the symmetry of the vibrations with respect to the zirconium atom varies according to whether the hydroxy groups stretch together in-phase (symmetric) or out-of-phase (antisymmetric). However, the assignment of symmetry on this level is dependent on the fact that there are two symmetrically-placed hydroxy groups per zirconium, which in reality will seldom be the case, and this level of symmetry is unlikely to be important.

Another vibration observed is the antisymmetric *twist*, in which the hydroxy group rotates around the Zr–O bond.

Displacement types of the coordinated-water molecules

The coordinated-water molecules were predicted to be largely inactive in the 370 - 730 cm^{-1} region studied. The main displacement type is the antisymmetric *twist*, in which the group rotates around the Zr–O bond. Vibrational activity of the coordinated-water molecules was predicted to be mainly in the region 820 - 920 cm^{-1}.

Predicting Raman intensities

Since the *DMol* program does not calculate Raman intensities, they must be estimated from the displacements of each vibration. When predicting Raman intensities, we can keep in mind the following general principles:

- The Raman activity of a vibration, and the intensity of the associated band in the Raman spectrum, is determined by the change in polarisability, $\Delta\alpha$, associated with the vibration.
- Symmetric vibrations tend to give intense Raman lines, while antisymmetric vibrations are usually weak and sometimes unobservable. Symmetric vibrations also tend to give polarised Raman lines.
- Stretching modes usually cause a higher change in polarisability than other modes, and are thus more Raman active and more polarised.

From these principles, the changes in polarisability for each displacement type have been estimated, and are listed in Table 8-7.

Summary of results

Table 8-7 summarises the displacement types, lists the estimated degree of symmetry and change in polarisability, and gives the frequencies at which these modes are predicted by the calculation.

Table 8-7: Summary of displacement types.

Group	Displacement type	Estimated degree of symmetry	Estimated change in polarisability	Principle observed frequencies* (cm^{-1})
Bridging-hydroxy groups	Perpendicular-to-plane stretch	high	medium	500-542 (7), 568†
	Parallel-to-plane stretch, in-phase	medium	high	430, 480-90 (3), 546, 549, 563
	Parallel-to-plane stretch, out-of-phase	low	medium	371, 377, 439, 460-65 (3)
	twist	low	low	380-390 (3) 431, 494†, 550, 568†
	wag	low	low	646, 674, 710-730 (6)
Terminal-hydroxy groups	stretch/bend	low to high	medium to high	381, 480-550 (15), 635-655 (4)
	twist	low	low	444, 447, 620-630 (4)
Coordinated-water	twist or rock	low	low	439, 580, 635-650 (4), 710-730 (6), 820-920 (16)

* Where a range of frequencies is specified, the number of modes in the range is given in parenthesis

† Symmetric around the D_{4h} symmetry of the molecule

From the above analysis, three displacement types stand out as the most likely to be Raman-active:

1. The bridging-hydroxy perpendicular-to-plane Zr–O stretch, illustrated in Figure 8-13a. The symmetry of this type is generally quite high, although the magnitude of the displacements are weaker than those of the parallel-to-plane stretch. Modelling predicts vibrations of this type to occur largely in the band 500 - 542 cm^{-1}.
2. The bridging-hydroxy parallel-to-plane Zr–O stretch. The most important will be the in-phase type, illustrated in Figure 8-13b. This is largely antisymmetric, but the associated atomic displacements are large. Modelling predicts most vibrations of this type to occur below 490 cm^{-1}, and some between 545 and 570 cm^{-1}.
3. The terminal-hydroxy Zr–O stretch. The main displacement is symmetric, although the stretch is always combined to some degree with an antisymmetric Zr-O-H bend. The stretch frequencies are predicted to be found in two bands: 15 modes in the range 480 - 550 cm^{-1}, and four in the range 635 - 654 cm^{-1}. There are also a number of stretching modes in between these two bands.

It is important to note that all three of these displacement types are dependent only on the Zr–$(OH^{br})_2$–Zr bridge and the Zr–OH^t ligand, not on the arrangement of the zirconium atoms into

a cyclic-tetramer or any other particular structure. This is important with regard to the different cation structures known to occur in zirconyl chloride and nitrate crystals.

8.4.6 Assignment of lines

We can now use the results of vibrational modelling to assign the observed Raman spectra of zirconyl salts, focussing on the depolarised band at 450 cm^{-1} and the polarised band at 580 cm^{-1}.

The principle difficulty, when comparing the vibrational analysis of the tetramer with the actual Raman spectrum, is that there are over 30 predicted modes within the frequency region where only two broad bands are observed. However, many of these modes can be eliminated after considering symmetry and polarisability change, to give the three major 'types' listed above.

We can also eliminate the vibrations of the terminal-hydroxy groups. The bands in the Raman spectrum of the crystalline salts are sharper than those in the spectrum of the solution, but the frequencies are largely unchanged. Since terminal-hydroxy groups are not present in the crystalline salts, their vibrations cannot make a major contribution to the spectrum. This leaves us with the vibrations of the hydroxy bridges.

The perpendicular-to-plane stretch of the hydroxy bridges has a high symmetry, and was predicted to occur mainly in the range 500 - 545 cm^{-1}. This is the best assignment for the polarised band at 580 cm^{-1}, although the predicted frequencies are roughly 50 cm^{-1} (~ 10 %) too low. This size of error is reasonable considering the errors obtained for the much simpler $TiCl_4$ molecule.

The parallel-to-plane stretch of the hydroxy bridges, with lower symmetry, seems to be a good candidate for the weakly polarised or depolarised band at 450 cm^{-1}. These vibrations are predicted to occur mainly in the region 430 - 490 cm^{-1}, which matches very closely. It is also possible that the Zr–OH^t stretch may contribute to this band in the salt solution.

8.4.7 Summary

The following points summarise the findings of this study:

- A simplified model of the 'cyclic-tetramer' species was prepared, and the optimal geometry and vibrational spectra were calculated using density functional theory calculations.
- The optimised geometry corresponded very closely to the structure determined by XRD for the tetramer species in crystalline $Zr(OH)_2Cl_2 \cdot 7H_2O$.
- The calculation of the vibrational spectrum assisted the assignment of the Raman spectrum. The polarised 580 cm^{-1} band was assigned to the $Zr–(OH^{br})_2–Zr$ stretch, with the paired hydroxy groups displaced symmetrically towards and away from each other. The depolarised band at 450 cm^{-1} was assigned to the low-symmetry $Zr–(OH^{br})_2–Zr$ stretch, in which the hydroxy groups are displaced between the adjacent pairs of zirconium atoms. *These results are in agreement with, and contribute to, the previous study of the Raman spectra of zirconyl salt solutions in Section 8.3*.
- First-principles vibrational modelling with density functional theory has been shown to be useful in the assignment of the Raman spectrum of a reasonably complicated set of transition-metal complexes.

8.5 Conclusions

The Raman spectra of zirconyl nitrates and chlorides have been reported and assigned, with the nitrates reported for the first time. The region below 650 cm^{-1} has been assigned using two complementary studies: a comparison of the observed spectra with known structures, and an *ab initio* vibrational modelling calculation using density functional theory. The polarised 580 cm^{-1} band was assigned to the Zr–$(OH^{br})_2$–Zr stretch, with the paired hydroxy groups displaced symmetrically towards and away from each other. The depolarised band at 450 cm^{-1} was assigned to the low-symmetry Zr–$(OH^{br})_2$–Zr stretch, in which the hydroxy groups are displaced between the adjacent pairs of zirconium atoms. Previous assignments have been shown to be inadequate. First-principles vibrational modelling has been shown to be useful in the assignment of the Raman spectrum of a reasonably complicated set of transition-metal complexes.

8.6 References

1. K. Nakamoto, *Infrared and Raman spectra of inorganic and coordination compounds*, 4th Edition, Wiley-Interscience, New York (1986)
2. P. Hendra, *Fourier Transform Raman Spectroscopy*, Ellis Harwood, New York (1991)
3. J. Weidlein, U. Müller and K. Dehnicke, "Die Schwingungsspektren von $ZrCl_4$ und $Zr(NO_3)_4$" *Spectrochimica Acta 24A* 253-258 (1968)
4. O.A. Govorukhina, S.D. Nikitina, V.N. Brusentsova and V.A. Masloboev, "Polytherm of the ZrO_2–HNO_3–H_2O system" *Russ. J. Inorg. Chem. 35* [12] 1804-1806 (1990)
5. G.V. Kozhevnikova, L.A. Myund and K.A. Burkov, "Raman spectra of zirconium oxyxhloride crystalline hydrate and solutions" *Izvestiya Akademii Nauk SSSR, Neorganicheskie Materialy 24* [3] 470-473 (1988)
6. K.A. Burkov, G.V. Kozhevnikova, L.S. Lilich and L.A. Myund, "The vibrational spectra of the tetrameric hydroxo -complex of zirconium (IV)" *Russ. J. Inorg. Chem. 27* [6] 804-802 (1982)
7. S. Hannane, F. Bertin and J. Bouix, "Etude de l'hydrolyse de Zr(IV) par spectrométrie Raman et RMN du proton. I. Mise en évidence et formation des espèces en solution" *Bull. Soc. Chim. Fr. 127* 43-49 (1990)
8. L.M. Sharygin, V.M. Galkin, S.M. Vovk and A.V. Korenkova, *Colloid Journal of the USSR 47* 95-99 (1985)
9. D.A. Powers and H.B. Gray, "Characterization of the thermal dehydration of zirconium oxide halide octahydrates" *Inorg. Chem. 12* [11] 2721-2726 (1973)
10. A. Clearfield and P.A. Vaugan, "The crystal structure of zirconyl chloride ocathydrate and zirconyl bromide octahydrate" *Acta Cryst. 9* 555-558 (1956)
11. T. C. W. Mak, "Refinement of the crystal structure of zirconyl chloride octahydrate" *Can. J. Chem. 46* 3493-3497 (1968)
12. C.F. Baes and R.E. Mesmer, *The hydrolysis of cations*, Wiley-Interscience 152-159 (1976)
13. G. M. Muha, "Structure of the complex ion in aqueous solutions of zirconyl and hafnyl oxyhalides" *J. Chem. Phys 33* [1] 194-199 (1960)
14. A. Singhal, L.M. Toth, J.S. Lin and K. Affholter, "Zirconium(IV) tetramer/octomer hydrolysis equilibrium in aqueous hydrochloric acid solution" *J. Am. Chem. Soc. 118* [46] 11529-11534 (1996)
15. J.D.F. Ramsay, "EXAFS study of polynuclear ions in solution" *Synchrotron radiation, Appendix to the Daresbury annual report 1988/89*, Compiled by C. Nave *et al*., Science and Engineering Research Council 38-39 (1989)
16. P. Benard, M. Louër and D. Louër, "Crystal structur determination of $Zr(OH)_2(NO_3)_2{\cdot}4.7H_2O$ from X-ray powder diffraction data" *J. Solid State Chem. 94*, 27-35 (1991)
17. M. Åberg and J. Glaser, "^{17}O and ^{1}H NMR study of the tetranuclear hydroxo zirconium complex in aqueous solution" *Inorg. Chim. Acta 206* 53-61 (1993)
18. G.A. Yagodin, "Stable polymeric zirconium compounds in nitric acid solutions" *Russ. J. Inorg. Chem. 15* [5] 659-662 (1970)
19. J. Livage, M. Chatry, M. Henry and F. Taulelle, "Complexation of Zr(IV) precursors in aqueous solutions" *Mat. Res. Soc. Symp. Proc 271* 201-212 (1992)
20. C.C. Addison, N. Logan, S.C. Wallwork and C.D. Garner, "Structural aspects of co-ordinated nitrate groups" *Quart. Rev. Chem. Soc 25* [2] 289-322 (1971)
21. M.R. Rosenthal, "The myth of the non-coordinating anion" *J. Chem. Ed. 50* [5] 331-335 (1973)
22. J. Andzelm and E. Wimmer, "Density functional Gaussian-type-orbital approach to molecular geometries, vibrations, and reaction energies" *J. Chem. Phys. 96* [2] 1280-1303 (1992)
23. T. Ziegler, "Approximate density functional theory as a practical tool in molecular energetics and dynamics" *Chem. Rev. 91* 651-667 (1991)
24. D. Porezag and M.R. Pederson, "Infrared intensities and Raman-scattering activities within density-functional theory" *Phys. Rev B 54* [11] 7830-7836 (1996)
25. J.D. Kubicki, G.A. Blake and S.E. Apitz, "Molecular orbital models of aqueous aluminum-acetate complexes" *Geochimica et Cosmochimica Acta 60* [24] 4897-4911 (1996)

26. M. Nara, H. Torii and M. Tasumi, “Correlation between the vibrational frequencies of the carboxylate group and the types of its coordination to a metal ion: An *ab initio* molecular orbital study” *J. Phys. Chem. 100* [51] 19812-19817 (1996)
27. G. Fogarasi, X. Zhou, P.W. Taylor and P. Pulay, “The calculation of ab initio molecular geometries: efficient optimization by natural internal coordinates and empirical correction by offset forces” *J. Am. Chem. Soc. 114* [21] 8191-8201 (1992)
28. J. Baker, “Techniques for geometry optimization: a comparison of Cartesian and natural internal coordinates” *Journal of Computational Chemistry 14* [9] 1085-1100 (1993)
29. R.J.H. Clark, B.K. Hunter, D.M. Rippon, “Vapor-phase Raman spectra, force constants, and values for thermodynamic functions of the tetrachlorides, tetrabromides, and tetraiodides of titanium, zirconium, and hafnium” *Inorganic Chemistry 11* [1] 56-61 (1972)

9. Small-angle X-ray scattering by the sol

9.1 Introduction

Small-angle X-ray scattering (SAXS) is a widely-used method for determining the size and, to some extent, the shape of colloidal structures. This chapter describes a SAXS study of the standard sol.

The four aims of this study were to determine:

1. the size and shape of particles in a standard ZN1.0 sol,
2. the size and shape of the species in the ZN2.0 solution,
3. any changes in the particle size and shape during ageing over 6 months, and
4. any effect of dilution to 0.2 M.

The changes that take place with dilution are of interest for two reasons: First, to gauge the scale of 'concentration effects' on the scattering profile; and second, because diluted samples were used for the dynamic light scattering measurements, and it is important to know if the particles change in size with dilution.

The analysis of the scattering profiles is fairly involved, and this chapter is dedicated to summarising the relevant theory, describing the equipment used, providing the full results, and discussing the analysis and potential problems. The principle results are summarised in Section 3.6, and discussed in the context of the other studies of the sol particles.

It should be noted that SAXS will only characterise the 'Zr–O(H) core' of the particles, and not any coordinated nitrate or water groups. The reason is that nitrate ions have a similar electron density to that of water, and thus a very small *scattering contrast* against the water matrix (see Section 9.2.1). Naturally, coordinated water molecules have an essentially zero scattering contrast against the water matrix.

Previous studies of zirconium salt solutions

Several SAXS studies have recently been carried out on zirconium salt solutions under various conditions.

Toth *et al*. examined $Zr(NO_3)_4$ solutions over the concentration range 0.035 - 1.0 M, all with pH of 2.2.[1] The radius of gyration, R_g, was determined from the Guinier approximation, and

remained constant at 4.6 ± 0.1 Å over the full concentration range. This result was interpreted to indicate that the basic scattering unit is the same size at all concentrations. Data for the 0.035 M sample was compared with simple models based on geometric shapes, and the 'best fit' matched a cylinder with diameter 9.6 Å and height 11.0 Å, which was interpreted to correspond to the cyclic tetramer structure $[Zr_4(OH)_8]^{8+}$. In fact, these dimensions correspond better with the octomer described by Singhal *et al.*,[2] but without more sophisticated modelling it is difficult to make the distinction.

Solutions of 0.05 M $ZrOCl_2$ were studied by Singhal *et al.*[2] The pH was varied by addition of either HCl or NaOH. At pH 0.1, an R_g value of 3.8 Å ± 0.2 was measured, which was attributed to the 'tetramer' species, described in Section 2.2.1. In solutions at pH 1.4, a structure with R_g of 5.1 ± 0.2 was identified, and at intermediate pH a mix of the two species was found. Where small amounts of NaOH were added to give higher pH, larger polymeric species were formed. The structures present in solution were determined by calculating expected scattering profiles from a range of molecular structures, and comparing these with the measured profiles. R_g values of 3.2 and 3.8 Å were calculated for the tetramer structures $Zr_4(OH)_8(H_2O)_{16}^{8+}$ and $Zr_4(OH)_8(H_2O)_{16}Cl_6^{2+}$, respectively. The number of chloride atoms present makes a significant contribution to the scattering characteristics of the species, and it was concluded that approximately six Cl^- anions were associated with each species in the second coordination shell. The larger species, with R_g of 5.2 Å, was identified to be an 'octomer' structure, and modelling suggested that this species consisted of two tetramers stacked on top of each other, joined by a single hydroxy bridge at each corner.

Polymerisation and condensation in the solution is greatly accelerated at elevated temperatures, leading to the formation and growth of particles.[3-5] Two SAXS studies of the ageing of zirconyl salt solutions during aging at between 80 and 100°C, over periods between 10 and 100 hours, have found that the primary particle formed is rod-shaped.[3,4] Rod-like primary particles, with a cross-sectional radius of ~ 4.3 Å, are initially formed, then aggregate together to form dense particles.[3]

9.2 SAXS theory

This section briefly covers the basic principles for the interpretation of small-angle X-ray scattering data, that are necessary for the understanding of this chapter. More detailed discussions are found in textbooks [6,7] and articles [8,9] dedicated to the subject.

9.2.1 Small-angle scattering

When X-rays pass through a material, they interact with the component atoms in the material and are scattered at a range of angles. This interaction may give rise to both diffraction (Bragg) and continuous-scattering (non-Bragg) phenomena. Diffraction is caused where scattering centers are ordered in a periodic structure, while in materials in which there is no periodic structure the only scattering is continuous.

The angle at which scattering occurs is related to the size of, and distance between, the scattering centres. Wide-angle scattering and diffraction, measured at scattering angles above approximately 5°, give information on the arrangement of scattering centers that are approximately the same size as the X-ray wavelength, *ie* atomic arrangements. Small-angle scattering, at angles of below approximately 5°, is characteristic of heterogeneities in the material having dimensions from several tens to several hundred times the X-ray wavelength.[7] At these small angles the scattering is practically independent of the short-range order of the atoms, depending only on the exterior form and dimensions of the heterogeneities. In practice, the upper and lower limits to the size of heterogeneities that can be characterised by scattering are determined by, respectively, the minimum angle that scattering can be practically measured and the scattering intensity.

X-rays are not the only radiation that is used for small-angle scattering experiments, and both visible light and neutrons have been used extensively. However, X-rays of a experimentally convenient wavelength are relatively easily generated, and are the most widely used.

X-ray scattering is measured as a function of scattered X-ray intensity, I, against scattering angle, 2θ, as it is for conventional wide-angle X-ray diffraction. The angle of scattering is generally expressed by the *scattering vector*, Q, [*] which is a function of both scattering angle and the wavelength of the scattered radiation, λ, as given in Equation 9-1.

[*] Note that various other symbols for Q have been used in other publications, such as q or h.

$$Q = \frac{4\pi \sin\theta}{\lambda}$$ **Equation 9-1**

The continuous scattering profile is most intense at very low angles, and the intensity falls as the scattering angle increases. An example is given in Figure 9-1.

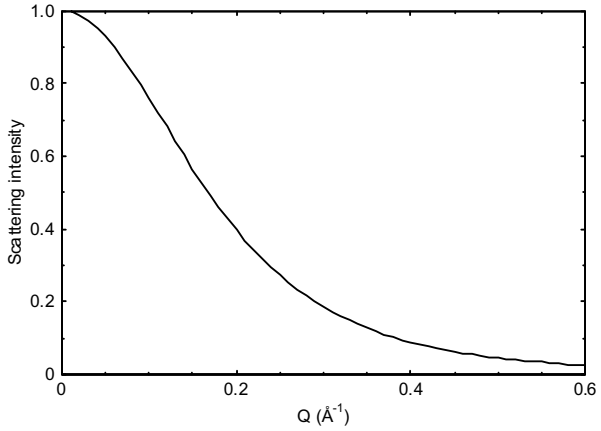

Figure 9-1: Example of a continuous-scattering profile.

If there is periodic order in the material, diffraction peaks will be superimposed on the continuous-scattering profile. When the Bragg diffraction law is combined with Equation 9-1, the relationship between the characteristic diffraction spacing, d, and Q can be expressed as $d \cdot Q = 2\pi$.

Although small-angle scattering is used to investigate a wide range of systems, the rest of this discussion will concentrate on the characterisation of randomly-oriented particles in a liquid medium.

The small-angle scattering intensity of particles in a medium, $I(Q)$, can be expressed as a combination of four components. Firstly, assuming that each scattered X-ray is scattered only once (single scattering), the detected intensity is completely proportional to the *number-density of scattering particles* in the material, ϕ. Secondly, the scattering profile of the particles can be detected because they scatter X-rays more (or less) strongly than the surrounding medium, which in turn is dependent on the electron density of the molecule. The difference in the scattering power of the particles with respect to the matrix is expressed as the *contrast* term, C. Contrast is dependent on the chemical nature of the particles and the medium. Thirdly, the *scattering function* of each particle, $F(Q)$, is determined by the scattering characteristics of the particle, such as size, shape, density, etc. This is the main

function of interest, and is discussed further in Section 9.2.3. Finally, the *structure function*, $S(Q)$, reflects the interference effects between particles. In dilute systems $S(Q)$ is effectively independent of Q, but in concentrated systems it can play a significant role as discussed in Section 9.2.4. The product of these four components gives the total scattering intensity, $I(Q)$, as expressed in Equation 9-2.

$$I(Q) = \phi \cdot C \cdot F(Q) \cdot S(Q) \qquad \textbf{Equation 9-2}$$

Since the values of both I and Q often span several decades, a useful way of plotting the scattering profile is on logarithmic axes, *ie* $\ln(I)$ against $\ln(Q)$. This is sometimes known as the *shape plot*, as the general shape of the scattering particles can be inferred from this plot in the high-Q region. As Q increases, the gradient of the scattering curve becomes more negative, and in a region at high-Q often reaches a constant gradient. The slope of this region is indicative of the shape of the scattering particles. A largely one-dimensional shape (rod) is indicated by a slope of –1, a two-dimensional shape (plate) indicated by a slope of –2, and for spheres the slope continues to increase to –4.

9.2.2 The radius of gyration

The *radius of gyration* of a particle, R_g, is an important parameter in the analysis of small-angle scattering data. It represents the distribution of the scattering centers in the particle as a function of their distance from the geometric centre of the particle. The radius of gyration can be calculated for particles of any shape, and is the only precise parameter which can be determined by conventional small-angle scattering experiments without invoking supplementary hypotheses, such as particle shape, etc.[7] *

The value of R_g for any particle can be calculated, given the geometry and density distribution. The formulas for calculating R_g for simple, homogenous shapes are well-known. The formula for a homogenous sphere is given in Equation 9-3, and that for a homogenous cylinder (either long-rod or flat-disk) is given in Equation 9-4. The parameter R is the sphere or cylinder radius, and H is the cylinder height.

$$R_g = \sqrt{3/5} \cdot R \qquad \textbf{Equation 9-3}$$

---

* Recently a technique has been developed to determine the absolute value of the contrast term from small-angle scattering measurements as well, using the phenomenon of multiple scattering.[10]

$$R_g = \sqrt{\frac{R^2}{2} + \frac{H^2}{12}}$$ **Equation 9-4**

A direct method of determining the values of R_g from scattering data is with the *Guinier approximation*, expressed in Equation 9-5.

$$I(Q) = I(0) \cdot e^{-\frac{Q^2 R_g^2}{3}}$$ **Equation 9-5**

The Guinier approximation is valid only for the region of the scattering curve at low Q values. A widely accepted limit to this region is $Q \cdot R_g < 1$. The standard method to use this equation is to plot the natural logarithm of the scattering intensity against Q^2, known as a *Guinier plot*. Where a straight-line section is present in the region of validity, the slope of the line will be $-R_g/3$. This can be shown by taking Equation 9-5 to the limit $Q \rightarrow 0$.[7]

The Guinier approximation assumes that the scattering particles are identical and dilute. Where there are several populations of different-sized particles, this may be indicated in the Guinier plot by more than one straight-line section. In principle, this allows the value of R_g to be determined for each distinct population of particles. However, multiple straight-line sections in this region can also be caused by other factors, for example, the shape of the scattering function for rod-shaped particles.[7]

Where the particle shape is known, further parameters may be derived from the low-Q data. The one-dimensional analogue of R_g is called the *radius of gyration of the thickness*, R_t, and is applicable to plate-shaped particles.[6] Similarly, the two dimensional analogue, the *radius of gyration of the cross-section*, R_c, is applicable to rod-shaped particles. In a method analogous to the Guinier approximation and Guinier plot, the value of R_t can be determined from the low-Q scattering profile using Equation 9-6.[6] The scattering data is plotted $\ln(Q^2 I)$ against Q^2, and the slope of the straight-line section is $-R_t$. The value of R_t can then be converted to the plate thickness, H, using the relationship $H = 2\sqrt{3} \cdot R_t$. A similar expression exists for R_c.

$$I_t(Q) = I_t(0) \cdot e^{-Q^2 R_t^2}, \text{ where } I_t(Q) = I(Q) \cdot Q^2$$ **Equation 9-6**

9.2.3 Modelling the scattering function

Models have been developed to describe the scattering function, $F(Q)$, from various geometric shapes, and these are derived and fully discussed in the literature.[6,7] The scattering

function for a homogenous sphere is given in Equation 9-7, and for a randomly-oriented homogenous cylinder in Equation 9-8,

$$F(Q) = \left[3\frac{\sin QR - QR\cosh R}{Q^3 R^3} \right]^2 \qquad \textbf{Equation 9-7}$$

$$F(Q) = \int_0^{\pi/2} \frac{\sin^2(QT\cos\theta)}{Q^2 T^2 \cos^2\theta} \cdot \frac{4J_1^2(QR\sin\theta)}{Q^2 R^2 \sin^2\theta} \cdot \sin\theta \cdot d\theta \qquad \textbf{Equation 9-8}$$

where R is the sphere or cylinder radius, T is half the cylinder height ($H = 2T$), and J_1 is a Bessel function of the first kind. The cylinder model can be used to describe both flat disks, where H is the thickness, and long rods, where H is the length. Functions for other shapes, such as ellipsoids, are also available.

Fitting these functions to a measured scattering curve, using a standard least-squares fitting routine, is a common method to determine the particle dimensions. It must be realised that each model describes the scattering from a dilute dispersion of identical particles of a given geometric shape. Any interaction between particles, polydispersivity, or non-ideal shapes will cause deviations in the predicted scattering curve.

It is also important to choose the most appropriate geometric model. Modelling is far more reliable if there is an *a priori* reason for postulating a certain geometry, such as evidence from another technique. In the absence of such evidence, there are two methods for choosing a model. The slope of the $\ln(I)$ *vs* $\ln(Q)$ plot can give a good indication of the shape, as discussed in Section 9.2.1. This can be successful of the particles are of a relatively simple shape. Alternatively, fitting can be done with several different models, and the model that provides the 'best fit' is chosen. Much care must be taken when using this approach. Guinier and Fournet state that when comparing different models for goodness-of-fit with the data, such a comparison is only valid if each model has the same value of R_g.[7] It is also important to control the number of parameters, as a model with more parameters may well provide a better fit, without any physical significance.

9.2.4 Concentration effects

The analysis techniques discussed up to this point have been based on the assumption that the system is dilute enough so that the particles are isolated from each other, and that scattering

from each particle is independent of scattering from neighbouring particles. As the concentration increases, and the average distance of separation becomes comparable to the dimensions of the particle, a range of effects will start to make a significant contribution towards the scattering profile.

The most important effect is *interference* between radiation scattered from neighbouring particles. This is expressed in the structure function, $S(Q)$, which is constant in dilute systems, and takes the form of an oscillating function in more concentrated systems. The form of this function is very difficult to predict unless the distribution of the particles is known. The practical result is that the measured scattering profile is modified, particularly in the low-Q region. A particularly severe example is given in Figure 9-2. If the amplitude of $S(Q)$ is large enough an 'interference peak' arises in the scattering profile. The location of this peak has been used to determine the average separation of the scattering particles, d, using the relationship $d \cdot Q = 2\pi$, but Guinier and Fournet point out that this method is not precise.[7]

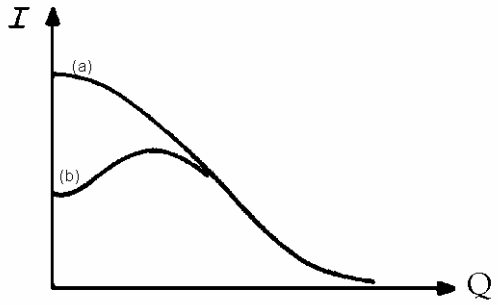

Figure 9-2: Scattering function a) of independent particles, b) with interference due to proximity of particles. Adapted from Glatter.[8]

The distortion of the low-Q region also decreases the slope of the Guinier plot, in turn decreasing the apparent value of R_g determined from the plot. The apparent R_g will decrease with increasing concentration.[7]

If the concentration of scattering particles is sufficiently high, then a significant number of X-rays will scattered more than once as they pass through the sample. *Multiple scattering* has the overall effect of increasing the average angle at which X-rays are scattered, thus decreasing the scattering intensity at low Q. This effect on the scattering profile can be calculated.[10]

A further concentration effect is due to *interactions between particles*, particularly if the particles are no longer randomly oriented, or if there are electrostatic or magnetic interactions. The consideration of these effects is beyond the scope of this thesis.

There are four approaches to minimising the concentration effects in a system. The first approach is simply to keep the concentration of the system as low as practical. Alternatively, the R_g value can be measured at a range of concentrations, and extrapolated to zero concentration with a Zimm plot.[8] These experimental approaches are only possible where the structure of the particles is not changed by dilution. It may be possible to estimate the structure function, and thus remove it from the scattering profile, but at best this procedure is difficult.[8] If this is not possible, then the fourth option is to ignore the whole concentration-dependent part of the experimental scattering curve.[8,11]

9.3 Experimental procedure

Instrumentation

All experiments were carried out using the SAXS instrument at the Research School of Chemistry, Australian National University.[12] This instrument is comprised of two primary parts: a rotating copper-anode X-ray source with beam collimators, and a 0.9 m Huxley-Holmes camera. The incident beam is focussed, in the horizontal plane, through the sample and onto a point on a horizontal detector wire. The unscattered beam transmitted through the sample is blocked by a beam-stop in front of the wire, while the X-rays that are scattered by the sample are measured along the length of the wire. The beam dimensions *at the sample* were 6 mm wide, by up to 1 mm high. The available Q range of the camera was approximately 0.013 to 0.58 $Å^{-1}$.

Since the beam is focussed onto the detector wire in the horizontal direction, and the wire is insensitive to any spread in the vertical direction, any 'smearing' of the signal due to the slit-type geometry is minimal. No 'desmearing' routines are required, unless working at close to the limit of resolution.[13] Figure 9-3 shows a scattering profile of 10 nm diameter spheres, without desmearing, measured on this instrument, and fitted by a scattering function for homogenous spheres.[14]

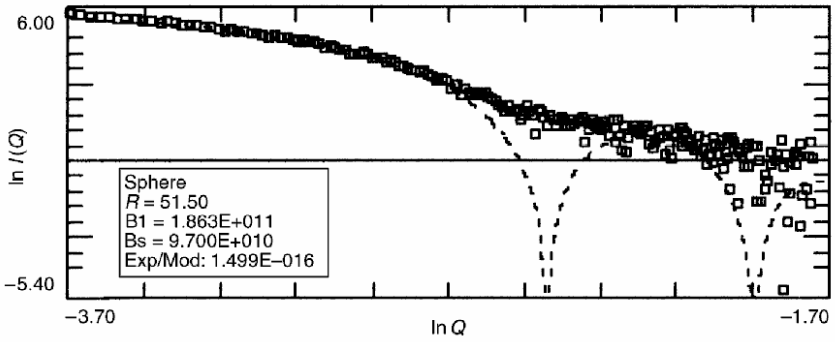

Figure 9-3: A scattering profile of 10 nm diameter spheres, without desmearing, measured by Singh and White on the ANU instrument, and fitted by a sphere model.[14]

Samples

Four samples were prepared according to the standard procedure described in Section 3.2, each with a Zr concentration of 1.0 M: a $Zr(OH)_2(NO_3)_2$ solution referred to as ZN2.0, two standard ZN1.0 sols, referred to as ZN1.0A and ZN1.0B, and a 'sol' with $Zr:NO_3$ ratio of

1:1.4, referred to as ZN1.4. The ZN1.4 sol represents a mid-point between the precursor solution, and the fully-formed sol. The scattering profile of each of these samples was measured approximately 5 days after preparation. The scattering profile of the ZN1.0A sol was measured again after 6 months ageing under ambient conditions. A further sample was prepared by diluting the ZN1.0A sol to 0.2 M. All samples are listed in Table 9-1.

Table 9-1

Sample name	$Zr:NO_3$ ratio	Age	Zr concentration
ZN2.0	1:2	5 days	1 M
ZN1.0A	1:1	5 days	1 M
ZN1.0AG	1:1	6 months	1 M
ZN1.0D	1:1	5 days	0.2 M
ZN1.0B	1:1	5 days	1 M
ZN1.4	1:1.4		1 M

Data collection

Samples were contained in 0.3 mm glass capillaries. The path length was kept small to minimise multiple scattering and absorption by the sample. The primary slits were adjusted so that the height of the beam was approximately the thickness of the capillary.

The 'transmission' though each sample, defined by the ratio of the measured beam intensity with and without the sample in place, was measured before and after each run.

The scattering profile of the particles had to be separated from the profile of the water matrix and sample container, so it was necessary to measure a 'background' scattering profile. In these experiments the 'background sample' was pure water in a glass capillary. Since the wall thickness varied considerably between capillaries, and also along the length of each capillary, the same section of capillary was used for both the sample and background profiles. Water was first sealed in a capillary and the background scattering profile measured. The water was then removed from the capillary, the sample solution introduced, and the capillary re-sealed. Care was taken that the beam passed though the same section of the capillary for both measurements.[*]

[*] For samples ZN1.0A and ZN1.0D, measured at an earlier stage of the experiments, the background scattering profile from a different capillary was used. The final subtracted profiles were distorted in the low Q region (< 0.1 Å^{-1}), which was not suitable for analysis. However, the high Q region appeared to be undistorted, and the analysis of these profiles gave similar results to the later measurements.

Data analysis

The sample and background profiles were first corrected for total transmission. The background profile were then subtracted from the sample profile to produce the final scattering profiles that are presented in this section.

The first few points at low Q affected by the beam stop were identified and removed. The measured scattering curves for each sample were plotted in a number of ways:

1. An I *vs* Q plot shows the unweighted scattering curve.
2. A $\ln(I)$ *vs* $\ln(Q)$ plot was used to identify the shape of the scattering particles, according to the principles outlined in Section 9.2.1.
3. A $\ln(I)$ *vs* Q^2 plot over the 'Guinier region' was used to identify the value of R_g by the Guinier approximation, discussed in Section 9.2.2. The upper limit of the valid range of the approximations was taken as $R_g \cdot Q < 1$.
4. Where the results suggest a plate-like structure, a $\ln(I \cdot Q^2)$ vs Q^2 'thickness plot' was used to identify R_t, which was then converted into the 'thickness' of the plate as discussed in Section 9.2.2.

Straight lines were generally fitted using a standard least-squares fitting routine, and errors were estimated from the goodness-of-fit. Since resolution is not very important, the data all in the plots shown in this chapter, except for Figure 9-12, was reduced by averaging consecutive groups of 3 data points. However, all fitting and modelling was done with the unreduced data.

The theoretical scattering profiles for a range of simple homogenous shapes were fitted to the data to determine the size and shape of the scattering particles, as discussed in Section 9.2.3. The models used were the sphere, plate (flat cylinder), rod (long cylinder), and ellipsoid models. All except the first of these models have only two variables. A least-squares fitting routine from the *Igor Pro* software package[*] was used to refine the dimensions of the 'model' particle to provide the optimum fit with the measured profiles. The resulting values give a strong indication of the shape and size of the scattering particles.

[*] IGOR Pro, Version 3.12, WaveMetrics Inc.

The choice of model to use was made on two criteria: first, the slope of the logarithmic plot, and second, a comparison of fits to the data by the different scattering profile models. Care was taken to compare models with the same R_g. Comparisons of different fits were made by eye on ln(*I*) *vs Q* plots, and using the calculated difference between the data and the fitted profile. Only the shape and dimensions that were chosen as the 'best fit' are reported here.

It was important that the concentration effects were minimised, so fitting was carried out only over a *Q*-range that was relatively free of these effects. In most cases, the minimum *Q* value fitted was 0.15 $Å^{-1}$.

9.4 Results and discussion

9.4.1 Results

All seven scattering profiles are presented in Figure 9-4 through to Figure 9-9, plotted on both linear axes and logarithmic axes. Where fitting of the scattering function has been carried out, the best fit is compared with the data. Where a constant slope can be identified in the ln(*I*) *vs* ln(*Q*) plot, a straight line is plotted though the data, and the slope, *m*, is given. Figure 9-10 compares four scattering curves from the 1.0 M samples. All numeric results from modelling and plotting are given in Table 9-2.

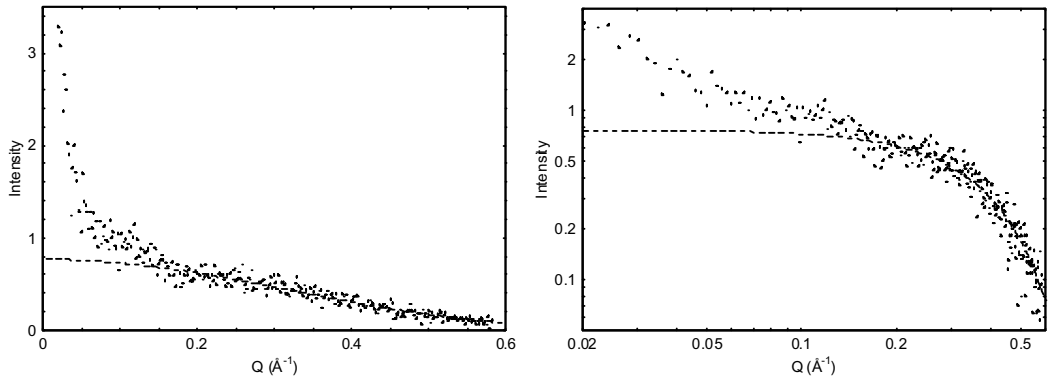

Figure 9-4: Scattering profile of sample ZN2.0, 1.0 M zirconyl nitrate solution, plotted on linear and logarithmic axes. The broken line represents the best fit for the sphere model.

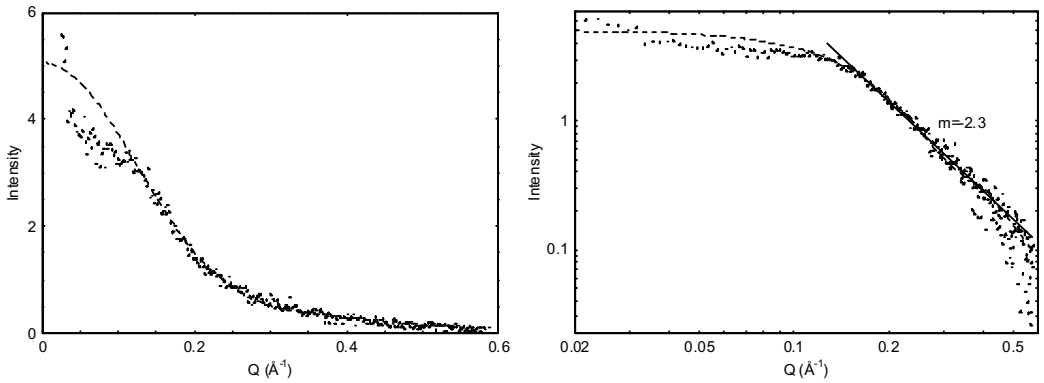

Figure 9-5: Scattering profile of sample ZN1.0B, unaged 1.0 M sol, plotted on linear and logarithmic axes. The broken line represents the best fit for the cylinder model.

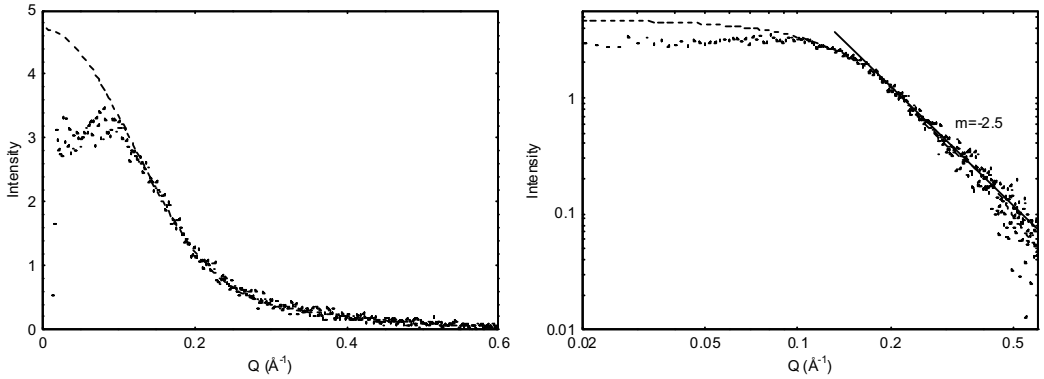

Figure 9-6: Scattering profile of sample ZN1.0A, unaged 1.0 M sol, plotted on linear and logarithmic axes. The broken line represents the best fit for the cylinder model.

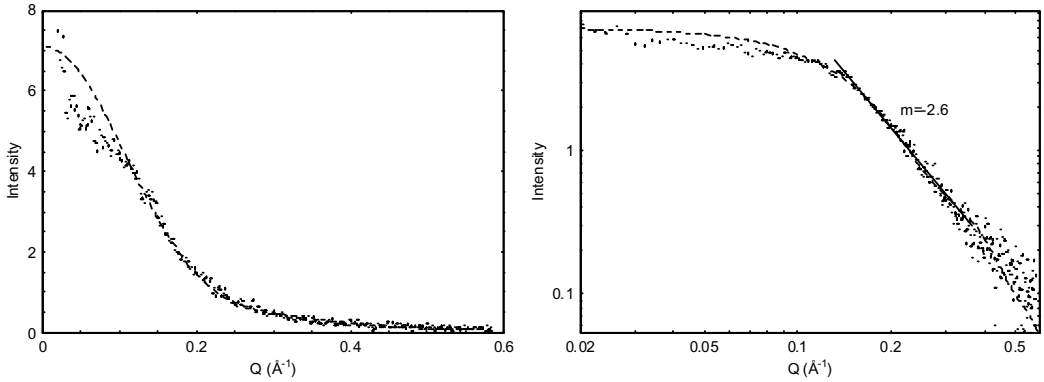

Figure 9-7: Scattering profile of sample ZN1.0AG, 1.0 M sol aged 6 months, plotted on linear and logarithmic axes. The broken line represents the best fit for the cylinder model.

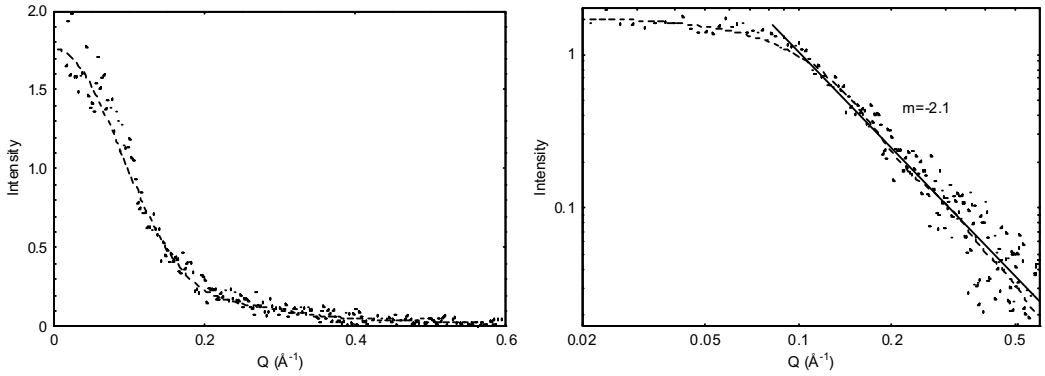

Figure 9-8: Scattering profile of sample ZN1.0D, sol diluted to 0.2 M, plotted on linear and logarithmic axes. The broken line represents the best fit for the cylinder model.

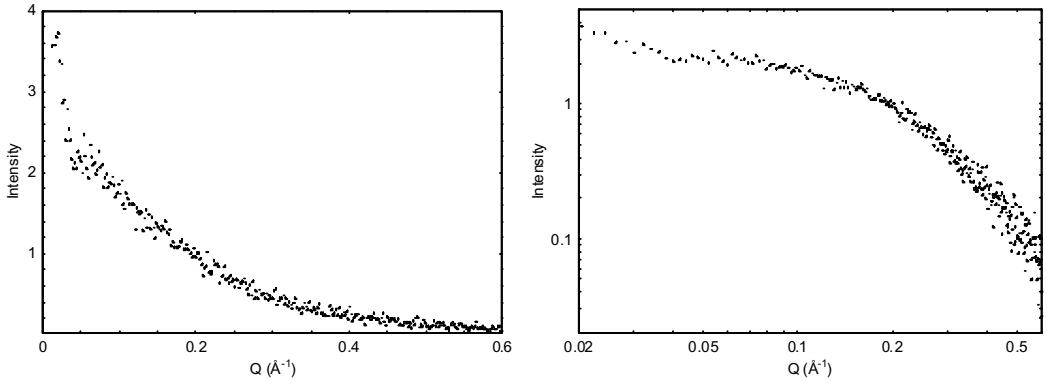

Figure 9-9: Scattering profile of sample ZN1.4, unaged 1.0 M sol with $Zr:NO_3 = 1.4$, plotted on linear and logarithmic axes.

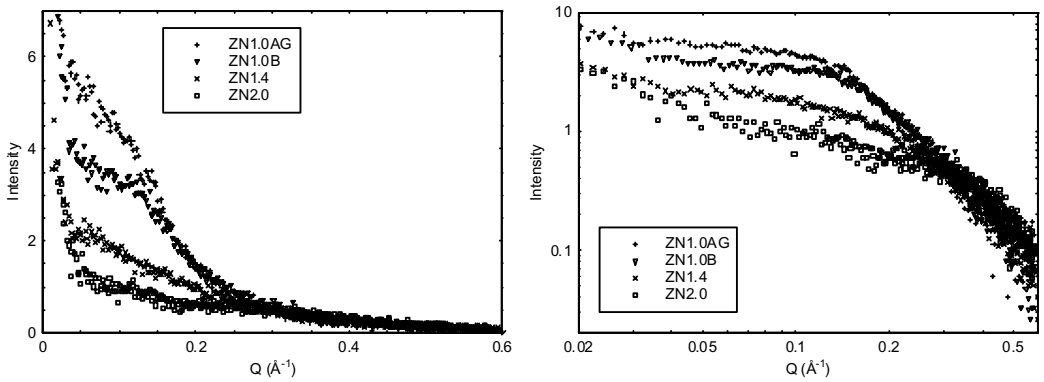

Figure 9-10: Comparison of 1.0 M solutions and sols, plotted on linear and logarithmic axes.

Table 9-2: Summary of results

Scattering profile	ZN2.0	ZN1.0B	ZN1.0A	ZN1.0AG	ZN1.0D	ZN1.4
R_g from Guinier slopes (Å)*	(39)	(38)	†	(36)	†	(38)
	(8.3)	6.2		8.4		(10)
	3.3					
Scattering-function model with 'best fit'	sphere	cylinder	cylinder	cylinder	cylinder	‡
Radius (Å)	5.2 ± 0.5	13.5 ± 1	14 ± 2	15.5 ± 1	19 ± 2	
Cylinder height (Å)	-	4.4 ± 1	6.0 ± 1	6.5 ± 2	3.5 ± 1	
R_g (Å)	4.0 ± 0.4	9.6 ± 1	10 ± 2	11 ± 1	13.3 ± 1.5	
aspect ratio	1:1	6:1	5:1	5:1	11:1	
Minimum Q fitted ($Å^{-1}$)	0.15	0.15	0.15	0.15	0.10	
Thickness from R_t value (Å)	-	5.5 ± 1	6.2 ± 1	9.0 ± 0.5	3.5 ± 0.7	3.5 ± 1
Slope of logarithmic plot	-	–2.3	–2.5	–2.6	–2.1	-

* Values in parenthesis are derived from slopes that are less than 50 % within the $Q \cdot R_g < 1$ limit.

† Some Guinier plots cannot be plotted due to distortion of the low-Q region.

‡ No scattering function fitting could be carried out on the scattering profile of ZN1.4.

9.4.2 Concentration effects and other considerations

Scattering profiles are most easily analysed for dilute systems of monodisperse particles. The system studied deviates considerably from this ideal, and a number of effects must be considered before analysis can take place. In particular, the sols in this study are quite concentrated, and some concentration effects can be expected.

Multiple scattering

The first potential problem is *multiple scattering*, in which an X-ray is scattered more than once as it passes through the sample. Calculations have been made to determine the fraction of X-rays that will be scattered more than once while passing through a 1.0 M Zr sol in a 0.3 mm capillary, using the equations presented by Sabine and Bertram.[10] It was calculated that the ratio of X-rays scattered twice to single-scattered X-rays would be approximately 1:1000. Although a number of approximations had to be made in the calculations, we can confidently regard multiple scattering as negligible. The main reason for the very low incidence of multiple scattering is that the particles themselves are very weak scatterers.

Interference

The second potential problem is that of *interference*, discussed in Section 9.2.4. The best way to avoid concentration effects such as this is to dilute the sample. This was only done for one sample, since it was anticipated that there could be some change in structure with dilution, and the scattering intensity was quite weak. The general approach taken was to disregard the low-Q region for modelling, which is the region that is most affected by interference.

There are two strong indications that there are significant interference effects for the 1.0 M sols. The first indication is a broad shoulder in the scattering profile at approximately 0.13 $Å^{-1}$, most noticeable in the plots with linear axes (eg Figure 9-5). By a simple Bragg relationship, this peak corresponds to an approximate 'average' inter-particle distance of 50 Å. Assuming that each particle in a 1.0 M sol has 50 - 100 zirconium atoms in it, as indicated in Chapter 3, each particle should have an average separation of 44 - 55 Å, which is good correlation with the observed peak.

Another indication of interference effects is given by comparing the scattering curves for a 1.0 M sol, ZN1.0B, and the 0.2 M sol, ZN1.0D. If the scattering intensity for the 0.2 M sol is multiplied by 5, then it can be directly compared, as in Figure 9-11, neglecting the relatively small change in particle size with dilution. Since the scattering intensity should be directly

proportional to the number of scatterers, this kind of comparison is valid as long as multiple scattering is insignificant. It can be seen that the two profiles coincide very closely over the Q-range 0.12 - 0.5 Å^{-1}, but diverge strongly at lower Q values. The decrease in relative intensity for the more concentrated sample can be directly attributed to interference.

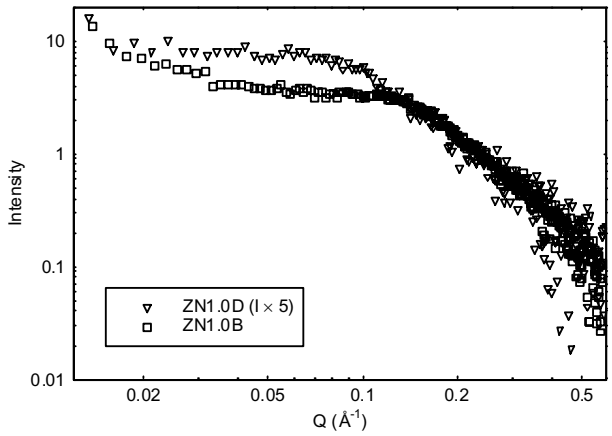

Figure 9-11: Comparison of the scattering curves of ZN1.0B and ZN1.0D, where the intensity of the ZN1.0D profile has been multiplied by 5.

Note also in Figure 9-11 that the intensities of the two profiles at very low angle (Q ~ 0.02) are very similar, which also indicates that there is negligible multiple scattering.

Polydispersity

A third potential problem is polydispersity. Most scattering equations assume a monodispersed system, although techniques for analysing scattering data from polydispersed systems have been developed. Polydispersity has not been analysed in this study for two reasons. Firstly, the dynamic light scattering study described in Section 3.7 indicated that the particles studies are relatively monodispersed, excluding a small fraction of much larger particles. Secondly, the signal-to-noise ratio is not high, and there is limited prior knowledge of the structure of the sol, which makes modelling a range of particle sizes very difficult.

Contrast

It should also be noted that it has been assumed here that the contrast term does not change during the formation of the sol. This assumption is largely justified by the results in Chapter 3, which indicate that the $Zr(OH)_2$ framework of the zirconyl cations remains intact in the particles.

9.4.3 Analysis

The slope of the logarithmic plots

The slope of any high-Q straight-line section of the ln(I) *vs* ln(Q) plot provides valuable information on the shape of the scattering particles, as discussed in Section 9.2.1.

No straight-line section is identified in the logarithmic plot of the ZN2.0 solution scattering curve. The gradient increases strongly beyond 0.3 $Å^{-1}$, increasing to greater than –3. This behaviour is characteristic of spherical scatterers. The scattering curve for the ZN1.4 sample has a similar form.

The logarithmic plots of the ZN1.0 sols contain a clear straight-line section, generally between 0.15 and 0.5 $Å^{-1}$. The slope of this section for the 1.0 M sols, ZN1.0A, ZN1.0B and ZN1.0AG, was between –2.3 and –2.6. A value of –2 indicates flat plate-shaped particles, and a value of –4 indicates spheres. The measured slopes of slightly greater than –2 is interpreted to mean that the particles are plate-like in shape, but with a relatively low aspect ratio. The modelling of the scattering function confirms this interpretation, finding an aspect ratio of approximately 5:1.

The logarithmic plot for the diluted sol ZN1.0D shows similar features to the scattering curve of the more concentrated sol, with a straight-line gradient of –2.1, very close to the theoretical value of –2. This indicates that the aspect ratio for the diluted sample is considerably greater than that of the concentrated samples. The aspect ratio calculated by fitting the scattering function (see below) is approximately 10:1.

Guinier plots

The information from the Guinier approximation, which is derived from the low-Q region of the profile, is likely to be strongly affected by the concentration effects. However, some useful indicative information can be gained.

For each Guinier plot, two or three distinct straight-line sections could be distinguished, each of which was interpreted to represent a distinct population of particles with an 'average' R_g corresponding to the slope of the line. An example of a Guinier plot for a ZN1.0 sol is given in Figure 9-12, and the plot for the zirconyl nitrate solution, ZN2.0, is given in Figure 9-13. Values of R_g determined from Guinier plots are listed in Table 9-2.

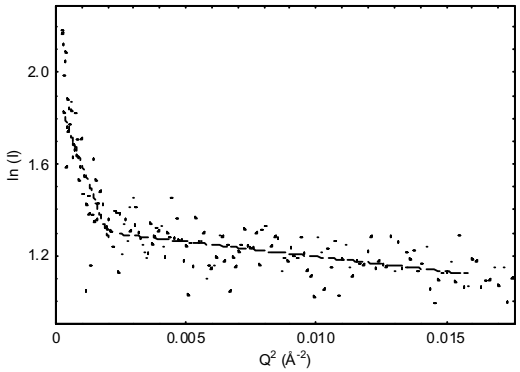

Figure 9-12: Guinier plot for ZN1.0B.

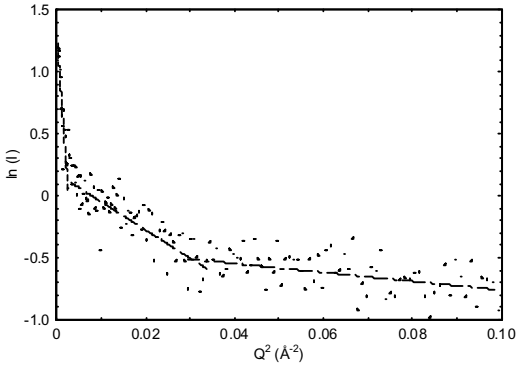

Figure 9-13: Guinier plot for ZN2.0.

The Guinier plot for each scattering profile had a straight-line section at relatively high Q values, well within the $R_g \cdot Q < 1$ limit of validity for the Guinier approximation, and which was interpreted to represent the R_g for the majority species. For the 1.0 M samples, these values were approximately 70 % of the R_g values determined by fitting the high-Q region with a scattering function. This effect is entirely consistent with interactions between particles.[7] For the sample diluted to 0.2 M, the R_g value derived from the Guinier plot was approximately 13 Å, which corresponds well with the R_g values determined by fitting the high-Q region, 13.3 ± 1.5 Å. This indicated that the concentration effects are greatly reduced with dilution to 0.2 M.

All Guinier plots also displayed a steep slope at very low Q, corresponding to a sharp rise in intensity < 0.04 $Å^{-1}$. The straight line fitting this region was only partially within the limit of validity. This slope indicated an R_g range of 35 - 40 Å, corresponding to spheres with a diameter of approximately 100 Å. To take into account the concentration effects to a first approximation, the above-mentioned factor of 70 % can be applied to the measured R_g, leading to a 'particle diameter' of approximately 140 Å. This value corresponds very well with the size of a small fraction of particles detected by dynamic light scattering (Section 3.7).

The Guinier plot for the ZN2.0 solution, shown in Figure 9-13, had in addition an intermediate slope. This slope corresponded to an R_g of approximately 8 Å, which is roughly the R_g value determined for the particles in the sols by the same method. This has been interpreted to mean that there is a small fraction of particles of this size in the solution, probably formed by partial hydrolysis during the time between formation of the solution and measurement. This fraction is small enough not to significantly influence the scattering profile at high Q.

Thickness plots

Where the slope of the ln(I) *vs* ln(Q) plots indicated that particles were plate-shaped, the scattering profile was plotted on a 'thickness plot'. The value of R_t was determined, which can be converted to an effective plate 'thickness' $2\sqrt{3}\cdot R_t$. These values, given in Table 9-2, are consistent with the 'height' of the modelled cylinders, with the exception of the 'aged' sol (see discussion in Section 9.4.4).

Fitting of scattering function models

Modelling the scattering profile over the high and medium Q-range provided more detail on the size and shape of the scattering particles.

For the ZN2.0 solution, there is no clear indication from the logarithmic plot of which scattering function model is most appropriate. Several models were tried, and both the sphere and cylinder models gave reasonable results. Each resulted in the same value of R_g, and the cylinder model resulted in a squat cylinder with an aspect ratio of 1.1:1. It is clear that the scattering particles are of low aspect ratio, close to spherical. Particles of this size and shape are consistent with the Zr_4 'tetramer' species. The calculated R_g value for the $Zr_4(OH)_8(H_2O)_{16}^{8+}$ species, with no associated anions*, was calculated by Sing *et al.* to be 3.2 Å.[2] The slightly higher R_g value from the scattering function may be due to the presence of a fraction of the 'octomer' structure, with R_g value of approximately 5.1 Å.

It was clear that the flat cylinder model was the optimum model to fit the data for the ZN1.0 sols. Not only did the slope of the logarithmic plots indicate a plate-shaped scattering particles, but the fit of the data by the flat-cylinder model compared very favourably with fits by the long-cylinder (rod), sphere, and ellipsoid models. An example is given in Figure 9-14. The dimensions of the X-ray scattering particles in 1.0 M sols were approximately 28 Å across and 5 Å thick, and R_g approximately 8.5 Å. The structure of these particles is discussed further in Section 3.9. Slightly larger plate-shaped particles were observed in the diluted sol, as discussed in Section 9.4.4.

* Since nitrate anions have a similar scattering cross-section to water, the contribution of the counter-ions to the scattering profile can be ignored.

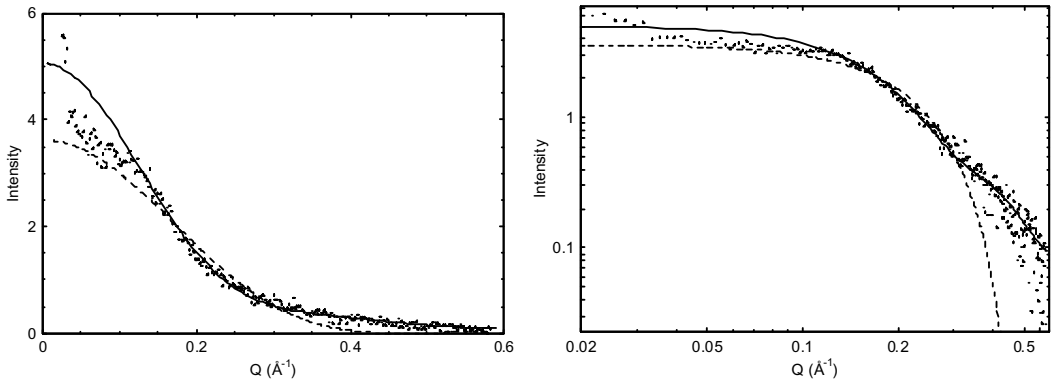

Figure 9-14: Scattering profile of sample ZN1.0B, fitted using a cylinder model (unbroken line) and a sphere model (broken line), plotted on linear and logarithmic axes. The modelled sphere has a radius of 10 Å.

A range of scattering function models were fitted to the scattering profile of the ZN1.4 sample, but the uncertainty in the resulting values means that none can be reported with any confidence.

9.4.4 Effects of ageing and dilution

Ageing

A comparison of the scattering profiles of new and aged sols is given in Figure 9-10. There is a significant increase in the scattering intensity in the Q region below 0.15 $Å^{-1}$, but essentially identical curves at higher Q. The implications of this is that there are more of the larger ~ 140 Å particles, which were detected in the Guinier plot, but that the primary scattering particle is not greatly changed in size. Concentration effects in the low-Q region make it difficult to make any firmer conclusions about the relative fraction of the larger particles.

When comparing the results for scattering function fitting of scattering profiles ZN1.0A and ZN1.0AG, which are from the same sample measured six months apart, it is evident that there is very little change in the shape or size of the primary scattering particle. The 'thickness plot' indicates that the average thickness of the particles in the aged sol is increased by approximately 50 %, but this is not reflected by the fitted scattering function. In considering the relative validity of these conflicting results, it should be noted that in the scattering equation for a cylinder of this size and shape, the thickness and scale factor are quite highly correlated, and so the thickness may be in error. At this point there is insufficient evidence to judge whether the particles become thicker with aging, but it is clear that little other change in the dimensions occurs.

Dilution

Table 9-2 shows that the modelled radius of the scattering particles is clearly larger after dilution of the sol, equivalent to the plate surface area increasing by 80 %. The modelled value for the thickness also decreases slightly. This change could be due to an actual change in size and shape of the particles with dilution, or a decrease in the concentration effects. Since the low-Q region was not included in scattering function fitting, and concentration effects at high Q are probably small, this change in size will be treated as real. However, the possibility that the increase in measured particle size is at least partially due to a decrease in concentration effects is acknowledged.

There is also a slight decrease in the measured average plate thickness. The combination of the increase in diameter and decrease in thickness results in the aspect ratio of the particles increasing from 5:1 to 11:1.

9.5 Conclusions

The following conclusions can be made from this detailed SAXS study:

- Low aspect-ratio particles with R_g ~ 4.0 Å dominate the X-ray scattering profile of the precursor zirconyl nitrate solution ZN2.0. The size and shape of these particles is close to that previously reported for the cyclic tetramer species $Zr_4(OH)_8$. The scattering profile at low Q also indicates the presence of a small fraction of substantially larger particles, which are approximately 140 Å in diameter.
- The particles in the 1.0 M ZN1.0 sol are plate-shaped, with dimensions approximately 28 Å across and 5 Å thick, excluding any coordinated water or nitrate. The small population of larger particles, identified in the precursor solution, is also identified in the sol.
- There is very little change in the shape or size of the primary particles during ageing over 6 months. The contribution of the larger (~ 140 Å) particles towards the low-Q region of the scattering curve increases a little with ageing.
- Dilution of the sol promotes growth of the sol particles at the edges.

The implications of these conclusions for the structure of the sol are discussed fully in Chapter 3.

9.6 References

1. L.M. Toth, J.S. Lin and L.K. Felker, "Small-angle X-ray scattering from zirconium(IV) hydrous tetramers" *J. Phys. Chem. 95* 3106-3108 (1991)
2. A. Singhal, L.M. Toth, J.S. Lin and K. Affholter, "Zirconium(IV) tetramer/octomer hydrolysis equilibrium in aqueous hydrochloric acid solution" *J. Am. Chem. Soc. 118* [46] 11529-11534 (1996)
3. A. Singhal, L.M. Toth, G. Beaucage, J. Lin and J. Peterson, "Growth and structure of zirconium hydrous polymers in aqueous solutions" *Journal of Colloid and Interface Science 194* 470-481 (1997)
4. J.A. Jutson, R.M. Richardson, S.L. Jones and C. Norman, "Small angle X-ray scattering studies of polymeric zirconium species in aqueous solution" *Mat. Res. Soc. Symp. Proc. 180* 123-128 (1990)
5. C.F. Baes and R.E. Mesmer, *The hydrolysis of cations*, Wiley-Interscience 152-159 (1976)
6. O. Glatter and O. Kratky, *Small Angle X-ray Scattering*, Academic Press, London (1982)
7. A. Guinier and G. Fournet, *Small-angle scattering of X-rays*, Trans. C.B. Walker, Wiley, New York (1955)
8. O. Glatter, "X-ray techniques" *International tables for crystallography C*, Edited by A.J.C. Wilson, Reidel, Dordrecht Holland (1992)
9. C.G. Windsor, "An introduction to small-angle neutron scattering" *J. Appl. Cryst. 21* 582-588 (1988)
10. T.M. Sabine and W.K. Bertram, "The use of multiple-scattering data to enhance small-angle neutron scattering experiments" *Acta Cryst. A55* 500-507 (1999)
11. K. Müller and O. Glatter, "Practical aspects to the use of indirect Fourier transform methods" *Makromol. Chem. 183* 465-479 (1982)
12. M. Aldissi, S.J. Henderson, J.W. White and T. Zemb, "Small angle X-ray and neutron scattering from electrically conducting block co-polymers" *Mater. Sci. Forum 27/28* 437-444 (1988)
13. Prof. J.W. White, Research School of Chemistry, Australian National University, Private communication (1999)
14. P.S. Singh and J.W. White, "Nucleation and growth of zeolite A under reagent controlled conditions. Part II" *Phys. Chem. Chem. Phys. 1* 4131-4138 (1999)

10. EXAFS spectroscopy of the gel

10.1 Introduction

X-ray absorption spectroscopy is a method to investigate the short-range structure around atoms of a specific element, using variations in the X-ray absorbance spectrum. It is particularly useful in determining the structure of materials that do not possess a high degree of long-range order. The technique used here measures oscillations in the absorbance spectrum, known as the *extended X-ray absorption fine structure* (EXAFS), and is known as EXAFS spectroscopy. It can yield interatomic distances, coordination-numbers, and parameters describing disorder.

The EXAFS technique is one of the few that enable the short-range structure of 'amorphous' solids to be characterised. Since the material studied in many of the Chapters in this thesis is amorphous, the EXAFS technique has proven highly valuable. However, since the theory and analysis of EXAFS data is relatively complex, the details of the EXAFS work has been collected in this chapter, while the results are discussed in the appropriate Chapters alongside the results from other characterisation techniques.

This chapter is divided into three major sections. Section 10.2 introduces the theory and practice of EXAFS spectroscopy, in order to give sufficient background for the subsequent chapters. The following two sections describe two EXAFS studies. For the principle study, described in Section 10.3, a standard ZN1.0 gel was prepared, and heated to various temperatures to represent stages of decomposition. These samples were characterised by a conventional EXAFS instrument at temperatures between 10 and 290 K. Low-temperature and variable-temperature measurements are important in obtaining accurate structural parameters. Section 10.4 presents an experiment in which EXAFS spectra were collected *during* heating of the gel, allowing *in-situ* characterisation of changes in the short-range structure.

Previous EXAFS work

There have been number of published EXAFS studies of zirconium oxides and hydroxides, in all cases using the Zr *K*-edge.

Various crystalline phases of pure and doped zirconia have been studied by EXAFS spectroscopy.[1-3] Measurements made at low temperatures and multiple temperatures have accurately determined the short-range structural parameters.

EXAFS spectra of some amorphous zirconia-precursors have been reported, and structural models fitted to the data.[4,5] However, measurements for these studies have only been made at ambient temperature, so the coordination-numbers and disorder parameters cannot be reliably determined. No structure has been resolved beyond the nearest Zr neighbour.

The crystallisation of zirconia-precursors has been studied to a certain extent by EXAFS. Antonioli *et al.* studied the crystallisation of a yttria-containing alkoxide-derived gel by heating the gel to different temperatures, but found the spectra of structures around the crystallisation stage difficult to model.[4] Tosan *et al.* reported only the uncorrected Fourier-transformed spectra of hydrothermally-treated gels, and the crystalline forms after calcination.[6] Turrillas *et al.* published Fourier-transformed spectra, measured *in-situ* by time-resolved EXAFS during crystallisation of a inorganic precursor.[7] Unfortunately, only a brief discussion and interpretation was provided.

Furthermore, there has been no report, for either crystalline zirconia or amorphous materials, of any attempt to take into account non-Gaussian distribution of atoms (anharmonicity). Clearly, there is plenty of potential for further experiments and more comprehensive analysis.

10.2 EXAFS theory and analysis

This section introduces the basic principles of EXAFS theory and analysis. Detailed discussion of all aspects of EXAFS spectroscopy can be found in books by Koningsberger [8] and Teo .[9] A useful discussion of the application of EXAFS spectroscopy to oxide ceramics has been written by Gautier-Soyer.[10]

10.2.1 X-ray absorption spectroscopy

The basic physical process that is used in X-ray absorption spectroscopy is the excitation of electrons from deep-core levels of a particular atom (*absorber atom*) by the absorption of a photon with an energy E. The excitation of the deep-core electron causes the emission of a photoelectron, which may be scattered by neighbouring atoms. The portion of the scattered wave that is scattered back to the absorber atom (backscattering) will overlap and interfere with the outgoing wave, as illustrated in Figure 10-1. The interference may be constructive or destructive, depending on the distance between the atoms, r, and the wavelength of the wave (which is determined by E). The resultant wave, which can be expressed as an oscillating function of E, is superimposed on the absorbance spectrum, and carries information on the nature of the neighbouring atoms around the absorber atom. In this work the selected absorber atom is zirconium.

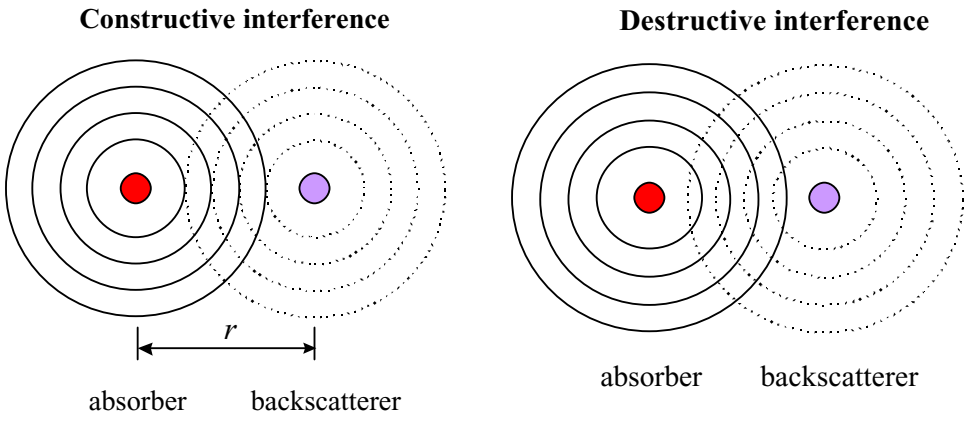

Figure 10-1: Schematic illustration of destructive and constructive interference, as the outgoing photoelectron wave from an 'absorber' atom is backscattered from a neighbouring atom.

The effects of this interference can be detected by X-ray absorption measurements. The absorbance of a material, μ, is determined by the attenuation of X-rays as they pass though the material. Figure 10-2 shows the X-ray absorbance of zirconium metal measured as a function of photon energy, known as an *absorbance spectrum*. The sharp increase in

absorbance corresponds to the point where the incident photons become equal to the binding energy of the electrons in a core energy level, in this case the *K*-level. This is known as the *absorption edge*.

Every absorber-backscatterer pair will create an interference oscillation on the absorbance spectrum in the region above the absorption edge. The sum of these oscillations for every scattering path gives a function, χ. This oscillating function may extend up to 1000 eV above the absorption edge, and is known as the *extended X-ray absorption fine structure*, or EXAFS. Since it is measured as a function of energy, it is often referred to as the *EXAFS spectrum*. The function depends essentially on the number, distance, disorder and type of the neighbouring atoms that cause the scattering, and so provides information on the average short-range structure around the absorber atom.

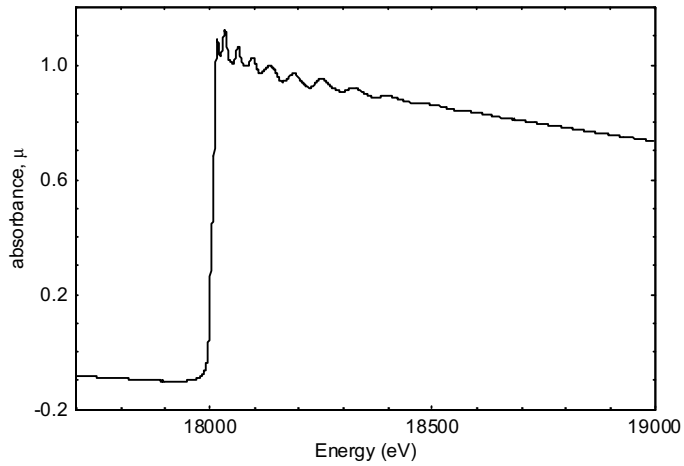

Figure 10-2: Absorbance spectrum of a zirconium foil, showing the Zr *K*-absorption edge at 18 000 eV, and the EXAFS oscillations.

The most important contribution to the EXAFS spectrum is from photoelectrons that are scattered directly from a single neighbouring atom back to the original absorber atom, known as *single-scattering*. Photoelectrons may also be scattered from one neighbouring atom to the next, before being scattered back to the absorber atom, in a process called *multiple-scattering*. Multiple scattering has little effect on the scattering from the nearest neighbours to the absorber atom, but becomes more significant as the distance from the absorber atom increases.

The region of the EXAFS spectrum that is able to be analysed is subject to upper and lower limits. Analysis of the EXAFS spectrum is generally limited to energies greater than ~ 50 eV

above the absorption edge. The region of the absorbance spectrum below this limit, close to the edge, is known as the *X-ray absorption near-edge structure* (XANES), and is strongly affected by a range of other effects such as multiple scattering and electronic transitions. The upper limit to the useable EXAFS region is determined by the signal-to-noise ratio.

10.2.2 The EXAFS equation

The EXAFS spectrum, χ, is measured as a function of energy, E, but is generally analysed as a function of the *electron wave vector*, k. The conventional unit for k is $Å^{-1}$. The relationship between E and k is defined in Equation 10-1, where m is the electron mass and $\hbar$ is Plank's constant divided by 2π. E_0 is the core electron threshold energy, which is the minimum energy required to free the electron, and is *approximately* the value of the corresponding absorption edge.

$$k = \sqrt{\frac{2m}{\hbar^2}\left(E - E_0\right)} \qquad \textbf{Equation 10-1}$$

The EXAFS spectrum is a sum of j individual waves, each from a neighbouring atom. The form of each wave is a diminishing sine curve, modified by an amplitude function. Equation 10-2 give the conventional expression for the sum of the waves, showing the *phase* component within the sine expression, while Equation 10-3 expands the *amplitude* component of the wave. Subscripts i and j refer to the absorber and scatterer atoms, respectively.

$$\chi(k) = \sum_j A_j(k)\sin(2kr_j + \alpha_{ij}(k)) \qquad \textbf{Equation 10-2}$$

$$A_j(k) = N_j S_i(k) F_j(k) e^{-2\sigma_j^2 k^2} e^{-2r_j/\lambda_j(k)} / (kr_j^2) \qquad \textbf{Equation 10-3}$$

Each of these components depend on various structural parameters of the material. The phase component depends on the distance between the absorber and scatterer atoms, r_j, and the total phase shift experienced by the photoelectron when it is scattered, $\alpha_{ij}(k)$. The amplitude component is largely determined by the backscattering amplitude from each atom, $F_j(k)$, which is the main function that must be calculated from theory, and is largely dependent on the atomic number and r_j. The amplitude reduction factor, $S_i(k)$, takes into account various many-body effects, and will be discussed further in Section 10.2.3. The value σ_j^2 is a 'disorder' term, a measure of the mean displacement of the scatterer atom from its average position with

respect to the absorber, and will be discussed further in Section 10.2.4. The value $\lambda_j(k)$ is the mean free path of the photoelectron, which can also be calculated from theory.

Often it is the case, or it must be assumed, that two or more atoms surrounding the absorber atom have identical values of r_j, and σ_j^2, and if they are of the same element they will share $F_j(k)$. In this case they can be treated as the same 'atom', with the parameter N_j included to represent the average number of such atoms. This value can also be used to represent average 'occupancies'.

Note that this equation does not explicitly include the effects of multiple scattering. Each multiple scattering path will contribute its own wave to $\chi(k)$, which can be dealt with by assigning an *effective* r_j, N_j, σ^2_j and $F_j(k)$.

It is worth pointing out that the measured EXAFS spectrum is a sum of all $\chi(k)$ functions for every absorber atom in the path of the X-ray beam. Thus only the *average* short-range structure can be determined, and X-ray absorption spectroscopy is limited to single-phase materials only.

10.2.3 The amplitude reduction factor

The amplitude reduction factor, $S_i(k)$, accounts for the amplitude loss to the photoelectron wave by many-body effects such as *shake-up* and *shake-off* processes at the central atom. Its value is largely dependent on the absorber atom, but is also sensitive to the chemical environment.[9] To a good approximation the value of $S_i(k)$ is transferable between chemically-similar systems with the same absorber atom.[9]

The value of $S_i(k)$ can be approximated by the theoretical value $S_0^2(k)$, the overlap of the initial and the final-state wave functions of the passive electrons which are excited along with the photoelectron. $S_i(k)$ may also contain other minor contributions. In EXAFS analysis, the term S_0^2 is generally used in place of S_i, and so in the Discussion section the amplitude reduction factor will be referred to as S_0^2.

It has been shown that the value of $S_0^2(k)$ varies with k, from unity at low k, to a value of less than unity, and generally above 0.6, at k greater than ~ 7 Å^{-1}.[9] At k greater than ~ 7 Å^{-1} the value of $S_0^2(k)$ is roughly constant. In cases where the high-k data is weighted more heavily in the data analysis, S_0^2 can be treated as being independent of k, effectively making it a scale constant for the amplitude component.

One problem in modelling EXAFS spectra is the correlation between the amplitude reduction factor and the coordination-number, N_j. As shown in Equation 10-3, these parameters are completely correlated, so that one cannot be determined without knowing the other. When analysing the EXAFS spectrum of a material with unknown values of N_j, the only way to resolve this difficulty, short of a theoretical calculation of S_0^2, is to determine the value of S_0^2 from the EXAFS spectrum of a chemically-similar reference material.

10.2.4 Disorder parameters

Thermal and static disorder

The presence of disorder is an important consideration when determining the structure of a material. Even in a crystalline material, the exact distance between a pair of atoms will not be equal to the average value, *r*. Disorder in the conventional EXAFS equation is represented by the term $e^{-2\sigma^2 k^2}$, where σ^2 represents the *mean square relative-displacement* of absorber and backscatterer atoms,[11] sometimes known as the *Debye-Waller factor*. This expression assumes that the true interatomic-distances take on a Gaussian distribution around the value *r*, and so σ^2 is equivalent to the *variance* of the distribution. The conventional unit for σ^2 is Å^2.

Disorder in any structure is due to two components. The first is a dynamic or *vibrational* component, which is a function of thermal lattice vibrations, and is roughly proportional to the absolute temperature. The second component is *static*, a function of the disorder in the material, and is independent of temperature. The total σ^2 can be simply expressed as the sum of these two components:

$$\sigma^2 = \sigma^2_{vib} + \sigma^2_{stat} \qquad \textbf{Equation 10-4}$$

The two components can be separated by measuring σ^2 at a range of temperatures, and fitting the temperature dependence with a phenomenological model, such as the Einstein-correlated or Debye-correlated models.

The *Einstein-correlated model* is a relatively simple way of describing the temperature dependence of σ^2 with temperature.[12] It is particularly suited to describe optical modes.[11] One form of the equation is given in Equation 10-5:

$$\sigma^2_{vib} = \frac{\hbar^2}{2k_b\mu_m\theta_E}\coth\left[\frac{\theta_E}{2T}\right]$$ **Equation 10-5**

where θ_E is the *Einstein temperature*, k_B is Boltzmann's constant, and $\hbar$ is Plank's constant divided by 2π. The reduced mass, μ_m, is the reciprocal sum of the two atomic masses: $\mu_m = (m_1^{-1} + m_2^{-1})^{-1}$. The Einstein temperature is the parameter used to describe the variation of σ^2_{vib} with temperature.

This model has been successfully used to determine optical modes of the phonon spectrum.[2,11] The expected vibrational frequency, *?* , in units of reciprocal wavelength, can be calculated from the Einstein temperature by Equation 10-6, where *h* is Plank's constant and *c* is the speed of light. The frequency can be converted to cm^{-1}, for comparison with experimental vibrational spectra.

$$\bar{\nu} = \frac{\theta_E k_B}{hc}$$ **Equation 10-6**

The *Debye-correlated model* is a more complex model, developed as an extension of the Debye models for specific heats and atomic thermal displacements.[11,13] For this model the *Debye temperature*, θ_D, describes the variation of σ^2_{vib} with temperature.

In general, the Einstein model is most suited to describing the σ^2 for the nearest neighbours to the absorber atom, and the Debye model for the rest of the structure.[11]

Anharmonicity

The conventional EXAFS equation, in Equation 10-3, assumes that the disorder possesses a Gaussian distribution, with the true distance between the absorber and backscatterer atoms distributed evenly around an average value *r*, with a variance of σ^2. While this assumption usually holds true for crystalline materials, where thermal disorder predominates, there is no reason for it to be true for materials with significant structural disorder. It is particularly important to take these effect into account when investigating amorphous and nano-particulate materials.[11,14-16] Deviation from a Gaussian distribution is known as *anharmonicity*.

The approach generally used is to expand the EXAFS equation using a series of *cumulants*, C_n, to describe the effective distribution for each absorber-backscatterer pair.[8,11,14] The even cumulants, C_{2n}, depend only on the amplitude of the EXAFS while the odd cumulants, C_{2n+1}, depend only on the phase. The first cumulant C_1 is the mean value, *r*, and the second cumulant

C_2 is the variance of the distribution, σ^2. When the distribution is Gaussian all further cumulants are zero. Otherwise, the asymmetry of the distribution is described by the third cumulant C_3, and possibly higher order odd cumulants C_5, C_7, *etc*. The symmetric deviation from the Gaussian shape is described by the fourth cumulant, C_4, and possibly higher order even cumulants. In practice, the amount of data limits the number of cumulants that can be fitted, and usually only the third and fourth are used.

10.2.5 Data treatment and modelling

Background removal

The first task in EXAFS analysis is to extract the EXAFS spectrum, $\chi(E)$, from the background absorbance spectrum $\mu_0(E)$. In practice the background absorption spectrum is an unknown function. In EXAFS analysis it is assumed to be a smooth, slowly oscillating function, generally simulated by a cubic spline curve with several segments. A balance must be struck between insufficiently fitting the background, allowing some of the background to 'leak' into the EXAFS spectrum, and fitting the EXAFS spectrum itself with the spline curve. The 'appropriateness' of the particular spline curve can be judged by examining the resulting EXAFS spectrum.

Weighting

Since the EXAFS equation expresses χ as a function of k, the $\chi(E)$ spectrum is converted to $\chi(k)$ using Equation 10-1. Although the amplitude of the oscillations falls rapidly with k, there is still much valuable information in the high-k region. To emphasise this region the amplitude of the spectrum can be weighted by a factor of k^n. Teo suggests the following values of n for backscatterer atoms of atomic weight, Z_j: $n = 1$ for $Z_j > 57$, $n = 2$ for $Z_j = 57$-36, and $n = 3$ for $Z_j < 36$.[9] It is important to use the same value of n for all results in a series of samples.

Fourier transformation

A very useful way of analysing the EXAFS spectrum is to obtain the modulus of the complex Fourier-transform of $\chi(k)$, referred to herein as the *Fourier-transformed spectrum*, or just *FT*. This provides a pseudo-radial distribution function around the absorber atom, with a series of peaks whose positions are equal to the coordination distances r_j, shifted by the phase shift $\alpha_{ij}(k)$. The intensity of the peaks are determined by the type of atom, the coordination-number N_j, and the disorder component σ^2_j. The examination of this function is a quick way to

visually analyse the information contained in the EXAFS spectrum. For example, Fourier-transformed spectra are given in Figure 10-4, in Section 10.3.3.

Fourier-transformation is carried out over a specified range of the weighted EXAFS spectrum, known as a *window*. The first part of the spectrum, approximately 3 - 4 $Å^{-1}$, is generally omitted from this range to avoid the XANES region.

Modelling

Analysis of EXAFS spectra to determine the short-range structure of materials is commonly carried out by modelling. This method involves a number of stages. First, a structural model is postulated, and the EXAFS spectrum expected from this structure is calculated from theory. The calculated spectrum is then compared with the observed spectrum, and the structural model is recursively adjusted to achieve the 'best fit' between the two spectra. The refined structural model should then be indicative of the short-range structure in the material being studied.

Models are generally defined in terms of *shells* of backscatterer atoms, containing N_j atoms of the same type, at a distance r_j from the absorber atom, with a variance in r_j of σ^2_j. Each atom in a shell is assumed to be structurally equivalent, and to make an identical contribution to the EXAFS spectrum. Third, fourth, and higher cumulants can also be added for each shell. The scattering function, $F_j(k)$, is calculated from theory such as FEFF.[17] Fitting of the model involves the variation of some, or all, of the parameters N, r and σ^2 for each shell by non-linear least-squares refinement. These models do not take into account the three-dimensional positions of the backscatterer atoms, and so cannot predict the effects of multiple scattering.

Another value that must be refined is the core electron threshold energy, E_0, which cannot be practically determined from theory.[9] It is generally believed to be within approximately 30 eV of the absorption edge. Fortunately, the value of E_0 is transferable between chemically-similar compounds, so can be roughly determined from a standard, but it is still useful to allow E_0 to vary to a certain extent. Note that E_0 is not a parameter in the EXAFS equations, but is used to convert between the energy scale and the k scale. Slightly different values of E_0 may apply to each single-scattering path involving a different type of backscatterer atom, which is attributed to charge-distribution effects that are neglected in the standard theory.[18] The practical effect of this is that different E_0 values may apply to different shells, particularly inner shells.

With up to four or more parameters for each shell, a fairly simple model can involve a large number of parameters. The theoretical limit to the number of parameters that can be determined from any particular set of data is expressed by the *number of independent points* of the data set, N_{IP}. This value is determined by the k-range used from the EXAFS spectrum, Δk, and the range used from the Fourier-transformed spectrum, ΔR, as expressed in Equation 10-7.

$$N_{IP} = 2 \cdot \Delta k \cdot \Delta R / 2\pi \qquad \textbf{Equation 10-7}$$

The number of parameters in the models used in this Chapter seldom exceed more than 20 % of the N_{IP} limit. Instead, a smaller limit is set up due to the *correlations* between parameters. Although each parameter affects all others to a certain extent, the most important correlation pairs are E_0 and r in the *phase* component, and N and σ^2 in the *amplitude* component. When modelling, great care must be take in limiting the effects of these correlations. Since each of these parameters have a different dependency on k, correlations can be minimised by using a large k-range.

10.3 Study 1: Multiple-temperature measurements

10.3.1 Introduction and aims

There are significant advantages to be gained from measuring EXAFS spectra at the lowest temperature possible. Thermal disorder is minimised, including any non-Gaussian components, which leads to a more intense spectrum that is much easier to model. The structural parameters can thus be determined more accurately, and the potential for correlation between σ^2 and N is minimised.

Further advantages can be obtained from measuring EXAFS spectra at a range of temperatures. This allows the thermal component of disorder to be determined by one of the models discussed in Section 10.2.4, leading to an even more accurate determination of σ^2, and possibly to other material properties such as vibrational frequencies. Multiple-temperature measurements are also the best method of assessing the presence of anharmonicity,[11,14,15] and is particularly important for studying amorphous materials or nanoparticles due to the inherent disorder.

This section discusses the main EXAFS study, in which samples of the standard gel have been heated to different stages of decomposition, then characterised by EXAFS at a range of temperatures. There were four general aims for this series of experiments

1. To determine the short-range structure of the standard ZN1.0 gel, with a better degree of accuracy than previous studies of zirconium oxy-hydroxide material.
2. To determine the short-range structure of the material at stages during decomposition, in order to investigate the decomposition reactions.
3. To determine the short-range structure of the amorphous material immediately before crystallisation. This should contribute towards an understanding of the crystallisation mechanisms of the metastable phase.
4. To demonstrate how careful analysis of EXAFS measurements can provide valuable information on the short-range structure of materials that is difficult to obtain by any other means.

The description of this study is divided into a number of parts. Firstly, the procedure is described in Section 10.3.2. The EXAFS spectra and Fourier-transformed spectra will then be presented and briefly compared in Section 10.3.3. The next two Sections will present data

needed for the modelling work: Section 10.3.4 will present the results from the reference materials, and the determination of the value of S_0^2 will be discussed in Section 10.3.5. The modelling results from the amorphous samples will be presented in Section 10.3.6, followed by the results for the crystalline sample in Section 10.3.7. Three-dimensional structural models have been developed from these results, which are fully discussed in previous chapters. The discussion here is mainly limited to the disorder parameters.

Two supplementary sections follow, both of which consider the disorder parameters further. Section 10.3.8 presents and compares the σ^2 values that have been calculated with, and without, a constraining model. Vibrational frequencies were calculated from the Einstein model for the Zr–O pairs, and these are presented and discussed in Section 10.3.9. Finally, the conclusions in Section 10.3.10.

10.3.2 Procedure

Preparation of samples and reference materials

Two reference materials and five samples were examined by EXAFS. The reference materials used were monoclinic zirconia and barium zirconate, which were prepared in the laboratory. Zirconium butoxide solution was hydrolysed with pure water, and calcined at 1650°C for 2 hours, to produce pure monoclinic zirconia. Barium carbonate and zirconium carbonate were mixed in the appropriate ratio, and fired at 1600°C to form phase-pure $BaZrO_3$.

The first sample was a gel, ZN1.0 from a standard ZN1.0 sol, prepared as described in Section 4.2. Portions of this gel were heated to different temperatures, to give the remainder of the 'unknown' samples, as listed in Table 10-1. The details of the heating procedure are given in Section 5.2. The temperatures 150 and 300°C were chosen to represent the main stages in the decomposition process, as indicated by the decomposition studies discussed in Chapter 5. The gel was also heated to 400°C to represent the amorphous structure immediately before crystallisation. The final sample, H470, was heated for an hour to promote maximum crystallisation of the metastable tetragonal phase.

Table 10-1

Sample reference	Heating temperature	Heating time
Gel	-	-
H150	150°C	5 min
H300	300°C	5 min
H400	400°C	5 min
H470	470°C	1 hour

The Raman spectra and XRD pattern of these samples are reported in Sections 5.3.1 and 5.3.3, respectively. All but the last of these samples is amorphous, with no indication of any crystalline phase. The XRD pattern and Raman spectrum of the H470 sample show that it is composed of the metastable t-ZrO_2 phase. However, TEM imaging, reported in Section 6.3.3, shows a microstructure in which dense crystallites are embedded in a lower-density matrix, most probably an amorphous phase. This indicates that crystallisation has not proceeded to completion after heating for an hour. The implication for EXAFS is that while the majority of the absorber Zr atoms will have a 'tetragonal zirconia' environment, a significant fraction of them will have the environment of the amorphous material.

All samples were ground finely, and thoroughly mixed with boron nitride to produce a sample with optimum absorbance. Powders were then pressed into flat disks.

Data collection and background removal

X-ray absorption spectra were recorded in transmission mode on the Australian National Beamline Facility (ANBF). The ANBF is a multi-capability, hard X-ray beam-line installed at the 2.5 GeV *Photon Factory* second-generation synchrotron light-source, located in Tsukuba Science City, Japan.

A Si (111) monochromator was used to select the energy of the X-ray beam incident on the sample. The beam first passes through an ion-chamber detector, which measured the incident intensity, I_0. It then passes through the sample, and the transmitted intensity is measured by a second detector. The beam then passes through a reference zirconium foil, and the intensity measured by a third detector. The incident intensity, sample absorption, and foil absorption are measured simultaneously as the beam energy is step-scanned over the range of interest. The reference foil spectrum is then used to calibrate each sample spectrum to an absolute energy scale.

Samples to be measured at below-ambient temperatures were held in a cryostat, cooled by liquid helium to a base temperature of 10 K. The atmosphere in the cryostat was helium at temperatures below 90 K, and nitrogen at temperatures above 90 K.

All absorbance spectra were measured across the Zr *K*-edge at 17 998 eV. The spectra were measured over the energy range 17 770 - 19 000 eV, with an energy resolution given in Table 10-2.

Table 10-2

Energy range (eV)	step size (eV)	region
17 780 - 17 980	10	pre-edge
17 980 - 18 050	0.5	edge
18 050 - 18 450	2	near post-edge
18 450 - 19 000	4	far post-edge

Samples were measured at a range of temperatures, between the base temperature of the cryostat and ambient temperature, as set out in Table 10-3.*

Table 10-3

Sample	Temperatures measured (K)			
m-ZrO_2	10	80	180	290
BaZrO3				290
Gel	10	80		290
H150	10	80	180	290
H300	10	80		290
H400	10	80		290
H470		80		290

Gaps in the experimental matrix are due to restricted beam time, or to a few measured spectra that were discarded because they contained anomalies that could not be corrected.

A background for each absorbance spectrum was simulated by a continuous spline, with segments evenly spaced in k-space, using the *Spline* routine in the X-FIT software package.[19] The background was removed, and the spectrum converted to a $\chi(k)$ function with an initial E_0 of 18 015 eV. The $\chi(k)$ function was weighted by k^3 to emphasise the high-k data. The ends of the Fourier-transformation window were positioned at nodes, at approximately 4 and 14 $Å^{-1}$.

Modelling

All modelling work reported here was carried out using the FEFFIT software package,[20] using the FEFF7 level theory.[17,21] FEFFIT is able to fit a model to multiple EXAFS spectra simultaneously.[14] Certain parameters, such as coordination-number, can be held constant for all data sets, while other parameters, such as σ^2 or C_3, can be independent for each data set. Furthermore, the software contains routines that allow σ^2 values for each data set to be constrained by either a Debye-correlated or an Einstein-correlated model. Thus the parameters for static and dynamic disorder can be refined directly from the experimental data,

* In this Chapter the *treatment* temperatures are referred to in °C, but the *measurement* temperatures in Kelvin for several reasons. Firstly, all other treatment temperatures in the thesis are given in °C. Secondly, the use of the absolute scale for the measurement temperature is more appropriate. Thirdly, the term 150°C implies an uncertainty of at least several degrees, while the term 423 K implies an uncertainty of less than one degree. Finally, the relationship between the treatment and measurement temperatures is of no particular interest.

instead of being determined graphically in a second stage. This reduces complexity, and improves both the consistency and error analysis of the calculations.

With relatively wide windows for the EXAFS spectrum in k-space and the FT, and up to four data sets, the number of independent data points was quite high, often greater than 100. The number of parameters refined was generally between 10 and 20 % of this limit.

The software automatically calculates the uncertainty in each parameter that is refined, and these values are reported in the Results section. The convention used to express uncertainties is that the uncertainty in the last (or sometimes last two) significant figures is given in parentheses, eg 2.57(3) is equivalent to 2.57 ± 0.03.

The software also calculates an R-factor, which gives a sum-of-squares measure of the fractional misfit between the Fourier-transformed measured spectrum and the Fourier-transformed calculated spectrum. The R-factor is defined in Equation 10-8, where N is the number of function evaluations.

$$R = \frac{\sum_{i=1}^{N}\left\{[\mathrm{Re}(\chi_{data_i} - \chi_{\mathrm{mod}\,el_i})]^2 + [\mathrm{Im}(\chi_{data_i} - \chi_{\mathrm{mod}\,el_i})]^2\right\}}{\sum_{i=1}^{N}\left\{[\mathrm{Re}(\chi_{data_i})]^2 + [\mathrm{Im}(\chi_{data_i})]^2\right\}} \qquad \textbf{Equation 10-8}$$

Some chemically reasonable assumptions were made in fitting. These are particularly important for the amorphous materials, where there was little prior knowledge of the short-range structure.

1. The first peak in the FT was attributed to the nearest-neighbour oxygen atoms and the second and third peaks in the FT were attributed to neighbouring zirconium atoms. It was assumed that the oxygen atoms beyond the nearest neighbours did not significantly affect the EXAFS spectrum, as oxygen scatters much more weakly than zirconium.
2. The effects of multiple scattering on the outer shells were neglected. Multiple scattering is most serious in high-symmetry structures, and little symmetry was expected in the amorphous samples.
3. Any nitrate groups coordinated to the zirconium atoms in the amorphous samples were neglected. Nitrogen atoms can be expected to scatter X-rays in a very similar way to oxygen atoms.

4. The value of S_0^2 was assumed to be invariant with k, essentially treating it as a scale factor. This assumption is generally valid as long as the high-k data is emphasised, as in multiplying the χ spectrum by k^3 (see Section 10.2.3).
5. Coordination-numbers, N, and positions, r, for each shell were assumed to be independent of temperature. Initially, a parameter was included in the model to allow for thermal expansion of the sample. However, it was found that this parameter did not affect the fit, and generally refined to a negligible value.

Models for each sample were refined simultaneously using all of the EXAFS spectra measured for that sample. Fitting was carried out against the Fourier-transformed spectra, over an appropriate r-range.

The first step was to fit a model to the EXAFS spectra of the crystalline reference materials. Two important pieces of information are gained. The first is the position of the shells, which can be compared to diffraction data, and are important to verify the accuracy of the modelling. The second is the value of S_0^2, which is required to determine the coordination-numbers. Values of S_0^2 determined for the reference materials were compared with values published in the literature.

Results for amorphous samples are reported for two models, the first using a single oxygen shell to model the first FT peak, and the second using two oxygen shells. A model based on tetragonal zirconia was used for the spectra of the H470 sample.

The position and number of atoms in each shell were allowed to vary independently for each 'unknown' sample. The E_0 value was allowed to vary for each spectrum, to allow for any inconstancies in calibration. A separate E_0 value was defined for the oxygen shells, to allow for charge distribution effects that are neglected in the standard theory.[18] The difference between the two E_0 values was constrained to be the same for all spectra from the one sample.

Where several spectra of the one sample (measured at a range of temperatures) have been modelled together, the disorder has been modelled in three stages:

1. The initial approach was to assign a separate σ^2 value to each shell for each spectrum, with no further cumulants, and allow them to refine independently. This approach resulted in a

large number of parameters for each model, and an increase in the uncertainties. This approach is primarily to check that the σ^2 values increase with temperature.

2. The σ^2 values are then constrained with a Debye or Einstein-correlated model, so that for each path the values refined are the static disorder, σ^2_{stat}, and the Debye or Einstein temperature, θ_E/θ_D. This approach is useful even when as few as two spectra are modelled, because of the restraints placed on the refined values of σ^2. An Einstein model was used for all nearest-neighbour oxygen shells, and a Debye model for all further shells. *All values given here are from models in which the σ^2 value for disorder is constrained by either a Einstein- or Debye-correlated model.* Where σ^2 values were not constrained, they were refined to values usually very close to that of the constrained models.
3. In the third stage, a third and fourth cumulant for the first two shells was introduced. When the refined values of a cumulant were less than the calculated uncertainty, that cumulant was deemed negligible and removed from the model.

When two oxygen shells are used to model the first FT peak of amorphous samples, it has been assumed that the values for σ^2 are equal. Although this approximation is not necessarily accurate, it is required to restrain the correlation between σ^2 and N. If σ^2 values of two overlapping peaks are allowed to vary independently, the N and σ^2 values were found to refine to physically unreasonable values. For the model based on t-ZrO_2 separate σ^2 values could be assigned to the oxygen shells. This is because restrictions can be placed on the coordination-numbers for each shell, which are known to be equal and close to 4.

10.3.3 Comparison of EXAFS spectra

Selected weighted EXAFS spectra, $\chi(k)\cdot k^3$, and the corresponding Fourier-transformed spectra (FT), are shown in Figure 10-3 and Figure 10-4, respectively. Most spectra in these Figures were measured at 10 K, but the H470 spectrum shown was measured at 80 K, which is sufficient for the purposes of comparison. The spectrum for the $BaZrO_3$ sample was measured at 290 K.

The EXAFS spectra and FTs for the ZN1.0 gel and the H150 sample are very similar. The first peak in the FT is attributed to the oxygen atoms immediately neighbouring the central zirconium atom. The next two peaks are attributed to two shells of zirconium atoms. There are no significant feature in the FT beyond 5 Å.

The EXAFS spectra and FTs for the H300 and H400 samples are also very similar. The EXAFS spectra contain much weaker oscillations, which is reflected in the FT as a much weaker second peak. The structural information in the FT ends at 3.5 Å.

The intensity of the EXAFS oscillations and the FT peaks for the crystalline samples, m-ZrO_2, $BaZrO_3$ and H470, are stronger than for those for the amorphous samples. This is due to the high short-range order, and the larger number of near-neighbours to the absorber atom. Structural information is available in the FT to at least 9 Å. The second FT peak of the H470 is particularly sharp and intense. This is attributed to the highly ordered nature of the t-ZrO_2 phase, in which cations are arranged in a nearly face-centred cubic structure.

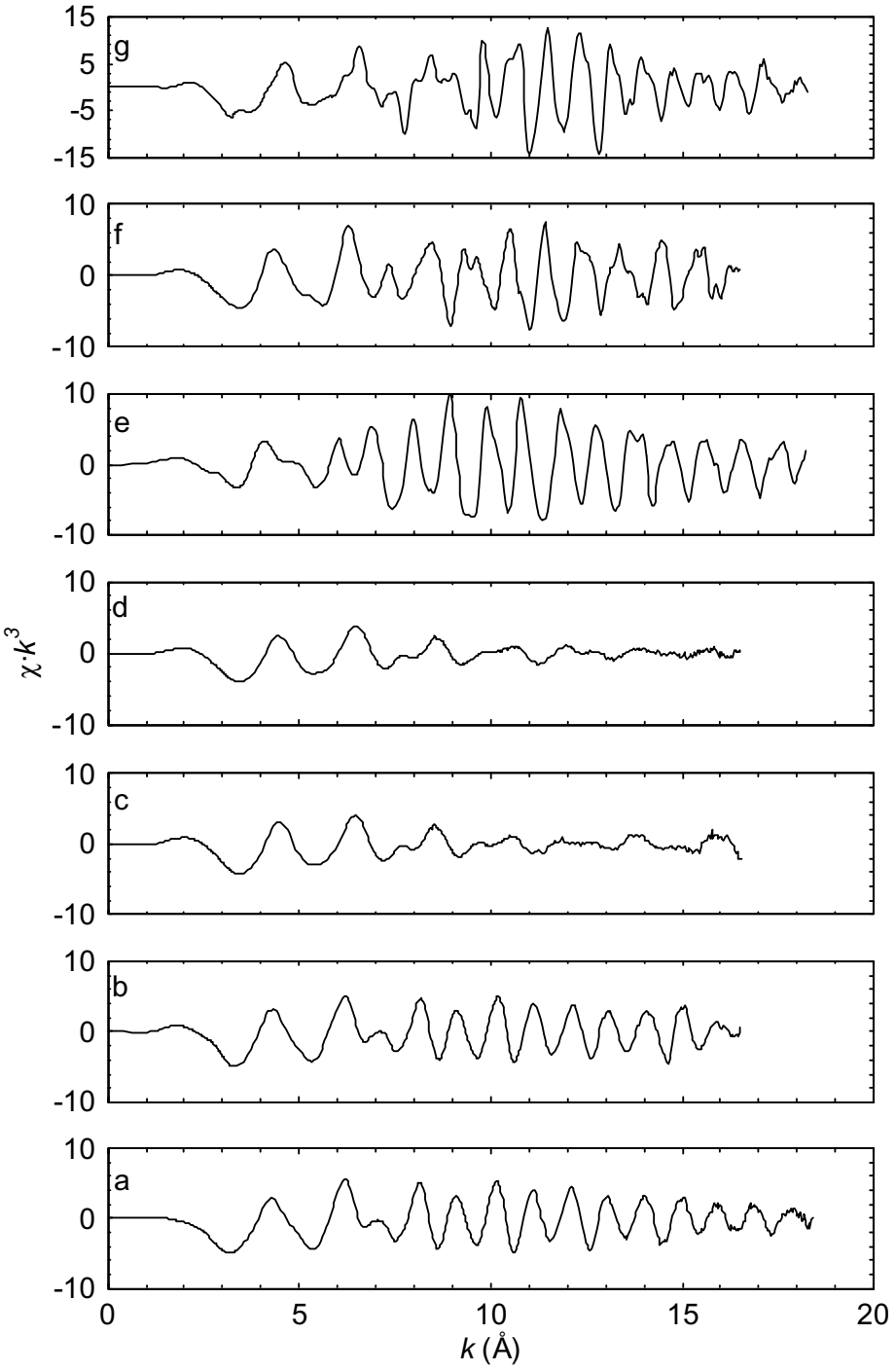

Figure 10-3: Weighted EXAFS spectra of a) ZN1.0 gel, b) H150, c) H300, d) H400, e) H470, f) m-ZrO_2 and g) $BaZrO_3$.

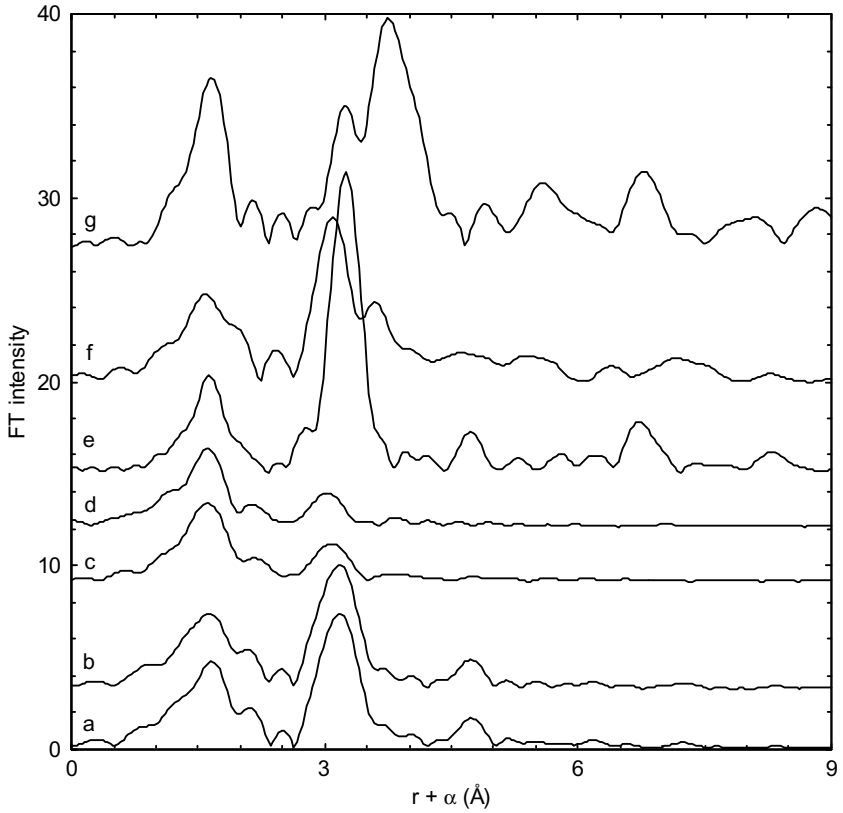

Figure 10-4: Fourier-transforms of spectra of a) ZN1.0 gel, b) H150, c) H300, d) H400, e) H470, f) m-ZrO_2 and g) $BaZrO_3$.

10.3.4 Reference materials

Monoclinic zirconia

Monoclinic zirconia (m-ZrO_2) was used as a reference, as it is a phase of zirconia that is readily available in a pure and highly-crystalline form. One advantage of monoclinic zirconia is that the contribution of multiple scattering to the EXAFS spectrum is quite small.[1]

Unfortunately, the short-range structure around each zirconium atom is complex, and modelling the EXAFS spectrum is difficult. Each zirconium atom in the m-ZrO_2 structure has zirconium and oxygen neighbours at a range of distances, as given in Table 10-4. This range of bond-lengths makes it problematic to treat each of these groups as a single 'shell', but there are too many variables to model each scatterer-absorber pair individually.[1] The average inter-atomic distance for the group of 7 oxygen nearest-neighbours is 2.16 Å, for the first group of 7 zirconium neighbours is 3.45 Å, and the second group of 4 zirconium neighbours is 3.98 Å.

Table 10-4

O neighbours		Zr neighbours	
d	*N*	*d*	*N*
2.053	1	3.334	1
2.056	1	3.433	2
2.153	1	3.460	2
2.162	1	3.469	1
2.183	1	3.580	1
2.224	1	3.929	2
2.280	1	4.030	2

The first task was to use the measured spectrum to determine a value of S_0^2. To minimise the effect of multiple scattering, only the first FT peak was modelled. Several models were used, as discussed below, none of which fully overcome the problems cause by the complexity of the structure. The refined values of parameters for two of these models are given in Table 10-5, and compared with those published by Li, Chen and Penner-Hahn.[1,2]

Table 10-5: Modelled parameters for the first FT peak of m-ZrO_2.

Parameter	Model 1	Model 2	Li *et al.*[1,2]
	7 O shells	Single O shell	Single O shell
S_0^2	0.9(1)	1.1(2)	0.85-0.9
r (Å)		2.11(1)	2.16*
Δr (Å)	–0.04(1)		
σ^2_{stat} Å$^2\times10^{-3}$	–0.9(2)	8(2)	7.0
θ_E	550(150)	590(150)	590
R-factor	7.2 %	8.0 %	5.8 %

*Fixed

One approach was to model each of the seven nearest oxygen neighbours that contribute to the first FT peak. To keep the number of parameters to a minimum, each shell was assumed to have the *same* σ^2_{stat} and Einstein temperature, and a single 'shift' parameter, Δr, was defined to describe the shift of the shells from the Zr–O distance known from diffraction studies. These simplifications, particularly for the disorder parameters, are not likely to be realistic, and it can be seen that the resulting σ^2_{stat} value is very low.

Another approach is to model the first FT peak with only one or two shells. The distribution of Zr–O distances in monoclinic zirconia falls naturally into two groups, and a model with two oxygen shells was tried, but this gave very poor results. A model with only a single oxygen shell, as used by Li, Chen and Penner-Hahn,[1] gave a substantially better fit. The modelled value of r is within the range of the known Zr–O bond lengths, but is 0.05 Å below the average. This is consistent with the Δr value for the seven-shell model. It is quite possible that at least some of this shift is due to variations in the σ^2 of the individual shells, so that the oxygen atoms that are closer to the zirconium atom may contribute more strongly to the EXAFS spectrum, thus reducing the effective average Zr–O distance. Li, Chen and Penner-Hahn *set* this distance to be 2.16 Å, with no refinement, treating the monoclinic zirconia as a standard. There are no other detailed EXAFS studies of m-ZrO_2 in the literature, so this question awaits more detailed study.

We must be cautious in interpreting the resulting value of S_0^2. If a range of oxygen positions are modelled by a single shell, the model will compensate for the extra width of the FT peak by increasing the σ^2, which also decreases the amplitude of the predicted oscillation. If the value of N is fixed, S_0^2 will then be forced to a higher value.

Having determined the value of S_0^2 to be approximately 0.9, as discussed in Section 10.3.5, the entire monoclinic zirconia spectrum was modelled with three shells, containing seven oxygen atoms, seven zirconium atoms, and four zirconium atoms, respectively. The modelled parameters are given in Table 10-6, the EXAFS spectrum compared to the model in Figure 10-5, and the Fourier-transformed spectrum compared with the model in Figure 10-6. The *R*-factor was 4.2 %.

Table 10-6: Modelled parameters for m-ZrO_2.

	O	Zr 1	Zr 2
Modelled values:			
r (Å)	2.112(10)	3.454(4)	3.997(7)
N, fixed	7	7	4
σ^2_{stat} (Å^2×10^{-3})	6.5(1.6)	4.1(4)	4.1(1.1)
θ^* (K)	560(170)	430(30)	360(60)
Reported by Li *et al*.[2]			
σ^2_{stat} (Å^2×10^{-3})	7.0	2.1	
θ^* (K)	590	320	

* Einstein model used for Zr–O shells, and Debye model used for Zr–Zr shells.

As discussed above, the modelled Zr–O distance is substantially less than that expected from the 'average' Zr–O distance. However, the modelled Zr–Zr distances are very close to those expected from Table 10-4. The disorder parameters (σ^2_{stat} and θ) for the oxygen shell are quite close to those reported by Li, Chen and Penner-Hahn, but are rather different for the zirconium shell.

Since the fitting of a realistic model to the data was so problematic, no attempt was made to model the third or fourth cumulants. There is no doubt that the fit would have improved considerably, but it would have yielded no useful structural information.

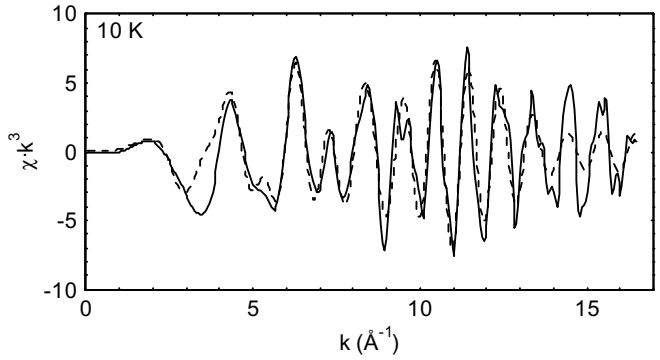

Figure 10-5: Weighted EXAFS spectrum of the m-ZrO_2 reference, measured at 10 K (solid line), compared with the modelled spectrum from the double oxygen shell model (broken line).

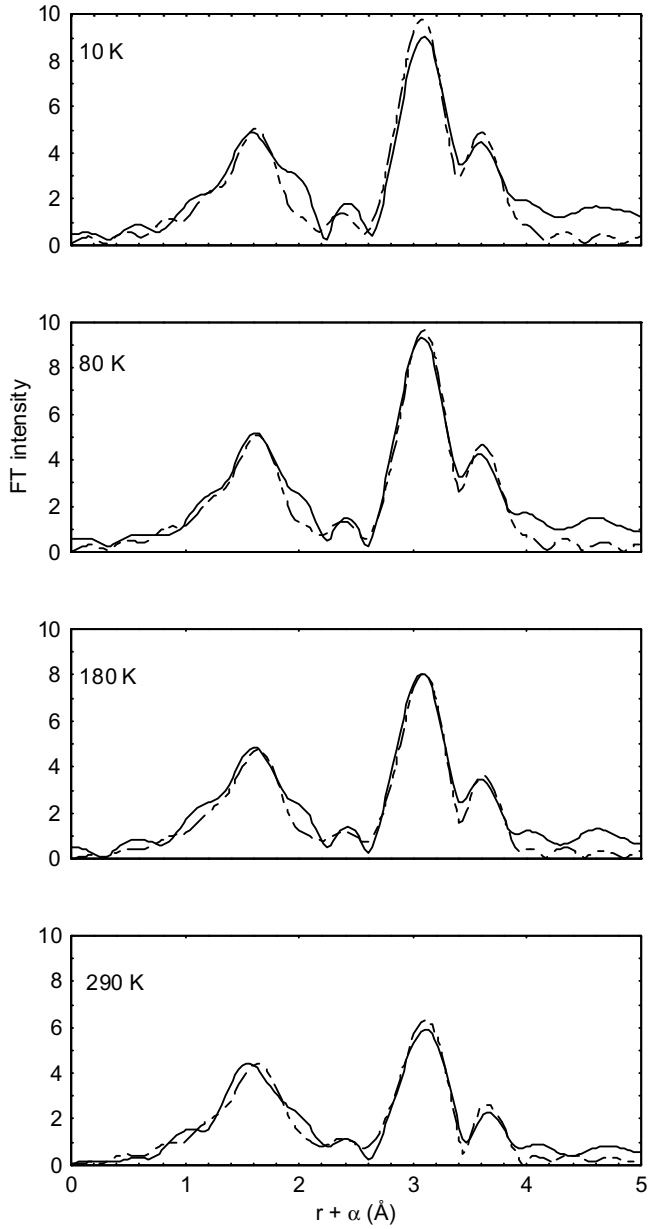

Figure 10-6: Fourier-transformed spectra of the m-ZrO_2 reference, measured at 10, 80, 180 and 290 K (solid line), compared with the modelled spectrum (broken line).

$BaZrO_3$

Only one spectrum was measured of $BaZrO_3$, at 290 K.

In contrast to monoclinic zirconia, the structure of $BaZrO_3$ is very simple, with a simple cubic structure.[18,22] Unfortunately, there are very strong multiple scattering paths at distances greater than 3.6 Å, that overlap with all single-scattering paths beyond the first oxygen neighbour.[22] As the σ^2 values associated with multiple-scattering paths could not be reliably modelled in this

analysis, *amplitude* information, such as S_0^2, was only able to be derived from the first FT peak. However, *phase* information, such as interatomic distances, could be derived from all FT peaks.

The first model used fitted the first FT peak with a single oxygen shell, in order to determine values of S_0^2, σ^2 and r. The value of S_0^2 calculated from the first oxygen shell was 0.98(17). This correlated well with the value of 0.95(5) reported by Haskel *et al.*.[18] The σ^2 value for the first shell was 0.0041(10), which was similar to the value of 0.004 reported by Landron, Duoy and Bazin.[23] The Zr–O distance was approx 0.02 Å less than the value determined from powder diffraction.[24]

The second model fitted the FT region up to 4.5 Å with all single- and multiple-scattering paths, and a single expansion coefficient calculated for the interatomic distances. This approach is possible because of the highly symmetric cubic structure. The r values calculated were 0.3 % less than the values known from diffraction, or approximately 0.013 Å for the zirconium shell.

10.3.5 Determination of S_0^2

As discussed in Section 10.2.3, it is necessary to determine the value of S_0^2 in order to determine coordination-numbers. Table 10-7 lists S_0^2 values for the zirconium atom in ZrO_2 or $BaZrO_3$ that have been determined from either the reference materials used in these experiments, alongside those that have been reported in the literature. After consideration of these results, an S_0^2 value of 0.9 was chosen for all subsequent modelling. Note that since any error in the S_0^2 value is transferred into the N value, an additional error of up to ± 10 % needs to be added to the uncertainties of the reported N values.

Table 10-7: Values of S_0^2 for Zr published in the literature or determined from reference materials.

Source	Value
Study of $BaZrO_3$ structure by Haskel *et al.*[18]	0.95(5)
Study of ZrO_2 polymorphs by Li *et al.*[1]	0.85 - 0.9
Reference m-ZrO_2, single oxygen shell model	1.1(2)
Reference m-ZrO_2, 13 oxygen- shell model	0.9(1)
Reference $BaZrO_3$, single oxygen shell model	0.98(17)

10.3.6 Amorphous samples

A 'best fit' model was obtained for each amorphous sample, using models with both single and double oxygen shells, and *without* third and fourth cumulants. The modelled interatomic parameters and coordination-numbers are listed in Table 10-8, the σ^2_{stat}, Debye/Einstein temperatures and σ^2 values at 10 K are listed in Table 10-9, and the *R*-factors for each fit are listed in Table 10-10. The measured data is graphically compared with the double oxygen shell models in both *k* space and *r* space, from Figure 10-7 to Figure 10-14 (for convenience the Figures have been placed at the end of this Section).

Table 10-8: Modelled interatomic distances and N values for amorphous samples.

	O		O1		O2		Zr1		Zr2	
	single O shell model		double O shell model							
	r (Å)	N	*r* (Å)	N	*r* (Å)	N	*r* (Å)	N	*r* (Å)	N
Gel	2.137(8)	9.7(9)	2.106(9)	7.6(6)	2.579(14)	4.2(6)	3.539(3)	3.8(2)	4.995(9)	1.9(8)
H150	2.139(7)	10.2(8)	2.092(6)	6.6(4)	2.583(9)	4.9(4)	3.535(2)	3.6(2)	4.984(7)	1.4(5)
H300	2.084(6)	6.1(5)	2.070(6)	5.1(4)	2.547(14)	1.6(2)	3.412(12)	4.1(8)	-	-
H400	2.070(5)	5.4(3)	2.067(5)	4.8(3)	2.563(19)	0.9(2)	3.371(11)	2.9(5)	-	-

Table 10-9: Modelled disorder parameters for amorphous samples.

	O			Zr1			Zr2		
	double O shell model								
	σ^2_{stat} ($Å^2\times10^{-3}$)	θ_E (K)	σ^2_{10K} ($Å^2\times10^{-3}$)	σ^2_{stat} ($Å^2\times10^{-3}$)	θ_D (K)	σ^2_{10K} ($Å^2\times10^{-3}$)	σ^2_{stat} ($Å^2\times10^{-3}$)	θ_D (K)	σ^2_{10K} ($Å^2\times10^{-3}$)
Gel	8.5(1.3)	700(200)	11(2)	1.9(3)	470(20)	3.6(3)	3(2)	380(100)	5(2)
H150	8.3(1.0)	700(200)	11(1)	2.1(2)	470(20)	3.8(2)	1(2)	330(60)	4(2)
H300	†	†	8.1(6)	11.2(1.5)	485(100)	13(2)	-	-	-
H400	4.5(7)	575(70)	7.6(7)	9.8(1.3)	500(120)	11.4(1.5)	-	-	-

† Values not determined.

Table 10-10: *R*-factors of models for amorphous samples

Sample	single O shell model	double O shell model
Gel	2.8 %	1.7 %
H150	3.2 %	1.6 %
H300	3.8 %	2.4 %
H400	2.7 %	2.2 %

The spectra were fitted reasonably well by a single oxygen shell for the first FT peak, and a single zirconium shell for the second peak. For the gel and H150 samples, the third FT peak was modelled by a single zirconium shell. The addition of an additional oxygen shell to the model significantly improved the fit, particularly for the gel and H150 samples. The second oxygen shell did not make such a great difference to the H300 and H400 samples, but it was retained to maintain consistency with the models for other samples. The model with two oxygen shells was chosen as the best representation of the structure for two reasons. Firstly, it reduced the fit error substantially, with resulting *R*-factors below 2.5 %. Secondly, the addition of the second oxygen shell reduced the coordination-number for the first oxygen shell to a chemically reasonable value (< 8).

Third and fourth cumulants were added to the models to account for the non-Gaussian distribution of atoms in each shell around their 'average' position at *r*. Each of these parameters generally refined to a value close to zero, and less than their calculated uncertainty, and so were deemed negligible and removed from the fit. A non-negligible C_3 value of $-1.0(4) \times 10^{-3}$ Å^3 was refined for the zirconium shell of the H400 sample, which changed the Zr–Zr distance to 3.26(5) Å, but otherwise made no significant difference to any other parameters. This result is not included in the Tables below to maintain consistency between models.

When comparing the measured and modelled $\chi(k)$ plots in Figure 10-7 and Figure 10-8, it is worthwhile to note that the FT window was between 4 and 13 Å^{-1}, and fitting took place in this region. However, the model follows the data closely to much higher *k* values, as high as 18 Å^{-1}. This indicates that the model used is reliable.

The ZN1.0 gel

A structure has been proposed from the modelled parameters for the unheated gel, which is fully described and discussed in Section 4.3.4. Only the disorder parameters will be discussed here.

The σ^2 values for the oxygen shells vary very little with temperature, as shown in Figure 10-17 in Section 10.3.8. This leads to a comparatively high Einstein temperature of 700 K, with a large uncertainty. The conclusion drawn is that the static disorder in the structure dominates the total disorder for the oxygen shells, thus the *N* and *r* values calculated can only be approximate. The σ^2_{stat} value of 0.0085 Å^2 indicates that the *average* structural variation of the oxygen shell position is ± 0.05 Å. This variation could be caused by a distribution of bond

lengths, several discrete Zr–O bond lengths, or a mixture of these two cases. However, the details of the Zr–O bonding are unlikely to be elucidated from this data without structural data from another source, as the addition of further oxygen shells to the model will result in too many independent parameters.

The σ^2 values for the zirconium shells were much lower than those for the oxygen shell. The σ^2_{stat} values were very similar to the corresponding values for the crystalline phases, indicating that there was very little structural disorder in the overall Zr–Zr structure.

Heat-treated samples

A simple comparison of the Fourier-transformed spectra in Figure 10-4 can reveal much about the decomposition and crystallisation that occurs during heating of the gel. It is evident that there is little change in structure with heating to 150°C, and that between 150 and 300°C there is a substantial decrease in short-range order. Changes in interatomic distances are also apparent. These conclusions are fully supported by the parameters modelled for each spectrum.

The changes in the modelled parameters with heat-treatment are fully discussed in Section 5.3.2.

Comparison with other EXAFS studies of amorphous zirconia precursors

The results from two other EXAFS studies of amorphous zirconia precursors are given in Table 10-11 for comparison. Note that these measurements were made at ambient temperature only.

Table 10-11: Results from previous EXAFS studies.

	Gel hydrolysed from alkoxide Antonioli *et al*.[4]			Precipitate from Zr sulfate solution Turrillas *et al*.[5]		
	r (Å)	N	σ^2 (Å$^2\times10^{-3}$)	*r* (Å)	N	σ^2 (Å$^2\times10^{-3}$)
O	2.04	2.0	5	2.08	2.0(5)	5
O	2.18	6.0	10	2.16	5.0(5)	11
Zr	3.37	4.1	15	3.27	1.7(1.0)	12
Zr				3.41	2.0(1.0)	12

Comparing the main Zr–O and Zr–Zr distances, it is evident that the structures reported by these studies are quite similar to each other. However, there is little resemblance between the

parameters reported for the oxygen shells and those refined for any of the samples in this study.

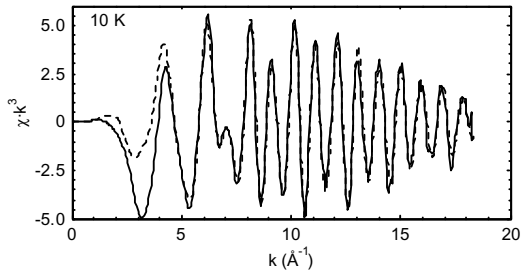

Figure 10-7: Weighted EXAFS spectrum of the ZN1.0 gel, measured at 10 K (solid line), compared with the modelled spectrum, with double oxygen shell (broken line).

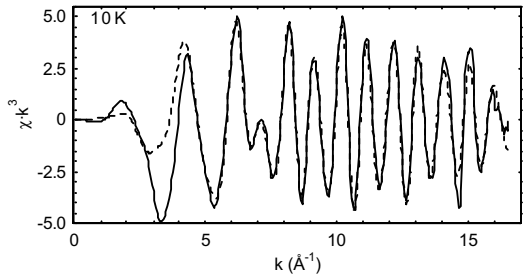

Figure 10-8: Weighted EXAFS spectrum of H150, measured at 10 K (solid line), compared with the modelled spectrum, with double oxygen shell (broken line).

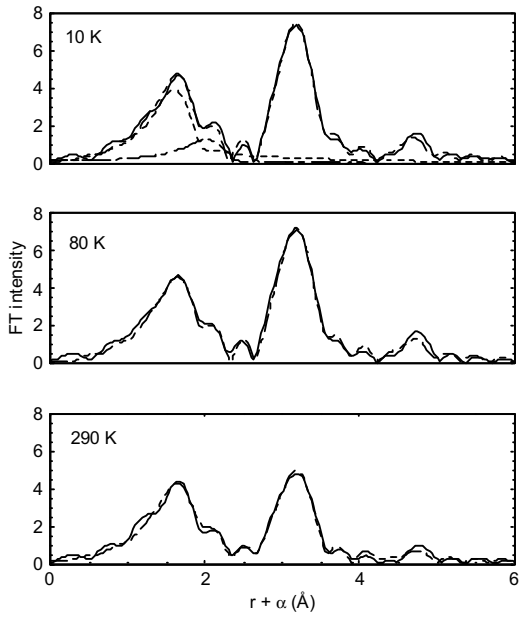

Figure 10-9: Fourier-transformed spectra of the ZN1.0 gel, measured at 10, 80 and 290 K (solid line), compared with the modelled spectrum (broken line). The 10 K plot includes the modelled profiles for the individual oxygen shells.

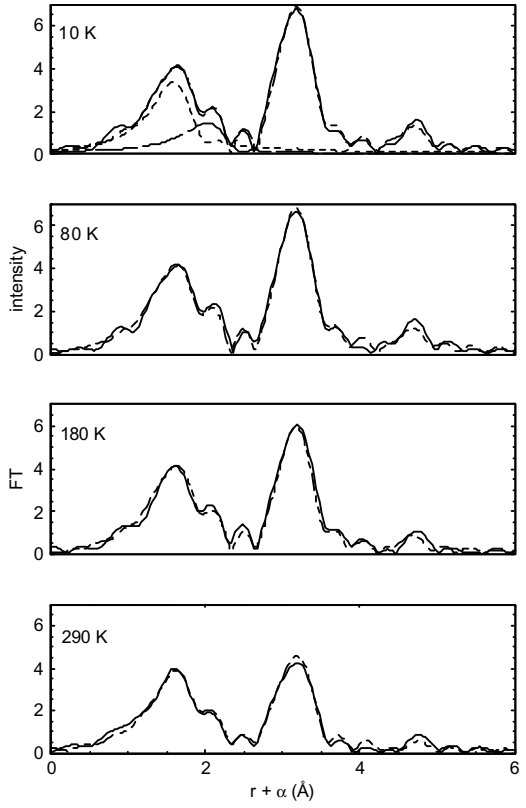

Figure 10-10: Fourier-transformed spectra of H150, measured at 10, 80, 180 and 290 K (solid line), compared with the modelled spectrum (broken line). The 10 K plot includes the modelled profiles for the individual oxygen shells.

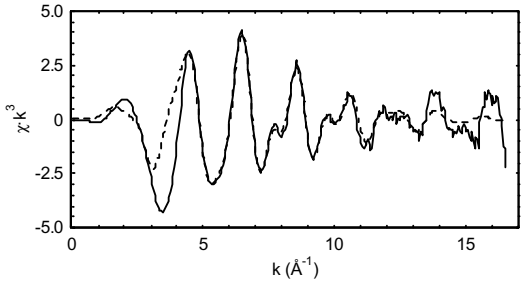

Figure 10-11: Weighted EXAFS spectrum of H300, measured at 10 K (solid line), compared with the modelled spectrum, with double oxygen shell (broken line).

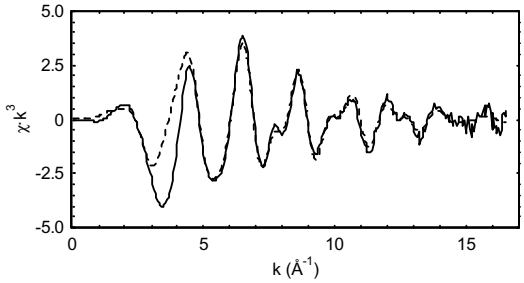

Figure 10-12: Weighted EXAFS spectrum of H400, measured at 10 K (solid line), compared with the modelled spectrum, with double oxygen shell (broken line).

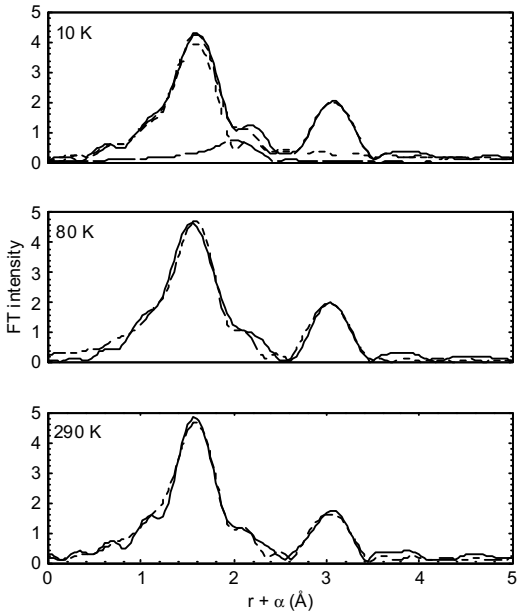

Figure 10-13: Fourier-transformed spectra of H300, measured at 10, 80 and 290 K (solid line), compared with the modelled spectrum (broken line). The 10 K plot includes the modelled profiles for the individual oxygen shells.

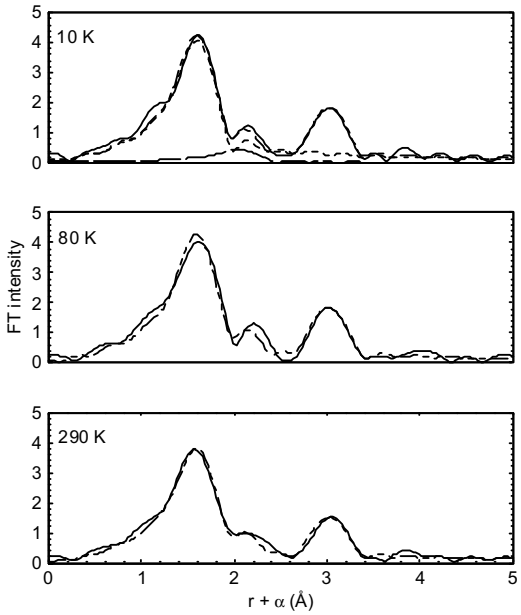

Figure 10-14: Fourier-transformed spectra of H400, measured at 10, 80 and 290 K (solid line), compared with the modelled spectrum (broken line). The 10 K plot includes the modelled profiles for the individual oxygen shells.

10.3.7 The crystalline sample

Unlike the amorphous samples, the H470 sample has an expected structure, that of crystalline tetragonal zirconia. The short-range structure of the tetragonal zirconia phase is quite simple.[1] Each zirconium atom is surrounded by two distinct shells of 4 oxygen atoms each, O_I and O_{II}, at distances of approximately 2.08 and 2.36 Å respectively. There are two closely-spaced shells of zirconium, which can be treated as a single shell of 12 atoms at 3.60 Å.

In the tetragonal structure, O_I and O_{II} are structurally equivalent. That is, an oxygen atom that is O_I to one neighbouring Zr atom will be O_{II} to another. This is why the coordination-numbers for the two oxygen shells should always be equal. However, it cannot be expected that the σ^2 value for the two shells will be equal.[2] The EXAFS σ^2 is the mean square *relative* displacement of the absorber atom and the backscatterer atom, and is dependent on both atoms of the pair. Depending on the predominant direction of both static distortion and dynamic vibration, the σ^2 values for the two pairs could well be different. In *diffraction* there is also a value σ^2, which represents the mean square displacement of an atom at a particular site *with respect to the entire lattice*. The value of σ^2 *for diffraction* will be the same for both O_I and O_{II} sites. This distinction has not been recognised by some diffraction practitioners.[25]

Only two spectra were available for the H470 sample, measured at 80 and 290 K. The model used for these spectra was based on the structure of tetragonal zirconia, with two oxygen shells to model the first peak, and a zirconium shell to model the second peak. The refined parameters for this model are tabulated in Table 10-12, together with the modelled values reported by Li, Chen and Penner-Hahn from a EXAFS study of 3 mol % yttria-stabilised tetragonal zirconia,[2] and the values reported by Igawa *et al*. from a neutron-diffraction study of pure, metastable tetragonal zirconia.[26] The model is compared with the weighted EXAFS spectrum in Figure 10-15, and the Fourier-transformed data in Figure 10-16. The *R*-factor for this fit was 1.2 %, which is exceptionally low.

Table 10-12: Comparison of modelled parameters for H470 with published values for t-ZrO_2.

	O_I	O_{II}	Zr
Modelled values:			
r (Å)	2.085(4)	2.317(10)	3.606(2)
N	3.5(4)	3.5(4)	8.1(4)
σ^2_{stat} ($Å^2 \times 10^{-3}$)	– 0.2(0.7)	3.5(4)	2.22(16)
θ^* (K)	490(40)	560(400)	375(8)
$\sigma^2_{10\,K}$ ($Å^2 \times 10^{-3}$)	3.3(1.0)	10(5)	4.6(1)
Reported by Li et al.[2]			
r (Å)	2.10	2.33	3.62
N	4†	4†	12†
σ^2_{stat} ($Å^2 \times 10^{-3}$)	0.5	4.9	2.3
θ^* (K)	560	383	252
Reported by Igawa et al.[26]			
r (Å)	2.082	2.359	3.612‡
N	4	4	12

* Einstein model used for Zr–O shells, and Debye model used for Zr–Zr shells.

† "Fixed to a reasonable integer" [1]

‡ Weighted average of two closely-spaced Zr–Zr distances.

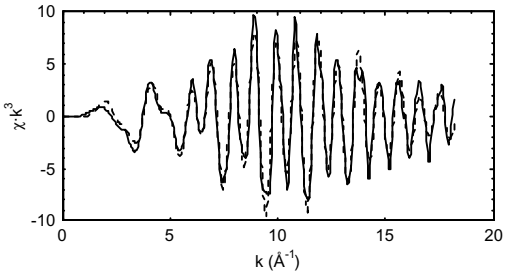

Figure 10-15: Weighted EXAFS spectrum of C470, measured at 80 K (solid line), compared with the modelled spectrum, with double oxygen shell (broken line).

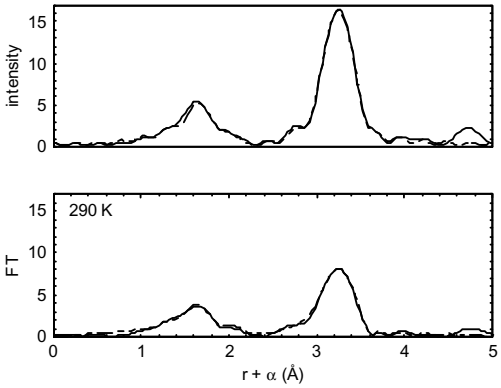

Figure 10-16: Fourier-transformed spectra of the H470 sample, measured at 80 and 290 K (solid line), compared with the modelled spectrum (broken line).

It can be seen that the modelled value of the Zr–O_I distance is very close to that expected, while the Zr–O_{II} distance is somewhat shorter. The oxygen coordination-numbers are a little below the theoretical value of 4. The distance modelled for the first Zr shell is also very close to the weighted-average position for the nearest zirconium neighbour, but the coordination-number is *two thirds* of the expected value.

A possible explanation for the differences in the coordination numbers is the presence of an amorphous phase, as suggested in Section 10.3.2. This phase would contain zirconium atoms that contribute to the total absorbance, but with fewer back-scattering neighbours to contribute to the EXAFS spectrum. Let us assume the amorphous phase to have a structure equivalent to that found for the H400 sample. The central zirconium atom would then have approximately five oxygen atoms coordinated around it at ~2.07 Å. These oxygen atoms would contribute towards the EXAFS spectrum significantly, keeping the *average* coordination-number for oxygen relatively high, but altering the average Zr–O distances.

In contrast, the zirconium atoms in the amorphous phase will have only three neighbouring zirconium atoms, at a distance of 3.37 Å. This Zr–Zr distance is much shorter than that for the crystalline material, so the EXAFS oscillations from these neighbours will not contribute much to the EXAFS oscillations from the 12 zirconium nearest-neighbours in the crystalline material. In the total spectrum, this will result in a measured Zr–Zr distance similar to that expected for the crystalline phase, but a considerably reduced coordination-number.

The main consequence of the presence of the amorphous fraction is that no reliable structural information can be derived for the oxygen shells.* This is unfortunate, in view of the continuing debate on the role of vacancies in the stabilisation of pure tetragonal zirconia at low temperatures, discussed in Section 2.4.2.2.

Since the amorphous phase does not contribute greatly to the Zr shell, some further information on disorder can be obtained. The Debye model values for the Zr shell are compared with those published for yttria-stabilised tetragonal phase, both large-grained[2] and *nanocrystalline*,[3] in Table 10-13. The refined σ^2_{stat} value closely matches that reported by Li, Chen and Penner-Hahn,[2] but the Debye temperature is considerably higher. Yuren *et al.* showed that the Debye temperature for the Zr–Zr pair in nanocrystalline zirconia increases with decreasing crystal size.[3] Since the H470 sample had a diffracting crystal size of approximately 30 nm, the relatively high Debye temperature is consistent with previously reported values.

---

* In principle the amorphous fraction could be simulated in the modelling procedure, but in practice this introduces too many variables, unless further assumptions are made about the structure of either phase. One could assume that $N_{Zr} = 12$, but this might not be accurate considering the probable multiple-scattering contribution to this shell.

Table 10-13: Comparison of disorder parameters modelled for the Zr shell of the H470 sample, with published values for t-$Zr(Y)O_2$.

	H470	Yuren *et al.*[3]		Li *et al.*[2]
diffracting crystal size (nm)	30	5	11	large*
σ^2_{stat} ($\times 10^3$ Å^2)	2.22(16)	*n.a.*	*n.a.*	2.3
θ_D (K)	375(8)	502	404	252

*material calcined at 1300°C

Considering the composite nature of this sample, it is quite likely that an even better fit could be obtained by adding third and fourth cumulants to the model. However, this is unlikely to yield any more useful information.

10.3.8 Comparison of unconstrained σ^2 values with models

Since a Debye- or Einstein-correlated model has been used to constrain the σ^2 values, it is important to check that this assumption is valid. Figure 10-17 shows plots of σ^2 that have been refined *without* any imposed model, and compare these to the Debye or Einstein model that has been fitted for each shell.

Very good correlation is achieved, and the Debye and Einstein models can be used with confidence. Note that the error bars for the unconstrained σ^2 values are considerably larger than the deviation from the modelled curve. This uncertainty is derived from the uncertainty in other correlated parameters, such as coordination-numbers and shell positions, and is reflected in the reported uncertainty for σ^2_{stat}, θ_D and θ_E values. The uncertainty in the total σ^2 values is generally quite large in comparison to the change in σ^2 with temperature, making the uncertainty for the vibrational components, θ_D and θ_E, very large.

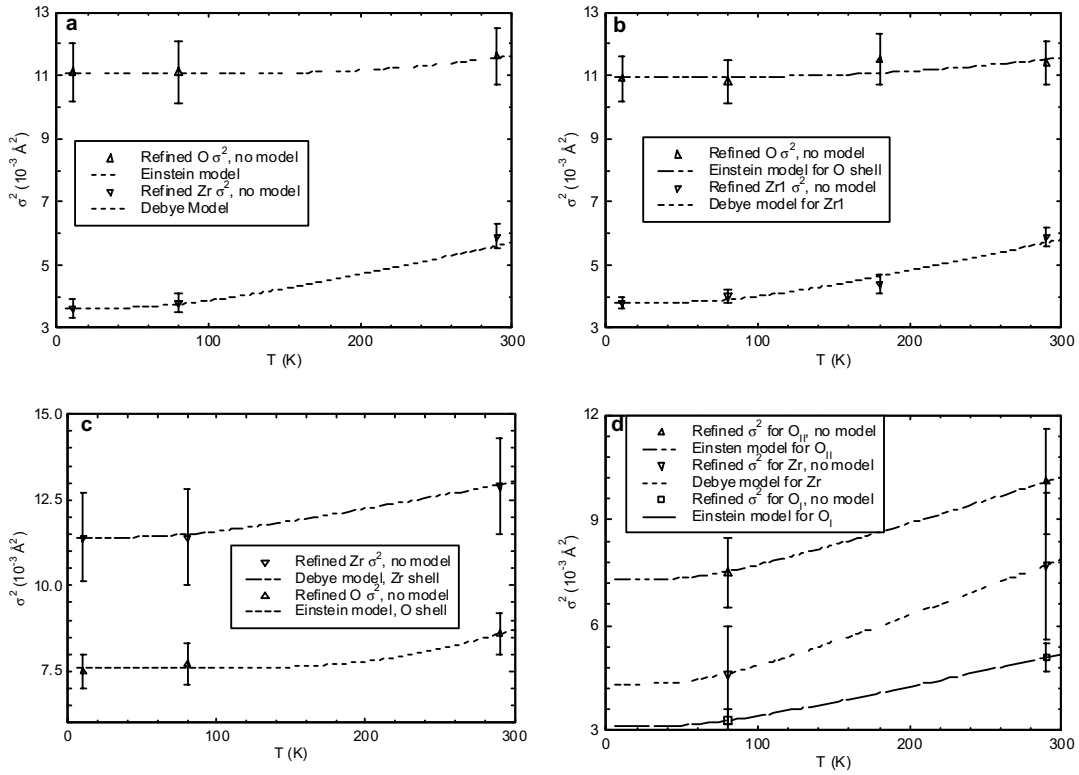

Figure 10-17: Comparison of unconstrained σ^2 values for oxygen and zirconium shells with the fitted Debye and Einstein models, for a) the ZN1.0 gel, b) H150, c) H400 and d) H470.

10.3.9 Vibrational frequencies

Vibrational frequencies, ? , have been calculated from the Einstein temperatures for the oxygen shells. Table 10-14 compares these values with the measured Raman frequencies of the amorphous samples. The Raman spectra of the amorphous samples have two main broad peaks below 700 cm^{-1}. In the ZN1.0 gel these peaks are relatively sharp, but they broaden and shift as the material decomposes, and are very broad in the H300 and H400 samples. Further details on these Raman spectra is provided in Section 5.3.1.

Table 10-14: Vibrational frequencies

Sample	θ_E (K)	? (cm^{-1})	Measured Raman frequencies (cm^{-1})
t-ZrO_2 O_I*	490(50)	340(30)	
m-ZrO_2	520(160)	360(110)	
Gel	700(200)	490(140)	545, 375
H150	700(200)	490(140)	550, 375
H400	575(70)	400(50)	~415, ~530

*Results for O_{II} had a very high uncertainty and are not included in the table.

The Raman spectra of the crystalline phases contain many peaks, and it was not anticipated that the simple vibrational and structural models used here would assist in assignment.

It is clear that the Zr–O vibrational frequencies predicted from the Einstein model are consistent with the frequencies at which Raman modes are observed. In particular, the Einstein temperature from the H400 sample had a relatively low uncertainty, although the material itself is generally more disordered than the unheated gel. The ~ 415 cm^{-1} peak in the Raman spectrum can then be assigned to the stretching of the Zr–O–Zr bridge. The very broad Raman peak is consistent with the large contribution of static disorder to σ^2.

The Einstein temperatures from the gel and H150 samples have a very large uncertainty, which prevents any assignment being made for the spectrum peaks. This uncertainty is caused by the relatively small change in σ^2 with temperature, the high degree of static disorder, and the practical requirement to link the σ^2 values of the two modelled oxygen shells.

10.3.10 Conclusions

The EXAFS study described in Section 10.3 can be summarised by the following conclusions:

- Fitting models to the EXAFS spectra of crystalline standards provided interatomic distances that were accurate to within 0.01 Å, and a reasonably reliable value of S_0^2 that was consistent with previously reported values.
- The short-range structure around the zirconium atom for a range of amorphous samples has been determined, in terms of interatomic distances, coordination-numbers and disorder parameters.
- The variation/disorder in interatomic distances was largely consistent with a 'Gaussian distribution', with third and fourth cumulants refining to negligible values.
- The Zr–O Einstein temperatures calculated for the amorphous samples were consistent with the observed Raman frequencies. The 415 cm^{-1} vibration observed in the spectrum samples heat-treated at 400°C was assigned to the stretching of the Zr-O–Zr bridge.

10.4 Study 2: Energy-dispersive EXAFS

The characterisation of materials after heating and cooling can provide only limited information on the processes that occur during heating. For this reason it is often useful to use time-resolved techniques to characterise the structural changes *in-situ*. This section describes the use of a time-resolved energy-dispersive EXAFS technique to characterise the decomposition and crystallisation of the standard gel during heating.

10.4.1 Energy-dispersive EXAFS

The length of time required to collect an absorption spectrum of sufficient quality and energy range to produce a useful EXAFS spectrum has prevented the development of time-resolved EXAFS techniques until quite recently. The main advance allowing time-resolved studies has been a large increase in X-ray intensity available from modern synchrotrons.

Several techniques have been developed to take advantage of this increased intensity. The most common adapts the conventional step-scanning method, in a technique known as *Quick-EXAFS*. The monochromator crystal is rapidly moved so that X-rays of each wavelength of interest are passed through the sample consecutively within a short period.

The technique used in this study, *energy-dispersive EXAFS* (ED-EXAFS), has been developed more recently, and uses a quite different approach. A monochromator crystal is bent slightly to become a *polychromator*, which produces a focussed, energy-dispersed X-ray beam, containing a (nominally even) distribution of a set range of energies over the width of the beam. The sample is placed at the focal point of the beam, and the transmitted beam is measured by CCD camera (See Figure 10-18). The X-rays detected at one end of the camera are at the low end of the energy range, while those detected at the other end of the camera are at the high end. In principle this allows for very rapid collection of absorption spectra over a wide energy range, and is well suited to time-resolved studies of reactions *in-situ*.

The ED-EXAFS technique is not without its difficulties, which are becoming to be appreciated with increasing experience.[27] One fundamental limitation is the inability to measure the 'intensity spectrum' of the incident beam, $I_0(E)$, *simultaneously* with the sample spectrum. Instead, the $I_0(E)$ spectrum must be measured either before or after the sample spectrum, which involves moving the sample out of the path of the beam. This exposes the measurements to fluctuations in the intensity of the beam. Although synchrotrons produce a very stable X-ray beam, the

changes in absorbance involved in the EXAFS spectrum are very small, and thus small fluctuations in the incident beam can be very significant. One symptom of this problem is distortions due to phase-contrast phenomena (or "speckle") associated with imperfections in the optics, and which appear as irregular fringes on the image. Another problem arises where the sample itself scatters X-rays at small angles, which is particularly a problem for powders.[27]

A further difficulty is the enhanced sensitivity to inhomogeneities in the sample. In principle, all wavelengths pass through the same section of sample at the focal point. However, since focussing and positioning are not perfect, and all samples have a finite thickness, X-rays of different energy will pass through different parts of the sample. Thus, it is important to achieve the greatest possible homogeneity in the sample to avoid a non-uniform background in the spectrum.

Very recently a third technique has been developed, known as *Turbo-XAS*. This is a 'hybrid' combination of the above two techniques, which overcomes some of the intrinsic problems of ED-EXAFS.[28]

10.4.2 Procedure

Sample preparation

As noted above, samples of very high homogeneity were required for these experiments.

The monoclinic zirconia reference was the same material described in Section 10.3.2. The zirconia powder was mixed with boron nitride powder, ground finely in ethanol, dried, and pressed into a wafer.

The gel sample examined was derived from a standard ZN1.0 type gel. Mixing a dry-ground gel with boron nitride did not produce a powder of sufficient homogeneity, so the crushed gel was thoroughly mixed and ground with boron nitride powder in water. The resulting mixture was then dried and pressed into a wafer. Mixing the gel with water dispersed it into a sol, similar to the sol from which the gel was originally formed, and drying caused the gel to form on the surface of the boron nitride particles.

Instrumentation

All experiments were carried out using beam-line 1-BM-B at the Advanced Photon Source (APS), Argonne National Laboratory, USA.* The APS is a 7 GeV, third-generation synchrotron X-ray source, providing an intense beam that allows very rapid collection of data.

The layout of the experimental optics is illustrated schematically in Figure 10-18. The silicon 'polychromator' crystal used the 220 reflection and was tuned to the 2nd harmonic for improved resolution. The energy range used for these experiments was approximately 17 800 to 19 000 eV. The sample was placed at the focal point of the beam, and the transmitted beam was detected by a 512 $\times$ 512 pixel CCD camera. An ion chamber in the beam path was used to measure beam flux, and a nickel filter was placed in front of the sample to eliminate higher harmonics.

A small furnace, based on a previously published design,[29] was built at ANSTO for the experiment. The cross-section of this furnace is illustrated schematically in Figure 10-19.

---

* This beamline is operated by the Synchrotron Research Instrumentation Collaborative Access Team (SRICAT), which focuses on the development of instrumentation and techniques for beamlines. To our knowledge energy-dispersive EXAFS had not been previously carried out on this beamline.

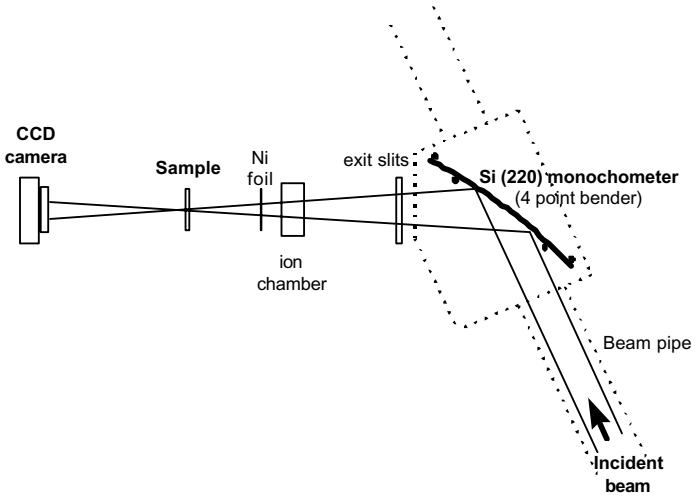

Figure 10-18: Schematic layout of the beam optics.

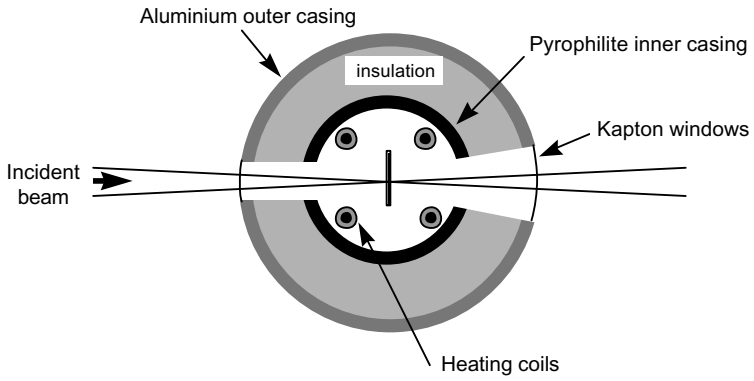

Figure 10-19: Schematic cross-section of the sample furnace.

Data collection

Due to the nature of the energy-dispersive optics, the incident intensity spectrum, $I_0(E)$, could not be measured simultaneously with the sample absorbance spectrum. Instead, the sample spectrum, $I_s(E)$, was measured first, then the sample (or the sample furnace) was moved out of the beam by stepping motors, and an $I_0(E)$ spectrum was measured. The 'dark-current' spectrum, $I_d(E)$, the CCD camera signal with no X-ray beam, was also collected and subtracted from each spectrum. The process of collecting these three spectra took a total of approximately 4 minutes. Thus, although the time to actually measure the sample spectrum was only a few seconds, the minimum time between sample spectra was relatively long.

The EXAFS spectra of the m-ZrO_2 reference was collected, with a 24 s collection time for each spectrum.

The gel-boron nitride sample wafer was mounted in the furnace, and heated to 600°C at a rate of 5°C/min. The spectra $I_s(E)$, $I_0(E)$ and $I_d(E)$ were collected approximately every five minutes, with a 10 s collection time for each spectrum.

Data treatment

The CCD camera measured transmitted intensity as a function of pixel position. The intensity was converted to absorbance by ratioing $I_s(E) - I_d(E)$ with $I_0(E) - I_d(E)$. The pixel position was calibrated to an energy scale by comparing the measured spectrum of reference materials with spectra of the same materials previously measured using conventional step-scanning apparatus. The conversion factor (in eV/pixel) was adjusted until the best match between the spectra was achieved. It was assumed that the pixel-to-energy scale was linear, *ie* that the energy dispersion of the beam was uniformly spread across the CCD detector. Although simple in principle, the results from this calibration process was not fully satisfactory, and the energy scale of the spectra may be slightly in error. This problem is amplified by the wide energy range required for EXAFS.

A background for each absorbance spectrum was simulated by a continuous spline, with four segments evenly spaced in k-space, using the *Spline* routine in the X-FIT software package.[19] Care was taken to define the background in a similar way to that used for the spectra discussed in the previous study in Section 10.3. The background was removed, and the spectrum converted to a $\chi(k)$ function with an E_0 value of 18 015 eV. The $\chi(k)$ function was weighted by k^3 to emphasise the high-k data. The ends of the Fourier-transformation window were at nodes, at approximately 4 and 10 Å^{-1}.

10.4.3 Systematic irregularities

Even though the beam flux was very high, the quality of the absorption spectra collected by the TRED technique was not nearly as good as that obtained by the conventional step-scanning technique. This was largely due to the presence of systematic, energy-dependent irregularities in the spectrum. Example absorption spectra are given in Figure 10-20. Each spectrum contained minor irregularities that initially appeared to be random 'noise', but a comparison of spectra revealed that many of these irregularities occurred consistently at the same energy. These irregularities remain despite ratioing with $I_0(E)$ and $I_d(E)$, and were not removed by

increasing the counting time. These irregularities may be equivalent to the 'speckle' discussed above in Section 10.4.1. It may also be related to small-angle X-ray scattering of the sample.*

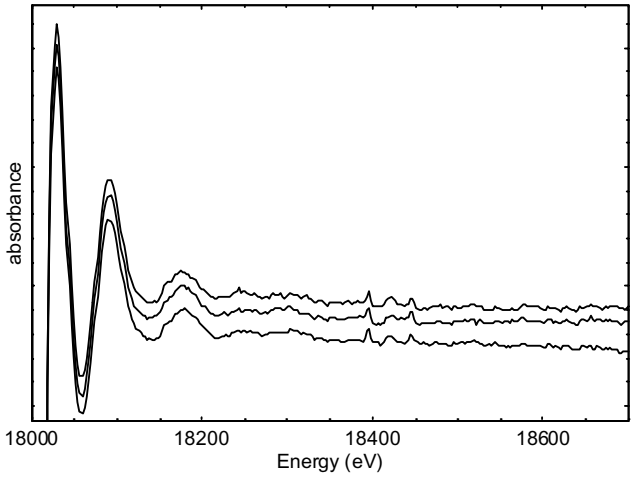

Figure 10-20: Three energy-dispersive absorbance spectra, measured at 180°C, 210°C and 250°C, during the decomposition of the gel. The systematic irregularities can be clearly seen.

More serious was the presence of much larger irregularities, or 'glitches', with much greater intensity than the EXAFS oscillations. These are probably directly due to imperfections in the monochromator crystal, and cannot be removed or smoothed. The first group was at 18390-18460 eV, which prevented any analysis at k values beyond 10 $Å^{-1}$.

The presence of these irregularities is a fundamental limit of doing EXAFS, over this energy range, on this beamline.

* Since these EXAFS experiments were carried out, it has been observed in SAXS experiments that fine boron nitride powder, the dilutant used for the samples, scatters X-rays very strongly.

10.4.4 Results and discussion

Scale conversion

The conversion factor determined was 2.55(5) eV/pixel. Any error in this value will offset the FT peak positions, which cannot be corrected for using conventional refinement programs. Assuming the error is proportional, an typical uncertainty of ± 0.05 eV/point would be equivalent to a systematic error in the position of the first FT peak of up to 0.05 Å.

Reference materials

The Fourier-transformed spectrum of monoclinic zirconia is shown in Figure 10-21, compared with an equivalent spectrum collected using the conventional wavelength step-scanning technique, presented in Section 10.3.4. Both spectra have been Fourier-transformed over the same window.

The spectra are quite similar in both the shape and position of the peaks. There is a slight discrepancy in the position of the first peak, which may be due to the calibration of the spectrum. This comparison indicates that ED-EXAFS spectra are comparable to those collected by the wavelength step-scanning technique.

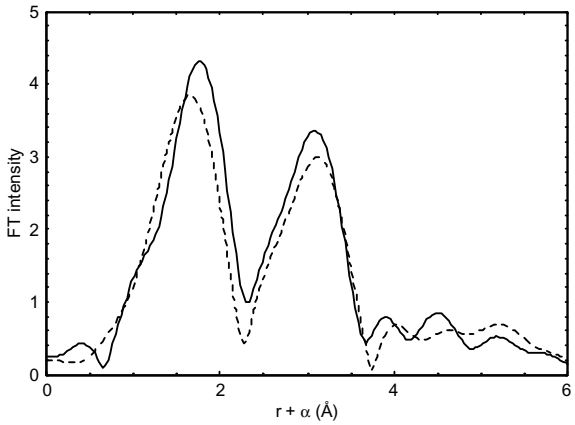

Figure 10-21: Fourier-transformed EXAFS spectra of m-ZrO_2, measured by ED-EXAFS (solid line), and conventional wavelength step-scanning (broken line).

***In-situ* characterisation during heating of a gel**

Spectra were collected at intervals of 20 - 40°C. Selected absorbance spectra covering the entire temperature range are shown in Figure 10-22, and corresponding Fourier-transformed EXAFS spectra are shown in Figure 10-23. The noise, systematic or otherwise, is quite

significant more than 200 eV beyond the edge. To show the changes that occur during crystallisation, Fourier-transformed EXAFS spectra, measured at 20°C intervals between 390 and 510°C, are given in Figure 10-24.

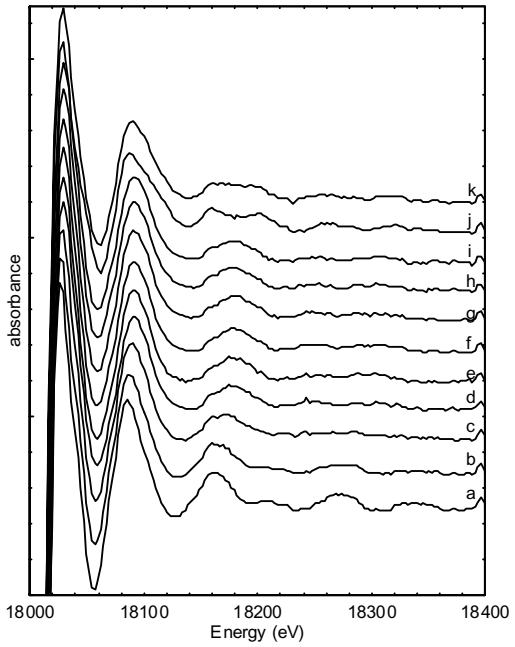

Figure 10-22: Selected energy-dispersive absorbance spectra, collected at temperatures (from a to k) 25, 100, 140, 180, 210, 250, 290, 350, 390, 450 and 510°C.

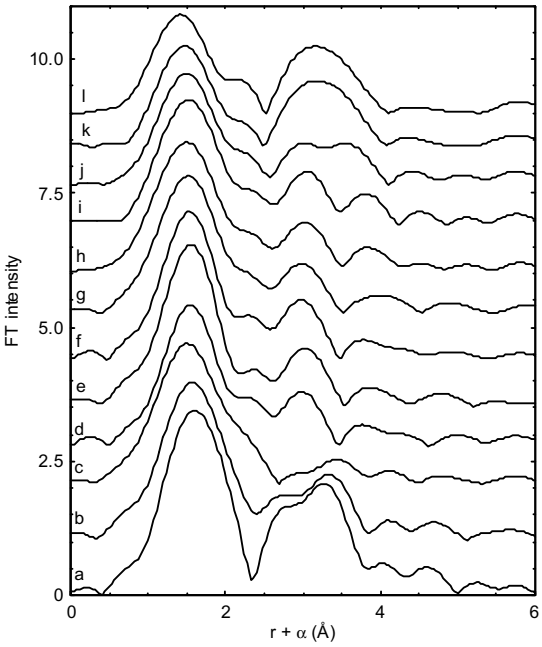

Figure 10-23: Selected Fourier-transformed ED-EXAFS spectra, collected at temperatures (from a to l) 25, 100, 140, 180, 210, 250, 290, 350, 390, 450, 510 and 550°C.

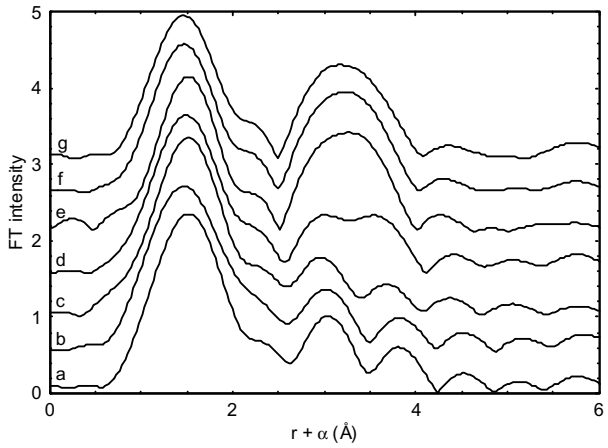

Figure 10-24: Fourier-transformed ED-EXAFS spectra, collected *in-situ* during crystallisation at temperatures (from a to g) 390, 410, 430, 450, 470, 490 and 510°C.

It is useful to compare these EXAFS spectra with those measured at ambient temperature after heating. Spectra of the samples discussed in Section 10.3 are given in Figure 10-25,

which can be compared with the near-equivalent spectra measured *in-situ*, given in Figure 10-26. All spectra are Fourier-transformed between 4 and 10 $Å^{-1}$.

As expected, the two spectra for the unheated gel are nearly identical. This confirms that there was no change in the short-range order of the gel when it was dispersed and re-gelled during the process of sample preparation.

Another observation is that the FT peaks measured *in-situ* at high temperature are weaker and broader than those in equivalent samples measured at ambient temperature. This is expected, and is due to the increased thermal vibrations of the structure.

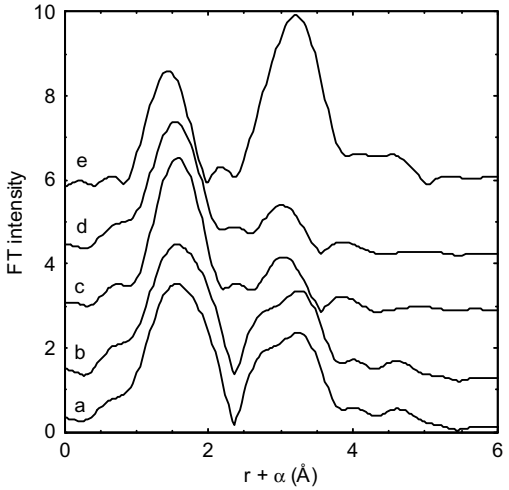

Figure 10-25: Fourier-transformed spectra, collected by conventional step-scanning at ambient temperature, of (a) the ZN1.0 gel, and (b-e) samples heated to 150, 300, 400 and 470°C.

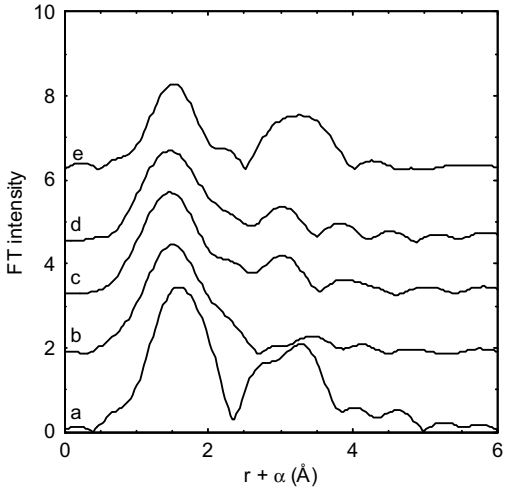

Figure 10-26: Fourier-transformed spectra, collected *in-situ* using TRED-EXAFS, at (a-e) 25, 140, 310, 410 and 470°C.

The structural information that can be obtained from these EXAFS spectra is much more limited that that available from the spectra discussed in the previous study, and the data was not suited to modelling.* This is due to the restricted *k* range available for analysis, the lower signal-to-noise ratio, and the much greater thermal disorder in the sample at elevated temperatures. The most useful information is the position of the FT peaks. Although these are subject to error due to uncertainties in calibration, the relative shifts in the peak position should be reliable. The high σ^2 values, due to thermal vibrations, would make coordination-numbers difficult to obtain.

* Some modelling of this data was attempted, but it was difficult to obtain consistent results. No results were obtained that added substantially to the information presented here or in Chapter 5.

The 25 - 180°C range corresponds with the decomposition of the gel to form a largely amorphous oxide. There are four collected spectra that cover this range, shown in Figure 10-23, spectra *a* - *d*. Over this interval the first FT peak shifts approximately 0.05 Å down to a lower position, while the second FT peak becomes much weaker while shifting to a higher position, by as much as 0.16 Å. By 180°C this second peak is replaced by a peak at a much lower position.

These shifts imply that during the first stage of decomposition (25-140°C) the Zr–Zr distances increase while the Zr–O distances decrease, a process consistent with the oxolation of hydroxy bridges, Zr–$(OH)_2$–Zr, to oxo bridges, Zr–O–Zr. In the next stage (140-180°C) the Zr–Zr distances become considerably shorter, but the structural mechanism for this is not clear at present. Possibly the Zr–O–Zr bonds become more angular, forcing the oxygen atoms out of the Zr–Zr plane, and allowing the zirconium atoms to approach each-other. This process is illustrated schematically in Figure 10-27.

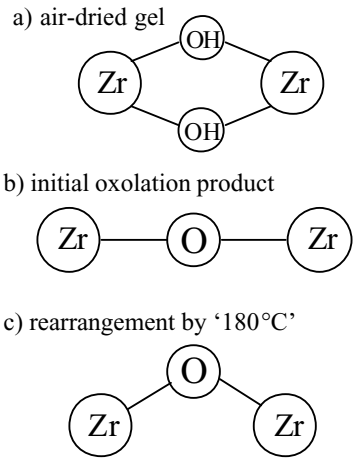

Figure 10-27: Possible mechanism for changes in Zr–O and Zr–Zr distance during the oxolation reaction from 25°C to '180°C'.

These changes in the FT spectrum are consistent with the differences between ambient-temperature spectra of equivalent samples, *a*, *b* and *c* in Figure 10-25. The change in modelled Zr–O distance was 0.04 Å. The main difference is in the temperature at which the changes occur, as can be seen from a comparison of Figure 10-25 and Figure 10-26. For the samples measured at ambient temperature, decomposition has just started after heating to 150°C, and is completed by 300°C. For the samples measured *in-situ*, decomposition has started by 100°C, and is complete by 180°C. The most likely explanation for this discrepancy

is that the furnace was 'over-heating' the sample by approximately 50°C in the early stages of the experiment, due to excessive radiant heat from the surrounding elements.

Another possible explanation is that the partially-decomposed sample at 150°C reverts back to its original structure after cooling, but there is no further evidence for any reversible processes from *in-situ* FT-Raman spectra in Section 5.3.1.

Between 180°C and 430°C there is very little change in the spectrum, and the structure appears to be quite stable. This is quite consistent with the results reported in Chapter 5.

As shown in Figure 10-24, crystallisation takes place entirely within a 40°C interval. Spectra at 430 and 470°C are characteristic of the material before and after the transformation, respectively. The spectrum measured at 450°C appears to be at an intermediate point *during* the crystallisation. The small number of spectra limits the information that can be obtained about the crystallisation process. Ideally the transformation from amorphous to crystalline could be modelled, but the small amount of data in the available k-range can not support the relatively complex model that would be required. The shifts in peak position and intensity with crystallisation are all consistent with the spectra measured in Section 10.3.

10.4.5 Conclusions

The following conclusions can be made from the energy-dispersive EXAFS study:

- Time-resolved ED-EXAFS characterisation of the decomposition and crystallisation processes gives spectra that are largely consistent with spectra measured at ambient temperatures.
- The decomposition process occurred in two stages. The first involved the oxolation of hydroxy bridges, leading to an increased Zr–Zr separation. The second stage resulted in a decreased Zr–Zr separation, and possibly involved the displacement of oxygen atoms out of the Zr–Zr plane.
- There is no or little change in the short-range structure of the material between 200°C and crystallisation at approximately 450°C.
- Changes in short-range structure associated with crystallisation take place within a 40°C interval.
- Energy-dispersive EXAFS is a powerful technique for characterising changes in short-range structure during heat treatment. However, improvements in spectrum quality, and a reduction of the time between collection of sample spectra, are required to make full use of the technique's potential.

10.5 References

1. P. Li, I.W. Chen and J.E. Penner-Hahn, "X-ray absorption studies of zirconia polymorphs. I. Characteristic local structures" *Phys. Rev. B 48* [14] 10063-10073 (1993)
2. P. Li, I.W. Chen and J.E. Penner-Hahn, "X-ray absorption studies of zirconia polymorphs. III. Static disorder and thermal distortion" *Phys. Rev. B 48* [14] 10082-10089 (1993)
3. W. Yuren, L. Kunquan, W. Dazhi, W. Zhonghua and F. Zhengzhi, "The EXAFS study of nanocrystalline zirconia" *J. Phys. C 6* 633-40 (1994)
4. G. Antonioli, P.P. Lottici, I. Manzini, G. Gnappi, A. Montenero, F. Paloschi and P. Parent, "An EXAFS study of the local structure around Zr atoms in Y_2O_3-stabilised ZrO_2 by the sol-gel method" *J. Non-Cryst. Sol. 177* 179-186 (1994)
5. X. Turrillas, P. Barnes, A.J. Dent, S.L. Jones and C.J. Norman, "'Hydroxide' precursor to zirconia: Extended X-ray absorption fine structure study" *J. Mater. Chem. 3* [6] 583-586 (1993)
6. J.-L. Tosan, B. Durand, M. Roubin, F. Chassagneux, L. Mosoni, F. Bertin and B. Moraweck, "pH-metric and Raman investigations of zirconium aqueous solutions and gels submitted to a reflux" *J. Non-Cryst. Sol. 160* 167-176 (1993)
7. X. Turrillas, P. Barnes, D. Gascoigne, J.Z. Turner, S.L. Jones, C.J. Norman, C.F. Pygall and A.J. Dent, "Synchrotron-related studies on the dynamic and structural aspects of zirconia synthesis for ceramic and catalytic applications" *Radiat. Phys. Chem. 45* [3] 491-508 (1995)
8. D.C. Koningsberger and R. Prins, *X-ray Absorption,* Wiley, New York (1988)
9. B.K. Teo, *EXAFS: Basic Principles and Data Analysis*, Springer-Verlag, Berlin (1986)
10. M. Gautier-Soyer, "X-ray absorption spectroscopy: A tool to study the local atomic and electronic structure of ceramics" *J. Eur. Ceram. Soc. 18* 2253-2261 (1998)
11. G. Dalba and P. Fornasini, "EXAFS Debye-Waller factor and thermal vibrations of crystals" *J. Synchrotron Rad. 4* 243-255 (1997)
12. E. Sevillano, H. Meuth, J.J. Rehr, "Extended X-ray absorption fine structure Debye-Waller factors. I Monatomic crystals" *Phys. Rev B 20* [12] 4908-4911 (1979)
13. G. Beni and P.M. Platzman, "Temperature and polarization dependence of extended x-ray absorption fine-structure spectra" *Phys. Rev. B 14* [4] 1514-1518 (1976)
14. K.A. Daly and J.E. Penner-Hahn, "Extracting dynamic information from EXAFS: Simultaneous analysis of multiple temperature-dependent data" *J. Synchrotron Rad. 5* 1383-1389 (1998)
15. J. Rockenberger, L. Tröger, A. Kornowski, T. Vossmeyer, A. Eychmüller, J. Feldhaus and H. Weller, "EXAFS studies on the size dependence of structural and dynamic properties of CdS nanoparticles" *J. Phys. Chem. B 101* 2691-2701 (1997)
16. E.A. Stern, P. L■vi◔┗, and Z. Zhang, "Thermal vibration and melting from a local perspective" *Phys. Rev. B 43* [11] 8850-8860 (1991)
17. *Ab initio Multiple-Scattering X-ray Absorption Fine Structure and X-ray Absorption Near Edge Structure Code*, FEFF Project, Department of Physics, FM-15 University of Washington, Seattle, WA 98195
18. D. Haskel, B. Ravel, M. Newville and E.A. Stern, "Single and multiple scattering EXAFS in $BaZrO_3$: a comparison between theory and experiment" *Physica B 208 & 209*, 151-153 (1995)
19. P.A. Ellis and H.C. Freeman, *J. Synchrotron Rad. 2* 190 (1995)
20. M. Newville, B. Ravel, D. Haskel, E.A. Stern, Y. Yacoby, "Analysis of Multiple Scattering EXAFS Data using Theoretical Standards" *Physica B 208 & 209*, 154-156 (1995)
21. A. L. Ankoudinov, *Relativistic Spin-dependent X-ray Absorption Theory*, Ph. D. Thesis, University of Washington (1996)
22. P.E. Petit, F. Guyot and F. Farges "Thermal evolution of $BaZrO_3$ and $SrZrO_3$ perovskites from 4 K to 773 K: an EXAFS study at Zr-K edge" *J. Phys. IV Fr. 7* 1065-1067 (1997)
23. C. Landron, A. Douy and D. Bazin, "From liquid to solid: residual disorder in the local environment of oxygen-coordinated zirconium" *Phys. Stat. Sol. B 184* 299-307 (1994)
24. R.W.G. Wyckoff, *Crystal Structures*, Interscience, New York (1948)
25. C.J. Howard, B.A. Hunter and D.-J. Kim, "Oxygen position and bond lengths from lattice parameters in tetragonal zirconias" *J. Am. Ceram. Soc. 81* [1] 241-243 (1998)
26. N. Igawa, Y. Ishii, T. Nagasaki, Y. Morii, S. Funahashi and H. Ohno, "Crystal structure of metastable tetragonal zirconia by neutron powder diffraction study" *J. Am. Ceram. Soc. 76* [10] 2673-2676 (1993)

27. S. Pascarelli, T. Neisius, S. De Panfilis, M. Bonfim, S. Pizzini, K. Mackay, S. David, A. Fontaine, A. San Miguel, J.P. Itié, M. Gauthier, A. Polian "Dispersive XAS at third-generation sources: strengths and limitations" *J. Synchrotron Rad. 6* 146-148 (1999)
28. S. Pascarelli, T. Neisius and S. De Panfilis, "Turbo-XAS: dispersive XAS using sequential acquisition" *J. Synchrotron Rad. 6* 1044-1050 (1999)
29. A.J. Dent, M. Oversluizen, G.N. Greaves, M.A. Roberts, G. Sankar, C.R.A. Catlow and J.M. Thomas, "A furnace design for use in combined X-ray absorption and diffraction up to a temperature of 1200°C" *Physica B 208 & 209* 253-255 (1995)

11. Major findings

Scope of the study

This thesis describes the evolution of structure that occurs in an inorganic, aqueous, sol-gel route for the preparation of zirconia. A number of broad issues concerning the solution-based processing of zirconia have also been investigated, particularly those involving the 'metastable' tetragonal zirconia phase.

The sol was prepared by forced hydrolysis of a zirconyl nitrate solution to form a stable dispersion of hydrous, colloidal particles. The gelation process was a physical, reversible aggregation of these particles. When heated, the gel decomposed to form partially-ordered, amorphous zirconium oxide, followed by crystallisation of the 'metastable' tetragonal phase. Further heating led to crystal growth and other processes, and eventually the transformation of the tetragonal phase to the thermodynamically-stable monoclinic phase.

At each of these stages different aspects of the material structure have been investigated, including the short-range order, crystalline lattice parameters, particle packing, porosity, and speciation of the nitrate anion. This has required a wide range of complementary characterisation techniques, including Raman spectroscopy, XRD, TEM, DTA/TGA, SAXS, DLS, EXAFS, NMR, and nitrogen sorption, some of which have been used in *in-situ* studies.

Major findings

The size, shape, and short-range structure of the particles in the sol and gel were investigated using Raman spectroscopy, DLS, SAXS, XRD and EXAFS. The particles were found to be plate-shaped, approximately 3 nm across and 0.5 nm thick, and composed of up to several stacked 'sheets' of partially-disordered zirconium hydroxide. The zirconium atoms are arranged in a regular, planar square lattice, joined by double hydroxy-bridges. Detailed evidence for this structure has not been previously reported. The structure is formed by polycondensation of the 'cyclic-tetramer' cations, which are initially present in the precursor zirconyl nitrate solution.

^{14}N NMR and Raman spectroscopy have been used to identify changes in the location and coordination of nitrate anions with the formation of the particles. All of the nitrate anions

present in the sol are located within the hydration sphere of the particle, but most are not directly coordinated to the surface. The absence of any anions in the 'solution' between the particles may play a role in the stabilisation of the sol.

Gelation is an entirely physical process, which is reversible upon addition of water, even after heating at 200°C. The arrangement of the particles in the gel may be either face-to-face stacking or a more disordered face-to-edge arrangement, depending on ageing of the sol over a period of months; this is attributed to changing charge-distribution on the particles. During gelation approximately half of the nitrate groups located in the hydration sphere become directly coordinated to the zirconium atoms.

The thermal decomposition of the gel was studied by DTA/TGA, XRD, EXAFS and Raman spectroscopy, and the stages involving dehydration, oxolation and loss of nitrate were identified. After heating to 300°C the material is largely amorphous zirconium oxide. The technique of time-resolved energy-dispersed EXAFS has been shown to have a promising role to play in this type of study.

The complex crystallisation process at 450°C was investigated, and was found to involve two near-simultaneous reactions: the exothermic crystallisation of the amorphous material into the tetragonal phase, and the endothermic conversion of residual nitrate groups to NO_x gas. A structural mechanism for crystallisation of the 'metastable' tetragonal phase was proposed, based on similarities between the tetragonal crystal structure and the disordered sheet structure in the amorphous material just prior to crystallisation. A high-quality X-ray diffraction pattern and Raman spectrum of the tetragonal phase were also reported.

The crystalline material consists of approximately 30 nm crystals, containing unusual 2 - 5 nm intracrystalline mesopores. These pores are derived from NO_x-containing bubbles in the amorphous material, and have been studied by TEM and nitrogen sorption.

The microstructure of the crystalline oxide was studied with further heating to 1000°C, using XRD, TEM and nitrogen sorption. The average crystal size remains at 30 nm until approximately 900°C, although faceting of the crystal surfaces develops. The lattice parameters of the tetragonal phase change with increasing heat-treatment, with the unit-cell

tetragonality (c/a) increasing from 1.017 to 1.020. This is a previously-unreported phenomenon which may be associated with the stability of the phase.

The tetragonal phase transforms to the monoclinic phase after heating to a 'critical temperature' between 900 and 950°C, and this temperature is associated with the loss of residual surface nitrate species and/or a substantial increase in the mass diffusion rate. It is shown that the crystal size and surface area has little influence on the tetragonal-to-monoclinic transformation, contrary to claims made by many previous reports. The evidence presented here does not unambiguously support any particular theory out of those reviewed in Section 2.4. However, if Garvie's 'surface-energy' theory holds, then it is clear that changes in the surface energy of the crystal play a far greater role in the stabilisation of the tetragonal phase than does the actual surface area or crystal size.

The tetragonal-to-monoclinic transformation itself occurs during cooling, between 400 and 100°C, and has been studied *in-situ* by time-resolved Raman spectroscopy. This technique has been found to be very useful to study zirconia phase transformations when synchrotron X-ray diffraction is unavailable. The transformation can be 'quenched' below approximately 100°C. A 'quenched' tetragonal phase will continue transforming to monoclinic when reheated to above 200°C, thus the tetragonal phase is thermodynamically metastable immediately before it transforms to the monoclinic phase. The 'stable' form of pure tetragonal zirconia is either thermodynamically stabilised (by surface species) or requires a nucleation event of some kind.

In an additional study, the Raman spectra of zirconyl chloride and nitrate salts were reported and assigned, replacing previously-reported assignments. First-principles vibrational modelling was shown to be useful in the assignment of the Raman spectrum.

The conclusions of this investigation contribute not only to the understanding of this particular route for processing zirconia, but also to a broader understanding of aqueous zirconium systems, the chemical processing of zirconia, and the tetragonal-to-monoclinic zirconia transformation mechanisms.

Appendix A. Preparation and characterisation of $Zr(OH)_3NO_3$

It was of interest to find a crystalline compound that could be studied as a chemical and structural analogue to the amorphous ZN1.0 gel. The compound $Zr(OH)_3NO_3$ was considered to be a good candidate for this purpose for two reasons. Firstly, it has a similar composition to the ZN1.0 gel, with very similar fractions of Zr, N, O and H. Secondly, it has a sheet-structure, as do the particles in the gel.

The crystal structure of $Zr(OH)_3NO_3$ was recently solved by Bénard and Louër.[1] The structure is built from neutral layers. Each zirconium atom is connected to three other zirconium atoms via a pair of hydroxyl bridges each, and is also coordinated by a symmetric bidentate nitrate group. The IR spectrum has been reported previously,[2] but not the Raman spectrum.

$Zr(OH)_3NO_3$ was synthesised by dissolving zirconium carbonate in nitric acid to form a sol/solution with a $Zr:NO_3$ molar ratio of 1:1, then heating at 80°C in a sealed container for several weeks. The XRD pattern confirmed that the product had the same structure as reported by Bénard and Louër, although it was somewhat less crystalline.

The Raman spectrum is given in Figure A-1. There is a single band at 1039 cm^{-1}, assigned to the bidentate nitrate ligand. The sharp bands below 650 cm^{-1} are distinctly different from those in the spectrum of the gel, or the spectra of any zirconyl salt. The assignment of these bands is beyond the scope of this study, but the strong differences in the spectra indicate that there is little similarity in the short-range structure with the gel or zirconyl salts. Furthermore, the DTA/TGA trace showed that the decomposition sequence was also quite different to that of the ZN1.0 gel.

Unfortunately, $Zr(OH)_3NO_3$ cannot be used as an analogue for the ZN1.0 gel structure. However, the Raman spectrum of this material has been reported for the first time.

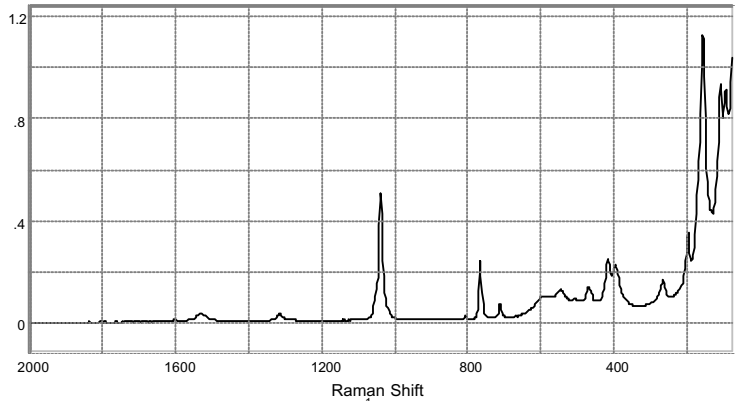

Figure A-1: Raman spectrum of crystalline $Zr(OH)_3NO_3$

References

1. P. Bénard and D. Louër, "The layer structure of $Zr(OH)_3NO_3$ determined *ab initio* using conventional monochromatic X-ray powder diffraction" *J. Phys. Chem. Solids 56* [10] 1345-1352 (1995)
2. O.A. Govorukhina, S.D. Nikitina, V.N. Brusentsova and V.A. Masloboev, "Polytherm of the ZrO_2–HNO_3–H_2O system" *Russ. J. Inorg. Chem. 35* [12] 1804-1806 (1990)

Appendix B. Determination of tetragonal:monoclinic phase ratios from Raman spectra

Introduction

This Appendix describes the development of a procedure by which the relative ratios of tetragonal and monoclinic phases can be calculated from a Raman spectrum.

A previously-published procedure for calculating zirconia phase ratios from Raman spectra used the *maximum intensity* of characteristic bands in the spectra of the monoclinic, yttria-stabilised tetragonal and yttria-stabilised cubic phases.[1] This method was too limited to be used in the work described in Chapter 7, and the method described in this Appendix has two major advantages:

1. The *integrated intensity* of the characteristic bands is used. This approach is particularly important for Raman spectra measured at elevated temperature, as considerable peak broadening is expected to occur, making the maximum intensity an unreliable indicator of the total intensity of the band.
2. The 'standard' materials used to construct the calibration curve are as similar to the 'experimental' materials as possible. The intensity of the Raman signal from a given phase may depend considerably on particle size, crystallinity and other factors, so it is highly desirable to perform calibration with materials that are as close as possible to the materials to be studied. Furthermore, the Raman spectrum of the stabilised tetragonal phase may have different relative intensities from the spectrum of the 'metastable' phase (depending on lattice parameters, etc), so samples of the metastable phase were used for calibration.

The general approach used was to take a number of samples containing both metastable tetragonal and monoclinic phases, and measure both the X-ray diffraction pattern and the Raman spectrum. The phase ratio for each sample was calculated from the XRD pattern and a calibration curve constructed.

Procedure

Samples were prepared by one of two methods. Two samples were prepared by heating a standard ZN1.0 gel at 700 or 900°C for an hour. This method was limited as it is difficult to prepared a sample with between 10 and 90 % monoclinic present. The second method was to prepare some near-pure-phase tetragonal zirconia and pure-phase monoclinic zirconia, by heating a finely-ground standard gel for an hour at 600 and 1000°C, respectively. The powders were then mixed in appropriate quantities to prepare three further samples.

Each sample was carefully packed into an XRD sample holder, and the X-ray diffraction pattern measured over the 2θ range 25 - 35°.* This range includes the principle peaks of the monoclinic and tetragonal diffraction patterns. The *volume fraction* of the monoclinic phase, f_m, was calculated by the method used elsewhere in this thesis.[2]

Care was taken to ensure that the same section of sample was characterised by both techniques. The Raman spectrum was measured immediately after the diffraction pattern was

* Scintag X1 Advanced Diffraction System, using Cu K_α radiation.

measured,* on the same powder surface. The powder was not removed from the XRD sample holder, but placed directly into the Raman spectrometer and the laser focussed on the surface. This precaution was taken as experience has shown that powder handling, particularly the packing of a powder into the XRD sample holder, can cause a significant fraction of the metastable tetragonal phase to convert to monoclinic.

The strongest band in the tetragonal zirconia spectrum (260 cm^{-1}) and the two strongest bands in the monoclinic spectrum (188 and 175 cm^{-1}) were chosen to be used in the phase-ratio calculation. A parameter, χ_m, was defined by Equation B-1 to represent the relative integrated-intensities of these peaks. The value of χ_m for each sample was then plotted against f_m to give the calibration chart. This approach is based on that used for the diffraction pattern.[2]

$$\chi_m = \frac{I^{175} + I^{188}}{I^{175} + I^{188} + I^{260}} \qquad \textbf{Equation B-1}$$

The integrated intensity, I, of the bands in the Raman spectrum was determined by fitting the 425 - 130 cm^{-1} region with standard 'peak-fitting' software. The peak-shape used was mixed Gaussian-Lorentzian, and for consistency the fraction of Lorentzian character was kept within certain limits for each peak.

Results and discussion

The resulting calibration curve is shown in Figure B-1. The estimated error for both f_m and χ_m is ± 0.03. There is a lack of data points between 20 % and 60 % monoclinic, however the chart is still useful for providing an approximate conversion between the Raman spectrum and the phase ratio.

The data points have been fitted by a third power polynomial, which is given in Equation B-2 and is also shown on the plot. Note that, according to the plot, very small fractions (< 3 vol %) of either phase cannot be detected by Raman spectroscopy. This is quite probably due to the limitations of the peak-fitting process.

$$f_m = 0.411\chi_m^3 - 1.20\chi_m^2 + 1.73\chi_m + 0.0360 \qquad \textbf{Equation B-2}$$

This calibration plot has been used in Chapter 7 to calculate phase volume fractions from Raman spectra measured with a conventional spectrometer. To do this it has been assumed that the relative Raman activity of the two phases are the same for conventional and FT-Raman spectrometers. Although any difference is likely to be small, ideally the calibration would have been repeated with the conventional Raman spectrometer, and at several different temperatures between ambient and 1000°C. However, neither of these experiments were practical due to time constraints and limited access to equipment.

* Bio-Rad FT-Raman II, using an excitation line of 1064 nm from a Nd:YAG laser. The effective resolution was 4 cm^{-1}.

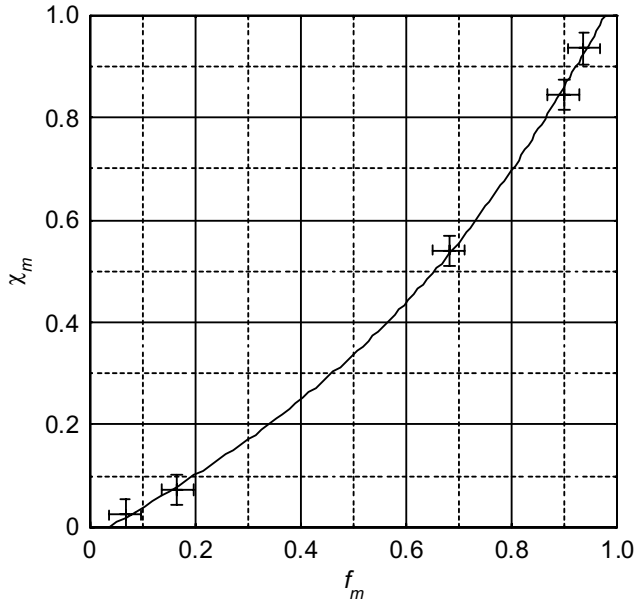

Figure B-1: Plot of the parameter χ_m^R against the volume fraction monoclinic, f_m.

References

1. C.G. Kontoyannis and M. Orkoula, "Quantitative determination of the cubic, tetragonal and monoclinic phases in partially stabilised zirconias by Raman spectroscopy" *J. Mater. Sci. 29* 5316-5320 (1994)
2. H. Toraya, M. Yoshimura and S. Somiya, "Calibration curve for quantitative analysis of the monoclinic-tetragonal ZrO_2 system by X-ray diffraction" *J. Am. Ceram. Soc. 67* [6] C119-C121 (1984)

My son, there is something else to watch out for. There is no end to the writing of books, and too much study will wear you out.

Ecclesiastes, Chapter 12.